POTENTIAL IMPACTS OF FORMATION WATERS ON THE INTEGRITY OF CLASS H CEMENT AND RESERVOIR ROCK IN CARBON [CO-] SEQUESTRATION SETTINGS

by

CIRCE ANDROMEDA VERBA

A DISSERTATION

Presented to the Department of Geological Sciences
and the Graduate School of the University of Oregon
in partial fulfillment of the requirements
for the degree of
Doctor of Philosophy

June 2013

DISSERTATION APPROVAL PAGE

Student: Circe Andromeda Verba

Title: Potential Impacts of Formation Waters on the Integrity of Class H Cement and Reservoir Rock in Carbon [Co-] Sequestration Settings

This dissertation has been accepted and approved in partial fulfillment of the requirements for the Doctor of Philosophy degree in the Department of Geological Sciences by:

Mark Reed	Chair
Jason Ideker	Core Member
John Logan	Core Member
Paul Wallace	Core Member
Ronald Mitchell	Institutional Representative

and

Kimberly Andrews Espy	Vice President for Research and Innovation; Dean of the Graduate School

Original approval signatures are on file with the University of Oregon Graduate School.

Degree awarded June 2013

DISSERTATION ABSTRACT

Circe Andromeda Verba

Doctor of Philosophy

Department of Geological Sciences

June 2013

Title: Potential Impacts of Formation Waters on the Integrity of Class H Cement and Reservoir Rock in Carbon [Co-] Sequestration Settings

The focus of this research is to characterize the risk of carbon sequestration under downhole conditions with regards to wellbore cement integrity. The primary research objective was to understand the geochemical interactions of simulated sequestration brines and wellbore cement. There are four key focuses of this study with regards to cement interaction: 1) Simulated brines saturated with Supercritical CO_2 and CO_2-O_2; 2) Adjacent formation host rock under sequestration conditions; 3) Geochemical modeling using CHIM-XPT based on the experimental studies of points 1) and 2) above; 4) Geomechanical strength tests of CO_2 exposed cements.

First, the interaction of cement with supercritical CO_2, CO_2-saturated brines, and CO_2-O_2 mixtures at 50 °C, 85 °C, and 28.9 MPa was evaluated. Cement exposed to a lower salinity brine (1 *M*) had a larger alteration depth (1.25 mm) compared to cement exposed to a higher salinity brine (2.2 *M*) (0.836 mm). CO_2-O_2 exposed cements displayed alteration depths of 1.6 mm at 85 °C and 0.7 mm at 50 ^{o}C for 1 *M*. The cement exposed to the 2.17 *M* solution had an alteration extending 1.685 mm.

The second focus studied the influence of adjacent formations and observed mineral trapping in the Grande Ronde Basalt-cement. Studies of Mt. Simon Sandstone-cement interaction provided evidence for high CO_2 storage capacity.

The third focus is geochemical modeling using CHIM-XPT. Pure CO_2 saturated brines yielded a pH of 3.0 at 1 *M* and 3.85 at 2.17 *M*. The CO_2-O_2 gas run calculated a pH of 3.96 at 1 *M* and 3.85 at 2.17 *M*. The Pasco solution after exposure had a pH of 6.97 and an estimated

dissolved 161 g of $CO_{2\ (g)}$. The pH of the Illinois Basin brine and Mt. Simon sandstone [and cement paste] was 5.8 with an estimated 139 g of CO_2 consumed. Lastly, geomechanical tests on CO_2 exposed cements indicated that addition of oxygen or changes in temperature play a key role in compressive and tensile strength, decreasing strength by 20-35%. This research highlighted the importance of representing the *in-situ* wellbore environment when conducting laboratory experiments.

This dissertation includes previously published and unpublished co-authored material.

CURRICULUM VITAE

NAME OF AUTHOR: Circe A. Verba

GRADUATE AND UNDERGRADUATE SCHOOLS ATTENDED:

University of Oregon, Eugene, OR
Northern Arizona University, Flagstaff, AZ
Oregon State University, Corvallis, OR

DEGREES AWARDED:

Doctor of Philosophy 2013, Geological Sciences, University of Oregon
Master of Science, 2009, Geology, Northern Arizona University
Bachelor of Science, 2007, Earth Sciences and Geology, Oregon State University

AREAS OF INTEREST:

Geochemistry
Planetary Geology

PROFESSIONAL EXPERIENCE:

Department of Energy, National Energy Technology Laboratory (2009-current)
U.S. Geological Survey, Astrogeology Branch (2007-2009)

GRANTS, AWARDS, AND HONORS:

ORISE Post Graduate Internship (2009-2010)
Federal DOE NETL through Oak Ridge MMIP Fellowship (2010-2013)
Best Poster Award American Ceramic Society Annual Cement & Concrete Meeting 2011

PUBLICATIONS:

Verba, CA., O’Connor, W., Rush, G. (2013) The Influence of Brine on Class H Cement Paste with CO_2 Injection. In review. International Journal of Greenhouse Gas Control.

Verba, CA., O'Connor, W., Rush, G., Palandri, J. (2013) Basalt and Sandstone Host Rock with Class H Portland Cement Under CO_2 Sequestration Conditions. In Review. International Journal of Greenhouse Gas Control.

Verba, CA., Reed, MH., Ideker, JH., Kutchko, B. Geomechanical Strength Tests for Portland Cement for Sequestration Purposes. NETL-TRS-X-2013; NRAP Technical Report Series; U.S. Department of Energy, National Energy Technology Laboratory: Morgantown, WV, 2013.

Lavalleur, H.J., Verba, C.A., Disenhof, C.R., O'Connor, W.K., Colwell, F.S. (2013). Changes in natural microbial communities exposed to geological carbon sequestration conditions in basalts. International Journal of Greenhouse Gas Control. In press.

Verba, CA., O’Connor, W., Ideker, J. (2012) Advances in Geological CO_2 Sequestration and Co-Sequestration with O_2. ACI-CANMET Special Publication in Recent Advances in Concrete Technology and Sustainability Issues. Prague, Czech Republic. 2012 Special Publication V. 298. pp. 1-16.

O'Connor, W., Rush, G., Verba, C. (2012) The NETL Aqueous Mineralization Process: Recent Developments and Novel Applications. NETL-Publication 335 Report.

ACKNOWLEDGMENTS

I would like to thank my NETL mentor Dr. Barbara Kutchko for her expertise in cement chemistry and William O'Connor for being an excellent science lead. Barbara, you are a great friend and a great colleague, and I am thrilled to be involved in future collaborations in cutting research. I want to give a special thanks to my co-advisors Dr. Jason Ideker from Civil Engineering at Oregon State University and Dr. Mark Reed from Geological Science at University of Oregon in bridging this research and supporting me. Jason, you have been a wonderful advisor that was very encouraging and engaging. Mark, I have learned a great deal about geochemical modeling from you and enjoyed your long distance email humor.

I also had a great team to support me during this process, I want to acknowledge Keith Collins at NETL and John Donovan from CAMCOR microanalytical facility for assistance on electron microscopy, Paul Danielson for his amazing assistance on microscopy tips and polishing, and Corinne Disenhof for XRD analysis. Mary Fantacone, thank you for your assistance in editing. In addition, I would like to say thank you to fellow graduate students for assistance with last minute proof reading: Matthew Adams and Tengfei Fu. Another person I'd like to thank is Kelly Rose; you are an intelligent scientist that I admire and look up to, and I am gracious for your words of wisdom. I must also thank my division director, Cathy Summers for allowing me to grow and pursue my Ph.D while working for the Department of Energy, NETL.

Finally, I would like to thank my family and network of friends. I want to thank my mother and sister, Karen and Dione Verba, for their late night phone conversations and advice. Daniel Darrow, thank you for being loving, being patient and supporting me while I pursue my dream. Kate Foster, you have been a wonderful friend. My dear friend Joshua Jameson (Yoshi), thank you for reminding me that I could do it.

If I forgot to thank anyone, you know I that I appreciate and thank you! It has been a long, sometimes difficult, journey and I value every single one of you for your assistance, compassion, and being a shoulder or an ear to chew on.

This research was supported in part by an appointment to the National Energy Technology Laboratory Research Participation Program, sponsored by the U.S. Department of Energy and administered by the Oak Ridge Institute for Science and Education. This report was prepared as an account of work sponsored by an agency of the United Sates Government. Neither the United States Government nor any agency thereof, nor any of their employees, makes any warranty, express or implied, or assumes any legal liability or responsibility for the accuracy, completeness, or usefulness of any information, apparatus, product, or process disclosed, or represents that its use would not infringe privately owned rights. Reference herein to any specific commercial product, process or service by trade name, trademark, manufacturer, or otherwise does not necessarily constitute or imply its endorsement, recommendation, or favoring by the United States Government or any agency thereof. The views and opinions of authors expressed herein do not necessarily state or reflect those of the United States Government or any agency thereof.

TABLE OF CONTENTS

Chapter Page

I. INTRODUCTION 1

II. BACKGROUND.. 6

2.1. Introduction...6

2.2. Cement Application, Hydration and Environmental Conditions 7

2.2.1. Cement Application 7

2.2.2 Chemical Constituents & Hydration Reactions 8

2.2.3. Durability Under High Pressure and Temperature 13

2.3. Chlorides, Salts, and Salinity 16

2.3.1. The Influence of Salts on Cement Paste 16

2.3.2. Salinity and Supercritical CO_2 19

2.4. Secondary Ettringite Precipitation 20

2.5. Why Sequestration? 23

2.5.1. Diffusion 24

2.5.2. CO_2 Cement Degradation 25

2.5.3. Degree of Alteration in a CO_2 Environment...................................... 28

2.6. Previous Research...30

2.7. Objectives: Experimental Improvements for CO_2 Sequestration.........................36

III. THE INFLUENCE OF BRINE ON CLASS H PORTLAND CEMENT PASTE WITH CO_2 INJECTION 41

3.1. Introduction...41

3.2. Experiment...45

3.2.1. Sample Preparation, Curing, and CO_2 Exposure 45

3.2.2. Sample Analysis 46

3.2.3. Geochemical Modeling 48

3.3. Results 49

3.3.1. pH Calculation 49

3.3.2. Hydration Prior to CO_2 Exposure 50

3.3.3. Brine Effects Under Supercritical CO_2 52

3.3.3.1. Cured and Unreacted *Surrogate* Brine 55
3.3.3.2. Big Sky 57
3.3.3.3. MGSC-Mt. Simon 57
3.3.3.4. *SECARB* 58

3.4. Discussion 59

3.4.1. pH estimate and mineral saturation states 59

3.4.2. CO_2 Exposure 61

3.4.3. Supercritical CO_2 versus CO_2-saturated brine exposure 63

3.4.4. Brine Composition and Chloride Content 65

3.4.5. Gain and Loss of Elemental Concentration 67

3.5. Conclusion 72

IV. ADVANCES IN GEOLOGICAL CO_2 SEQUESTRATION AND CO-SEQUESTRATION WITH O_2 74

4.1. Introduction 74

4.2. Research Significance 77

4.3. Experimental Procedure 77

4.4. Analytical Procedure 78

4.5. Experimental Results And Discussion 79

4.5.1. Solid and Solution Chemistry 84

4.5.2. Semi-Quantative XRD 86

4.5.3. pH Estimate and Mineral Saturation 89

4.5.4. Corrosion of Stainless Steel Autoclaves 90

4.6. Further Research 91

4.7. Conclusions 91

V. BASALT AND SANDSTONE HOST ROCK WITH CLASS H PORTLAND CEMENT UNDER CO_2 SEQUESTRATION CONDITIONS 93

5.1. Introduction 93

5.2. Materials & Methods 97

5.2.1. Analytical Techniques 100

5.2.2. Geochemical Modeling 101

5.3. Results 102

5.3.1. XRD & Solid Composition 102

5.3.2. Grande Ronde Basalt-Pasco Solution 103

5.3.2.1. Effect of CO_2 on hydrated cement paste 103

5.3.2.2. Basalt-cement Interface 104

5.3.2.3. Basalt Core 106

5.3.3. Mt. Simon Sandstone- Illinois Basin Brine 108

5.3.3.1. Effect of CO_2 on cement paste 108

5.3.3.2. Interface between Mt. Simon Sandstone and cement paste 109

5.3.3.3. Sandstone Core 109

5.4. Geochemical Modeling 110

5.4.1. Columbia River Basalt + Pasco Solution + CO_2 110

5.4.2. Columbia River Basalt +Cement paste + Pasco Solution + CO_2 113

5.4.3. Mt. Simon Sandstone + Illinois Brine + CO_2 115

5.4.4. Mt. Simon Sandstone + Cement paste+ Illinois Brine + CO_2 117

5.5. Discussion 119

5.5.1. Grande Ronde Aqueous Phase Chemical Analysis 119

5.5.2. Mt Simon Sandstone Aqueous Phase Chemical Analysis 120

5.5.3. Laboratory Experiments and Modeling Comparison 122

5.6. Conclusion 124

VI. GEOMECHANICAL STRENGTH TESTS FOR PORTLAND CEMENT FOR SEQUESTRATION PURPOSES 127

6.1. Introduction: 127

6.1.1. Cement Chemical Constituents & Hydration Response 128

6.1.2. CO_2 Sequestration & Challenges 130

6.1.3. Formation of $CaCO_3$ 131

6.1.4. Mineral Precipitation & Expansion 132

6.1.4.1. Carbonation of Cement 133

6.1.4.2. Delayed Ettringite 134

6.2. Materials & Methods 137

6.2.1. Cement and CO_2 Conditions 137

6.2.2. Sulfuric Acid Conditions 137

6.2.3. Strength Applications 138

6.3. Results and Discussion 139

6.3.1. Alteration from Sulfuric Acid 139

6.3.2. Tensile Point Load Tests 140

6.3.3. Compression Tests 143

6.4. Conclusions 145

VII. CONCLUSIONS 147

7.1. Summary 147

7.2. Immersion Test Conclusions 148

7.2.1. Pure CO_2: 148

7.2.2. Co-Sequestration: 149

7.2.3. Host rock-cement-brine interaction: 150

7.3. Geochemical Modeling Conclusions 150

7.4. Tensile and Compression Conclusions 152

APPENDICES

A. CLASS H CEMENT EXPOSED TO SUPERCRITICAL CO_2 153

Scanning Electron Microscopy Backscatter and X-ray Elemental Maps 153

X-ray Diffraction Patterns: Class H Cement Exposed To Supercritical CO_2 193

B. CLASS H CEMENT EXPOSED TO SUPERCRITICAL CO_2-O_2......................... 153

Scanning Electron Microscopy Backscatter and X-ray Elemental Maps 153

X-ray Diffraction Patterns: Class H Cement Exposed To Supercritical CO_2-O_2.......................... 193

C. MT. SIMON SANDSTONE & GRANDE RONDE BASALT BONDED TO CLASS H CEMENT EXPOSED TO SUPERCRITICAL CO_2........................... 195

Scanning Electron Microscopy Backscatter and X-ray Elemental Maps 153

D. ALS Laboratories Mineral And Solution Chemical Data And Analytical Errors.......................... 223

ALS Laboratory Group: Minerals.......................... 223

ALS Laboratory Group: Analytical Chemistry and Testing Services for Solution 223

REFERENCES CITED.......................... 228

LIST OF FIGURES

Figure Page

2-1. Schematic of drilling a well to completed depth (DOE, 2007). 7

2-2. SEM Secondary Electron image (SE) A: Alite; B: Belite with twinning. From Campbell (1996). 9

2-3. Hydration of cement as it sets and hardens with hydration products (in cement nomenclature, see below for chemistry) Adapted from Locher et al., 1976 in PCA 2011 Design and Control of Concrete Mixtures, 15th edition. 10

2-4. Secondary electron SEM image of A) C-S-H structure which appears very cilia-like and fills in between unhydrated cement grains; B) Needle-like ettringite (AFt) and $Ca(OH)_2$ appears as hexagonal. http://www.cementlab.com 11

2-5. The effect of temperature on the hydration kinetics of a Class G oil well cement (Nelson, 1990). The higher the temperature, the more rapid the cement hydrates and hardens. Hydration is dependent on temperature. 14

2-6. Solid phase percolation at setting for different w/c. Matrix is filled with water (blue), black particles are cement grains, and gray shells as the hydration products. (a) Hydration products have percolated, relatively low w/c and has set; (b) the same degree of hydration as (a), but has higher w/c and not set; (c) at a higher degree of hydration, the sample with the same w/c as in (b) has set (modified from Zhang et al., 2010). 15

2-7. Comparison of predicted mutual solubilities of CO_2 and H2O using the activity coefficient at 30, 60, and 90°C and 1–600 bar for solutions up to 4 *M* NaCl as tabulated by Duan and Sun (2003) (solid lines) and Rumpf et al. (1984) (dashed lines) to that calculated of Spycher & Pruess (2005). CO_2 solubilities computed by Duan and Sun (2003) using their full solubility model are also shown for comparison (symbols). 19

2-8. Pressure and temperature phase diagram for CO_2 demonstrating the critical point in which CO_2 acts as a supercritical fluid >7.38 MPa and > 31.1^{o}C. Modified from TUV NEL (http://www.tuvnel.com/) 23

2-9. Schematic displaying calcium migration and dissolution in the formation of alteration fronts (Kutchko et al., 2007). 27

2-10. Bjerrum plot: Dissolved CO_2 (aq), HCO_3^{-}, CO_3^{2-}, H^{+}, and OH^{-} ions as a function of pH. At modern seawater pH, dissolved inorganic carbon is in the form of bicarbonate (modified by Ridgwell & Zeebe, 2005). 28

3-1. BSE images before CO_2 exposure: A) 28-day air-cured cement with atmospheric carbonation (indicated by black dashed line) and no hydration halo; B) 28-days distilled water-cure of cement resulted in aggressive cation (but not Mg) leaching. Dashed line separates the leached from unaltered cement; C) sample of 28 day curing in brine resulting in limited Ca cation leaching and a large hydration shell (enlarged) on anhydrous cementitious phase and large external crystals (EDS X-ray maps in Fig. 3-2). Semi-quantitative chemical compositions are shown for each zone. 50

3-2. Upper image shows SEM-EDS (Ca, Cl, Na) element X-ray maps for 28-day Surrogate brine cured cement focusing on the exterior portlandite and NaCl crystals, the outline of which indicates that a likely pseudomorph of NaCl is replacing the portlandite crystals. Lower image shows a magnified BSE image with cubic NaCl grains within the pseudomorph. 51

3-3. SEM montage image which displays alteration around the outer rim of the cement cylinder (outlined by white dotted line). 53

3-4. SEM BSE image of samples exposed to supercritical CO_2 (left) and CO_2-saturated Surrogate brine (right) after 84 days. Dotted line indicates alteration boundaries: 1) porous silica zone, 2) $CaCO_3$ zone, 3) an apparent Ca-depleted cement. Scale bars are 300 µm. 53

3-5. Chlorine concentration (EDS) given in wt. % at the bottom and shown by brightness in the images. A) Cement cured in distilled water to indicated base Cl (0.11%) from epoxy contamination; B) 28-days cure Surrogate brine (prior to CO_2) with uniform Cl concentration (~1%) and precipitation of

NaCl (bright white); C) CO_2 exposure for 84 days in the Surrogate brine with several zones of Cl enrichment including a 2.2% enrichment in Ca^{2+} depleted zone and 1.4% adjacent into unaltered cement. The chloride X-ray maps were used as a proxy for carbonation and alteration depth. 54

3-6. Development of alteration depth with exposure time in the Surrogate brine. SEM BSE: Exposure time is given from left to right: (A) 28 days, (B) 56 days, and (C) 84 days. Dashed lines on BSE images show zone boundaries. Cylinder surface is on the left side of images. Zone 1: outermost porous silica zone, 2: the $CaCO_3$ zone and 3: Ca-leached zone, The Cl-enriched zone inward from the Ca-leached zone is not apparent here. 55

3-7. The average alteration depth (average based calculation 96 data points) on cement paste, increasing with time exposed to supercritical CO_2, depicting interactions of different brine types. 55

3-8. A calcium SEM-EDS X-ray map of the alteration from the SECARB brine sample (highest salinity of 2.2 *M*) that formed a fracture during rapid depressurization in the curing process. This sample shows calcite (pale yellow) in the fracture along with a darker orange that represents the de-calcified margin i.e. where fracture traverses into the cement paste cylinder pulling calcium to form calcite, or where calcium has diffused into solution. 59

3-9. A SEM BSE image where cement exposed to supercritical has two coencentric carbonation fronts. The altered cement has lost calcium to form the inner calcite band. 64

3-10. Titanium isocon plot with average concentrations of species of the leached cement paste zone of remnant porous silica to a fresh cement composition with a 95% confident interval=Ti ±2σ. 69

3-11. Titanium isocon plot with average concentrations of species in altered cement that has been carbonated against a fresh cement composition with a 95% confident interval=Ti ±2σ. 70

3-12. Titanium isocon plot with average concentrations of species in altered cement paste (SEM-EDS apparent calcium depleted zone) against fresh cement composition with a 95% confident interval=Ti ±2σ. 71

4-1. Carbonation and alteration depth of portland cement cylinders exposed to A) 84 days and pure-CO_2 at 50^oC, B) 53 days CO_2-O_2: 85^oC, and C) 66 days CO_2-O_2 50^oC. Zone 1 is the porous-Si, zone 2 is $CaCO_3$, and zone 3 is the Ca^{2+} leading into unaltered cement. Dashed line indicates finely distributed Ca^{2+} leached zone; no boundary. Scale bar 1 mm (0.04 in). 80

4-2. Minerals and polymorphs in CO_2-O_2 injected samples. A) Calcium silicate polymorph, B) Hydrotalcite forming on ferrite grains, C) Ettringite needles in the Ca^{2+} depleted zone, and D) Cubic halite grains within the carbonated zone. 82

4-3. Montage backscatter (BSE) image (left) and Ca^{2+} EDS map (right) of CO_2-O_2 exposure sample with diffuse alteration boundary (white outline) extending into the cylinder. Scale 4.5 mm (0.18 in) 83

4-4. A) Chloride attack on stainless steel autoclave and B) thermocouple thermowell corrosion result of CO_2-O_2 exposure tests. 90

5-1. Basalt encased in cement after 84 days of exposure to supercritical CO_2. A) 2.54 x 152.4 mm (1"x 6") Grand Ronde basalt core in CO_2-saturated brine lacking surface crystals and supercritical CO_2 with portlandite crystals on the surface. A-A' and B-B' indicate where thin section were of the basalt in cement. B) Top surface of the cylinder. The white box is seen in (c); C) Transmitted polarized light microscopy of the interface between basalt (polymineralic and colorful) and cement (dark fine, grained) with grey calcium carbonation band of the basalt. The yellow-gold color indicates mineral replacement, primarily carbonation. Scale bar 200 µm. 99

5-2. Sandstone encased in cement after 84 days of exposure to supercritical CO_2. A) 2.54 x 152.4 mm (1"x 6") Mt. Simon sandstone core in CO_2-saturated brine (reddish color) and supercritical CO_2 (gray). A-A' and B-B' shows where thin section were cut of the sandstone in cement. B) Top view of the cylinder with an approximate box to represent a close up of the boundary. C) Bottom cut of the cylinder. Transmitted polarized light microscopy of the interface between sandstone and cement with thin calcite band (gray) that has filled in a pre-existing fracture. Scale bar 500 µm.. 100

5-3. A SEM-BSE montage image of the Grande Ronde basalt/ portland cement interface with elemental (EDS-X-ray maps) overlays of Mg, Fe, Ca^{2+}, O. The purple hues: cement; blue hues basalt where the darker hues represent alteration. The thin orange rim is the (Ca, Fe, and Mg) carbonate band. Large pieces of the cement have broken are off after exposure to supercritical CO_2. Scale bar 10 mm. 104

5-4. SEM BSE images A) Basalt-cement and B) Sandstone-cement samples exposed to supercritical CO_2 for 84 days. Dotted line indicates alteration boundaries: 1) porous silica zone, 2) $CaCO_3$ zone, 3) Ca-depleted cement............ 105

5-5. Changes in the solution composition of the CO_2-saturated Pasco Basin at 35^oC and 10 MPa. Na^+, Mg^{2+}, and Si^{4+} increase in concentration from mineral dissolution. K^+ peaks at 21 days and begins to slowly decline. HCO_3- slowly increases after CO_2 injection and the pH increases. No change in calcium (detection limit 10 mg/l) indicates $CaCO_3$ in the cement has not started to dissolve.. 106

5-6. A) Transmitted polarized photomicrograph of the Grande Ronde basalt CO_2-exposure experimental test. Bright orange carbonate species infilling edges of zeolites within the basaltic vesicles. Scale bar 200 µm. B) SEM-BSE cameo image with Mg, Fe, Ca^{2+}, O EDS-X-ray maps overlaid. Reddish hue represents iron rich carbonate, dark blue represents carbonate (magnesite and calcite). Ol: altered olivine; Mt: magnetite. Scale bar 50 µm. 107

5-7. A SEM-BSE montage image of the Mt. Simon sandstone-Class H Portland cement in a CO_2-saturated Pasco Basin solution with Mg^{2+}, Fe^{2+}, Ca^{2+}, O^{2+} EDS-X-ray maps. Brown-red represents altered cement; the blue is unaltered cement. The blue-green rim which follows the entire interface is calcium carbonation. The dark green color represents the sandstone. The checkered pattern of light blue is an artifact of the scanning and stitching of BSE images. Scale bar 20 mm. 108

5-8. SEM BSE image with EDS X-ray map overlay of the Mt. Simon sandstone sample (no cement) exposed to CO_2 with amorphous silica surrounding quartz (qtz) grains, thin calcium carbonation covering with halite (white), and sylvite (bright teal) precipitation. Scale bar is 50 µm. 110

5-9. CHIM-XPT plot of the Grande Ronde Basalt immersed in Pasco Basin solution with 50 grams of CO_2 titrated until saturation pressure of 102 bars. Plot shows the change of mineral phases and chemical species with titrated basalt. 112

5-10. CHIM-XPT graph of CO_2 is titration into 161 g of cured cement and 125 g Grande Ronde Basalt in 1 kg of Pasco Basin fluid to a saturation pressure 102 bars. Plot shows the change of mineral phases and chemical species with titrated basalt. 114

5-11. CHIM-XPT graph of Mt. Simon sandstone in 1.04 kg Illinois basin fluid and with 139 g CO_2 is titrated to 104 bars. Plot shows the change of mineral phases and chemical species with titrated sandstone. 116

5-12. CHIM-XPT plot of cured cement with Illinois basin fluid and Mt. Simon sandstone with CO_2 is titrated into the system. Plot shows the change of mineral phases and chemical species with titrated sandstone. Quartz is shown as supersaturated, but is not involved in the reaction as it is treated as an inert mass. 118

5-13. Trend of aqueous species between the cured cement-basalt-Illinois basin brine. Changes in the solution composition of the CO_2-saturated Illinois Basin brine at 35°C and 10 MPa. Right-hand side Y-axis applies to aqueous Si^+ and HCO_3^-; left Y-axis all other species. Na^+ and Mg^{2+} concentration fluctuates. Si solution initially decreases and then returns to initial levels. HCO_3 spikes at 63 days, marking the depletion of portlandite in the cement. The actual concentrations of Na^+ and HCO_3^- were multiplied by 0.1 for plotting. 121

6-1. Geologic sequestration from CO_2 production to CO_2 injection into a reservoir with a caprock (DOE, 2007). 130

6-2. Schematic displaying calcium migration and dissolution in the formation of alteration fronts (from Kutchko et al., 2007). 132

6-3. Close up of cement paste pore space filled with secondary ettringite needles extending into fractures. 136

6-4. Alteration of hydrated portland cement exposed to CO_2-O_2 under sequestration conditions and then atmospheric conditions with 7% sulfuric acid for 7 days. A) Degradation of cement paste core cured with minor gypsum precipitation at 85^{o}C and B) Crystalline precipitation of gypsum on portland cement exposed to CO_2-O_2 at cured 50^{o}C. 140

6-5. Average tensile strength for cured portland cement samples exposed to CO_2; cured cement samples exposed to CO_2-O_2; CO_2-O_2 and sulfuric acid leach, and a marble sample used for high pressure and natural temperature. 142

6-6. Compressive strength of cement samples comparing cured cement at 50^{o}C, co-sequestered simulated, CO_2-O_2 mixed gas for 56 days at both 50^{o}C and 85^{o}C, and sulfuric acid submerged cement cured at both 50^{o}C and 85^{o}C................ 144

LIST OF TABLES

Table Page

2-1. Abbreviations and cement constituents (from Neville, 2004). 9

2-2. Typical composition (weight %) and fineness of API cements in oxide nomenclature. American Society for Testing and Material (ASTM) equivalents are included (modified from Nelson,1990). 12

2-3. Table of previous research compiled to compare cement type, curing conditions, experimental conditions and total alteration/carbonation depth. 39

3-1. Derived from basin-specific data: Brine compositions of 3 of 7 NETL Phase III Partnership sites and lab created Surrogate. 44

3-2. Solid analysis of raw cement powder, cured cement paste, and hydrated cement after supercritical CO_2 exposure. Time (days) is time of exposure to cement (28, 56, and 84 days).Curing solution seen in Table 3-3. Altered cement analyzed discussed in methods. 45

3-3. Analyses of the aqueous solutions from brine-cured cement paste and hydrated cement paste after CO_2 exposure. Time (days) is time of exposure to CO_2 (28, 56, and 84 days). 48

3-4. Semi-quantitative estimates of mineral weight percent (wt %) composition (from JADE 9 Whole Pattern Fitting; no internal standard used). Errors are large because the sample collected was a slice of the altered cement rind, but it included a substantial amount of unaltered cement. Amorphous silica is difficult to quantify, but is representative of the accepted range of C-S-H. High concentrations of $CaCO_3$ mirror lower concentrations of $Ca(OH)_2$ reflecting carbonate replacement of the portlandite upon CO_2 alteration. 52

3-5. Depth of alteration for each sample based on 15 (section) samples, 90 total measurements, average calculated on 24 data points; using the average standard deviation. The brine notation: duration- autoclave-brine exposed to Surrogate (1 M) in cured brine solution; Surrogate (1 M) in new brine post-cure; SECARB (2.17 M) brine; Big Sky (1.19 M); MGSC Mt. Simon (1.272 M) brine. 62

4-1. Total alteration depth of CO_2 and CO_2-O_2 exposure at 50/85^oC. Alteration depth of CO_2 from Verba, 2011. 80

4-2. Brine solution chemical compositions of the post-cured solution and the post-gas exposure solutions taken at several exposure intervals (mg/l). 84

4-3. Solid chemical compositions of the unhydrated cement, the cured hydrated cement paste, and cement paste post-CO_2 and CO_2-O2 exposure (wt%).......... 85

4-4. XRD analyses of CO_2 and CO_2-O_2 exposure comparing the semi-quantified concentrations of minerals present due to gas and temperature differences in weight percent. 87

5-1. Initial solid composition (weight %) for the hydrated Class H cement paste, Grande Ronde Basalt, and Mt Simon Sandstone before subjected to supercritical CO_2. 97

5-2. The initial composition of the solutions prior to cement curing or supercritical CO_2 injection. Pasco brackish solution with 0.013 total mol/L being dominant with NaCl, Na_2SO_4 and NaF. Illinois Basin brine with 1.267 M dominated by NaCl, $CaCl_2$, $MgCl_2$, and Na_2SO_4 (source: Riedel (PNL), Illinois Geological Survey). 98

5-3. Solid composition for the Grande Ronde Basalt-Class H cement and Mt. Simon sandstone- cement after exposure to supercritical CO_2 (84 days). 103

6-1. Point load test data to determine tensile strength of 1) marble, cement paste cured in 1 M NaCl, $CaCl_2$, and $MgCl_2$, brine (no exposure to gas), 2) CO_2, 3) CO_2-O_2 exposed cement, and then 4) submerged in H_2SO_4. 141

6-2. Compressive tests on hydrated portland cement cured in a 1 M NaCl, $CaCl_2$, and $MgCl_2$, brine, then cement samples exposed to CO_2-O_2 at 50^oC and 85^oC, and then samples submerged in sulfuric acid at 50^oC and 85^oC. 143

CHAPTER I

INTRODUCTION

Climate change and the ensuing increase of global air and ocean temperatures can be linked to the rise of carbon dioxide (CO_2) levels, which can be attributed to anthropogenic influences (IPCC, 2007). There are many challenges in understanding mitigation of climate change and reducing CO_2 emissions to the atmosphere. One proposed method involves geologic carbon sequestration by capturing CO_2 from large industrial power plants and injecting into deep geologic formations (IPCC, 2007). Potential storage sites include depleted or active oil reservoirs, deep saline bearing formations, and unminable coal seams. In this research, sedimentary formations are considered as they are wide spread and have a storing potential of 1,000-10,000 Gt CO_2 for predicted duration of 1,000 years (IPCC, 2005).

However, there are concerns with CO_2 sequestration. Potential CO_2 leakage pathways include active or reactivated faults, open fractures, breaches through the confining strata, and active or abandoned oil or gas wells drilled for exploration and production (Bachu and Celia, 2009). Wellbores typically use portland cement to line and/or plug the well in order to provide zonal isolation and to support the steel casing. Wellbores are vulnerable due to the reactivity of the cement when in contact with injected CO_2. CO_2 can escape from a wellbore from regions between the steel casing and cement, between the cement and rock formation, and through the cement itself (Duiguid & Scherer, 2009).

Supercritical CO_2 will dissolve in the various formation solutions, effectively forming carbonic acid which will react with the portland cement in the well. Previous work studying the effects of supercritical CO_2 in contact with wellbore cement have been documented for enhanced oil recovery (EOR) and laboratory experiments (e.g. Carey et al., 2007, Kutchko, 2007; 2008 and others). However, many of these studies address pure or simple brine solutions instead of addressing the effects of actual basin brines on CO_2 solubility and cement alteration rates. This research builds upon those previous studies in that simulated formation brines and formation rocks were used to determine wellbore cement integrity under CO_2 storage conditions.

The primary research objective was to evaluate geologic sequestration conditions of supercritical CO_2 on wellbore-seal integrity and to understand the geochemical interactions of simulated sequestration brines. To achieve the research objective there were four primary focuses of this study:

1. Investigate the impact of supercritical CO_2 species and simulated brines saturated with CO_2, or CO_2 -O_2 on Class H Portland cement under co-sequestration conditions.
2. Evaluate the influence of supercritical CO_2 on host rock formation and the bonded cement under sequestration conditions.
3. Conduct geochemical modeling using CHIM-XPT based on these experiments.
4. Perform geomechanical strength tests on cements after exposure to CO_2 settings.

The first focus of this study was to characterize supercritical CO_2 interaction with Class H portland cement, assuming little interaction with the host rock in brine-bearing formations. The initial investigation includes examination of cement paste subjected to both humid supercritical CO_2 and CO_2-saturated brines for up to 84 days at 50 °C and 28.9 MPa to simulate downhole CO_2 storage conditions. The experiment is conducted again to incorporate a CO_2-O_2 mixed gas injection to determine co-sequestration potential. Both of the gas studies include:

Analysis of the effects of distilled water and synthetic brines, based on several U.S. Department of Energy (DOE) National Energy Technological Laboratory (NETL) Phase III Regional Partnership sites, with a variety of Na-Mg-Ca-Cl brine compositions and salinities (1–2.17 *M*). were investigated. Microstructural and chemical characterization of brine and cement phases were completed using X-ray diffraction (XRD), petrographic analysis, scanning electron microscopy (SEM) with energy dispersive spectroscopy (EDS), and solid and solution analyses.

Using these techniques, the total microstructural alteration and carbonation depth of the cement subjected to supercritical CO_2 were compared. In addition, the relationship of the cement and the interaction of the acidic brine during CO_2 injection is proposed to determine volume and mass transfer. This is accomplished by using a Ti isocon elemental plot to determine elements that may have been gained or lost within the cement as quantified from an electron microprobe (EMPA).

The second focus of the study was to investigate CO_2 leakage pathways at the interface of the formation host rock and the cement sheath. One potential method of permanently storing CO_2 is through physical mineral trapping. The Columbia River Basalt formation bonded to cement is considered as it provides aqueous ions for carbonation to occur. The basalt is immersed in a brackish Pasco Basin solution, with a salinity near 0.013 *M*. In addition to mineral trapping of CO_2, hydrodynamic trapping could allow for carbon storage capacity in a large silicic formation such as the Mt. Simon Sandstone immersed in Illinois Basin brine, with salinity of 1.28 *M*.

The third focus includes calculating aqueous species and the pH in a cement-brine-gas system. A thermodynamic geochemical model (CHIM-XPT) was used to calculate mineral saturation and the pH at wellbore conditions. The modeling uses experimental solution data from portland cement exposed to supercritical CO_2, CO_2-O_2, and CO_2-SO_2 mixed gas as well as experimental solutions from basalt and sandstone bonded to cement. CHIM-XPT balances chemical reactions and determines equilibrium states of the solution under pressure and temperature based on the experimental data from the gas-liquid-gas immersions tests at 50°C and pressure of 28.9 MPa.

The final focus was to investigate the impact on mechanical stability once hydrated wellbore cement is subjected to acidic gas conditions. Marble, hydrated cement, and hydrated cement exposed to supercritical CO_2 conditions were examined. Compressive and tensile strengths of the cement paste after exposure to mixed gas composition of CO_2, CO_2-O_2, and CO_2 -O_2- sulfuric acid were measured.

The following section provides a description of each chapter of this dissertation. A transition will describe the proceeding chapter.

Chapter II: This chapter contains the background information about cement types, cement chemistry, cement hydration, and wellbores types. Chapter II also includes the chemical reaction of cement once CO_2 is introduced into the system. This chapter also discusses ettringite precipitation and the influence of chlorides on hydrated cement.

Chapter III: This chapter describes the effects of various brine types on Class H portland cement in a pure CO_2 environment. This will be submitted to International Journal of Greenhouse Gas Control and is formatted as such. All written documents was completed by Circe Verba after experiments were completed. Experimental assistance was done by William O'Connor and Hank Rush at NETL. Mark Reed assisted in geochemical modeling (CHIM-XPT). Contributions were made from Jason Ideker and Barbara Kutchko. All co-authors provided editorial assistance. Chapter III includes previously published and unpublished co-authored material.

Chapter IV: The focus in this study is the alteration of cement under mixed CO_2-O_2 conditions with mixed brines at 50°C and 85°C. This was published in ACI-CANMET Special Publication in Recent Advances in Concrete Technology and Sustainability Issues. 2012. Chapter IV corresponds with focus 1 and focus 3. Co-authored material is included from Jason Ideker and William O'Connor. Coauthors provided editorial assistance. Experimental assistance to William O'Connor and Hank Rush. James Palandri and Mark Reed assisted in geochemical modeling (CHIM-XPT).

Chapter V: This chapter presents a comparison of experimental settings and geochemical modeling (CHIM-XPT) of carbon sequestration conditions of host rock Columbia River Basalt-cement and Mt. Simon Sandstone-cement in their respective brines. Chapter V corresponds with focus 2 and focus 3. Chapter V will be submitted to the International Journal of Greenhouse Gas Control and is formatted as such. Chapter V include material from co-authors William O'Connor, Gilbert Rush, and James Palandri.

Chapter VI: Chapter VI corresponds with Focus 4 in which tensile and compression tests were completed on hydrated cement samples exposed to specific gas compositions and conditions. This chapter is formatted to be a future internal National Energy Technology Laboratory, National Risk Assessment (NRAP) Partnership Technical Report Series (TRS) publication. Co-authored material is included from contributions from Jason Ideker, Barbara Kutchko, and Mark Reed. The paper was written by myself, with my coauthors providing editorial assistance. Experimental set-up assisted by John Logan.

Chapter VII: Conclusion of the dissertation

The appendices include:

- Appendix A: SEM electron backscatter images and correlating elemental maps and XRD patterns for pure CO_2 injection.
- Appendix B: SEM electron backscatter images and correlating elemental maps and XRD patterns for CO_2 -O_2 injection.
- Appendix C A subset of SEM BSE-EDS images of host rock-cement interface and XRD patterns.
- Appendix D: Tables to include ALS Laboratory mineral and solution methods and analytical errors.

CHAPTER II

BACKGROUND

2.1. Introduction

For decades, the high demand for energy has necessitated drilling into the subsurface for fossil fuels. As a consequence of burning fossil fuels and other human activities, there has been a sharp rise in atmospheric CO_2 levels and a commensurate increase in global temperatures. Currently research has begun on removing and sequestering atmospheric CO_2 by injecting it into deep geological formations using similar steel casings and oilwell cements. During petroleum extraction, Class G and portland oilwell cement is pumped into a steel casing where it is subjected to high subsurface pressures and temperatures. The wellbore environment may affect the chemical and physical behavior of the cement during hydration. Injected CO_2 may further alter wellbores within the storage formation (Nelson, 1990). It is therefore vital to determine the durability of oil well cement in candidate CO_2 storage formations by conducting experiments that simulate pressure, temperature, and formation fluids of the wellbore.

This dissertation takes an interdisciplinary approach of civil engineering and geology to answer this question by combining geochemical and geomechanical research to investigate how the diffusion of CO_2 into wellbore cement impacts cement integrity. This chapter addresses the application of different types of wellbores, cement hydration, and the factors that influence cement paste relevant to this research. During the initial experimental analyses, chlorides and secondary ettringite precipitation on hydrated (hardened) cement were shown to be potential hazards and will be addressed in subsequent chapters.

2.2. Cement Application, Hydration and Environmental Conditions

2.2.1. Cement Application

Drilling oil wells dates back to 7th century China and the first modern wells using portland cement pumped into a steel casing and bonded to the wall rock were drilled 1903 and this method is still used today (Riva & Atwater, 2008; Barron, 2009). Modern oil wells include: 1) exploration wildcat wells to obtain geological or geophysical information in potential oil or gas reservoirs, 2) appraisal wells drilled after oil discovery to determine the size of the deposit, and 3) production wells for oil and gas.

In drilling an oil well, a rotary drill is used to make a hole 5-36 inches in diameter and a smaller-diameter steel casing is placed inside the hole to strengthen the wellbore (Fig 2-1). The space between the steel casing and rock formation, the annulus, is filled with portland cement providing both zonal isolation and casing support. Nelson (2006) states that zonal isolation is primary function of the cement and prevents fluids (water, oil, gas) from migrating to different zones outside of the casing. Abandoned wells are typically sealed with cement plugs to prevent vertical migration of fluids out of the wellbore (Nelson, 1990).

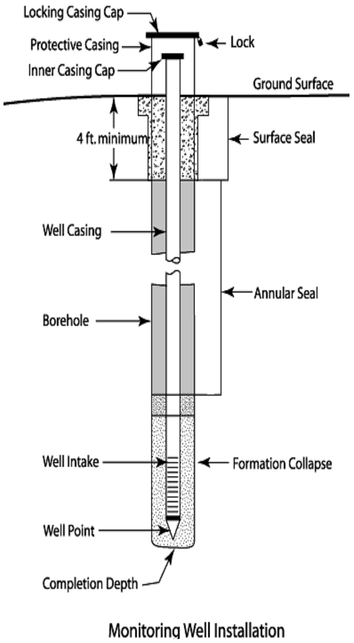

Monitoring Well Installation

Figure 2-1. Schematic of drilling a well to completed depth (DOE, 2007).

Additives and admixtures, classified as accelerators, dispersants, extenders, fluid-loss control agents, lost circulation control agents, retarders, weighting agents, and/or brand specific additives such as surface hardener are often added to the cement thus modifying the characteristics of the cement slurry. There are also supplementary cementitious materials (SCM's) that can be added to the cement that include fly ash, furnace slag and pozzolans; SCMs are not used in the research presented here and will not be discussed in detail.

2.2.2 Chemical Constituents & Hydration Reactions

The main ingredients in portland cement are calcium and silica. Naturally occurring calcium carbonates, such as limestone, provides the calcium component whereas silica is provided by clays and shale. The clays may also contain iron oxides (Fe_2O_3), alumina (Al_2O_3) and alkalis. The raw materials are crushed, combined in the required proportions, and heated to 1450-1550^{o}C in a high temperature kiln. The resulting "clinker" is allowed to cool, mixed with 3 to 5% gypsum to prevent flash set, and ground to make the final product of portland cement (Taylor, 2001). Cement chemistry uses an abbreviated form of the chemical symbol based on the oxide content of relevant species as follows: CaO becomes C; SiO_2 is S; Al_2O_3 is A; Fe_2O_3 is F; H_2O is H.

The major components of unhydrated portland cement are tricalcium silicate (Ca_3SiO_5), dicalcium silicate (Ca_2SiO_4), tricalcium aluminate ($Ca_3Al_2O_6$), and calcium aluminoferrite (Ca_4AlFeO_5) (Table 2-1). To prevent flash set, or instantaneous setting, gypsum is added when grinding the clinker). Ca_3SiO_5, called alite, is often impure and contains trace elements (Fig. 2-2A). The second calcium silicate, Ca_2SiO_4 is commonly called belite (Fig. 2-2B) and when contaminated with trace elements is referred to as a polymorph (β-C_2S) (Taylor, 1997). The calcium silicates are the major constituents of unhydrated cement and form hydration products in the cement paste. Semi-amorphous calcium-silicate-hydrate (C-S-H) is the primary constituent of portland cement and is as high as 70% in some cement types.

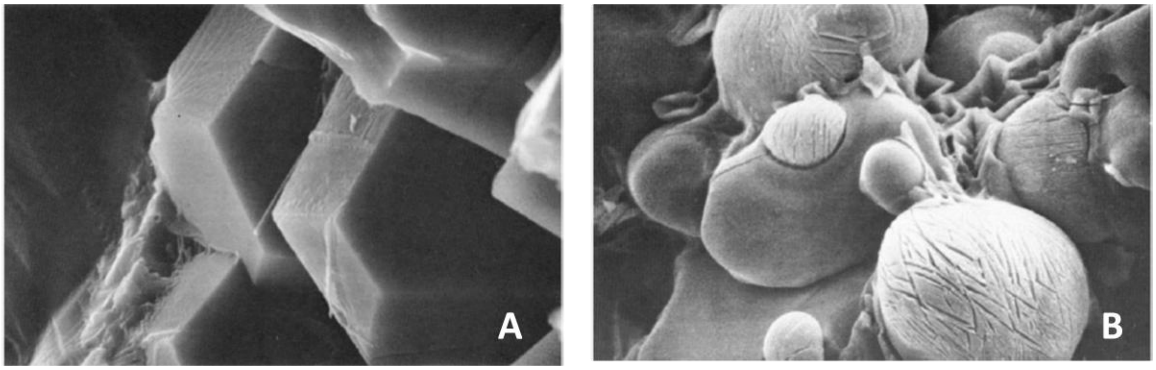

Figure 2-2. SEM Secondary Electron image (SE) A: Alite; B: Belite with twinning. From Campbell (1996).

Table 2-1. Abbreviations and cement constituents (from Neville, 2004).

Oxide Composition	Compound Name	Abbreviation	Common Name
$3CaO{\cdot}SiO_2$	Tricalcium silicate	C_3S	Alite
$2CaO{\cdot}SiO_2$	Dicalcium silicate	C_2S	Belite
$3CaO{\cdot}Al_2O_3$	Tricalcium aluminate	C_3A	Aluminate
$4CaO{\cdot}Al_2O_3{\cdot}Fe_2O_3$	Tetracalcium aluminoferrite	C_4AF	Ferrite

When ordinary portland cement (OPC), an additive-free cement powder, is mixed with water, hydration products are formed. The hydration products form at different rates- depending on the temperature and pressure used during the mixing process, the hydration phases will have different varying stability and morphology (e.g. Hewlet, 1998). Temperature also influences the degree of hydration where higher temperatures increase the rate of hydration and impact the initial strength. The progress of hydration is shown in Figure 2-3.

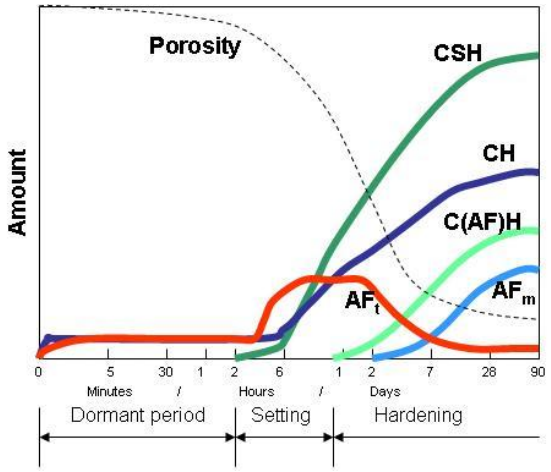

Figure 2-3. Hydration of cement as it sets and hardens with hydration products (in cement nomenclature, see below for chemistry) Adapted from Locher et al., 1976 in PCA 2011 Design and Control of Concrete Mixtures, 15th edition.

The primary hydration products formed from ordinary portland cement are a semi-amorphous calcium-silicate-hydrate ($Ca_3Si_2*3H_2O$) gel, called C-S-H in cement chemistry notation (reaction 1 and 2) (70-80%) and calcium hydroxide ($Ca(OH)_2$), commonly called portlandite and CH in cement chemistry notation (reaction 1) (15-20%) (Figure 2.4). The C-S-H begins to nucleate on the surfaces of the unhydrated cement grains and forms an inner and outer product within hours during the induction phase of the cement hydration (Hewlet, 1998; Nelson, 1990). The setting period occurs over several days at a high hydration rate, called the acceleration and deceleration periods. At this time the C-S-H begins to form a network and the $Ca(OH_2)$ begins to precipitate. At the end of the setting period nearly 30% of the cement has reacted (Taylor, 1997). Hydration of the cement paste continues into the diffusion period where the hydration products continue to form a more cohesive network; however, the cement never fully reaches 100% hydration and will continue to hydrate over time (Nelson (1990)

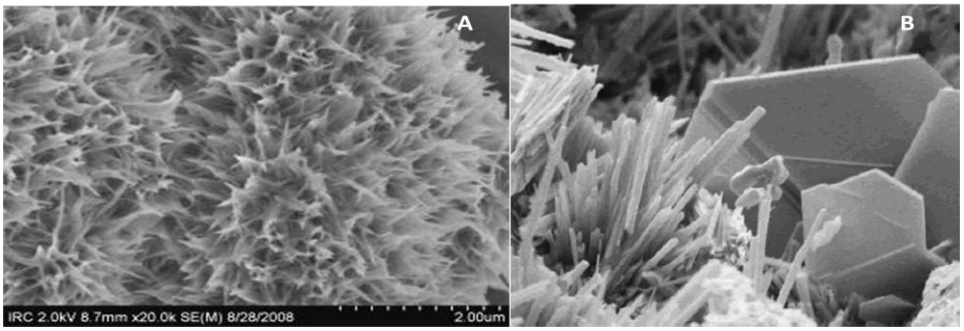

Figure 2-4. Secondary electron SEM image of A) C-S-H structure which appears very cilia-like and fills in between unhydrated cement grains; B) Needle-like ettringite (AFt) and Ca(OH)$_2$ appears as hexagonal. http://www.cementlab.com

Although C-S-H and Ca(OH)$_2$ are the primary hydration products, two minor hydration products form that contain aluminate or sulfate phases. The aluminate phases are the most reactive and have a significant impact on initial cement strength (Nelson, 1990). The $Ca_3Al_2O_6$ and gypsum provide aluminate, calcium, hydroxyl, and sulfate ions to form ettringite ($Ca_6Al_2(SO_4)_3(OH)_{12}\cdot 26H_2O$) (reaction 3). As the gypsum is consumed, ettringite converts to a calcium monosulfoaluminate hydrate called monosulfate ($Ca_2(Al,Fe)(OH)_6)]\cdot X\cdot nH_2O$) (reaction 4) Alumina is released as the reaction continues and eventually, carbonate will displace the sulfate or hydroxyl in monosulfate. The reactions from Nelson (1990) follow in both cement nomenclature and chemical notations:

Cement notation:

$$2C_3S + 6H \rightarrow C_3S_2H_3 + 3CH \qquad (1)$$

$$2C_2S + 4H \rightarrow C_3S_2H_3 + CH \qquad (2)$$

$$C_3A + 3CSH_2 + 26H \rightarrow C_6A\$_3H_{32}\,(AF_T) \qquad (3)$$

$$C_6A\$_3H_{32} + 2C_3A + 22H \rightarrow 3C_4A\$H_{18}\,(AF_M) \qquad (4)$$

Chemical notation:

$$2Ca_3SiO_5 + 6H^+ \rightarrow Ca_3Si_2\cdot 3H_2O + 3Ca(OH)_2 \qquad (1)$$

$$2Ca_2SiO_3 + 4H^+ \rightarrow Ca_3Si_2\cdot 3H_2O + Ca(OH)_2 \qquad (2)$$

$$Ca_3Al_2O_6 + 3CaSO_4\cdot 2H_2O + 26H^+ \rightarrow Ca_6Al_2(SO_4)_3(OH)_{12}\cdot 26H_2O \qquad (3)$$

$$Ca_6Al_2(SO_4)_3(OH)_{12}\cdot 26H_2O + 2CaAl_2O_6 + 22H \rightarrow Ca_2(Al,Fe)(OH)_6)]\cdot X\cdot nH_2O \qquad (4)$$

Cement is divided into different classes by the American Petroleum Institute (API) *Specifications for Materials and Testing for Well Cements*. Industrial preference classes A, B, C, G, and H are further divided into three grades: O - ordinary, MSR - moderate sulfate resistant, and HSR - high sulfate resistant (Table 2-2) (Nelson, 1990; Barron, 2009). A specific range of bore depths, environments, pressures, and temperatures is recommended for each class of cement (Mehta & Monteiro, 2006, Nelson & Guillot, 2006). Cement fineness is listed as the Blaine fineness (ASTM C 204) and is a parameter of the fineness of the cement particle size given in units of surface area; cement fineness influences the rate of hydration and the final strength.

Table 2-2. Typical composition (weight %) and fineness of API cements in oxide nomenclature. American Society for Testing and Material (ASTM) equivalents are included (modified from Nelson,1990).

API Class	Ca_3SiO_5	Ca_2SiO_4	$Ca_3Al_2O_6$	Ca_4AlFeO_5	Typical Fineness (cm^2/g)	ASTM Type
A	45	27	11	8	1600	I
B	44	31	5	13	1600	II
C	53	19	11	9	2200	III
D	28	49	4	12	1500	-
E	38	43	4	9	1500	-
G	50	30	5	12	1800	(II)
H	50	30	5	12	1600	(II)

The time it takes for the cement to harden is called the wait-on-cement (WOC) time and is typically tested in the laboratory before placement of the concrete in a construction setting. Taylor (1997) points out that the viscosity of cement paste depends on the water-cement (w/c) ratio, additives (supplementary cementitious materials, SCMs) or accelerators/retarders. Table 2-2 shows typical compositions of portland cement based on cement fineness and the ASTM equivalent.

Oil well cements are typically made of portland cement clinker or blended hydraulic cements that use pozzolans, retarders or chemical inhibitors to delay the setting time in some circumstances. The most commonly used portland cements in the drilling industry are Classes G and H. These classes are chemically identical, but Class G is coarser grained, which slows the setting time. Both are moderately sulfate-resistant and are intended for use at depths up to 2.5 km without admixtures. Both Class G and H are considered appropriate for potential CO_2 sequestration and are addressed in this dissertation.

2.2.3. Durability Under High Pressure and Temperature

Wellbore cements are found in environments with temperatures ranging from below freezing up to 350 ºC (700 ºF) and from near ambient pressures (shallow wells) up to more than 30,000 psi (200 MPa). The physical development and chemical characteristics of the cement paste are highly dependent on the pressure and temperature conditions at which the cement is cured (Nelson, 1990). Therefore it is essential to consider pressure and temperature conditions during cement hydration in any laboratory experiment. Hydration products are essentially the same in ambient conditions up to 40˚C, but as temperatures increase, the microstructure and morphology of the C-S-H gel becomes more fibrous and individualized. High temperatures during hydration increases the initial rate of hydration of the cement and the C-S-H gel in cement becomes unstable if cured at temperatures above 110˚C (Fig. 2-5). Increasing the hydration temperature also reduces the degree of hydration, and ultimately the strength of the cement. One explanation given for this is that a dense layer of C-S-H gel forms around the Ca_3SiO_5 which prevents full hydration of the cement.

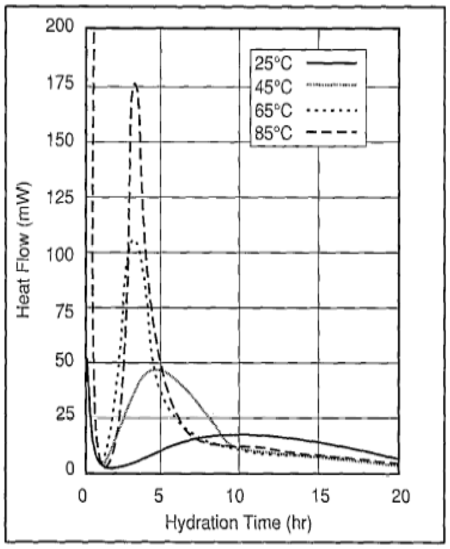

Figure 2-5. The effect of temperature on the hydration kinetics of a Class G oil well cement (Nelson, 1990). The higher the temperature, the more rapid the cement hydrates and hardens. Hydration is dependent on temperature.

Increased temperature during curing also accelerates the conversion of hexagonal aluminate hydrates to a cubic form; in curing temperatures above 80˚C aluminate gel (C_3AH_6) is formed. Strength development is decreased with increased temperatures and under simulated downhole conditions, cement strengths typically decrease with age (Bearden, 1959). These findings were the impetus for classes of oilwell cements developed by the API (American Petroleum Institute) for intended usable depths (Table 2-1) (Nelson, 1990; Bearden, 1959). In addition, as curing temperatures increase, the effect of increased pressure becomes more pronounced. As the curing pressure increases, earlier compressive strength development and ultimately higher compressive strength are observed (Nelson, 1990).

Other observed influences of temperature and pressure on cement hydration include a study by Bresson and Zanni (1998) in which the replacement of ettringite with hydrogrossular $CaO_3Al_2O_3(SiO_2)_{3-x}(H_2O)_{2(0-3)}$ in cement cured at ~80^{o}C and a pressure of 6.998 MPa. At temperatures above 160^{o}C or pressures above 34.47 MPa, the C-S-H begins to polymerize into a hillebrandite [$Ca_2(Si)_3(OH)_2$], jaffeite [$Ca_6(Si_2O_7)(OH)_6$], or tobermorite-like structure

($Ca_5Si_6O_{16}(OH)_2 \cdot 4H_2O$ or $Ca_5Si_6(O,OH)_{18} \cdot 5H_2O$) (Bresson et al., 2002; Bresson and Zanni, 1998). The early stages of hydration influence porosity of the C-S-H particles and this porosity originates from the hydration of Ca_3SiO_5 Bentur et al. (1979). Both the degree of hydration and the water-cement ratio influences the porosity and nucleation of C-S-H (Fig. 2-6). Temperature increase expedites cement hydration by facilitating the rapid nucleation of hydration products and resulting in early setting, depending on the w/c ratio (Zhang et al., 2010).

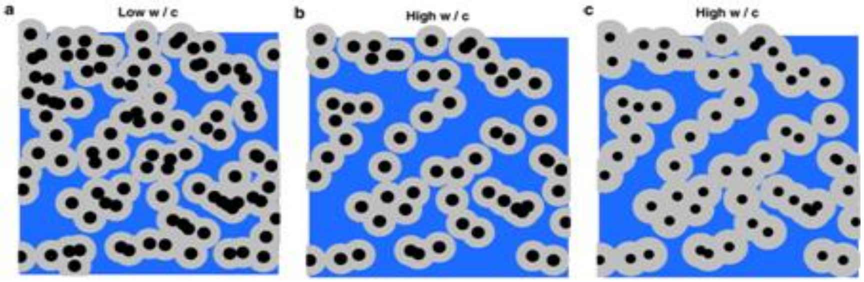

Figure 2-6. Solid phase percolation at setting for different w/c. Matrix is filled with water (blue), black particles are cement grains, and gray shells as the hydration products. (a) Hydration products have percolated, relatively low w/c and has set; (b) the same degree of hydration as (a), but has higher w/c and not set; (c) at a higher degree of hydration, the sample with the same w/c as in (b) has set (modified from Zhang et al., 2010).

Cement gains strength as it hydrates and hardens. The strength of the paste is dependent upon the ratio of water to cement. A mixture with a high w/c is more workable and flows easier than a low w/c ratio mixture. However, if the w/c is too high, the cement could have a lower final strength. Typical values of w/c are between 0.35 and 0.40 and are set to provide adequate workability without sacrificing final strength. Examination of the hydration of a 0.35 w/c Class H OPC, Zhang et al. (2010) showed that at 60^oC there was an initial set after 2.25 hours, whereas at 10^oC initial setting occurred at 10 hours. Lower w/c cement pastes require less hydration of the cement products and set more quickly as seen in Fig. 2-5 and 2-6. Higher water content mixtures enable more complete hydration of the cement paste, but have a longer setting period.

Kutchko et al. (2007) also found changes in the physical properties of cement at higher pressure and temperature conditions. The authors describe a change in the microstructure and distribution of the $Ca(OH)_{2(s)}$ in the cement during curing. The smaller, more evenly distributed $Ca(OH)_{2(s)}$ crystals formed under these conditions provide a uniform and effective barrier to CO_2 attack, important factor in the sequestration of CO_2 in abandoned oil wells.

2.3. Chlorides, Salts, and Salinity

2.3.1. The Influence of Salts on Cement Paste

Cement paste or concrete is often exposed to many environmental factors, including deicing salts, ions from the soil, ground water, seawater, and atmospheric pollutants. For example, subsurface chloride-rich brines can be corrosive to cements or concretes with steel reinforcement. Likewise, the penetration of chlorine into cementitious materials may form detrimental phases that lead to expansion or cracking. Chloride in the pore solution molecularly binds in the lattice structure of C-S-H, adsorbed either as H_2O or OH^- during hydration of Ca_3SiO_6. Free water can also become trapped within the C-S-H clusters (Beaudoin et al., 1990).

Salt can cause efflorescence, or discoloration, of the cement and deposition of salt on the cement surface. In extreme cases salt precipitation can cause expansion of the cement. Salt precipitation is dependent on nucleation sites, pore spaces, capillary forces, and the source of salts (Scherer, 2004). Water within the rock formations can contain dissolved salts and as the water evaporates, the increased chloride concentration results in the precipitation of the salt in any porous media, including cement. Scherer (2004) reported crystal growth and subsequent damage from internal salt subflorescence on prismatic limestone and sandstones has been observed. Repulsive forces drive salt crystal growth and in a supersaturated system expansion can occur in cement.

Chloride ingress is also known to corrode the steel found within reinforced concrete (Taylor, 1997). This means that the progression of chlorides could corrode the steel casing within the wellbore, leading to premature deterioration or failure of the wellbore. Chloride corrosion is initiated when chloride ion activate the steel surface by forming an anodic and cathodic reaction. Chloride anions act as an electrochemical catalyst in the anodic reaction (Neville, 1995; Ghodes et al., 2012). The positively charged Fe^{2+} releases 2e- into the aqueous salt solution, which converts to $FeCl_2$, and then is oxidizes into ferric hydroxide and HCl (Neville, 1995). This consequently results in chloride pitting and steel corrosion which may further lead to cracking or spalling of the cement.

A study of cement systems exposed to chlorides reacts with the aluminate phases in the paste, most commonly $Ca_3Al_2O_6$, forming Friedel's salt ($3CaO\cdot Al_2O_3\cdot CaCl_2\cdot 10H_2O$) (Birnin-Yauri et al., 1998). Friedel's salt is an ettringite-type mineral in which sulfate ions are replaced by chloride ions. When combined with gypsum in a 10% NaCl solution, a chloride-type phase from Ca_4AlFeO_5 sometimes produces a ferrite (Fe substitution) Friedel's salt (Csizmadia et al., 2001). Kuzel's salt ($3CaO\cdot Al_2O_3\cdot 1/2CaCl_2\cdot 1/2CaSO_4\cdot 10H_2O$), a chloro-sulfate AFm phase, is another potential salt precipitate (Birnin-Yauri et al., 1998). Both Friedel's and Kuzel's salt phases are poorly understood and may be key to understanding the reactive transport of chloride from solution. Neither Friedel's or Kuzel's salt are expected to precipitate in the Class H cement type used in this dissertation because there is no calcium aluminoferrite present. Class H cement does however, contain Ca_4AlFeO_5 which could become reactive. Formation water or seawater could provide the necessary reactants to eventually form these salts under real-world conditions. Additional issues include internal sulfate attack as well as mineral expansion or contractions within the hardened cement paste.

The salts studied in this dissertation include NaCl, $MgCl_2$, $CaCl_2$, and trace Na_2SO_4. Wellbore cement in contact with subsurface brine is susceptible to chloride attack from each of these salts. NaCl is the most documented and most frequent subsurface environmental source of chloride. Calcium chloride is a Type C accelerating chemical admixture for concrete by ASTM

C494, and was once used to accelerate cement hydration to reduce the set time in cold climates. $CaCl_2$ is no longer used as an additive due to its inherent chloride content. Surface use of $MgCl_2$ as a deicer in freeze-thaw cycles results in substantial physical degradation. Other than the typical deicer effects there is little published data about effects of $MgCl_2$, however some studies have shown that corrosion from a magnesium-based salt could result in non-cohesive magnesium silicate hydrate (M-S-H) which promotes aggravated scaling and loss of cohesion (Cody, et al., 1996).

Another concern is "sulfate attack" where sulfates from either an external or internal source react with the calcium components within the hardened cement paste. An external sulfate attack is when sulfate ions from an external source (e.g., soil or groundwater) migrate into the cement matrix. Internal sulfate attack occurs from a sulfate source within the cement paste itself (e.g., gypsum in the aggregate within concrete). The ingress of sulfate species and the subsequent reactions with calcium components within the cement can produce expansive minerals such as gypsum, ettringite, or thaumasite. Formation of these minerals after the cement paste has hardened can cause expansion or cracking, a lack of cohesion and strength, and scaling of cement at atmospheric conditions. Thaumasite $[Ca_3Si(OH)_6*12H_2O]\ (SO_4)(CO_3)$ is the product of sulfate attack combined with limestone aggregate or atmospheric/aqueous CO_2 (Nelson, 1990; Zhang, et al., 2011). However, thaumasite typically forms only at low temperatures (4-10^{o}C) so is not applicable to the research presented here and will not be discussed. Solutions enriched in magnesium sulfate result in aggressive attack on the cement because the calcium is replaced with Mg^{2+} to form brucite ($Mg(OH)_2$) and M-S-H; the displaced calcium then converted to gypsum (Zhang, et al., 2011). Internal sulfate attack is described in greater detail in Section 2.4: Secondary Ettringite Precipitation.

2.3.2. Salinity and Supercritical CO_2

Salinity plays an important role in CO_2 solubility in fluids. Higher salinity decreases CO_2 solubility that in turn would likely result in different alteration rates of cement paste (this dissertation and suggested by Spycher & Pruess, 2005). The addition of salts must be considered when examining thermodynamic properties of a non-ideal aqueous phase. Spycher & Pruess (2005) suggest that the activity coefficient of CO_2 and H_2O in geochemical modeling changes in the presence of salts (Fig. 2-7). Compiled experimental and modeled data from earlier studies comparing various ionic salt strengths in the compressed gas phase subjected to CO_2 were examined between the amount of gaseous water (in mole fraction) to the liquid water activity within a specific pressure-temperature range.

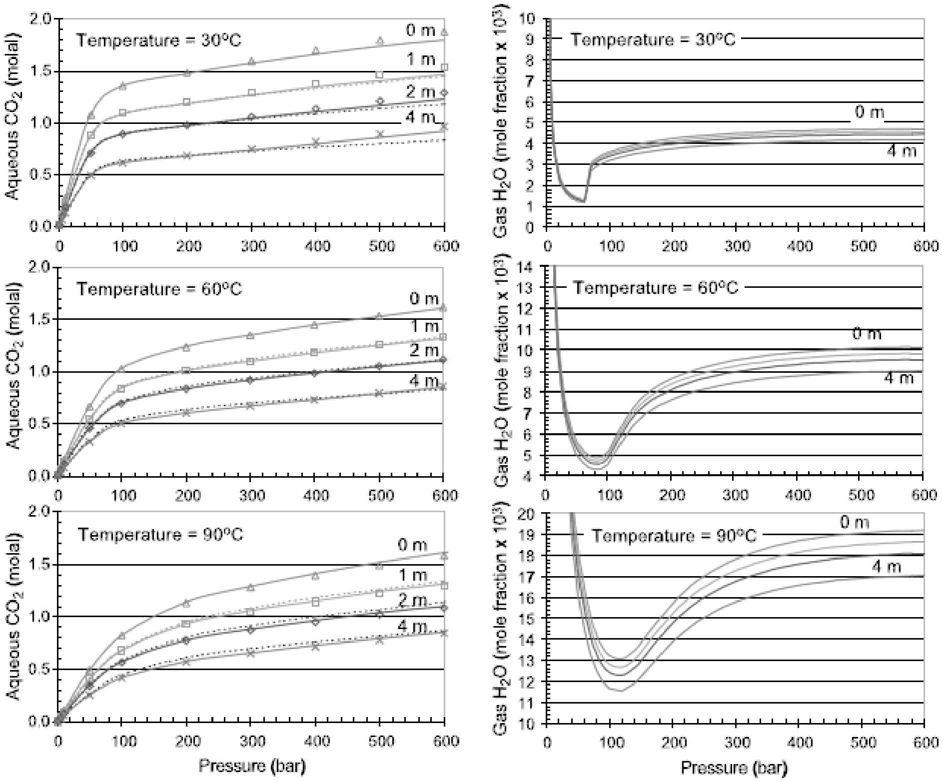

Figure 2-7. Comparison of predicted mutual solubilities of CO_2 and H_2O using the activity coefficient at 30, 60, and 90°C and 1–600 bar for solutions up to 4 m NaCl as tabulated by Duan and Sun (2003) (solid lines) and Rumpf et al. (1984) (dashed lines) to that calculated of Spycher & Pruess (2005). CO_2 solubilities computed by Duan and Sun (2003) using their full solubility model are also shown for comparison (symbols).

The results of the Spycher & Pruess (2005) solubility model can be combined with various activity coefficients and compared to experimental solubilities (i.e. Rumpf et al. 1984; Duan and Sun, 2003). Injection of CO_2 into brine also increases aqueous phase salinity, thus encouraging salt precipitation (Spycher & Pruess, 2005, Pruess & Müller, 2009). Halite (NaCl) has been found in aquifer gas storage systems where a supercritical (CO_2) drying boundary enables minerals to form as the cement hydrates (Pruess & Müller, 2009; Lorenz & Müller, 2003).

2.4. Secondary Ettringite Precipitation

There is much debate in the scientific community about the importance of ettringite in cement paste. The formation of ettringite in typical OPC occurs when calcium and sulfate ions from the gypsum react with the aluminate and hydroxyl ions from the $Ca_3Al_2O_6$ to form a calcium trisulfoaluminate hydrate ($Ca_6Al_2(SO_4)_3(OH)_{12}\cdot 26H_2O$). Early reactions of ettringite formation do not result in degradation because the cement paste is still hydrating and is "plastic" (Taylor et al., 2001). However, secondary [delayed] ettringite formation (DEF) after the primary cement curing stage may lead to loss of cement paste integrity, degradation, expansion, and fracturing under atmospheric conditions in mature cement paste or concrete (Glasser, 2001). Ettringite usually transforms into monosulfate with time, however under wet conditions monosulfate can revert back into ettringite. Ettringite requires more space than monosulfate, and is opportunistic by nature by filling fractures and pore space that leads to further expansion. At internal temperatures above $70^{o}C$ ettringite can form in cement paste where it acts as an internal sulfate attack (Taylor et al., 2001, Colleparadi, 2003; Scrivener, 2005). External sulfate attack can occur from the chemical reaction of cement paste that is in contact with sulfate-rich soil or fluids.

There are several different potential mechanisms to explain why DEF leads to expansion and potential degradation. One proposed mechanism, the "Uniform Paste Expansion Theory", states that DEF cracking in cement and concrete in atmospheric conditions occurs uniformly and isotropically in the C-S-H of the cement paste (Johansen et al., 1993; Taylor, 2001). Any recrystallization around anhydrous cement grains or aggregates in concrete can lead to fractures. The "Ettringite Crystal Growth Theory", proposes that expansion is due to the pressure of the precipitating ettringite that causes microfractures to form in the cement paste (e.g. Diamond, 1994; 1996). Scherer (1999) suggests that in confined spaces, small crystals exert pressure that cause the hydrated cement to expand if alumina and sulfate become supersaturated to precipitated ettringite. This second theory has been challenged and instead it has been suggested that ettringite is undersaturated in the pore solution and insufficient to generate enough crystal growth pressure to expand the cement (Johansen et al., 1993; Taylor, 1993) .

There are a number of cases, both in the laboratory and the field, documenting detrimental DEF. For example, in studies of premature cement degradation in Texas, DEF was found to be the main cause of degradation when temperatures are excessively high due to the heat of hydration in the concretes (Lawrence et al.,1999; Hobbs, 1999). When exposed to 100^{o}C, portland cement mortar developed DEF that continued to increase over a period of one year and ettringite bands appeared to widened the fractures Yang et al. (1999). Other studies have shown that DEF damages concrete, even in the absence of high temperatures, (Diamond, 1996; Colleparadi, 1998) because sulfate in the clinker is slowly released (Taylor et al., 2001). Famy et al. (2001) concluded that ettringite precipitation continued after hardening of the cement that small needle-like crystals became unstable resulting in recrystallization. These authors investigated the relationship of elevated temperature and sulfate, but concluded there is not sufficient evidence that DEF itself causes damage. Thermal decomposition of ettringite or late sulfate released from C-S-H is an example of an internal sulfate attack. This sulfate ion release can result in damage in a sulfate free environment (Diamond, 1996; Colleparadi, 1998; 2003). External sulfate attack sulfate rich soil or fluids, chemically react to the cement paste is the more common type of sulfate attack and the most applicable to the wellbore environment. Additional external damage includes cracking and spalling due to the ingress of sulfate into cement pores (Colleparadi, 2003). Ettringite formation during external sulfate attack are due to 1) decalcification of C-S-H to form gypsum, 2) sulfate attack on calcium aluminate hydrates and monosulfate hydrates; and 3) sulfate attack on both C-S-H and $Ca(OH)_2$ to form thaumasite (Colleparadi, 1998; 2003).

In contrast to the above observations supporting DEF, others maintain that the mechanisms of ettringite formation and expansion are not exclusive and that the existing data are insufficient to establish whether DEF is the true culprit Taylor et al. (2001). The authors further argue that the presence of microscopic ettringite crystals in fractures does not indicate distress in the cement paste, but rather that the paste itself has expanded.

While there is no agreement in the scientific community of the mechanisms of DEF and the causes of expansion, there is agreement that expansion does occurs in cements and/or concrete that are subject to higher temperatures. Cement paste expansion and microfractures are both potential leakage pathways for injected gases or liquids to escape either out of the wellbore through hydrated cement or at the wellbore cement-steel casing interface.

Although ettringite is not a primary hydration phase in Class H Portland cement owing to the limited in Al^{3+} concentrations and restricted aluminum mobility. This cement type does contains an unhydrated aluminate, Ca_4AlFeO_5, which may allow bonding for secondary ettringite precipitation. Sulfate ions from gypsum can be absorbed into the C-S-H gel during the hydration of the calcium silicates. This C-S-H tied sulfate is initially relatively unreactive, and could be later released under the correct environmental conditions (Nelson, 1990). The stability of ettringite is temperature and pH dependent and exists in a pH range of 9 to 13.4 Stark & Bollard (1999). This is the typical pH range for cement paste in normal conditions. However, if the cement undergoes pH changes, as expected in carbon sequestration settings, this could initiate sulfate leaching from the C-S-H. In addition, sulfate in the formation water that could induce external sulfate attack and potentially secondary ettringite formation in a mature Class H cement.

2.5. Why Sequestration?

The increase of atmospheric carbon dioxide has a significant impact in warming the Earth's surface, increasing air and ocean temperatures globally, and widespread melting of ice caps (IPCC, 2007). Therefore, it is essential to reduce anthropogenic CO_2 in order to mitigate climate change. Nearly 82% of the US energy demand is currently being met with fossil fuels (IEA, 2013). Coal generates over 40% of U.S. electricity and is one of the greatest causes of anthropogenic CO_2 released into the atmosphere. Sequestering CO_2 generated by carbon fossil fuels in power generation into the deep subsurface, saline sedimentary formations which have a storing potential of 1,000-10,000 Gt CO_2 with a predicted duration of 1,000 years (IPCC, 2005). Potential CO_2 storage sites are at depths greater than 800 m, pressures greater than 7.38 MPa, and temperature greater than 31.1^{o}C. Under these conditions CO_2 is in a supercritical state (Fig. 2-8) enabling more CO_2 to be stored in a smaller space.

The major drawback of storing CO_2 in geological subsurface formations is that dissolution of supercritical CO_2 into brine may cause wellbore cement degradation. Oil well cements may be compromised and leak the stored CO_2 if carbonic acid attack is significant.

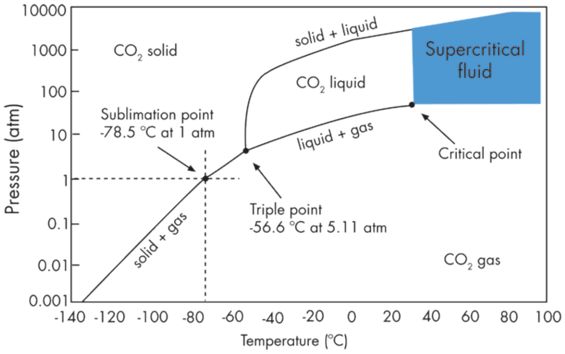

Figure 2-8. Pressure and temperature phase diagram for CO_2 demonstrating the critical point in which CO_2 acts as a supercritical fluid >7.38 MPa and > 31.1^{o}C. Modified from TUV NEL (http://www.tuvnel.com/)

2.5.1. Diffusion

Portland cement is not thermodynamically stable in a CO_2-rich environment. Cement hydration products are metastable and cement alteration will occur. An aggressive solution (e.g., CO_2-enriched brine) can migrate into the porous cement paste. The movement of fluid and ions from solution into cement paste is through three primary mechanisms (Bertolini et al., 2004). The predominant process is diffusion due to concentration gradients. Capillary suction presumably occurs within the capillaries of the cement paste or advection due to pressure gradients between the cement and reservoir can absorb water. The pores of the cement contain a small amount of water which can affect local reactions and cement hydration. Furthermore, electrochemical potential gradients maintain pore solution electroneutrality which is dependent on the species velocity, incorporated into each individual concentration flux reaction (Bertolini et al., 2004 and Glasser et al., 2008).

In conditions of stationary mass in a steady state, the relative diffusive flux of a component from a higher to a lower concentration is described by Fick's First Law (i.e. Taylor, 1997) where F is the "diffusion flux" [(amount of substance) per unit area per unit time; mol/m^2s], D is the diffusion coefficient or diffusivity in dimensions of [m^2/s], C (in ideal mixtures) is the concentration in dimensions of the amount of substance per unit volume (mol/m^3), and x is the length.

$$F = -D\frac{dC}{dx}$$

Diffusion is rarely in a steady state, so the flux is dependent on time and is governed by Fick's Second Law. This equation assumes that the concentration of the diffusing ion changes with time, that the coefficient of diffusion (D) is constant with time, and that the cement is homogeneous. Therefore, diffusion should not change with depth into the cement. The equation is derived from the Fick's First law and the conservation of mass.

$$\frac{\delta C}{\delta t} = \frac{\delta^2 C/\delta C}{\delta x^2}$$

Fick's Second Law of Diffusion is the typical method of estimating the depth of calcium carbonate (carbonation) of cement. Diffusion is limited by the reaction rate of the acid-base carbonation, and reacts faster than the diffusion (loss) of ionic species from the cement. Subsequently, the diffusion with a constant concentration boundary condition is used to estimate the depth of alteration in a cement paste. The predicted rate is inversely proportional to the square root of the age of cement or concrete (Taylor, 1997).

$$L = \alpha t^{1/2}$$

The uptake of CO_2 within the cement is represented by L = depth of carbonation, t = time of exposure, and α = a constant related to the rate of diffusion of ionic species through the cement matrix. The constant α depends on cement parameters such as permeability, porosity, tortuosity, and chemical composition of the cement. If Fickian diffusion is controlling the rate of cement carbonation a plot of L vs $t^{1/2}$ will be linear (Taylor, 1997).

The carbonation of the cement is limited by the rate of oxygen diffusion and the carbonation front proceeds into the cement as a propagated front with time. The rates of carbonic acid and oxygen diffusion are dependent on cement factors such as the porosity, pore size distribution, water, curing time, temperature and the amount of dissolved CO_2, and therefore cement paste is treated as a porous medium (i.e. Taylor, 1997).

2.5.2. CO_2 Cement Degradation

Species that diffuse into the cement paste bind with alkaline anhydrous cement phases and hydrated cement products. The gaseous carbon dioxide dissolves into the water to form aqueous CO_2 (reaction 5). Carbonic acid is a weak acid, and only a small fraction will dissociate. Equation 6 demonstrates this dissolution and follows Henry's Law under equilibrium conditions where the activity of dissolved CO_2 is equal to Henry's Law constant and multiplied by the partial pressure of gaseous CO_2 (Plummer et al., 1982). Both pressure and temperature affect carbonate solubility. Higher pressure increases solubility and lower temperatures increase CO_2 concentration. For example, dissolution of CO_2 at 25°C at atmospheric pressures gives a $K_H = 10^{-1.5}$, and it is expected that at higher pressure that more CO_2 will dissolve. Approximately 1% of the dissolved CO_2 reacts with water to form carbonic acid, which further dissolves into $2H^+$ and CO_3^{2-} ions in a sequestration setting at 50^oC (reaction 7) Kutchko et al., (2007) .

$$CO_{2(g)} \rightarrow CO_{2(aq)} \quad (5)$$

$$a_{CO2(aq)} = K_H PCO_2 \quad (6)$$

$$CO^{2+} H_2O \leftrightarrow H_2CO_3 \leftrightarrow HCO_3^- + H^+ \leftrightarrow 2H^+ + CO_3^{2-} \quad (7)$$

Once in solution, the dissociated CO_2 constituents react with cementitious materials. Portlandite ($Ca(OH)_2$) within the cement is dissolved and reacts with HCO_3^- or CO_3^{2-} in the pore solution and is replaced by CO_2-based solid phases such as aragonite, calcite, or vaterite, which fills pore spaces (equations 8 and 9). Ongoing diffusion of carbonic acid leaches Ca^{2+} from the cement resulting in amorphous silica or decalcification of the cement paste (reaction 10). The diffusion of calcium out of the cement is driven by the fluctuating pH and causes further degradation. The following equations demonstrate this reaction process (Fig. 2-9 as suggested by Kutchko et al., 2007):

$$Ca(OH)_{2(s)} \rightarrow Ca^{2+}_{(aq)} + 2OH^-_{(aq)} \quad (8)$$

$$Ca^{2+}_{(aq)} + HCO_3^-{}_{(aq)} + OH^-_{(aq)} \rightarrow CaCO_{3(s)} + H_2O \quad (9)$$

$$2H^+ + CO_3^{2-} + C\text{-}S\text{-}H_{(s)} \rightarrow CaCO_{3\,(s)} + H_2O_{(aq)} + am\text{-}SiO_{2(s)} \quad (10)$$

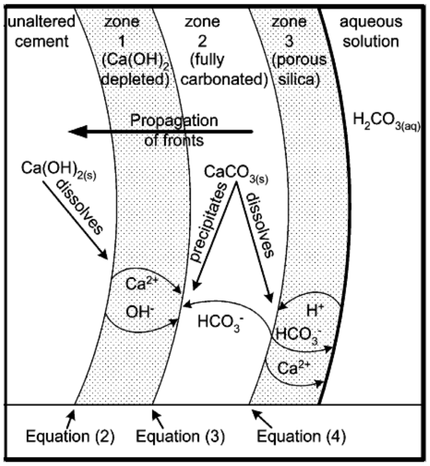

Figure 2-9. Schematic displaying calcium migration and dissolution in the formation of alteration fronts (Kutchko et al., 2007).

Figure 2-9 also demonstrates how the dissociated acid reacts with hydrated $Ca(OH)_2$ and anhydrous calcium silicates in the cement. The carbonated water diffuses into the cement matrix, initially increasing the compressive strength, and reducing cement permeability as a result of volume expansion of the calcium carbonate (Shen, 1989). Calcite has a higher molar volume than portlandite (36.9 cm^3/mol compared to 33.1 cm_3/mol for $Ca(OH)_2$) (Glasser et al. 2008). This volumetric expansion may result in microfractures that could provide pathways for interaction with carbonic acid.

Cement degradation continues with CO_2 injection because the solubility of $CaCO_3$ is lower than that of $Ca(OH)_2$. The relative solubility for $CaCO_3$ at 18˚C is 0.99×10^{-8} and 9.95×10^{-4} for $Ca(OH)_2$ at 20˚C (Glasser, 2001). Carbonate ions are initially the dominant species at a high pH (>10.3) and will continue to diffuse into the cement and react with the calcium ions in solution to precipitate $CaCO_{3.}$ New equilibria are introduced because carbon dioxide-saturated water diffuses into the cement paste (Bruckdorfer, 1986). If the local cement pH is stable at 12.4 and portlandite is still present, the $CaCO_3$ is stable and the dissolved carbon dioxide is found primarily as carbonate (CO_3^{2-}) (Thaulow et al., 2001). This can be compared to the Bjerrum plot

(Fig. 2-10) in which seawater is compared to the concentration of dissolved carbonate species as a function of pH to display the carbon cycle mechanism with atmospheric CO_2.

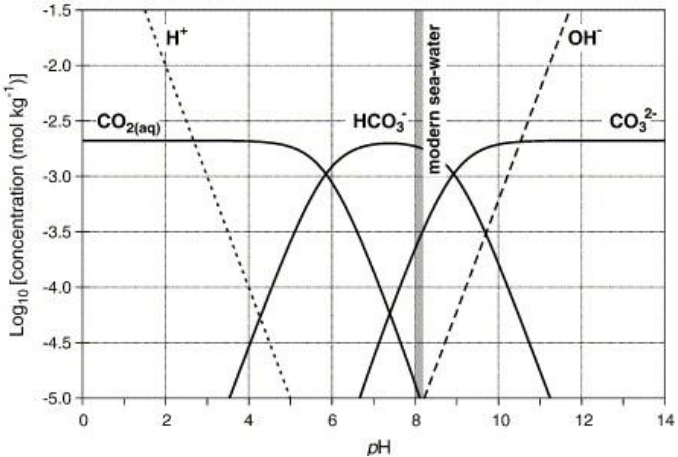

Figure 2-10. Bjerrum plot: Dissolved CO_2 (aq), HCO_3^-, CO_3^{2-}, H^+, and OH^- ions as a function of pH. At modern seawater pH, dissolved inorganic carbon is in the form of bicarbonate (modified by Ridgwell & Zeebe, 2005).

However, bicarbonate (HCO_3^-) begins to dominate the aqueous system at a range of pH 6.3-10.3, marking the depletion of $Ca(OH)_2$ (Thaulow et al., 2001). When the available calcium is consumed, this results in an increase of aqueous H^+ and the solution becomes more acidic (decreasing pH). If the injected CO_2 concentration is maintained and continuous, the calcium carbonate will dissolve, resulting in water-soluble calcium bicarbonate diffusing out of the cement and into solution (Thaulow et al., 2001). The loss of cementitious material, specifically Ca^{2+} cations, will increase permeability and porosity of the cement, and eventually result in a remnant amorphous silica gel-like network with no structural integrity (Bruckdorfer, 1986). In some cases the carbonate will replace C-S-H in the cement (St. John et al., 1998).

2.5.3. Degree of Alteration in a CO_2 Environment

In a given environment, the reactivity of CO_2 is controlled by the cement composition, partial pressure, temperature, and water to cement ratio (Shen, 1989). The temperature and pressure during curing conditions, as discussed in the hydration section, determines the microstructure of the cement (Onan, 1984). The formation of crystalline C-S-H due to higher temperatures would restrict the amount of portlandite present in the cement; this would therefore impact both the carbonation and degradation rate of the cement. For example, the initial carbonation process is controlled by the concentration of available $Ca(OH)_2$ that reacts with supercritical CO_2 and the water-cement ratio is significant because it establishes the cement permeability and total precipitated $Ca(OH)_2$ (Milestone et al., 1986; Thaulow et al., 2001).

The cement system is quite complex; a saturated environment could have both dissolution and calcium migration from greater depths in the cement paste (Glasser, 2001). Carbon dioxide must enter the cementitious material in order for the carbonation process to start. The quantitative transport balance between the migration and dissolution is not well understood, but is modeled based on various studies using a simplified Richards' equation or other diffusion-based equations, such as Fickian or Elovich methods (e.g. Glasser, 2001; Kutchko et al., 2008). Richard's equation specifically is the movement of water incorporating Darcy's law for saturated flow in porous media using non-linear partial differential equation (Richards, 1931).

Furthermore, Glasser et al. (2008) states that chemical dissolution and species migration into pore solution controls the extent of the carbonation process. This then leads to the formation of zoned regions where each zone represents a microenvironment with local equilibrium between the cement, pore water, and the CO_2 source. Richardson (1988) described three reaction zones for carbonation occurring under natural conditions where 1) calcium hydroxide exists in the inner non-carbonated zone; 2) calcium carbonated zone, and 3) the exterior layer is characterized by the dissolution of $CaCO_3$ (also representative in Fig. 2-9). As discussed above, dissolution of $CaCO_3$ occurs only where there is abundant aqueous CO_2 interaction. The zone thickness correlates with additives, curing conditions, exposure time, paste type and quality, and CO_2 solubility (Glasser 2001).

2.6. Previous Research

Permanent storage of CO_2 sequestered is critical to prevent risk to groundwater, human welfare, and vegetation (IPCC, 2005). There are two fundamental escape routes for sequestered CO_2: 1) natural and 2) manmade. Natural potential CO_2 leakage pathways include natural active or reactivated faults, open fractures, interruptions and breaches through the confining strata (DOE, 2007). Although analysis of natural systems is important, this dissertation focuses on manmade influences. It is widely believed that the most likely route of potential CO_2 leakage is through the significant number of wellbores which penetrate candidate sequestration sites (Gasda, 2004; Duiguid et al., 2004; 2005; Bachu and Celia, 2009; Watson & Bachu, 2009). Pre-existing factors, such as poor cement emplacement or poor cement consolation can also lead to breaches or fractures. In the placement of cement, there is potential for leakage into the annulus, the zone between the steel casing and the cement, between the cement and the rock formation, and through cement itself (Gasda, 2004). Additionally, alteration or leakage could occur with the cement plugs that block vertical migration of fluids in abandoned wells.

The durability of well cements in contact with injected CO_2 plumes has long been a concern related to enhanced oil recovery (EOR) and gas injection examination (i.e. Onan (1984), Bruckdorfer, 1986). There are direct implications for carbon capture and sequestration (CCS) applications. Both static and flow conditions have been examined in laboratory immersion experiments to characterize reaction products, measure changes in physical properties, and measure alteration depths using a variety of additives, curing conditions, and solution or cement compositions.

Onan (1984) examined the effects of carbonic acid on Classes B, C, and H cements using a variety of water-cement ratios and additives. The cement was pre-cured for 3 days at 82˚C and 6.5 MPa, and exposed to supercritical CO_2 for intervals of two, three, and four weeks. A second test condition exposed samples to a temperature and pressure of 41˚C and 19.3 MPa for one and six weeks. Onan (1984) observed that the depth of penetration ranged from 0.32-0.64 cm and found that the C-S-H crystals converted into vaterite, aragonite, and eventually into stable calcite and SiO_2-gel.

Bruckdorfer (1986) studied class A, C and H oil well cements under 20.68 MPa and 79.4˚C cured for 72 hours for 4-6 weeks under CO_2 exposure. The smaller Class H and C cements samples showed an 80% strength loss. At 51.7˚C and 29.68 MPa, the authors found that increasing the water-to-cement ratio increased CO_2 resistivity in Class H cement (Bruckdorfer, 1986).

A study was done by Andac and Glasser (1999) on ordinary portland cement with 10% municipal solid waste fly ash (water to cementitious materials ratio (w.cm) with fly ash of 0.40). The cement was aged for 24 hours and pre-cured for an additional 60 days at 100% humidity, then exposed to a constant bubbling CO_2 source for 214 days with a constant pH of 6.5 to 6.8 in flow-through recycled distilled water. The researchers found the penetration depth to be 600-800 µm with a zone ~200 to 300 µm thick low in calcium followed by a cracked zone, another leached zone low in calcium with a ~80 µm thick Ca-rich zone (calcite/ vaterite), and another calcium depleted zone.

Early experimental studies in a flush system with controlled pH utilizing HCl in a 1% NaCl solution at room temperature and later compared to 20 ^{o}C and 50^{o}C (Duguid et al., 2004; 2005) resulted in extreme and rapid degradation. This experiment set the primary conditions to which many studies have adhered. Duguid et al. (2004) documented the reaction rate, cement porosity, and thickness of the reacted layers. This study predicted a 30-year carbonation depth of 2,630 mm (pH 2.4 at 50^{o}C) and 723 mm (pH 3.7 at 20^{o}C) in the cement samples. The initial and steady state pH values were used to determine the reaction rate with the assumption that portlandite dissolution controlled the reaction. In comparison to the cured neat cement samples, the porosity of the CO_2 reacted cement paste samples increased by 10–45%. The addition of bentonite to the cement paste resulted in an increased alteration compared to the neat cement. The authors concluded that exposure to carbonated brines could impact the wellbore seals. In addition, Duguid and Scherer (2010) examined cement in a flow-though [flush] system at two separate temperatures (20°C and 50°C). The exposure conditions were the same as Duiguid et al. (2005), but also included a leachant with a brine saturated with $CaCO_3$ and NaCl equilibrated brine. This resulted in no carbonation of the hydrated cement at a pH of ~5 at 50°C.

Barlet-Gouédard et al (2006, 2009) also performed experiments using portland cement with an antifoam agent, a dispersant, and a retarder in fresh water (not brine). The authors stated that conditions downhole would be relatively static near the wellbore cement. These cement samples were cured for 72 hours at 90°C and 20.68 MPa and exposed to CO_2 up to 6 months. The authors concluded that portland cement is not resistant enough to supercritical CO_2, and predicted carbonation depth of 133 mm in supercritical CO_2 and 113 mm in CO_2-saturated water after 30 years. The authors also indicated that spalling was seen at the interface between the supercritical CO_2 and CO_2-saturated water. The simple water composition appeared to be aggressive, and contributed to higher alteration rates. These rates are substantially different from Duiguid et al. (2005).

Rimmelé et al. (2008) then proposed a two-stage evolution within the cement paste. It is predicted that the dissolution rate is different in a supercritical CO_2 environment and the CO_2-saturated brine. They estimated that calcium carbonate precipitation was responsible for an initial sealing stage. However, an increase in porosity occurred in the second stage and was attributed to the dissolution of calcium carbonate. Thus the dissolution occurred early resulting in heavier degradation in CO_2-saturated water than in supercritical CO_2.

Kutchko et al. (2008) examined Class H portland cement after nine days of P_{CO2}=30.3 MPa and 50°C exposure. These static immersion tests resulted in a 220 μm alteration zone [carbonated cement]. Total alteration depth after 20 years of exposure were extrapolated using

Monte Carlo Simulation and Elovich diffusion predicted to be ~1.7 mm in supercritical CO_2 zone and 1 mm in CO_2-saturated in a 1% NaCl brine. These alteration zones are comparable in the same magnitude to Class G portland cement in a 4 molar (M) NaCl solution at 90^{o}C and 28 MPa (Barlet-Gouédard et al., 2009). These authors found rates are 1/10th of the alteration to the Class G Portland cement in a 4 M NaCl compared to Kutchko et al. (2007) suggesting that salinity does play a role in alteration. This dissertation will explore the difference in brine composition. The two studies only examined a simple brine comprised of NaCl.

In addition to the neat cement immersion tests, Kutchko et al. (2009) also discovered that the combination of Class H cement with type F flyash and 2% bentonite in a 1% brine (15 MPa and 50^{o}C) resulted in dramatic alteration of the cement. The total carbonation depths are estimated at 170-180 mm in supercritical CO_2 and 520 mm in CO_2 saturated brine. The authors imply that fly ash, typically used for its pozzolanic properties to replace cement content in concrete, should not be utilized in carbon capture and sequestration applications.

Pratt et al. (2009) also examined portland cement cured at room temperature with a 100% relative humidity (PCO_2=15 MPa and 50^{o}C) and found 0.2 mm alteration within 12 weeks. In this study, the cement appeared to contain relic anhydrous cement grains and decomposed C-S-H. Experiments by Sweatman et al. (2009) had comparable rates of carbonation with Class G cement that were cured in water at (PCO_2=13.8 MPa and 60^{o}C) with 40% relative humidity with CO_2 after 12 weeks.

Other laboratory experiments performed by Kutchko et al. (2011) found that the alteration of cement exposed to acid gas (H_2S-CO_2) had significant alteration and mineral changes. These experiments were at a PCO_2=15 MPa and 50^{o}C with 21 mmol% of H_2S, resulted in carbonation and a sequence of oxidation-reduction sulfide reactions (ettringite and pyrite precipitation). The authors suggest that the mineralogical changes were controlled by local pore water pH.

Matteo & Scherer (2012) also examined the pH boundary of hydrochloric and carbonic acid effects on Class H portland cement within a temperature range of 30-80^{o}C. The authors concluded that extrapolating rates from batch experiments must be used with caution because there is a time dependence of alteration reaction rates. The main point was that the leached species could impact the dissolution kinetics and quantifying future alteration is difficult.

Another study demonstrated that a pre-cracked cement core with CO_2 flow test had the ability for self-healing (Sweatman et al., 2009). First the system was subjected to a flow with fresh water, and then purged with CO_2-saturated water. After 57 min, the authors found that no water flowed, an indication of self healing, and that the factures had carbonated. This publication discusses a comprehensive approach for remedial solutions to ensure long-term, effective CO_2 zonal isolation in existing wells and in old wells to be plugged or abandoned. The technology to inject CO_2 into geologic formations has been utilized in other locations outside of the United States, e.g. in Sleipner, Norway (Holloway, 2005).

Laboratory results are comparable to analysis of cement cores in the SACROC unit in Texas used in enhanced oil recovery (EOR) in which CO_2 was flushed for over 30 years to recover oil (Carey et al., 2007). The SACROC (Pennsylvanian age limestone with Wolfcamp shale caprock in West Texas) unit for example, is a very shallow reservoir for natural gas recovery, enhanced oil recovery, and not a direct storage area for CO_2 at depth. Crow et al. (2009) also compared cement cores from a natural CO_2 reservoir in Colorado. Bachu and Watson (2009) also studied 79 wells in Alberta, Canada CO_2 was used for EOR operations and acid gas (H_2S and CO_2 mixture). It was found that well failure is higher in converted wells compared wells specifically designed for injection. The examination of differences in the wellbore depth based on salinity and pressure gradient is also important to understand. A study by Scherer et al. (2011) revealed the importance of the wellbore environment, including adjacent brine composition from different depths when considering long-term cement alteration. Scherer et al. (2011) found significant differences in the altered state of the cement samples attributed to changes in salinity and host rock at different depths.

The wellbore environment also includes the surrounding formation rock. Hydrodynamic trapping occurs because the density of the CO_2 is less than that of most brines. There are three basic mechanisms that hold the CO_2 in place in the geologic formation. These include stratigraphic, residual, and mineral trapping. The buoyancy causes the majority of supercritical CO_2 to rise and spread laterally beneath the reservoir caprock (e.g. siltstones, shales, and coal). Residual trapping is when free-CO_2 migrates and becomes tapped between rock grains; the CO_2 is trapped by capillary forces, and then dissolves into formation water. Lastly, when dissolved CO_2 reacts with host rock, it can form carbonate minerals and thus trap it in a stable form.

Silicic type geologic formations can be large with caprocks capable of storing large amounts of CO_2. For example, the U.S. Department of Energy's National Energy Technology Laboratory (NETL) Phase III Regional Partnership pilot tests have been proposed in many large sandstone-bearing formations in the National Carbon Sequestration Database and Geographic Information System database (NATCARB, 2008). Literature on silicic-limestone sequences demonstrates sequestration from laboratory simulations and modeling (e.g. Dilmore et al., 2008; Xu et al., 2005; Rosenbauer et al., 2005; and Bennion et al., 2008). There are many factors that must considered in host rock formations, specifically the relative permeabilities are functions of rock properties, such as wettability. For example, Rosenbauer et al (2005) demonstrates the requirement to understanding supercritical CO_2 within host brines by examining ionic and hydraulic trapping of CO_2 within limestone and carbonated mineral formation in plagioclase-rich arkosic sandstone. In addition, Xu et al. (2005) modeled CO_2 mineral-trapping in forms of dawsonite and ankerite in a sandstone-shale model based on Gulf Coast sediments. The relative permeability of brine-CO_2 systems is dependent on in-situ conditions such as pressure, temperature, and water salinity (Bennion and Bachu, 2008). Furthermore, Dilmore et al. (2008)

estimated nearly 0.36 Gt of dissolved CO_2 in the Oriskany formation solution and estimated that 8.8 Gt of supercritical CO_2 brine were displaced in the formation based on the calculated solubility of CO_2.

Basalts are another rock type that could be ideal for geological sequestration applications. Flood basalts are highly permeable and could store CO_2 via physical trapping or geochemical mineralization (Reidel et al., 2002; McGrail et al., 2006). Typically, target sequestration formations require an impermeable caprock, like shale, to keep CO_2 within the injected formation. Basalts may allow for the supercritical fluid to interact with host rock and form *in-situ* mineralization. Mineralization experiments have shown that the interaction of basalt and supercritical CO_2 leads to precipitation of carbonate minerals, therefore basalt could potentially provide a repository to store CO_2 in the solid state (e.g. O'Connor, et al., 2003; McGrail et al., 2006; Schaef et al., 2009a,b). McGrail et al. (2006) also determined that the Columbia River Basalt Group (CRBG) has an estimated area of ~170,000 km^2 and has the potential to store up to 100 Gt of $CO_{2.}$ The CRBG basalts are heterogeneous in composition and contain variable concentrations of plagioclase, augite, pigeonite, as well as trace amounts of orthopyroxene, titaniferous magnetite and ilmenite (Reidel, 2005). Pre-existing secondary minerals in vesicles, such as zeolite and limonite, react with dissolved supercritical CO_2 and precipitate silica nodules and magnesite-calcite (O'Connor, et al., 2002). Schaef et al., 2009 also found that the silica dissolution kinetic rates of the Columbia River Basalt (CRB) for a range of temperatures (25–90^{o}C) under mildly acidic to neutral pH ($3<pH<7$) would provide an opportunity for converting CO_2 into a stable form.

2.7. Objectives: Experimental Improvements for CO_2 Sequestration

Many previous studies have failed to fully examine the wellbore environment in the laboratory. Specifically, composition and salinity should be a key consideration regarding geochemical interactions with cement under supercritical CO_2 for sequestration purposes. This dissertation provides insights as to how the well cement integrity, or between the host rock, may be compromised based on real and stimulated brines. This study is compared to previous studies in relation to alteration depth of cement paste as listed in Table 2-3.

The first objective is to investigate how brine impacts Class H portland cement in a pure CO_2 sequestration setting at conditions of 50^{o}C and PCO_2=28.9 MPa for 84 days. Some of the previous experimental studies of cement degradation when exposed to CO_2 do not actually mimic downhole conditions. Many experimental variables such as the salinity, temperature and pressure conditions are well below actual conditions in proposed CCS sites. Using the well depth and assuming a geothermal gradient of 30˚C/km and a pressure gradient of 10.5 MPa/km (Zoback, 2007; Ehrenberg & Nadeau, 2005), pressures and temperature can be predicted. For example, the Department of Energy Phase III Regional Sequestration Partnerships CO_2 injection sites can vary from 2.29 km with temperature of 69^{o}C and pressure of 24.1 MPa to 3.2 km with temperature up to 126^{o}C and pressure of 32.5 MPa (Verba et al., 2010).

The secondary objective is to compare these results to a mixed injection for co-sequestration intentions using CO_2-O_2 gas mixtures. There would be a potential economic advantage to co-sequestration of CO_2 along with other gases, thereby reducing the cost of CO_2 capture and in some cases eliminating a step to remove pollutant gases such as SO_2 and H_2S. An additional step to understanding CO_2 sequestration exposure is an examination of increased temperature. Many previous studies include surface temperatures up to 50^{o}C, which is too low for probable wellbore condition. As previously discussed, the C-S-H structure is heavily influenced by higher temperature conditions that may weaken cement resistance to acid attack.

The third objective is to analyze the interaction between the interface of host rock and Class H Portland cement with their respective basin solutions at 35^{o}C and PCO_2= 10 MPa for up to 84 days. These host rocks include Columbia River Basalt and Mt. Simon sandstone. Following these experiments, geomechanical tests were conducted. The goal was to determine the tensile and compressional strength of marble, hydrated cement, and hydrated cement after exposure to gas composition of CO_2, CO_2 -O_2 ,and CO_2 -O_2-sulfuric acid [SO_2 proxy].

The goal of this study is to better understand carbon sequestration in downhole conditions and how CO_2 can impact wellbore cement integrity. By combining civil engineering and geology, this research examines the influence of chlorides and the impact of secondary mineral precipitation on hydrated [hardened] Class H portland cement.

The next chapter, chapter III discusses the change of cement composition and stability that is driven by brine reactions while under supercritical CO_2 at elevated pressure and temperature conditions. Supplemental information in the Appendix A for this chapter includes SEM-EDS X-ray maps to determine carbonation and alteration depth of the cement. XRD patterns related to Chapter III are also included in Appendix A.

Table 2-3. Table of previous research compiled to compare cement type, curing conditions, experimental conditions and total alteration/carbonation depth.

Author	**Cement type**	**Curing conditions**	**Experimental conditions**	**Carbonation Depth**
Duguid et al. (2004)	(1) Class H cement + DI water, w/c = 0.38 (2) Class H cement + 6% bentonite + DI w/c = 0.70 Size: 7.3–7.7 mm ×140–260 mm	Cured in 0.5 M NaCl Room temp. 28 days	CO2-sat. brine (1) pH 3.7: bubble CO2 to 0.5 M NaCl (2) pH 2.4: bubble CO2 to 0.5 M NaCl + HCl Flow-through: 8.2–8.3 cm3/min Temperature (1) 23 ?C (2) 50 ?C Duration: 1.3–7.2 days	Entirely
Duguid et al. (2005)	Cement samples: Class H cement, w/c = 0.38 Size: 7.5 mm ×200 mm	Cured in 0.5 M NaCl Temperature: 20 or 50 ? 12-month old	CO2-sat. brine (1) pH 3.7: bubble CO2 to 0.5 M NaCl (2) pH 2.4: bubble CO2 to 0.5 M NaCl + HCl Flow-thru: 8.3–8.7 cm3/min (velocity: 230–245 cm/day) Temperature (1) 20 ?C (2) 50 ?C Duration: up to 31 days	(1) 0.066 mm/day (pH 3.7,20 ?C) (2) 0.24 mm/day (pH 2.4, 50 ?C)
Barlet-Gouédard et al. (2006, 2007)	Cement samples: Portland cement + antifoam agent + dispersant + retarder fresh water (1) 12.7 (dia.) ×25.4 mm (2) 25.4 (dia.) x 50.8 mm	Cured at 20.68 Mpa; 90 ?C for 72 h	(1) Wet supercritical CO2 (2) CO2-saturated water, Static vessel Temperature: 90 ?C PCO2 : 28 MPa Duration: 0.5 days, 2 days, 4 days, 1 week, 3 weeks, 6 weeks, 3 months, 6 months	(1) Supercritical CO2: L (mm) = 0.26t1/2 (2) CO2-saturated water: L (mm) = 0.22t1/2t – hour
Kutchko et al. (2007)	Class H cement paste samples w/c = 0.38 Size: 12 mm ×130 mm	1% NaCl for 28 days (1) 22 ?C, 0.1 MPa (2) 22 ?C, 30.3 MPa (3) 50 ?C, 0.1 MPa (4) 50 ?C, 30.3 MPa	(1) Wet supercritical CO2 (2) CO2-saturated 1% NaCl Static vessle Temperature: 50 ?C PCO2 : 30.3 MPa Duration: 9 days	(2) CO2-saturated brine: 0.2 mm in 9 days under curing condition 50 ?C, 30.3 MPa
Kutchko et al. (2008)	Class H cement paste samples w/c = 0.38 Size: 12 mm ×130 mm	1% NaCl for 28 days 50 ?C, 30.3 MPa	(1) Wet supercritical CO2 (2) CO2-saturated 1% NaCl Static vessle Temperature: 50 ?C PCO2 : 30.3 MPa 1 year extrapolation	Elovich/Monte Carlo (mm) = 0.016t1/2 (2) CO2-saturated brine: L (mm) = 0.09 ln(t) + 0.17 t – day (1) Supercritical CO2: 1.7 mm (2) CO2-saturated water: 1 mm
Kutchko et al. (2009)	Cement samples: Class H cement + fly ash + 2% bentonite (1) Fly ash/cement = 35:65, w/s = 0.51 (2) Fly ash/cement = 65:35, w/s = 0.56	1% NaCl for 28 days 50 ?C, 15 MPa	(1) Wet supercritical CO2 (2) CO2-saturated 1% NaCl Static vessle Temperature: 50 ?C PCO2 : 15 MPa Duration: 5, 7, 9, 14, 31 days	(1) Fly ash/cement: 35:65 Supercritical CO2 and CO2-saturated brine: 170–180 mm (2) Fly ash/cement: 65:35 CO2-saturated brine: 520 mm
Barlet-Gouédard et al. (2009)	Cement samples: Portland cement + antifoam agent + dispersant + retarder fresh water (1) 12.7 (dia.) ×25.4 mm (2) 25.4 (dia.) x 50.8 mm	Cured at 20.68 Mpa 90 ?C for 72 h	Repeat of 2006, 2007 (1) CO2-saturated brine (salinity of 220 g/L) Static vessel Duration: 2 days	(1) CO2-saturated brine: insignificant

Duguid and Scherer (2010)	(1) Class H cement + DI water, w/c = 0.38 (2) Class H cement + 6% bentonite + DI w/c = 0.70 Size: 7.5 mm ×200 mm	Cured in 0.5 M NaCl Temperature: 20 or 50 ? 12-month old	(1) pH 3.7: bubble CO2 to 0.5 M NaCl (2) pH 2.4: bubble CO2 to 0.5 M NaCl + HCl (3) pH 5: CaCO3-saturated NaCl brine equilibrated with a 100% CO2 atmosphere Flow-thru (1) 23 ?C (2)/(3) 50 ?C Duration up to 26 days	No carbonation in reaction (3)
Kutchko et al. (2011)	Class H cement paste samples w/c = 0.38 Size: 12 mm ×130 mm	0%, 1%, 10% NaCl 50 ?C, 15 MPa 28 days	(1) Wet supercritical CO2 (2) CO2-saturated 1% NaCl (3) Wet supercritical 21 mol% H2S-CO2 (4) Solution with dissolved H2S-CO2 Duration: 28 days	Formation of pyrite/ ettringite Depths not directly measured
Sweatman et al. (2009	Class G cement paste cast into sandstone 25.4 × 63.5 mm	Water 60oC 13.8 Mpa for 28days	(1) Wet (40% R.H.) supercritical CO2 (2) CO2-saturated water Static vessel Temperature: 60 ?C PCO2 : 13.8 MPa Duration: 15, 90 days	(1) Supercritical CO2: 0.2 mm in 12 weeks
Verba (2013)	Class H cement paste samples w/c = 0.38 Size: 25mm x 152 mm	Simulated formation brine (1-2.17 *M* or mol/ various Na-Mg-Ca-Cl 50 ?C, 28.9 MPa 28 days	(1) Wet supercritical CO2 (2) CO2-saturated 1% NaCl Static vessel Temperature: 50 ?C PCO2 : 28.9 MPa Duration: 28, 56, 84 days	(2) 1 *M*- 1250 µm; 2.2 *M* 800 µm after 84 days

CHAPTER III

THE INFLUENCE OF BRINE ON CLASS H PORTLAND CEMENT PASTE WITH CO_2 INJECTION

Chapter III will be submitted as a manuscript to the Journal of Greenhouse Gas Control, a peer reviewed journal. All written documents were completed by Circe Verba after experiments were completed. William O'Connor and Hank Rush at NETL assisted with the experiments and Dr. Mark Reed assisted in geochemical modeling (CHIM-XPT). Co-authors provided editorial assistance. This dissertation includes previously published and unpublished co-authored material.

3.1. Introduction

Long-term (>1,000 years) geologic sequestration of CO_2 has the greatest potential in deep sedimentary, brine-bearing formations with large storage capacity (e.g. Bergman & Winter, 1995; Bruant et al., 2002; DOE, 2007). Candidate saline formations have an impermeable caprock, typically of shale, to prevent leakage. Experimental and field studies of carbon dioxide sequestration show that supercritical CO_2 may react with the portland cement seal between the well casing and the geologic formation rock causing failure of the cement seal by degrading the cement, allowing CO_2 to migrate into the surrounding environment (Bruant et al., 2002; Hitchon, 1996). However, other studies show that alteration from CO_2 is slow and the cement is not altered to the extent that leakage would occur.

Given that portland cement is an intrinsically metastable material made of calcium-rich alkaline compounds, it is susceptible to acid attack by CO_2. If the wellbore seals are compromised, CO_2 could be released into the atmosphere or freshwater aquifers. Cement reaction with CO_2-saturated formation water is influenced on the degree of cement hydration, moisture availability, and temperature.

Cement paste durability has been studied for both CO_2-Enhanced Oil Recovery (EOR) and acid gas injection. Previous studies investigating the viability of CO_2 sequestration have shown that in simulated downhole conditions, CO_2-saturated brine results in alteration and carbonate mineral replacement (carbonation) of the Class H Portland cement. These laboratory solutions are typically a 1% NaCl solution and pH is controlled by HCl, a simplified version of what would occur in the natural setting (Duguid & Scherer, 2009, Kutchko et al., 2007; Rimmelé et al., 2008). The protocols for the experimental methods used here were adopted from Kutchko et al. (2008) where Class H ordinary portland cement was exposed to CO_2 sequestration conditions for up to one year and alteration depths extrapolated to indicate ~1 mm of alteration after 20 years of exposure. The alteration depths found by Kutchko et al. (2008) are 1/10th greater than those for a Class G ordinary portland cement in a 4 *M* NaCl solution at 90^{o}C under 280 bars of pressure (Barlet-Gouédard et al., 2009). The lesser degree of alteration suggests that salinity does have a role in cement alteration. Enhanced oil recovery (EOR) studies from the SACROC unit in Texas found alteration rates similar to those of Kutchko et al. (2008), although the exact sample depth and formation salinity are unknown (Carey et al., 2007; personal correspondence). Fabbri et al. (2009) found microfracturing and carbonation throughout the entire cement sample in experiments using an anti-foam agent, a dispersant and a retarder at 90^{o}C and 28 MPa.. Also in the Fabbri et al (2009) study, cement samples stored in fresh water and oven dried prior to CO_2 exposure were completely degraded.

Scherer et al. (2011) also examined wellbore cement extracted from a well at two different depths and although the initial cement used was identical, there were significant differences in alterations of the cement samples that they attributed to differences in salinity at different depths. This research demonstrates the importance of the wellbore environment, including adjacent brine composition and host rock formation, when considering long-term cement alteration.

Hydration of portland cement produces a network of semi-amorphous, gel-like calcium-silicate-hydrate (C-S-H) and portlandite (calcium hydroxide, $Ca(OH)_2$) surrounding the anhydrous clinker grains (Nelson, 1990). Class H cement used in this study has little $Ca_3Al_2O_6$ and thus little to no ettringite or calcium monosulfoaluminate precipitation.

Previous studies of cement under supercritical CO_2 conditions have revealed key components of the process: from layered alteration zones from the proximal CO_2-rich external side of the exposed cement to the distal unreacted cement (Kutchko et al. 2007). Dissolved CO_2 in water produces carbonic acid, H_2CO_3, that reacts with the cement seal and generates a strong pH gradient from the unreacted cement pore water (pH ~13) to the external carbonated solution (pH ~3). The stability of the cement phases is primarily controlled by pH. As the pH decreases, portlandite (pH ~12-13) and C-S-H (pH ~10-11) dissolve sequentially (Lecolier et al., 2006). Reaction of portlandite with CO_2 produces $CaCO_{3(s)}$ that fills pore space and decreases cement paste porosity. The formation of $CaCO_3$ initially increases compressive strength and provides a temporary buffer under acidic conditions, but $CaCO_3$ becomes increasingly unstable in continuous acidic conditions (Thaulow et al., 2001; Glasser, 2001). The diffusion of the aqueous calcium species is driven by Ca^2 concentration gradients that form in response to pH gradients. The calcite layer temporarily isolates portlandite and unreacted cement paste from the acidic CO_2-charged fluid.

Once residual portlandite on the proximal side of the calcite zone has dissolved, $CaCO_{3(s}$ begins to dissolve and calcium is leached from calcium silicate hydrate (C-S-H), leaving behind a zone of remnant amorphous silica that lacks strength and ultimately reduces the integrity of the cement (Thaulow et al., 2001; Kutchko, 2007). The change in cement paste mineral content and the precipitation of new minerals is herein described as alteration and the maximum extent of acid attack.

This study builds on previous cement- supercritical CO_2 experimental work (Kutchko et al., 2007; 2008) and field studies (Scherer et al., 2011) by addressing the effect of basin mixed brines ($CaCl_2$, $MgCl_2$, NaCl) saturated with CO_2 in a sequestration environment on Class H cement. Brine compositions used in this study simulate formation water at potential CO_2 sequestration sites found in the Mississippi Tuscaloosa sandstone, the SW Wyoming Nugget Sandstone, and the Mt. Simon sandstone in the Illinois basin (Table 3-1). We hypothesize that the degree of alteration of cement is dependent on the salinity, chemical components of the brine, and the effects of CO_2. It is well established that higher salinity decreases CO_2 solubility (e.g. Barlet-Gouédard et al., 2009), which could lead to different degradation rates. The injection of CO_2 into brine also increases aqueous phase salinity, which encourages precipitation of salts in supercritical CO_2 settings (Spycher & Pruess, 2005, Pruess, K., & Müller, 2009).

Table 3-1. Derived from basin-specific data: Brine compositions of 3 of 7 NETL Phase III Partnership sites and lab created Surrogate.

Regional Partnership	**Formation**	**Brine Species**	**Mole/L**
Big Sky	Nugget (SS)	$CaCl_2$	0.11
SW Wyoming	23 wells (NATCARB)	$MgCl_2$	0.01
	10-11,000 ft	NaCl	1.07
		Total	**1.19**
SECARB	Tuscaloosa (SS)	$CaCl_2$	0.34
SW Mississippi	28 wells (NATCARB)	$MgCl_2$	0.05
	9-10,000 ft	NaCl	1.78
		Total	**2.17**
MGSC	Mt. Simon (SS)	$CaCl_2$	0.17
Illinois	11 wells	$MgCl_2$	0.06
	(Hazen data – ISGS)	NaCl	1.02
	7,500 ft	$NaHCO_3$	0.01
		Na_2SO_4	0.02
		Total	**1.27**
Surrogate	Hydraulic lab	$CaCl_2$	0.16
	simulated brine	$MgCl_2$	0.02
		NaCl	0.82
		Total	**1.00**

3.2. Experiment

3.2.1. Sample Preparation, Curing, and CO_2 Exposure

Portland Class H well cement (Lafarge) was prepared as recommended by the American Petroleum Institute (API), with a water-cement (w/c) ratio of 0.38 (API, 1997). The powder analysis of the cement (weight percent) was 64.5% tricalcium silicate (Ca_3SiO_5), 11.77% dicalcium silicate (Ca_2SiO_4), 13.24% calcium aluminoferrite (Ca_4AlFeO_5), no tricalcium aluminate ($Ca_3Al_2O_6$), 2.94% MgO, 2.8% SO_4^{2-}, 0.16% total alkali content (Na_2O), 0.62% free lime; using Bogue equations from Table 3-2, loss on ignition (LOI) was computed to be 0.73

Table 3-2. Solid analysis of raw cement powder, cured cement paste, and hydrated cement after supercritical CO_2 exposure. Time (days) is time of exposure to cement (28, 56, and 84 days).Curing solution seen in Table 3-3. Altered cement analyzed discussed in methods.

Species	Cement Powder	Cured Cement	Post-Cure Surrogate Sample			Fresh Surrogate Sample			Secarb Sample			Big Sky Sample			MGSC Sample		
			28	56	84	28	56	84	28	56	84	28	56	84	28	56	84
				(Days)			(Days)			(Days)			(Days)			(Days)	
Al_2O_3	2.78	2.40	2.28	2.32	2.20	2.29	2.22	2.26	2.31	2.22	2.14	2.19	2.18	2.17	2.21	2.24	2.06
BaO	0.07	0.05	0.05	0.05	0.04	0.05	0.05	0.04	0.05	0.05	0.04	0.05	0.05	0.04	0.05	0.05	0.04
CaO	64.02	54.55	52.25	50.65	47.51	51.20	50.01	49.82	51.68	50.46	49.83	50.78	48.81	48.03	49.45	50.50	48.50
Fe_2O_3	4.37	3.64	3.54	3.62	3.42	3.57	3.49	3.54	3.57	3.46	3.33	3.43	3.44	3.32	3.47	3.58	3.19
MgO	2.94	2.49	2.28	2.29	2.21	2.30	2.21	2.27	2.33	2.26	2.21	2.23	2.21	2.20	2.24	2.25	2.13
SiO_2	21.07	17.95	17.89	18.23	16.59	18.25	18.73	17.02	18.10	18.08	16.35	17.85	18.42	16.77	18.10	18.37	15.45
TiO_2	0.20	0.17	0.14	0.16	0.20	0.14	0.14	0.18	0.15	0.14	0.17	0.13	0.14	0.20	0.14	0.14	0.17
LOI[*]	0.73	16.85	20.10	20.70	23.90	20.20	21.00	22.90	19.95	21.50	23.00	22.10	23.00	23.50	23.00	21.00	26.50
Total	96.64	98.55	98.73	98.24	96.30	98.21	98.05	98.27	98.35	98.37	97.29	98.96	98.45	96.46	98.86	98.33	98.26
C[1]	0.07	1.65	2.88	3.12	2.52	2.48	3.52	2.35	2.39	3.35	2.23	3.60	3.72	2.45	4.07	3.15	3.18
CO_2	0.30	6.10	10.50	11.40	9.20	9.10	12.90	8.60	8.80	12.30	8.20	13.20	13.60	9.00	14.90	11.50	11.70
FeO	0.19	0.19	0.06	0.13	0.13	0.06	0.06	0.13	0.06	0.06	0.06	0.06	0.06	0.06	0.06	0.06	0.06
H_2O[2]	<0.01	5.55	3.49	3.86	7.12	3.79	3.91	49.30	3.47	4.14	7.72	3.68	4.02	7.60	3.70	3.45	6.91
Leco S	0.17	0.06	0.16	0.12	0.16	0.23	0.12	0.17	0.13	0.11	0.16	0.12	0.13	0.13	0.10	0.12	0.13
SO_3[3]	2.48	2.00	1.63	1.93	1.78	1.53	1.83	1.80	1.78	1.88	1.85	1.68	1.83	1.90	1.70	1.88	1.90

[*] LOI: Loss on Ignition, measured as the weight loss after 1 hour at 1000 C, in air.

[1] Inorganic carbon

[2] Free moisture (H_2O), measured as the weight loss after 1 hour at 105 C, in air.

[3] Sulfate sulfur- carbonate leach

[Cr_2O_3, K_2O <DL; MnO < 0.05; Na_2O < 0.04; P_2O_5 <0.105; SrO < 0.06]

The cement was cast into 1" diameter x 6" (25 mm x 152 mm) PVC-pipe forms. The cement was removed from the molds 24 hours. Six cement samples were cured in 1.2 L stainless steel (316 CrNiMo) vessels containing either their respective brines or distilled water for 28 days at 50°C and 28.9 MPa. Following the curing interval, the cement cylinders were placed vertically into autoclave vessels, three cylinders per autoclave, and filled with 600 ml of brine, enough to cover the bottom half of the specimens. The autoclaves were purged with CO_2 to displace the air, brought up to 50^oC, and injected with CO_2 to final pressure (28.9 MPa). CO_2 was injected through a gas line at the bottom of the autoclave vessels to simulate the highest potential of mixing and dissolution of CO_2 into the brine. The cement cylinders were exposed to CO_2 for durations of 28, 56, and 84 days. At the end of each time point, one cement cylinder was removed and a sample of brine was collected, the autoclave was then re-pressurized with CO_2. Wet porosity measurements with a helium porosimeter on all cement samples after exposure were inconclusive and not discussed in this paper.

The experimental conditions simulated the supercritical CO_2 headspace and CO_2 saturated brine environment of the sequestration environment. Subsurface conditions are assumed to be static owing to low permeability and porosity of the formation (Rimmelé et al., 2008; Zhang & Bachu, 2011). The cement cylinders were exposed to various CO_2-saturated brines ($CaCl_2$, $MgCl_2$, NaCl) to simulate saline formation waters and depths at three Department of Energy, National Energy Technology Laboratory (NETL) Phase III Regional Partnership sites. The composition of the brines and pressure temperature variables were derived from the National Carbon Sequestration Database and Geographic Information System database (Table 3-1) (NATCARB, 2008). The partnership sites include the Big Sky Carbon Sequestration Partnership (Big Sky), the Southeast Regional Carbon Sequestration Partnership (*SECARB*), and the Midwest Geological Sequestration Consortium (MGSC). A control *Surrogate* brine was adjusted to a 1 *M* (mole/l of brine) concentration to examine saturation and salinity effects (Table 3-1).

3.2.2. Sample Analysis

After exposure to supercritical CO_2, the samples were examined using a petrographic optical microscope and an FEI Inspect F, Field Emission Scanning Electron Microscope (SEM) and Oxford Instruments INCA X-ray analyzer (EDS). The SEM examination included backscattered electron imaging (BSE) and microanalysis energy dispersive spectroscopy (EDS). Samples were cut with white mineral oil and prepared with ethanol into thin sections and one inch SEM mounts. Samples were stored in vacuum-sealed mylar bags to prevent atmospheric carbonation. A vacuum evaporated Palladium coating was deposited to provide conductive surface. Elements were semi-quantitatively determined by their intensities in EDS X-ray maps and spot analysis. Elemental concentrations for quantification and measurement of alteration depth were optimized by a Cu-Kα standard. Elemental X-ray mapping documented alteration of the cement paste by identifying the distribution of calcium, silica, and chlorine in 18 samples. Each sample was divided into a grid and scanned at 96 individual locations on the cement cylinder, producing a stitched montage SEM image that displayed total elemental distribution. Given the heterogeneous nature of cement, it is difficult to quantify true elemental concentrations by the mass distribution as seen in SEM-EDS X-ray mapping; therefore, a CAMECA electron microprobe with wavelength dispersive spectrometer was utilized with a 10 kV accelerating voltage to determine change in the cement composition.

Representative of CO_2 exposed cement slices, 1.25 mm thick, were ground into a powder with a ceramic mortar and pestle for solid analysis. Altered and fresh cement compositions were determined by ALS Global Minerals, a commercial laboratory that specializes in solid rock analysis. Their methods include using an appropriate mixture of wet chemical, gravimetric and instrumental inductively coupled argon plasma spectroscopy (ICP-MS and ICP-AES) suited to determining all necessary components, as reported in Tables 3-2, 3-3, and detailed in Appendix D. All solutions were analyzed by ALS Geochemistry Laboratory Group with the appropriate methods describe in Appendix D. Chemical analysis using alkalinity titration (method EPA310.1) of $CaCO_3$ for bicarbonate and carbonate were completed using both sodium carbonate and hydrochloric acid methods. Ion chromatography (method EPA300.0) was used to determine aqueous concentrations of Br, Cl, and SO_4. Lastly, method SW6010B was used with nitric acid digested preparations with (ICP-AES) for metals in solution.

Table 3-3. Analyses of the aqueous solutions from brine-cured cement paste and hydrated cement paste after CO_2 exposure. Time (days) is time of exposure to CO_2 (28, 56, and 84 days).

	Concentrations, mg/L										
Sample	**Ca**	**Cr**	**Fe**	**Mg**	**Ni**	**K**	**Si**	**Na**	**Cl**	**SO4**	**pH**
Post-Cure Surrogate Brine	6280	0.87	0.02	600	0.12	338	0.37	26700	36100	50	6.5
28 days	620	0.02	0.08	612	6.74	364	44.80	21480	35700	34	11.7
56 days	1474	<DL	0.40	549	12.18	348	53.32	16200	37600	37	5.84
84 days	2237	<DL	0.54	668	21.71	365	49.44	21300	40000	30	6.43
Fresh Surrogate Brine	8450	0.02	0.02	626	<DL	6.13	7.64	24160	40700	<1	6.5
28 days	1869	0.03	0.17	1395	12.58	59.8	47.60	25530	37300	8	8.55
56 days	1770	<DL	0.55	948	15.85	56.6	53.68	18200	38100	7	5.73
84 days	1694	<DL	0.26	784	22.94	57	52.01	19700	39700	8	5.95
Secarb Brine	19000	0.04	0.03	1418	<DL	8.03	2.97	66260	83300	10	
28 days	7951	0.05	0.13	2056	12.43	62	39.60	64440	72400	4	6.65
56 days	5455	0.01	0.74	1373	15.74	61.2	43.36	37100	73600	4	5.27
84 days	6848	<DL	1.74	1528	27.18	59.7	34.12	30600	74400	4	5.55
Big Sky Brine	7255	0.09	0.01	<DL	0.01	48.7	0.62	32980	44300	52	
28 days	910	0.02	0.07	830	16.60	53.6	47.50	32920	42600	44	7.15
56 days	301	<DL	0.15	433	15.21	52.9	53.72	23200	43400	45	5.81
84 days	452	0.01	2.24	481	26.77	58.9	47.22	26300	46800	44	5.55
MGSC Brine	7102	0.05	0.18	2251	18.49	30.2	36.90	49780	49600	152	
28 days	5509	0.02	<DL	2310	<DL	31.2	35.24	34690	44470	160	6.89
56 days	5680	<DL	2.18	1697	24.77	31.4	41.07	21600	50900	304	5.75
84 days	3853	<DL	0.12	1313	43.00	36.8	40.92	22700	50900	294	5.93

*Cr, Ti below detection limit <DL

*F not detected

Cementitious phases were characterized using X-ray diffraction (XRD) collected by a Rigaku Ultima III with a 40KV/40mA Cu Kα source and a step speed of $1^{o}\theta$/min over a scan angle 2θ of $5^{o}$to 90^{o} at NETL-Albany. The qualitative analysis of XRD data was performed using Jade v9.1.4 Plus software and the International Center for Diffraction Data (ICDD) pattern databases (ICDD, 2008).

3.2.3. Geochemical Modeling

The carbonic acid produced by a high PCO_2 phase is the principal driver of the cement alteration reactions observed in this study. The pH in the bulk solutions were calculated under experimental pressure, temperature and brine composition conditions, because it cannot be measured *in-situ*. To determine the pH at pressure and temperature conditions we applied geochemical programs CHIM-XPT and SOLVEQ-XPT to pH measurements taken from the post-cured *Surrogate* brine experiments. CHIM-XPT calculates aqueous activity coefficients using an extended Debye-Hückel equation of Helgeson, et al. (1981) and gas fugacities by Spycher and Reed (1988). An H+ mass balance method was applied to calculate pH with the programs SOLVEQ and CHIM-XPT (Reed and Spycher, 1984). Aqueous and mineral thermodynamic data are from Shock et al. (1998). Multiple iterations were used on stable and metastable phases based on the distribution of aqueous species, minerals, and gases from equilibrium constants from SOLTHERM thermodynamic database (Reed & Spycher 1984; Reed, 1998). Equilibrium constants in SOLTHERM are computed using SUPCRT92 (Johnson et al., 1992), as modified for mineral thermodynamic data for silicates, oxides, hydroxides, carbonates, and gases from Holland and Powell (1998), with thermodynamic data for the cement minerals portlandite, jennite, tobermorite, Si-hydrogarnet and ettringite from Matschei et. al. (2007). Sulfide and other non-silicate mineral data are from the SLOP98 database (Shock, et al., 1998).

3.3. Results

3.3.1. pH Calculation

The pH of the bulk solution in the autoclave were measured at atmospheric pressure yielded the following pH's after the experimental periods of 11.74 after curing for 28-days, pH= 8.55 after 28-days, pH= 5.84 after 56-days, and pH= 6.43 at 84-days of exposure to supercritical CO_2. The pH at elevated P_{CO2} was calculated with the geochemical modeling program CHIMI-XPT based on the solution composition and measured pH yielding 3.0 at 50°C and 28.9 MPa CO_2 pressure in the 1 *M* brine at 28 days of reaction. In the 2.17 *M* brine, the computed pH is 3.85.

3.3.2. Hydration Prior to CO_2 Exposure

To understand the process of hydration and the effects of curing on the cement paste prior to CO_2 exposure, three cement control samples were prepared for 28 days under the following conditions: 1) air-cured (atmospheric), 2) distilled water-cured, and 3) *Surrogate* brine-cured (1 *M*) (Table 4-4, Fig. 3-1). The air-cure cement samples showed the $CaCO_3$ efflorescence of <100 µm thick as commonly observed on cement reacting with atmospheric CO_2. SEM observations show abundant unhydrated ferrite and calcium-silicate cement grains in the cement sample cured in air, due to limited water available for hydration.

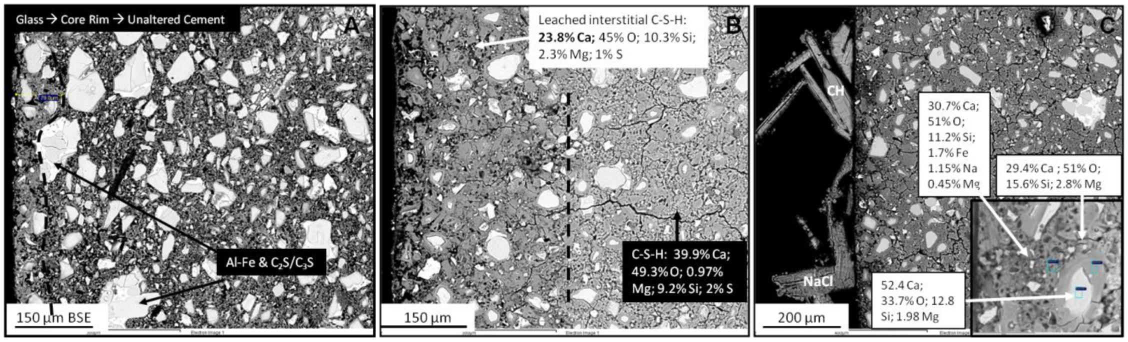

Figure 3-1. BSE images before CO_2 exposure: A) 28-day air-cured cement with atmospheric carbonation (indicated by black dashed line) and no hydration halo; B) 28-days distilled water-cure of cement resulted in aggressive cation (but not Mg) leaching. Dashed line separates the leached from unaltered cement; C) sample of 28 day curing in brine resulting in limited Ca cation leaching and a large hydration shell (enlarged) on anhydrous cementitious phase and large external crystals (EDS X-ray maps in Fig. 3-2). Semi-quantitative chemical compositions are shown for each zone.

Previous studies have shown significant degradation of Class G cement samples submerged for six months in pure water and exposed to CO_2 (Gouédard et al., 2007). Rimmelé (2008) showed that Class G cement samples submerged in fresh water exposed to CO_2 for only three weeks had completely altered the cement. This called for the investigation to determine the influence of salt-free water on hydrated cement samples before supercritical CO_2 exposure. Prior to gas injection, the cement paste cured in distilled water exhibited calcium leaching to a depth of ~300 µm. After 28 days, the dissolution of $Ca(OH)_2$ and C-S-H left an exterior leached zone with roughly half the calcium concentration of the unaltered cement (24% calcium in altered cement as compared to measured hydrated cement paste of with 40% of calcium). Further, the exterior of the sample cured in distilled water had spalled, resulting in the loss of cement paste, which could be the onset of degradation prior to acidic conditions.

To understand the effect of the brine on the cement paste before exposure to supercritical CO_2, we examined cement cured in a *Surrogate* (1 *M*) brine (Fig. 3-1). In contrast to the sample cured in distilled water, the sample cured in the 1 *M Surrogate* brine showed little evidence of calcium leaching from the cement, likely due to the high concentrations of calcium in the brine. Ongoing hydration is evident as seen in SEM-BSE images in which hydration shells developed on the anhydrous cement are made of inner and outer C-S-H products with interstitial $Ca(OH)_2$. SEM-BSE and X-ray mapping also showed microcubic halite on large hexagonal $Ca(OH)_2$ crystals on the exterior surface of the cement cylinders and within the cement pores (Fig. 3-1c and Fig. 3-2). The secondary minerals were confirmed with wet preparation XRD analyses.

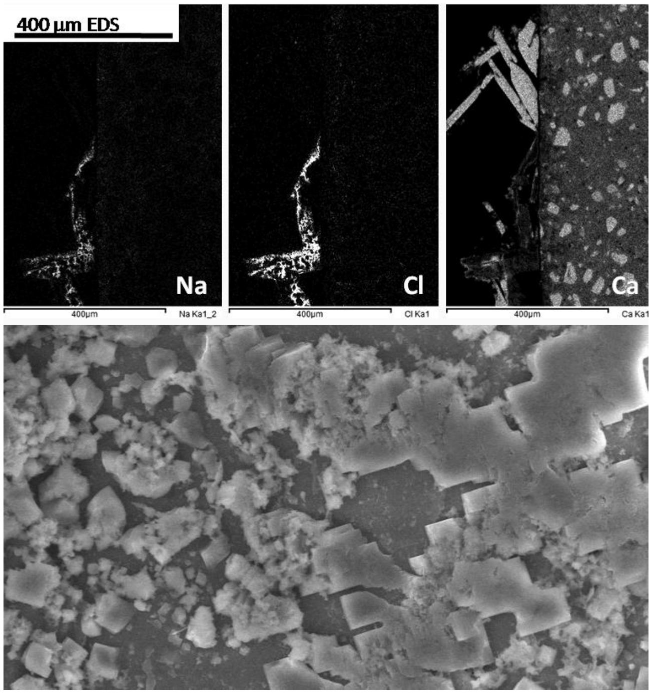

Figure 3-2. Upper image shows SEM-EDS (Ca, Cl, Na) element X-ray maps for 28-day *Surrogate* brine cured cement focusing on the exterior portlandite and NaCl crystals, the outline of which indicates that a likely pseudomorph of NaCl is replacing the portlandite crystals. Lower image shows a magnified BSE image with cubic NaCl grains within the pseudomorph.

3.3.3. Brine Effects Under Supercritical CO_2

XRD analyses of the cement samples cured in simulated brines subsequently exposed to CO_2 (Table 3-4) showed that all samples contained calcium carbonates, brownmillerite (Ca_2FeAlO_5), portlandite ($Ca(OH)_2$), unhydrated cement phases belite (Ca_2SiO_4), and alite (Ca_3SiO_5). Calcite is the dominant calcium carbonate species, with trace amounts of aragonite and vaterite present, in some samples, discussed in detail below.

Table 3-4. Semi-quantitative estimates of mineral weight percent (wt %) composition (from JADE 9 Whole Pattern Fitting; no internal standard used). Errors are large because the sample collected was a slice of the altered cement rind, but it included a substantial amount of unaltered cement. Amorphous silica is difficult to quantify, but is representative of the accepted range of C-S-H. High concentrations of $CaCO_3$ *mirror lower concentrations of* $Ca(OH)_2$ *reflecting carbonate replacement of the portlandite upon* CO_2 *alteration.*

ID	Used Surrogate Brine	Fresh Surrogate Brine	Secarb	Big Sky	Mt Simon
Portlandite $Ca(OH)_2$	20	18	9	4	12
Brownmillerite Ca_2FeAlO_5	9	8	7	8	6
Hatrurite [1] Ca_3SiO_5	14	11	14	9	10
Larnite $Ca_2(Si0_4)$	5	6	2	3	3
Hydrotalcite $Mg_6Al_2(CO_3)(OH)_{16}*4H_2O$	6	6	7	5	3
Amorphous	31	38	28	17	27
Total $CaCO_3$ (Calcite, vaterite)	16	18	33	54	40

Reported error x3; Material Data Inc., JADE

[1] Reported with combined calcium silicate pattern

All cement exposed to supercritical CO_2 had alteration zones on the outer rim of the cylindrical samples similar to that described by Kutchko et al., (2008) (Figs. 3-3 and 3-4). The alteration consisted of the following zones (Fig. 3-4): 1) an outer reddish-orange porous amorphous silica zone, 2) a well crystallized $CaCO_3$ band, 3) an apparent, subtle Ca-depleted zone observed by SEM-EDS analysis where decalcification processes are minimal on portlandite and 4) a distinct Cl-enriched zone, not previously identified.

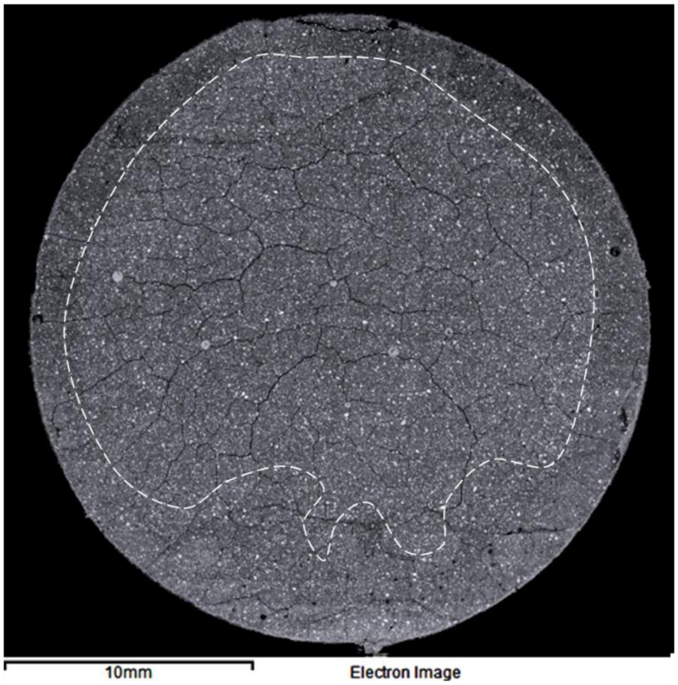

Figure 3-3. SEM montage image which displays alteration around the outer rim of the cement cylinder (outlined by white dotted line).

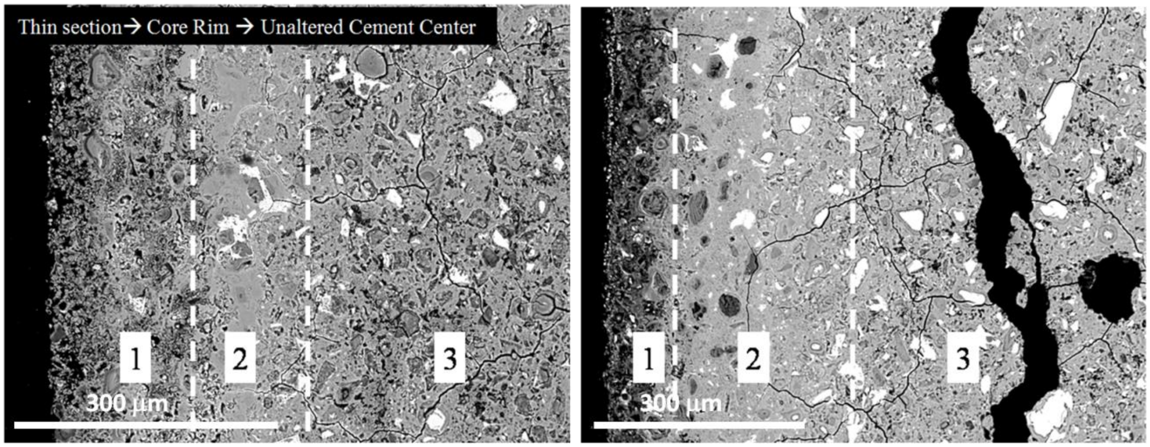

Figure 3-4. SEM BSE image of samples exposed to supercritical CO_2 (left) and CO_2-saturated *Surrogate* brine (right) after 84 days. Dotted line indicates alteration boundaries: 1) porous silica zone, 2) $CaCO_3$ zone, 3) an apparent Ca-depleted cement. Scale bars are 300 µm.

Analyses of the brines show that calcium concentration decreased substantially following CO_2 injection (28, 56, and 84 days, Table 3-3), indicate that calcium migrated into the cement matrix or precipitated out of solution as crystals. In some cases (Table 3-3) the calcium concentration decreased initially and then increased later, this is likely a result of re-dissolution of

Ca-rich phases. Given the large volume of brine relative to the calcium loss in cement, it is highly likely that the brine is the source of calcium.

The ingress of chlorine from the brine into the cement is seen in Figure 3-5. The distribution of chlorine within the altered cement is significant because the Cl^- appears to attach to the semi-amorphous C-S-H gel. The chlorine distribution served as a SEM index of the penetration depth of acid attack on the cement. Micro-halite crystals, <5 µm in size, were primarily present in the apparent calcium depleted zone of the altered cement paste. In addition, NaCl precipitation in cement paste may be an indication of supersaturation of halite in cement pore and may be due to water abstraction into the hydrating cement.

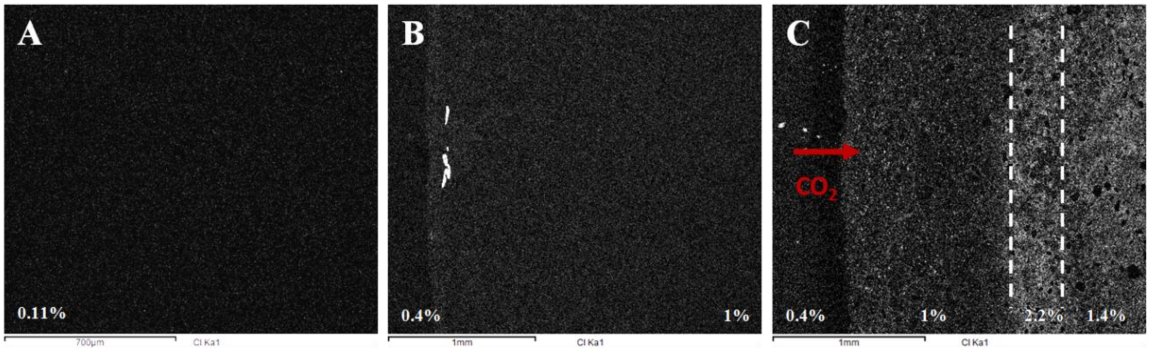

Figure 3-5. Chlorine concentration (EDS) given in wt. % at the bottom and shown by brightness in the images. A) Cement cured in distilled water to indicated base Cl (0.11%) from epoxy contamination; B) 28-days cure *Surrogate* brine (prior to CO_2) with uniform Cl concentration (~1%) and precipitation of NaCl (bright white); C) CO_2 exposure for 84 days in the *Surrogate* brine with several zones of Cl enrichment including a 2.2% enrichment in Ca^{2+} depleted zone and 1.4% adjacent into unaltered cement. The chloride X-ray maps were used as a proxy for carbonation and alteration depth.

The alteration depths in cement samples were dependent on the type of brine into which they were submerged in and increased with exposure to supercritical CO_2 (Fig. 3-6 and 3-7). Newly formed portlandite crystals (50- 1200 µm length) and halite cubes (0.5-5 µm in size) were observed on the exterior surface of all the cement samples cured in brines prior to gas injection. Cement adjacent to inner portlandite regions was less degraded, perhaps because $Ca(OH)_2$ locally neutralized the carbonic acid.

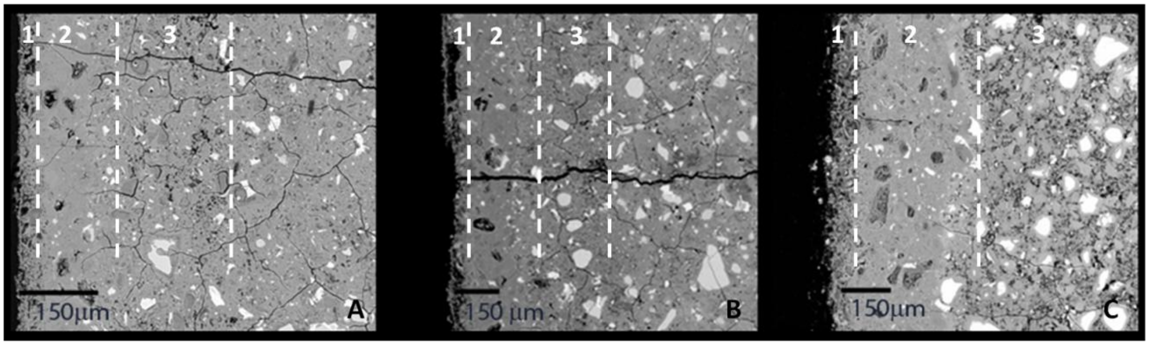

Figure 3-6. Development of alteration depth with exposure time in the *Surrogate* brine. SEM BSE: Exposure time is given from left to right: (A) 28 days, (B) 56 days, and (C) 84 days. Dashed lines on BSE images show zone boundaries. Cylinder surface is on the left side of images. Zone 1: outermost porous silica zone, 2: the $CaCO_3$ zone and 3: Ca-leached zone, The Cl-enriched zone inward from the Ca-leached zone is not apparent here.

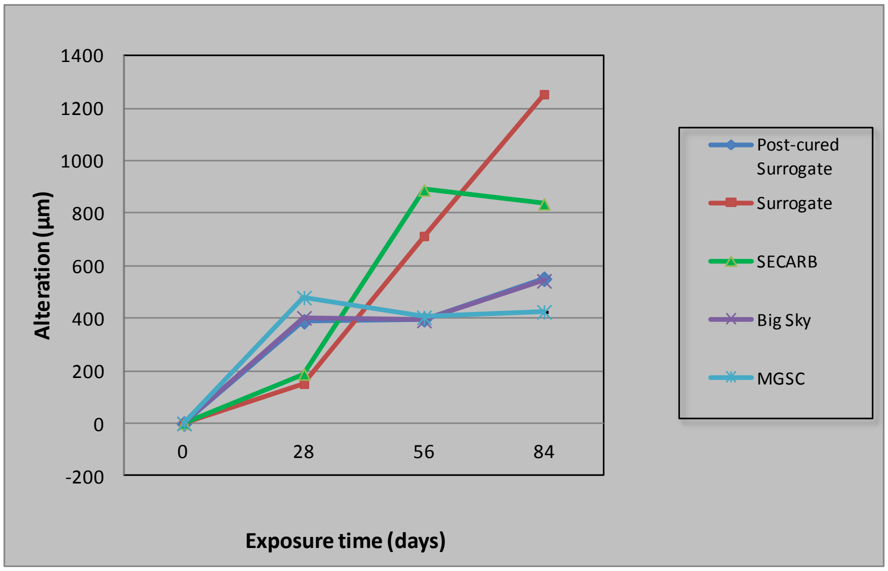

Figure 3-7. The average alteration depth (average based calculation 96 data points) on cement paste, increasing with time exposed to supercritical CO_2, depicting interactions of different brine types.

3.3.3.1. Cured and Unreacted *Surrogate* Brine

The composition of formation fluid in contact with cement changes as it reacts during the curing process. In a natural setting, the formation waters may flow away from the cured cement in some cases and be replaced by unreacted formation water. To examine alteration in a conventional cured system (loaded brine), a cement sample referred to as "post-cured" was retained in its curing solution, labeled as the cured *Surrogate* (1 *M*) brine. A maximum alteration depth of 551 µm was observed after 84 days of CO_2 exposure. After 84 days, the CaO wt% in the exposed cement sample decreased by 7% compared to unexposed cement. This sample had the least total alteration with 14 wt% $CaCO_3$, high amounts of unaltered portlandite, and Ca_3SiO_5. The aqueous solution data shows an initial decrease of aqueous Ca^{2+} from 6280 to 620 mg/l because the aqueous Ca^{2+} moved into the cement. This is likely a result of a chemical gradient of high calcium content in the brine. However, as acid attack progressed, the calcium compounds within the cement matrix dissolve and leach out of the cement causing aqueous calcium to increase from 620 mg/l to 2237 mg/l (Table 3-3).

To simulate an influx of new formation water (brine) after curing, cement samples were immersed in unreacted (new) *Surrogate* brine with CO_2 (labeled in Table 3-3 as "Fresh *Surrogate* Brine"). Petrographic analysis of the cement immersed to the fresh *Surrogate* brine (1M) revealed a non-uniform, narrow carbonate band along the rim of the cement cylinder. Continued exposure to CO_2 led to a wider, well crystallized $CaCO_3$ band with a widening amorphous silica zone. The cement cured in the fresh *Surrogate* brine and exposed to supercritical CO_2 had the largest penetration depth, exceeding 1 mm at 84 days. At the end of the experimental interval, portlandite crystals were not observed on the cement cylinder surface submerged in fresh brine. The precipitation and dissolution of secondary calcium minerals can be traced by a change in the solution composition as seen in Table 3-3. There is a decrease of 6700 mg/l aqueous Ca^{2+} in solution as the cement paste reacts with CO_2 over 84 days. The change in calcium concentration is also visible in the solid analyses (Table 3-2) suggesting a total loss of 4.73 wt% of CaO in the cement. The CO_2 content of the cement is 13 wt% after 56 days of exposure. Under the continuous influx of CO_2 for 56 days in the fresh *Surrogate* brine, the solution data marks the start of calcium carbonate dissolution. Calcite dissolution and subsequent leaching of calcium resulted in an amorphous silica exterior. XRD analyses of the altered cement paste shows a total of ~18 wt% calcite precipitated and nearly 38 wt% amorphous silica at the end of the experiment.

Solution data showed an increase of 760 mg/l aqueous magnesium after 28 days, indicating dissolution of Mg^{3+} from the cement paste. There was also a slight increase in aqueous Si of 44 mg/l), evidence that most of the silica remained in the cement (Table 3-3). Increases of aqueous species correlate with carbonation and less cement degradation in petrographic analysis in the fresh brine sample than in the cured brine sample that had remained in the *Surrogate* curing solution.

3.3.3.2. Big Sky

The cement paste samples immersed in the *Big Sky* brine had a depth of alteration of 402 µm after 56 days and increased to 540 µm after 84 days of supercritical CO_2 exposure. SEM and petrographic analysis showed that the cement reached maximum carbonate (>50 wt%) at 28 days as calcite replaced interstitial portlandite (9% unreacted $Ca(OH)_2$) left in the hydrated cement. The exterior surface of the cement cylinder was heavily covered in $Ca(OH)_2$, which was not seen in the other samples. Relative to the other brine cured cements, there appeared to be less calcium leaching, a thinner porous silica zone, and less Cl enrichment. The lack of a strong chloride boundary in the cement indicates less diffusion of brine into the cement. However, in regions of the cement cylinder surface lacking $Ca(OH)_2$ crystals, calcite was nearly double in thickness compared to the 1 *M* brine. The supply of calcium from the coating of portlandite neutralized the carbonic acid, making it difficult to quantify the Big Sky sample and total alteration.

3.3.3.3. MGSC-Mt. Simon

Although the salinity of the MGSC-Mt. Simon brine (1.272 *M*) is similar to that of the *Surrogate* brine, the Mt. Simon brine is a natural formation water (Table 3-1) and contains more magnesium and sulfate. The sulfate concentration in this brine could induce external sulfate attack on the cement, which could produce ettringite ($Ca_6Al_2(SO_4)_3(OH)_{12}\cdot 26H_2O$). However, SEM-EDS X-ray maps show that prevalent sulfur is bound in the C-S-H. Dissolution of gypsum (added in the initial cement mix to prevent flash setting) allowed aqueous SO_4^{2-} to increase from 152 mg/l to 300 mg/l after 56 days.

The hydrated cement sample shows precipitation of secondary portlandite and two polymorphs of calcium carbonate. The alteration zone in the cement in the MGSC-Mt. Simon brine ranged from 404 to 479 µm in depth, with a thick calcite band and an adjacent "finger-like" vaterite zone that intruded into the unaltered cement. SEM and petrographic analyses displayed secondary portlandite crystals, >1 mm in size (Fig. 3-2). The total 40 wt% $CaCO_3$ can be compared to the change of aqueous Ca^{2+} in the Mt. Simon brine. The calcium decreased from 7102 mg/l to 509 mg/l (Table 3-3) as cement carbonated and portlandite formed. The aqueous Ca^{2+} subsequently increased to 5700 mg/l after 56 days, and then decreased to 3800 mg/l after 84 days. Aqueous magnesium concentration decreased from 2251 mg/l to1313 mg/l after exposed to supercritical CO_2 for 84 days. Furthermore, the cement paste also lost roughly 2.5 wt% SiO_2 (Table 3-2).

3.3.3.4. *SECARB*

The *SECARB* brine had the highest initial concentration of aqueous Ca^{2+} and overall salinity (2.2 *M*). The cement samples exposed to the *SECARB* brine had an initial alteration depth of 188 µm after 28 days. The maximum alteration depth of 836-889 µm was established by day 56. XRD indicates semi-quantitatively 28% amorphous silica, 33 wt % total $CaCO_3$, and only 9% hydrated cement remaining within the first millimeter of the cement sample. The majority of the portlandite had altered to calcite. Furthermore, SEM-EDS images of the *SECARB* brine reaction with the cement cylinder exterior show secondary portlandite crystals coated with brucite ($Mg(OH)_2$). SEM imaging also revealed fractures in the cement paste, likely due to depressurization of the experimental chamber after curing. A well-crystallized distributed calcite filled these fractures after CO_2 exposure (Fig. 3-8). This sample also had enlarged pores (45-150 µm) where C-S-H had deteriorated within the outer-most millimeter of the cement cylinder, as seen by a loss of ~ 6 wt% CaO $_{(s)}$ (Table 3-2). The loss of aqueous species is reflected in the solution (Table 3-3), where aqueous Ca^{2} decreased from 19,000 to 7951 mg/l and aqueous Mg^{2+} yielding a net loss of 500 mg/l owing to brucite precipitation.

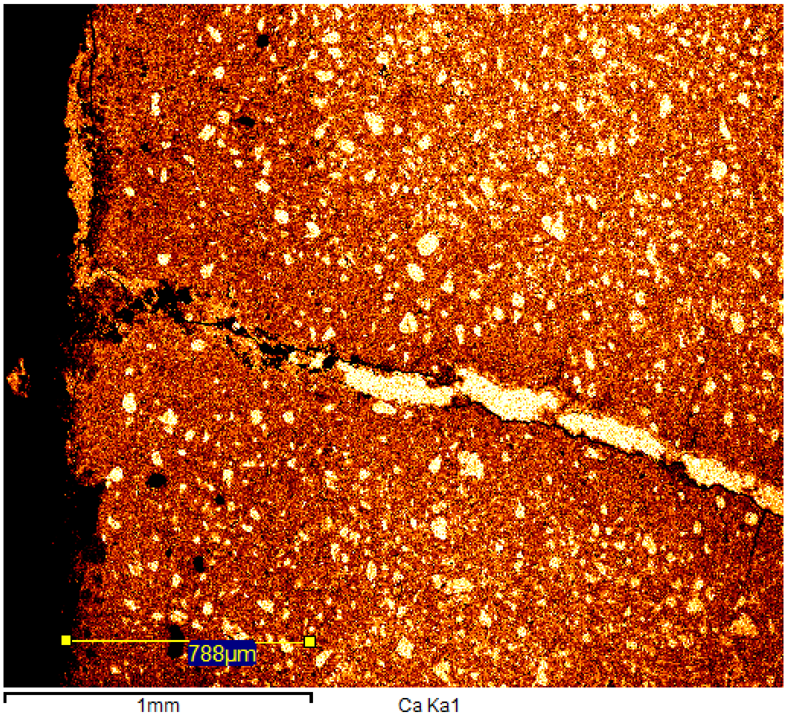

Figure 3-8. A calcium SEM-EDS X-ray map of the alteration from the *SECARB* brine sample (highest salinity of 2.2 *M)* that formed a fracture during rapid depressurization in the curing process. This sample shows calcite (pale yellow) in the fracture along with a darker orange that represents the de-calcified margin i.e. where fracture traverses into the cement paste cylinder pulling calcium to form calcite, or where calcium has diffused into solution.

3.4. Discussion

3.4.1. pH estimate and mineral saturation states

Carbonic acid is the principal driver of the cement alteration observed in these studies. Geochemical modeling was used to calculate supercritical CO_2 reactions with brine and cement paste under pressure and temperature. At 50°C and a CO_2 pressure of 28.9 MPa the calculated pH is 3.0 in the 1 *M* (*Surrogate*) brine. This pH agrees with a pH of 2.97 calculated by Kutchko et al. (2007). The higher salinity *SECARB* (2.17 *M*) brine has a computed pH of 3.85. These low solution pHs would drive carbonic acid into the cement and produce a pH gradient between the external brine and the unaltered cement, resulting in the observed zoned alteration. The total alteration depth of the *Surrogate* (1 *M*) and *SECARB* (2.17 *M*) cured cement samples reflect the influence of salinity. The higher salinity lowers CO_2 solubility, and thus lowers the acidity of the solution, possibly causing decreased alteration relative to less saline waters.

The pH plays a key role in understanding mineral saturation states. For example, the calculated alkaline pH of 11.74 reflects the dominance of portlandite after the brine has semi-equilibrated as the cement paste cures before CO_2 exposure. Then the dissolution of portlandite neutralizes the acid in the brine initially, as seen after 28 days of exposure to supercritical CO_2. Similarly, the precipitation of calcite beneath the porous silica zone requires a much greater pH than pH =3 and reflects the gradient in pH in the alteration halo, from a pH= 3.0 at the surface to a pH= ~12 in the interior where portlandite within the fresh cement is unaltered.

Using the computed pH of the post-reaction brine chemical analyses at 84 days, mineral saturation indices were computed for the brine. The calculations indicate that all minerals except quartz and its polymorphs are undersaturated in the brine. The calculated undersaturated (log(Q/K)=-1.20) aqueous amorphous silica in the brine is comparable to the low concentration of silica leached into the solution. The silica in the cement is the last to dissolve after all Al^{3+}, Ca^{2+}, Fe^{2+}, and Mg^{2+} has leached out of the outermost zone of the cement, as indicated by SEM-EDS. Therefore, we can conclude that the silica in the cement exterior is still intact, and the solution data is comparable to the undersaturation of silica as calculated by the model.

In addition, CHIM-XPT calculated the conditions of the *Surrogate* brine as having a pH of 3.0, approximately 47 g CO_2 dissolved in solution and 1.059 total moles of HCO_3^- generated as the calcium carbonate dissolves. In the natural setting, a large amount of CO_2 gas would be in contact with a relatively small amount of cement, therefore driving Ca^{2+} from the carbonated zone into the brine. This would advance the carbonate front further into the cement.

Lastly, the brine was undersaturated in halite (log(Q/K)=-2.15), however, halite crystals did form within the pores of the cement as the cement hydrated. Although the bulk solution was undersaturated in halite in the CHIM-XPT calculation, halite also formed on the outer surface of cement, suggesting that the model does not apply to the cement cylinder surface. The external halite shows that the bulk brine composition, which is halite undersaturated, does not react immediately upon contact with the cement, and the lack of stirring enables dehydrated of the cement surface.

3.4.2. CO_2 Exposure

Dissolved CO_2 is the dominant driver for alteration of the metastable hydrated cement. In contrast to the shallow alteration depth found in earlier studies, our results show that the mixed Na-Ca-Mg brines altered the cement to depths of 800 µm at 2.17 *M* brine (*SECARB*) and 1250 µm in the 1 *M* brine (*Surrogate*) after 84 days (Table 3-5). These alteration depths substantially exceed the 1 mm penetration depth predicted after 20 years of CO_2 exposure using both low and high salinity simple (NaCl) brines (Kutchko et al., 2008; Barlet-Gouédard et al., 2009). Our results do agree with those of Barlet-Gouédard et al. (2009). This study further suggests that cement alteration is related to salinity because the salts affect the reaction kinetics. Salinity also correlates with the pH of brines after CO_2 is injected into the system. The 1 *M* salinity brine is acidic (pH=3.0) and this contribute to an alteration that exceeded 1 mm in 84 days. The cement immersed in the 2.17 brine was less degraded with a less concentration of H^+ (higher pH of 3.85).

Table 3-5. Depth of alteration for each sample based on 15 (section) samples, 90 total measurements, average calculated on 24 data points; using the average standard deviation. The brine notation: duration- autoclave-brine exposed to Surrogate (1 M) in cured brine solution; Surrogate (1 M) in new brine post-cure; SECARB (2.17 M) brine; Big Sky (1.19 M); MGSC Mt. Simon (1.272 M) brine.

ID #	Average Depth of Alteration (µm)	
28-Used Surrogate	389	±49
56-Used Surrogate	397	±35
84-Used Surrogate	551	±154
28-Surrogate	151	±20
56-Surrogate	714	±61
84-Surrogate	1254	±441
28-SECARB	188	±35
56-SECARB	889	±259
84-SECARB	836	±66
28-Big Sky	402	±20
56-Big Sky	392	±82
84-Big Sky	543	±62
28-MGSC	479	±295
56-MGSC	404	±52
84-MGSC	425	±102

The cement in the higher salinity brine, *SECARB*, (2.17 *M)* was less altered than compared to cement in the *Surrogate* brine (1 *M*). The *SECARB* is at a higher pH (pH 3.85) than the *Surrogate* brine and alteration was 840 µm deep, approximately half that of the *Surrogate* cement sample. The *Surrogate* (1 *M*) showed the deepest alteration, 1.25 mm, after 84 days probably because the lower salinity allowed more CO_2 to dissolve and react more with the cement paste (Table 3-5). In general, the penetration depth increased and zones became increasingly well defined over time. The shallow, finely distributed initial $CaCO_3$ thickened as the carbonation front propagated inward with increased exposure time, particularly in the *Surrogate* and *SECARB* brines. Secondary portlandite precipitation detected on the sample surface may have temporarily slowed dissolution of calcium carbonate. The total alteration of the *SECARB* cement sample is likely due to lower CO_2 solubility in *SECARB* brine.

The calcite vein in cement exposed to the *SECARB* brine (Figure 3-8) is evidence of the "self-healing" ability of cement. Calcite precipitation may be dependent on the higher aqueous calcium concentration and higher pH of the *SECARB* sample. However, the calcite vein is subject to dissolution in the CO_2-dominated setting in every case, as explained above. Self-healing cement, may nevertheless, be vital in understanding how to prevent gas leakage. The calcite vein present in the cement exposed to *SECARB* brine has the highest concentration of calcium among the compositions tested.

The development and spatial spread of the CO_2-induced alteration over 28, 56, and 84 days is shown in SEM images in Fig. 3-6, and total alteration depth over time in Fig. 3-7. The slope of the best-fit line after 84 days of exposure to CO_2 is plotted for each brine type over time. The coefficient of correlation in Figure 3-7 shows that there is a linear relationship where the alteration depths increase with time for the Big Sky and *Surrogate* (fresh and "post-cured" at 1 *M*) samples. Alterations in cement submerged in *SECARB* (2.17 *M*) also follows the trend of increasing alteration with time. However, the relationship between alteration depth and time of exposure for the MGSC (Mt. Simon) is not a linear, demonstrating poor correlation. This poor correlation is likely due to the complexity of the brine, subsequent reactions and secondary precipitation of halite and portlandite.

3.4.3. Supercritical CO_2 versus CO_2-saturated brine exposure

The alteration effects in the cement exposed to the supercritical CO_2 in the headspace differ significantly from the cement exposed to the CO_2 saturated brine. The upper portion of the cement exposed to supercritical CO_2 is representative of the transition zone into the headspace of a wellbore above the brine.

The supercritical CO_2-exposed cement formed a series of complex, concentric alteration fronts that propagated inward over time: a remnant silica exterior that ranges from 10-60 microns in thickness, a concentrated $CaCO_3$ band averaging 150 µm thick, an altered cement zone depleted in calcium, and a second zone of more finely distributed carbonates that intrudes unevenly into the unaltered cement (Fig. 3-9). These concentric carbonation fronts have been also been observed in other studies by Rimmelé et al. (2008) and Barlet-Gouédard (2007). In the supercritical samples, there is a phase that is similar to wollastonite ($CaSiO_3$) rather than unhydrated Ca_2SiO_3 or Ca_3SiO_5 located between the two carbonation bands in the supercritical CO_2 samples.

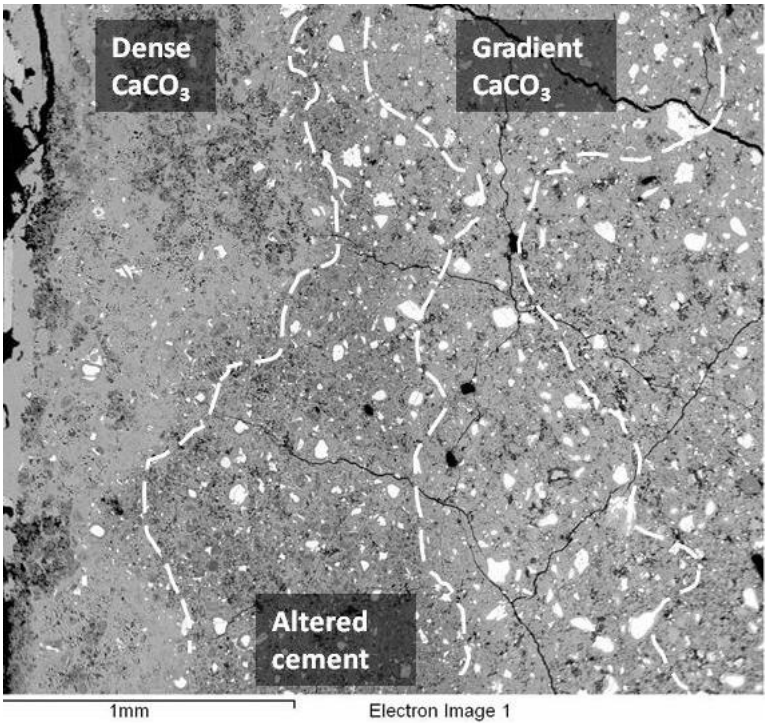

Figure 3-9. A SEM BSE image where cement exposed to supercritical has two coencentric carbonation fronts. The altered cement has lost calcium to form the inner calcite band.

Additional differences in the reactions in the hydrated cement exposed to supercritical CO_2 or saturated CO_2 also exist. In the CO_2 saturated brine exposed samples, petrographic analyses shows that hydration products typically lose their calcium first. There appears to be no preferential leaching as calcium is pulled from anhydrous cementitious phases such as the calcium silicates, as well as leaching C-S-H or $Ca(OH)_2$. In addition, the porous, remnant silica zone within the supercritical CO_2 headspace displays evidence of wicking. SEM images also show altered calcium aluminoferrite. In typical cement hydration, the anhydrous calcium aluminoferrite phase is slower to react relative to the fast reacting calcium silicate phases; Al^{3+} and Fe^{3+} are usually immobile, unless under acidic conditions. Based on elemental X-ray mapping of the supercritical CO_2 exposed cement, it appears that the Al^{3+} and Fe^{3+} are now tied to the C-S-H, whereas Mg has migrated out of the amorphous silica zone. In addition, SEM-WDS analyses show that Mg is converted into magnesite ($MgCO_3$) adjacent to the calcite band in the supercritical CO_2 cement samples only. From these data, we conclude that the supercritical CO_2 demonstrates a higher degree of reaction in comparison to cement paste submerged in CO_2-saturated brine.

3.4.4. Brine Composition and Chloride Content

This study demonstrates the importance of simulating the wellbore environment in experimental laboratory studies of wellbore cement and CO_2 interactions. The composition of natural formation brines (Ca, Mg, Na) can influence the alteration of cement exposed to supercritical CO_2 under storage conditions. Species within the brine contributed to the precipitation of $Ca(OH)_2$ and NaCl, and brucite. Cement samples submerged and cured in distilled water and various brines were studied to determine alteration and hydration effects prior to CO_2 injection. Analysis by SEM of the cement cured in distilled water showed evidence of calcium leaching and $Ca(OH)_2$ and C-S-H dissolution which likely led to spalling (deterioration). This suggests that laboratory cement samples should not be stored in water as it will induce or expedite alteration prior to gas exposure.

The salinity of the brine will influence CO_2 solubility and thus the pH of solution. This influence is ultimately reflected in the total alteration depth of the exposed cement. According to solubility models from Spycher & Pruess (2005) the saturated concentration of CO_2 for 0 *M* NaCl solution is 1.5 mol/kg water (60°C at 286 bars). The saturated concentration of CO_2 for a 1 *M* NaCl solution is 1.25 mol/kg of water, and for a 2 *M* NaCl brine it is 1.0 mol/kg water. However, by utilizing the geochemical model of Duan et al. (2006), the calculated solubility of CO_2 at 1 *M* total (0.82 *M* NaCl, 0.02 *M* $MgCl_2$, & 0.16 *M* $CaCl_2$) m_{CO2}= 1.098 mol/kg. The higher salinity brine at 2.17 *M* total (1.78 *M* NaCl, 0.05 *M* $MgCl_2$, & 0.34 *M* $CaCl_2$) m_{CO2}= 0.8714 mol/kg. Therefore there is a slight difference between models in determining the CO_2 solubility, but the relationship of salinity to total alteration depth remains the same. Cement submerged in 1 *M* solution had an alteration depth of 1.3 mm, with a calculated pH= 3.0 with a speculated CO_2 solubility 1.098/1.25 mol/kg. Cement submerged in a 2.17 *M* solution had an alteration depth of approximately 0.84 mm with estimated lower CO_2 solubility of 0.8714/1.0 mol/kg in the brine.

SEM analysis revealed the presence of halite and portlandite on the outside of the cylindrical cement sample, likely from secondary mineral precipitation. This precipitation could contribute to reduced cement porosity and permeability thus slowing the influx of acidic fluid and the alteration rate during CO_2 exposure. Pruess & Muller (2009) determined that the injection of CO_2 into saline aquifers may cause formation "dry-out" and precipitation of NaCl near the injection well. The primary mechanisms include brine displacement away from the injection well, dissolution/evaporation of brine into the injected CO_2 plume, upflow of CO_2 due to buoyancy effects, backflow of brine, and molecular diffusion of dissolved salt. We expect that a similar mechanism may have contributed to the deposits of halite (NaCl) on the surface of the cement samples. Halite precipitation requires higher dissolved salt concentrations in the pores than is available in the brine itself. We propose, that based on the conditions of experimental system and observations that molecular diffusion of dissolved salts can precipitate halite in cement. However fluid properties, parameter of displacement, fraction of pore space must be considered.

Portland cement has chloride binding properties where chloride chemically bonds to the gel-like C-S-H during hydration of Ca_3SiO_6 (Beaudoin et al., 1990). Chloride migration though the cement sheath could corrode the steel casing within the wellbore. It is likely that with prolonged exposure, the chloride-enriched solution would migrate into the cement and ultimately reach the steel casing. Chloride-induced corrosion of the steel could, in turn, result in premature deterioration of the cement and spalling of the wellbore, leading to CO_2 leakage.

Sulfate ions in the brine may cause expansive minerals such as gypsum, ettringite, or thaumasite to form, leading to the cement cracking due to sulfate attack. The MGSC (Mt. Simon) brine (1.272 *M*) exemplifies the complex nature of formation brines (Table 3-1) and includes a low concentration of aqueous sulfate. The cement sample submerged in the sulfate-enriched brine and exposed to supercritical CO_2 developed portlandite on the cylinder exterior and well crystallized calcite by day 28. The presence of portlandite indicates that the calcite is still stable, the local pH of the cement exterior is higher than the surrounding acidic solution. It is possible that there is limited ingress of sulfate due to sulfate's ionic size. The secondary portlandite may have inhibited further degradation of the cement and prevented external aqueous sulfate from migrating into the cement and produce secondary ettringite

3.4.5. Gain and Loss of Elemental Concentration

In cementitious hydration products such as $Ca(OH)_2$ and C-S-H microprobe points were selected on the likelihood of having reacted with supercritical CO_2. To quantify changes in the cement, the composition of altered cement was plotted against the original composition of the cement in using the isocon method described by Grant (1986; 2005). Species that are substantially immobile, such as Ti define the isocon as a straight line from the origin through the immobile species concentrations with a 1:1 slope. Species that plot above the isocon are enriched, whereas species that plot below the isocon are lost.

Alteration zones within the hydrated cement sample cured in *Surrogate* brine after CO_2 exposure are 1) a silica porous zone, 2) a calcium carbonate zone, and 3) an apparent calcium depletion zone. The elemental composition was averaged and the data transformed to fit on the plot. The confidence interval was plotted using the mean measured Ti to twice sample standard deviation [95% confidence interval=Ti $\pm 2\sigma$] in which species concentrations that are unchanged by alteration falls in the highlighted zone.

The porous silica zone is found at the exterior rim of the cement paste sample where species have been leached into solution or migrated into the adjacent zone. This zone is made up of a remnant network of C-S-H consisting mostly of semi-amorphous silica and anhydrous cement phases. Alteration trends identified in Fig. 3-9 are a comparison of the porous silica zone to the fresh cement composition and show an enrichment of Al^{3+} and Fe^{3+} and an apparent depletion of S, Ca, Cl, Na, O, and Mg. However, due to the large error bars for the other elements, Mg and Ca may, in fact, be the only depleted elements . The degree of elemental loss is expected in the porous silica zone because carbonic acid has leached most of the exterior of the cement and only Si and Ti are apparently unchanged.

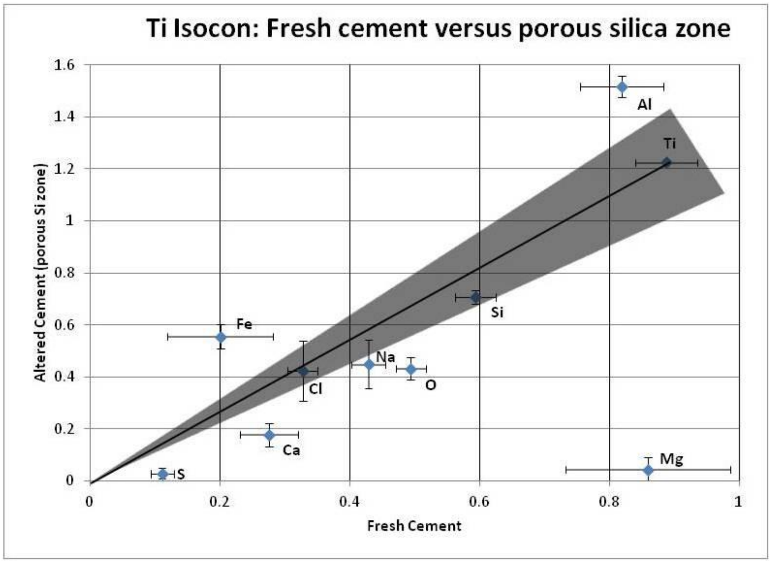

Figure 3-10. Titanium isocon plot with average concentrations of species of the leached cement paste zone of remnant porous silica to a fresh cement composition with a 95% confident interval=Ti ±2σ.

The nearly complete depletion of Mg in the remnant amorphous silica zone indicates that magnesium is unstable and lost to solution as seen in Table 3-3. Alumina is also amphoteric in nature and has a pH stability of ~4-8.5 (Pourbaix 1974). These data suggest that Al_2O_3 is unstable under the acidic conditions and migrates out of the cement and is seen as increased concentration in the porous silica zone. The increase in iron in this zone corresponds to the Fe decrease seen in the other zones. Solid ICP-AES analysis confirms the loss of iron (Table 3-2), indicating that iron is also migrating out of the cement. The potential influence of iron leaching from the stainless steel (316 CrNiMo) autoclave cannot be discounted which may have resulted in increase of iron in solution. However, Ni/Cr concentrations are remain low.

The alteration trends seen when the calcium carbonated zone is compared to fresh cement show a small increase in Al, but this difference is likely due to an increase of the average deviation. The graph shows no change in S, Si, or Fe, all of which are within the error bars (Fig. 3-10). There is a 2.21 wt % increase in calcium, but this calcium enrichment falls within the 2σ error and may not be statistically significant. The enrichment of Na indicates that sodium may be replacing the calcium within the semi-gel like structure of C-S-H; this, in turn, limits halite precipitation within this calcite zone. The marked depletion of Mg seen in the diagram indicates that there is no Mg substitution within the calcium carbonate and, instead, Mg is lost to the solution. This loss of magnesium in the cement can also be seen to the increase of aqueous Mg solution analyses (Table 3-3; fresh *Surrogate* brine row). Depletion of sulfur in the calcite zone is comparable to the minor increase seen within the porous silica zone demonstrating the migration of sulfur from gypsum or bonded to the C-S-H gel.

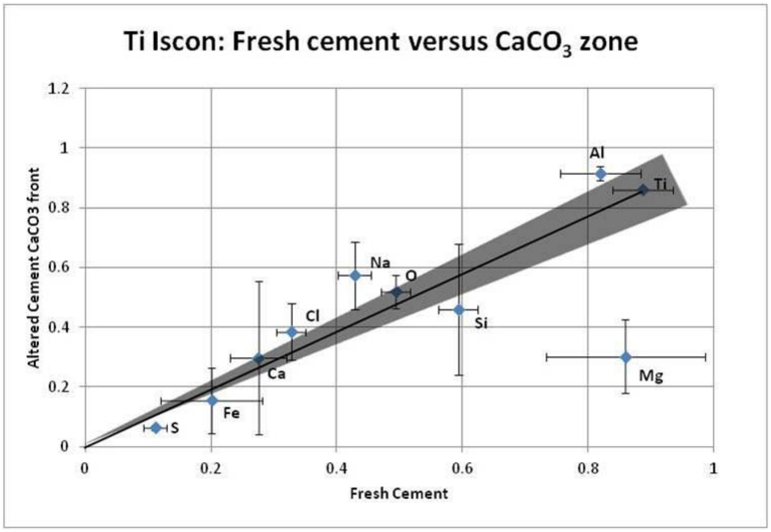

Figure 3-11. Titanium isocon plot with average concentrations of species in altered cement that has been carbonated against a fresh cement composition with a 95% confident interval=Ti ±2σ.

The alteration trends in Figure 3-11 generated by comparing the apparent calcium depleted zone to fresh cement indicate an enrichment of Na, Cl, Mg and a very slight depletion of Fe. The increase of Mg is likely due to ingress of Mg^{2+} from the brine, or may be the result of a stability zone for $MgCO_3$ that would be difficult to quantify if there were trace precipitation. The excess of Na and Cl corresponds to the SEM-EDS chloride X-ray mapping as well as the secondary precipitation of halite crystals in the zone adjacent to the carbonate band (Fig. 3-11). Concentrations of Ca, S, Si, O, Al appear to be largely constant (Fig. 3-3).

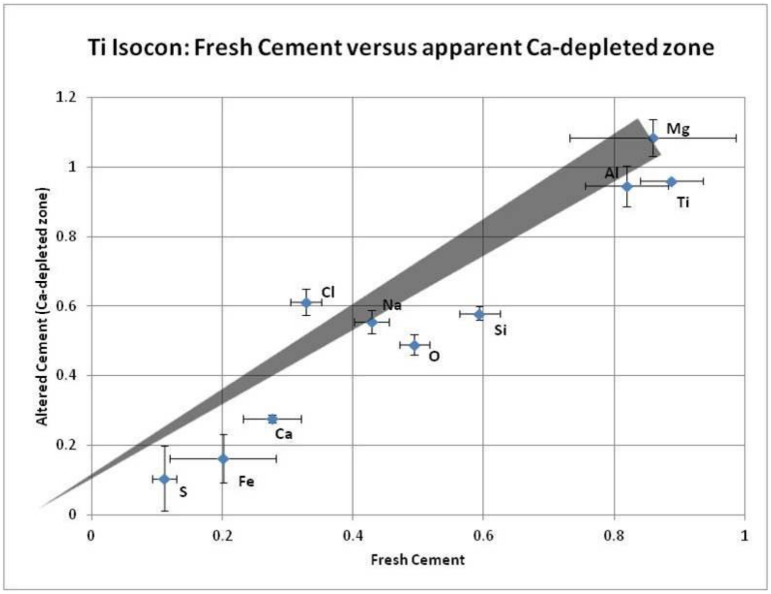

Figure 3-12. Titanium isocon plot with average concentrations of species in altered cement paste (SEM-EDS apparent calcium depleted zone) against fresh cement composition with a 95% confident interval=Ti ±2σ.

There are several implications in the enrichment and depletion of chemical species of the cement paste. Kutchko et al (2008) rationalized a calcium leached zone visible in SEM-EDS images of cement paste exposed to supercritical CO_2. The SEM-EDS images in this study also show an apparent loss of calcium based on calcium distribution. However, microprobe data and isocon analysis indicate there is no significant loss of calcium (Fig. 3-12). There are at least two explanations for this conflicting information. One explanation is that to the eye, the SEM-EDS images appear to depict calcium loss because distribution is associated with intensity and displayed in brightness. However, images are based on average atomic number, the higher the intensity (brighter) the higher average atomic number. The SEM can detect to a resolution of 0.3 average of atomic number, so human perception is not the result. The more likely explanation is the limitation of data from the electron microprobe analysis. The 10 kV beam may have excited unhydrated Ca-rich grains below the cement surface producing secondary fluorescence and thereby elevating the apparent calcium concentration. Furthermore, the carbonation front does not have a defined alteration boundary and this may affect the observed calcium distribution.

The fresh *Surrogate* brine (Table 3-3), shows that calcium concentration had dropped from 8450 mg/l to 1694 mg/l by day 84. A portion of the calcium must have been fixed in calcite in the cement and the Ca^{2+} in the brine would decrease the tendency to draw calcium from the adjacent alteration zone of the cement; in addition, the isocon graph does not show significant Ca-enrichment. Some of the calcium from the brine is likely found in the portlandite crystals seen on the cement surface. This is not seen in the calcium-depleted zone formed by exposure to an 1% NaCl brine in the Kutchko et al. (2008). Further investigation is required to determine the effect of CO_2 on the formation of the carbonation with the cement paste and if the source of aqueous calcium is from the brine.

3.5. Conclusion

In this study, to simulate deep wellbore sequestration conditions based on actual brine-bearing formations in Illinois, Mississippi, and Wyoming (USA), Class H portland cement was exposed to CO_2-saturated brine and supercritical CO_2 at $50^{o}C$ and 28.9 MPa. The brine composition significantly influenced mineral precipitation and CO_2 solubility. The dissolution of supercritical CO_2 in the brine formed carbonic acid that reacted with the cement resulting in secondary mineral precipitation, and apparently calcium depletion in the cement exterior. Our results show that Ca^{2+} diffused from the brine into the cement enabling $CaCO_3$ precipitation. However, continued injection of supercritical CO_2 ultimately resulted in dissolution of the cement.

In this study, the alteration depths seen in cements submerged in the mixed Na-Ca-Mg brines used were far greater and occurred during a shorter period of time compared to the findings of Kutchko et al. (2008), using only NaCl brines, . Kutchko et al. (2008) calculated 1 mm alteration after 20 years with simple 1% NaCl brine. The overall alteration depth of the lower salinity brine (1 *M*) was 1.250 mm whereas the higher salinity brine (2.2 *M*) had an alteration depth of 800 µm. Calculations of pH at sequestration depths with program CHIM-XPT calculated a pH of 3.0 in a 1 *M* brine and 3.85 in a 2.17 *M*. brine. The pH gradient of 3.0 to ~12 affects the cement stability and so the cement was more vulnerable to acid attack in our studies.

The integrity of the wellbore environment is an important factor to consider under CO_2 conditions. The complexity of the brines resulted in lower alteration depths and encouraged mineral precipitation both during the curing process and after CO_2 injection. The ingress of chloride bonded to the C-S-H structure of the cement paste caused halite to precipitate. Chloride diffusion into the cement could corrode the steel casing and there was no evidence of external sulfate attack or precipitation of secondary sulfate minerals. However, SEM analyses suggested that dissolved gypsum resulted in sulfate bonding to C-S-H.

SEM EDS X-ray mapping also shows a significant calcium depletion zone between the calcite band and unaltered cement also observed by Kutchko et al. (2007; 2008), electron microprobe showed no calcium depletion based on a comparison to calcium concentration with immobile titanium. The high concentration of aqueous calcium in the brines used in this study also showed that when the local pH in the cement is $pH \geq 8$, self-healing fractures permit calcite formation. Furthermore, freshwater accelerated cement degradation. Exposing cement to distilled water or brackish solutions appears compromise the integrity of the cement prior to injecting the gas as evidenced in both the physical and microscopic observations made in this study.

CHAPTER IV

ADVANCES IN GEOLOGICAL CO_2 SEQUESTRATION AND CO-SEQUESTRATION WITH O_2

Chapter IV has been peer reviewed and published in the Special Publication for the Recent Advances in Concrete Technology and Sustainability Issues in October, 2012. Chapter IV compares the effect of CO_2 and CO_2-O_2 gases on Class H portland cement. Co-authored material is included in Chapter IV. The paper was written by myself, with my coauthors providing editorial assistance. Experimental assistance to William O'Connor and Hank Rush. Dr. Mark Reed assisted in geochemical modeling (CHIM-XPT).

Citation:
Verba, CA**.,** O'Connor, W., Ideker, J. (2012) Advances in Geological CO_2 Sequestration and Co-Sequestration with O_2. ACI-CANMET Special Publication in Recent Advances in Concrete Technology and Sustainability Issues. Prague, Czech Republic. 2012 Special Publication V. 298. pp. 1-16.

4.1. Introduction

The Intergovernmental Panel on Climate Change recommended that mitigation of anthropogenic CO_2 derived from the use of fossil fuels for energy production is necessary. (IPCC, 2005). To this end, brine-bearing formations with large potential storage capacity for geologic sequestration of CO_2 have been identified (Bergman and Winter, 1995; Bruant, 2002; DOE, 2007). Candidate formations include enhanced oil recovery reservoirs and pilot tests sites in saline formations under the National Energy Technology Laboratory (NETL) Phase III Regional Partnership programs (Carey et al.,2007; McGrail et al., 2006). Proposed wellbores use oil-well type portland cements to plug the well and bond the host rock to the steel casing, and are subjected to specific bore depths, high temperature, and high pressure environments (Mehta and

Monteiro, 2006; Nelson, 1990). In addition, injection of CO_2 into a brine-bearing formation results in the formation of carbonic acid. Portland cement is not thermodynamically stable under these conditions and is subject to dissolution and ionic migration in a CO_2-rich environment. Thus the integrity of the wellbore seal may be compromised, providing a potential leakage pathway up the wellbore into the atmosphere and/or surrounding substrates (Duguid et al., 2009).

CO_2 exists both as a supercritical fluid ($SCCO_2$) and dissolved in CO_2-saturated brines at sequestration injection depth (Hitchon, 1996). The production of carbonic acid (H_2CO_3) from dissolution of CO_2 into water, heavily alters cement as the portlandite (CH) is dissolved and replaced by $CaCO_{3\ (s)}$, which fills pore spaces (Thaulow et al., 2001). Compressive strength increases initially and $CaCO_3$ provides a pH buffer (Kutchko et al., 2008). Ongoing diffusion of carbonic acid leaches Ca^{2+} from the cement, creating a zoned alteration rind of amorphous silica. $CaCO_3$ solubility is significantly lower than that of CH so $CaCO_3$ becomes unstable, causing bicarbonate to reach aqueous saturation and local dissolution of calcium species (Thaulow, 2001; Glasser, 2001). The diffusion of calcium species out of the cement is driven by the fluctuating pH and propagates further degradation. The following equations show the degradation process:

$$CO^{2+}\ H_2O \leftrightarrow H_2CO_3 \leftrightarrow H^+ + HCO_3^- \qquad (1)$$

$$HCO_3^- + H^+ \leftrightarrow 2H^+ + CO_3^{2-} \qquad (2)$$

$$Ca(OH)_{2(s)} \rightarrow Ca^{2+}_{(aq)} + 2OH^-_{(aq)} \qquad (3)$$

$$Ca^{2+}_{(aq)} + HCO^-_{3\ (aq)} + OH^-_{(aq)} \rightarrow CaCO_{3(s)} + H_2O \qquad (4)$$

$$H_2CO_{3\ (aq)} + C\text{-}S\text{-}H_{(s)} \rightarrow CaCO_{3\ (s)} + H_2O_{(aq)} + am\text{-}SiO_{2(s)} \qquad (5)$$

$$H_2CO_{3\ (aq)} + CaCO_{3\ (s)} \rightarrow Ca(HCO3)_{2\ (aq)} \qquad (6)$$

The precipitation of salts is encouraged as suggested by Pruess and Müller (2009), because injection of CO_2 into the brine increases aqueous phase salinity. Downhole conditions are assumed to be static due to low formation permeability and porosity, so the CO_2 system and cement reaction can be considered homogeneous (Zhang and Bachu, 2011).

Previous findings suggest that the rates of alteration are low (1 mm to 1 cm [0.04 to 0.4 in] over 30 years) in simple brines (Carey et al, 2007; Duguid et al., 2005; Kutchko et al., 2008). It is therefore suggested that CO_2 sequestration is a probable means of carbon storage at those conditions. However, formation brines range in salt species and in salinity, which impact the degree of cement alteration. In the subject study, where salinity was ≤ 1 *M*, higher CO_2 solubility led to a depth of cement degradation exceeding 1 mm (0.04 in). Where salinity was >1.2 *M*, depth of degradation was ~0.5 mm (0.02 in) after CO_2 exposure of the same duration (Verba et al., 2010).

Carbon dioxide co-sequestration studies have been limited to SO_2 models (Crandell et al., 2010; Palandri and Kharaka, 2005) and experimental work with CO_2-H_2S, where Fe^{2+} in the C-S-H and iron substitution in ferrite clinker precipitated ettringite and pyrite (Jacquemet et al., 2008; Kutchko et al., 2011). The interest in co-sequestration is driven by the high cost of CO_2 capture from conventional combustion flue gas, thus novel types of fossil fuel energy conversion systems, such as oxy-fueled combustion, chemical looping combustion, and coal gasification are under investigation. The flue gas from these technologies consists mostly of CO_2 and is therefore ready for sequestration without post-combustion separation. However, excess O_2 and oxidized acid gas species such as SO_2 remain at low concentrations (1-4%) in the untreated combustion flue gas, requiring separation or a co-sequestration methodology. The latter could provide an economic advantage by eliminating the need to remove the O_2 and SO_2 prior to injection. However, these gas species would likely produce a more aggressive environment and potential degradation to cement well seal integrity that is not currently well understood.

4.2. Research Significance

This research addresses a critical issue in carbon sequestration evaluation and the basic understanding of wellbore cement stability in a CO_2-rich environment. The experimental conditions selected for this study apply to *in-situ* conditions at potential CO_2 injection sites in the United States. The multiple chloride species and variable concentrations comprising the synthetic brines in this study mark a departure from prior studies. The addition of flue gas co-contaminate gases could provide an economic advantage due to reduced separation costs and potential storage enhancement (physical or mineral trapping). However, the impact of co-sequestration on cement integrity is not clearly understood.

4.3. Experimental Procedure

Class H portland (Lafarge, North America) well cement was prepared based on the American Petroleum Institute (API) practices 10B with a w/c of 0.38 (API, 1997). The cement powder (weight percent) comprised of approximately 64.5% tricalcium silicate (C_3S); 11.77% dicalcium silicate (C_2S); 13.24% calcium aluminosulfate (C_4AF); no tricalcium aluminate (C_3A); 2.94% MgO; 2.8% SO_4^{2-}; 0.16% total alkali content (Na_2O); 0.62% free lime, and a loss on ignition (LOI) of 0.73. The cement paste was cast into 25 mm diameter x 152 mm (1x6 in) long PVC-pipe forms, cured at temperatures of 50^oC and 85^oC under a hydraulic pressure of 28.9 MPa (4200 psi), in 1.2 L stainless steel (316 CrNiMo) static autoclave vessels filled with 600 mL of the synthetic brine. After 24 hours, the forms were removed and the cement paste cylinders held at temperature and pressure for the remainder of the 28 day curing period prior to injection.

The cement paste cylinders were in contact with several CO_2-saturated brines to simulate formation brines and depths at three NETL Phase III Regional Partnership injection sites. Discussion of results using the various brines will be presented in a subsequent publication. This paper focuses on the synthetic "control" brine adjusted to a 1 *M* concentration (0.82 *M* NaCl, 0.02

M $MgCl_2$, & 0.16 *M* $CaCl_2$) modeled after several NETL sandstone formation brine chemistries (NATCARB, 2008).

The CO_2 mixed gas exposure tests were performed using two gas mixtures, 1) pure CO_2 and 2) a mixture of 96% CO_2 + 4% O_2. The tests were conducted at geothermal gradients designed to simulate the sequestration environment, including a supercritical CO_2 headspace and CO_2-saturated brine. The two temperatures were investigated to determine the effect of temperature on the cement paste and specifically on C-S-H structure. Following the curing interval, the autoclaves were purged with the CO_2-gas mixture and then maintained at temperature and pressure for exposure intervals up to 84 days (after the initial 28-day cure). Corrosion of the stainless steel autoclaves was observed during conduct of CO_2-O_2 exposure tests, and is discussed later.

4.4. Analytical Procedure

Petrographic analyses were performed with an optical microscope, and an FEI Inspect F Scanning Electron Microscope (SEM) was used to obtain backscattered electron (BSE) images and energy dispersive spectroscopy (EDS) data on polished epoxy-impregnated mounts. SEM elemental intensities were optimized using a Cu-Kα standard for quantification and measurement of alteration depth, determined by EDS and spot analysis. Alteration in the cement paste was mapped by measuring the distribution of calcium, silicon, and chlorine in 14 samples over a total of 84 sites. Electron microprobe analysis (EMPA) using wavelength-dispersive spectrometry (WDS) with standard errors, and a correction matrix for cement [oxide weight percent concentrations] was utilized for quantification. Please refer to Appendix B for supplement material which includes SEM-EDS maps to determine carbonation and alteration depth of the cement. X-rays diffracted by specific analyzing crystals (TAP: Na, Al, Mg; LPET: Si, Ca, S, Cl; and LIF: Fe, Ti) determine composition by comparison with intensities of known standards [$Ca_{10}(PO_4)_6Cl_2$, MgO, SiO_2, TiO_2, $CaSO_4$ (anhydrite), Fe_3O_4 (magnetite), and $Na_3KAl_4Si_4O_{16}$

(nepheline)] to the unknown materials in the cement paste. Analysis of cements is very difficult due to the composition of hydrated phases and its intrinsic heterogeneity. Atomic number, adsorption, and fluorescence (ZAF), time dependent intensity (TDI), background continuum, and oxide corrections provide a summation of concentrations representative to the stoichiometric analysis of calcium silicate grains, hydration products, and within alteration zones.

The cementitious phases were identified using X-ray diffraction (XRD) collected by a Rigaku Ultima III with a 40KV/40mA Cu k-α source and a step speed of 1^{o}/min over a scan angle, 5^{o}-90^{o} 2θ. The qualitative analysis of XRD data was performed using the International Center for Diffraction Data (ICDD) pattern databases and Jade Plus software v9.1.4 (International, 2008). XRD patterns are also included in Appendix B.

The composition of the hydrated paste (ground into powder and vacuum sealed) was determined by several methodologies, including a LECO gas analyzer for sulfur and carbon, lithium meta-borate fusion with X-ray fluorescence (XRF) for metal oxides, carbonate leach and gravimetric analysis for SO_4, CO_2 by coulometer, and acid digestion and titration for FeO. Solution alkalinity was determined by titration, using sodium carbonate and hydrochloric acid. Nitric acid digestion with inductively coupled argon plasma spectroscopy (ICP-AES) methods were used for metals analysis, while ion chromatography was used for Br, Cl, and SO_4.

4.5. Experimental Results And Discussion

Results from pure CO_2 exposure tests (Verba, 2010) were compared to the CO_2-O_2 experimental results, each using the same raw cement batch composition, brine chemistries, and experimental conditions. This methodology isolated the change in conditions to the addition of 4% O_2 to the gas mixture, thus any change in mineralogy, alteration depth as indicated by $CaCO_3$ and Ca^{2+} depletion, and stainless steel corrosion can be attributed primarily to the O_2 addition.

Verba et al. (2010) found that exposure of Class H cement to pure CO_2 at $50^{o}C$ and 28.9 MPa (4200 psi), in higher salinity brines of 1-2 *M* NaCl, $MgCl_2$, and $CaCl_2$, resulted in alteration zones in the cement that increase in depth and become more defined with time. The carbonation depths versus time are provided in Table 4.1, while the alteration zones are depicted in Fig. 4-1a.

Table 4-1. Total alteration depth of CO_2 and CO_2-O_2 exposure at 50/85°C. Alteration depth of CO_2 from Verba, 2011.

Gas Type	Temperature (°C)	Exposure Duration	Alteration depth (µm)
CO_2	50	28	151±20
CO_2	50	56	714±61
CO_2	50	84	1254±441
CO_2-O_2	85	28	253±59
CO_2-O_2	85	53	737±94
CO_2-O_2	85	73	1585±422
CO_2-O_2	50	28	514±109
CO_2-O_2	50	56	680±132
CO_2-O_2	50	73	700±100

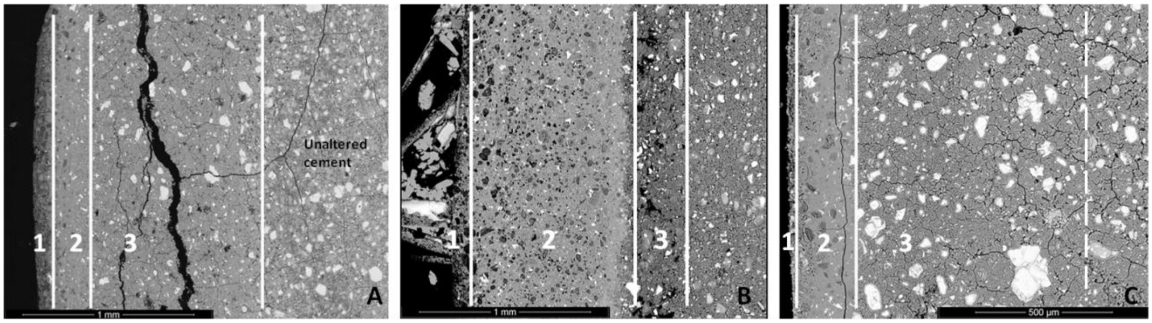

Figure 4-1. Carbonation and alteration depth of portland cement cylinders exposed to A) 84 days and pure-CO_2 at 50°C, B) 53 days CO_2-O_2: 85°C, and C) 66 days CO_2-O_2 50°C. Zone 1 is the porous-Si, zone 2 is $CaCO_3$, and zone 3 is the Ca^{2+} leading into unaltered cement. Dashed line indicates finely distributed Ca^{2+} leached zone; no boundary. Scale bar 1 mm (0.04 in).

Total alteration depth extended into the core up to 1254±441 µm (0.049 in) after an 84-day exposure period. Alteration included large hydration halos surrounding C_2S and C_3S grains because continuous hydration allowed for conversion into interstitial CH and C-S-H. Remnant calcium silicates and hydration products were in the Ca^{2+} depletion zone whereas all calcium silicates in the carbonated zone turned into amorphous silica with a banded appearance from zoning loss of Ca^{2+}. SEM-EDS and EMPA confirmed a Cl-enriched (~3 wt%) and S-enriched zone (1-3 wt%) in the Ca^{2+} depletion zone, presumably incorporated into the C-S-H structure. EMPA identified both Fe^{3+} (at <5%) and Fe^{2+} (<2%) in the C-S-H structure.

The higher salinity and multiple chloride species in the brine led to precipitation of large (50-1200 µm; 0.047 in) CH crystals on the exterior of the cement cylinder. Small cubic halite grains (1-15 µm) also crystallized in the cement while the cement maintained a lower pH (<6) and was dehydrated in the presence of early $SCCO_2$. The precipitation of the additional minerals, specifically exterior CH, reduced the maximumimum alteration depth and permeability after an exposure of 84 days.

CO_2-O_2 (96% CO_2 + 4% O_2) exposures led to more rapid cement degradation and ionic migration behavior compared to the pure CO_2 studies (Fig. 4-1b,c). The cement cylinders displayed a banded Si-porous zone of remnant silicates, a $CaCO_3$ band with thickness dependent on temperature, and a Ca^{2+} depleted zone. EMPA analyses found that the C-S-H structure contained roughly 1.5 wt% Fe^{2+} and had 20-30% water bound unaltered C-S-H. Significant differences from the pure CO_2 studies included: 1) the transformation of calcium silicates (C_2S) with bordering ferrite grains into polymorphs with significant twinning and 5-10% less Ca^{2+}; 2) precipitation of dendritic hydrotalcite [$Mg_6Al_2(CO_3)(OH)_{16}\cdot 4H_2O$] on C_4AF grains; and 3) the precipitation of 10-50 µm long ettringite [$Ca_6Al_2(SO_4)_3(OH)_{12}\cdot 26H_2O$] needles within pores specifically in Ca^{2+} depleted zones (Fig. 4-2). The authors suggest that change in pH between the solution and the cement within the Ca depletion zone allowed for ettringite formation, coupled with leaching of Ca^{2+} and Al^{3+}, as well as S previously bound in C-S-H.

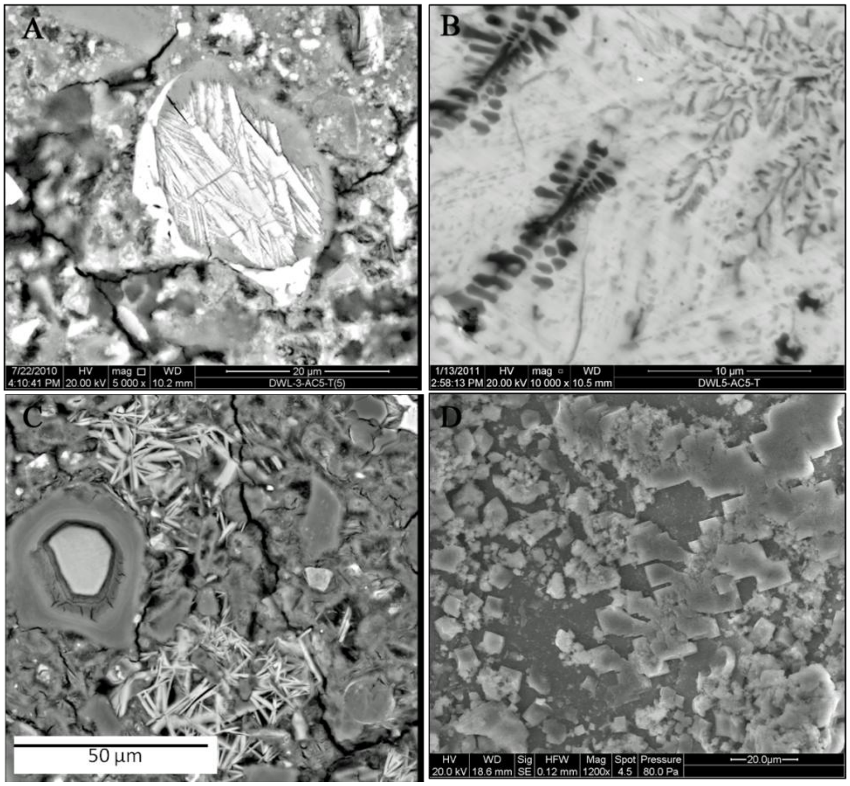

Figure 4-2. Minerals and polymorphs in CO_2-O_2 injected samples. A) Calcium silicate polymorph, B) Hydrotalcite forming on ferrite grains, C) Ettringite needles in the Ca^{2+} depleted zone, and D) Cubic halite grains within the carbonated zone.

Ettringite formation occurred after the primary curing stage and during the CO_2-O_2 gas exposure interval, after carbonation had occurred as determined by SEM and XRD analysis. This secondary [delayed] ettringite formation (DEF) can lead to loss of cement paste integrity, degradation, expansion, and fracturing (Glasser, 2001). Expansion of the cement paste or the development of microfractures could serve as potential leakage pathways for the injected gases or liquids, either out of the wellbore or to the wellbore steel casing. Microfractures ranging from 0.5-3 µm wide extend from many of the pores containing ettringite, and propagated in the least resistant pathway around mineral grains. These are not interpreted as an artifact of sample prep, due to the small fracture sizes, where fractures induced during sample prep often cut across mineral grains and stem into larger fractures. Etched and pitted features were also observed on the silicates and C_4AF, evidence of acid attack. EMPA data suggests <2% of the carbonate band contained $FeCO_3$, which could not be confirmed via other instrument analyses in such trace amounts.

Total alteration depth versus time of the CO_2-O_2 exposure samples is listed in Table 4-1. At both temperatures, the alteration depth exceeded initial depths (28-days) in comparison to pure-CO_2 exposure, but displayed disseminated and nonuniform alteration as shown in Fig. 4-3.

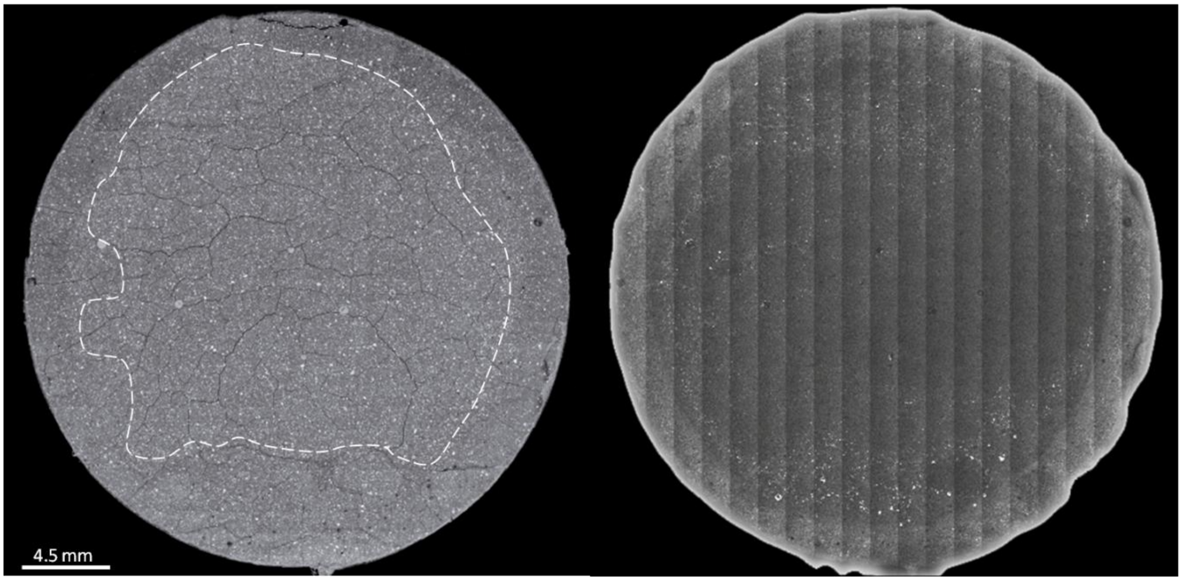

Figure 4-3. Montage backscatter (BSE) image (left) and Ca^{2+} EDS map (right) of CO_2-O_2 exposure sample with diffuse alteration boundary (white outline) extending into the cylinder. Scale 4.5 mm (0.18 in)

The 85°C sample showed the highest rate of degradation with a large, thicker initial $CaCO_3$ band compared to pure CO_2 exposure. At 28 days of exposure, the alteration depth was minimal, up to 253±59 µm (0.01 in). After 53 days, the alteration zone extended to a depth of 916±94 µm (0.036 in), and the Ca^{2+} depleted zone ranged from ~0.5- 1 mm (0.02-0.04 in), with large pores up to 160 µm (0.0063 in) in diameter. After 73 days, pieces of the cement shed off from the cylinder exterior, and alteration exceeded 1-2 mm (0.04-0.08 in). Thus, degradation increased in the higher temperature static conditions from 53-73 days of exposure. The 50°C sample, on the other hand, displayed an alteration depth at 514±109 µm (0.02 in) after 28 days, exceeded 680±132 µm (0.027in) after 56 days, but remained fairly constant over the duration of the test exposure.

4.5.1. Solid and Solution Chemistry

The composition of the brine after curing and post gas-exposure intervals is included in Table 4-2. Composition of the unhydrated portland Class H cement, hydrated cement paste and post-gas exposure cement samples are included in Table 4-3.

Table 4-2. Brine solution chemical compositions of the post-cured solution and the post-gas exposure solutions taken at several exposure intervals (mg/l).

(mg/L)	Surrogate CO_2 50°C				Surrogate CO_2-O_2 50°C				Surrogate CO_2-O_2 85°C		
	Cured	Exposure			Cured	Exposure			Cured	Exposure	
Duration (days)	28	28	56	84	28	28	56	66	28	28	53
HCO_3	*	*	*	*	665	945	335	287	335	451	402
Cl-	40700	37300	38100	39700	28000	31000	33000	17000	28000	31000	28000
SO4 2-	<1	8	7	8	480	50	100	100	1200	100[1]	100[1]
Ca	8450	1869	1770	1694	3400	4400	3800	3600	4100	2000	2100
Cr	0.0226	0.033	<DL	<DL	1.4	5.8	3.3	28	0.7	8.5	0.5[1]
Fe	0.0196	0.167	0.549	0.263	5	36	20	200	5	66	5[1]
K	6.13	59.8	56.6	57	750	79	120	110	600	50[1]	62
Mg	626	1395	948	784	79	360	430	660	50	360	350
Na	24160	25530	18200	19700	14000	16000	17000	21000	13000	17000	14000
Ni	1[1]	12.58	15.85	22.94	1	61	180	380	1[1]	750	260
Si	7.644	47.6	53.68	52.01	5.1	51	51	46	2.5[1]	78	9
Free CO_2	*	*	*	*	5.10E-05	1300	62	46	1.0E-04	950	17

[1] concentration at or below detection limit

* no measurement

The product solids from the pure-CO_2 tests showed a slight decrease in SiO_2 concentration between the post-cure and post-gas exposure samples, and leaching of Si from the cement was clearly evident from the Si concentration in the product solution over time, which increased from <10 to >50 mg/l. These results are reflected in the 57-205 µm deep amorphous silica zone identified in the cement cylinders by microanalysis, which is indicative of dissolution of the CH and C-S-H in that zone, mobilization of the Ca^{2+} cations, followed by re-precipitation of most of the free silica. The CaO content in the pure CO_2 exposure cement decreased nearly 5 wt% after 84 days, apparently due to leaching of Ca^{2+} cations from the cement, as described previously. However, the Ca^{2+} trend in the product solution decreased dramatically over time, from >8000 to <2000 mg/l, once CO_2 was injected. This apparent contradiction is best explained by calcium carbonate precipitation during the CO_2 exposure interval which exceeded the Ca^{2+} dissolution rates. Locally, CH and C-S-H had become depleted and replaced by $CaCO_3$, whereby CO_3^{2-} decreased because bicarbonate became the dominant aqueous species in the system.

Table 4-3. Solid chemical compositions of the unhydrated cement, the cured hydrated cement paste, and cement paste post-CO_2 and CO_2-O2 exposure (wt%).

Oxide wt%	**Cement Powder**	**Cured Paste**	**CO_2 50°C**	**CO_2-O_2 50°C**	**CO_2-O_2 85°C**
SiO_2	21.07	17.95	17.02	18.39	17.99
Al_2O_3	2.78	2.4	2.26	2.3	2.33
Fe_2O_3	4.37	3.64	3.54	5.64	3.77
CaO	64.02	54.55	49.82	52.25	52.45
MgO	2.94	2.49	2.27	2.39	2.29
Na_2O	0.05	0.09	<0.01	<0.01	0.01
K_2O	0.11	0.1	0.01	0.01	0.02
Cr_2O_3	0.01	0.01	0.02	0.02	<0.01
TiO_2	0.2	0.17	0.18	0.15	0.16
MnO	0.06	0.05	0.05	0.07	0.07
P_2O_5	0.131	0.113	0.105	0.107	0.116
SrO	0.1	0.08	0.06	0.08	0.08
BaO	0.07	0.05	0.04	0.05	0.06
LOI[1]	0.73	16.85	22.9	17.05	18.9
Total	96.64	98.55	98.27	98.5	98.25
C	0.07	1.65	2.35	1.14	0.9
CO_2	0.3	6.1	8.6	3.5	3.2
FeO	0.19	0.19	0.13	0.26	0.19
H_2O [2]	<0.01	5.55	4.93	11.9	13.7
S	0.17	0.06	0.17	0.11	0.17
SO_3[3]	2.48	2	1.8	1.93	1.68

[1] LOI: Loss on Ignition, measured as the weight loss after 1 hour at 1000 C, in air.

[2] Free moisture, measured as the weight loss after 1 hour at 105 C, in air.

[3] Sulfate sulfur- carbonate leach

Solids analysis for the cured hydrated cement and post-gas exposure cement samples for the CO_2-O_2 gas mixture tests indicated little to no change in SiO_2 and CaO concentration at both temperatures (85°C and 50 °C). This was reflected by the thinner silica-porous band observed in the cement cylinders during microanalysis. While Si concentration in solution increased in both the 50°C and 85°C tests, these concentrations compare favorably with those observed in the pure CO_2 tests, and are thus likely indicative of equilibrium concentrations at the experimental parameters utilized. Aqueous Ca^{2+} concentration initially increased after 28 days of exposure, from 3400 mg/l to 4400 mg/l in the 50°C sample, as cations diffused into solution, but then decreased in concentration after longer exposure time, likely due to $CaCO_3$ precipitation. In contrast, the higher temperature solution displayed a 50% decrease in Ca^{2+} concentration after both 28 and 53 days of exposure. These trends suggest that calcium carbonate mineral precipitation was favored kinetically at the higher temperature.

The free water content in the CO_2-O_2 exposure samples was 7-8 wt % greater than that in the pure-CO_2 samples. However, chemically-bound water content, calculated as the difference between the LOI and other volatiles (CO_2, free moisture, and sulfate) in those same samples was virtually zero, while that in the pure CO_2 samples was 4-7 wt%. This could be interpreted as an indication of the advanced degradation of the cement paste, resulting from the CO_2-O_2 exposure tests, in which all of the hydration water bound in the CH (replaced by $CaCO_3$), ettringite, and C-S-H was freed due to advanced alteration of those phases. The loss of Fe from ferrite grains was not evident based on the solids analysis, because the Fe_2O_3 concentration in the cement pastes was either relatively constant or increased. The increase in Fe, Ni, and Cr concentrations in solution, specifically in the higher temperature sample, suggests that these cations were derived from corrosion of the stainless steel autoclave, which complicates the interpretation of the cement alteration.

4.5.2. Semi-Quantative XRD

Crystalline phase identification of dominant mineral species and precipitated phases post-CO_2 exposure were completed by XRD on the exterior ~2 mm (0.08 in) rim of the cylinders

(Table 4-4). Phases identified in typical hydrated portland cement analysis included portlandite (CH: $Ca(OH)_2$), brownmillerite (C_4AF: $2*Ca_2AlFeO_5$), alite (C_3S: Ca_3SiO_5), belite (C_2S: β-Ca_2SiO_4), a hydrated calcium silicate polymorph pattern (Ca_3SiO_5-type), and an amorphous background hump, indicative of C-S-H. The influence of CO_2 mixed gas exposures on the cements shows the formation of ettringite, hydrotalcite, and carbonates, including calcite, vaterite, aragonite, and trace dolomite.

Table 4-4. XRD analyses of CO_2 and CO_2-O_2 exposure comparing the semi-quantified concentrations of minerals present due to gas and temperature differences in weight percent.

	Pure CO_2 50°C	96% CO_2-4% O_2 85°C		96% CO_2-4% O_2 50°C	
	84 days	28 days	53 days	28 days	56 days
Portlandite $Ca(OH)_2$	24.2±4.2	10.5±1.8	11.2±2.1	19.5±1.2	12±2.1
Brownmillerite Ca_2FeAlO_5	8.8±1.5	8.3±1.2	8.3±1.8	12.4±1.8	5.3±0.9
Hatrurite Calcium Silicate Ca_3SiO_5	17±2.1	6.3±1.2	13.8±3.9	12.1±2.1	10±2.4
Larnite $Ca_2(SiO_4)$	16.6±4.8	13.4±3.9	13.5±3.9	9.5+0.3	2.7±1.5
Ettringite $Ca_6(Al(OH)_6)_2(SO_4)_3(H_2O)_{25.7}$	0	3.9±0.9	7.5±2.1	9.6±2.1	12±2.4
Hydrotalcite $Mg_6Al_2(CO_3)(OH)_{16}*4H_2O$	trace	2.3±0.9	2.3±1.2	4.2±1.2	3.5±0.9
Total $CaCO_3$ (Calcite, Vaterite, Aragonite)	22.5±3.9	54.6±3.3	54.2±1.9	26.7±1.2	23.2±2
Amorphous	1.9±0.9	0.6±0.3	2.2±4.2	6±0.3	30.7±4.2

Error = reported error x3, Materials Data Inc., Jade

Carbonation differences were identified between the different gas-exposure samples. The amount of total carbonate is higher in the CO_2-O_2 cement samples than the pure-CO_2 samples. As expected when $CaCO_3$ is a dominate precipitant, CH is low, and vice versa. At both temperatures, the concentration of CH in the CO_2-O_2 tests is significantly lower (50% less) than that in the CO_2 tests. Carbonate formed more rapidly in CO_2-O_2 than pure CO_2, with total $CaCO_3$ nearly double (54.6±3.3 wt%) at elevated temperature, an indication that temperature has a significant influence on carbonation rates as well as C-S-H degradation. The lower temperature sample reflected an increased amorphous content with less carbonation than the higher temperature sample. The addition of oxygen may increase the solubility and efficiency of mineral dissolution in a ligandtype complex behavior. Although calcite was the dominant carbonate, both vaterite and aragonite appeared to have higher saturation with increasing temperature from 50 to 85°C.

Precipitation of a hydrotalcite-type (HT) phases is known to occur in hydrated cement, and while only trace amounts were found in pure-CO_2 samples, significant amounts were found throughout all the CO_2-O_2 samples after petrographic and SEM examination. The precipitation of HT is believed to result from hydration coupled either a) with Mg salt attack or b) as an alternative to brucite formation. With a constant supply of Mg-rich brine for hydration, the combination of a less permeable $CaCO_3$ zone and rapid penetration rate of O_2 allowed nucleation of this carbonate only on C_4AF grains, rather than within the C-S-H structure. This released Fe^{3+}, which may have contributed to the cylinder's dark brownish-red, rusty color, more so than seen in the pure-CO_2 exposed samples. The source of Fe was assumed to primarily be the stainless steel autoclave, with only small concentrations derived from C-S-H and ferrite clinker. No siderite, goethite or Fe-oxide were identified by XRD within the cement itself. However, spalled solids collected from the bottom of the vessel did contain goethite and Fe-oxides, which corroborates the presumed source of Fe.

The ettringite increase is of interest because Class H cement has little or no C_3A content; therefore, the main source of Al is from the C_4AF. In the pure-CO_2 samples, sulfur was bound in the C-S-H structure and was fairly uniform in unaltered cement paste. The gypsum (~5 wt%) addition to the cement did not differ in either test as the same cement batch was used. Ettringite was absent in pure CO_2 samples, and increased over time in CO_2-O_2 studies at both exposure temperatures. The ettringite precipitation appeared to be dependent on the rate of CO_2 and O_2 migration into the cement, and occurred after hydrotalcite had formed. As with previous studies examining the Fe-replacement in alumino-ferrite grains, the addition of O_2 must influence the Fe^{2+} present, resulting in ettringite precipitation. This increase, coupled with the formation of microfractures, suggests that detrimental DEF could be initiated at higher temperature exposure.

4.5.3. pH Estimate and Mineral Saturation

The measurement of pH at experimental conditions is difficult but of great interest because carbonic acid produced in a high-pressure CO_2 system is a primary component in the cement reaction sequence. Geochemical modeling of the influence of CO_2 and the CO_2-O_2 mixture was conducted using CHIM-XPT methods outlined by Reed and Spycher (1984) and Reed (1998) with multiple iterations to demonstrate kinetically-favored phases used to predict mineral saturation and pH at downhole conditions. At selected temperature and pressure conditions CHIM-XPT computed the distribution of thermodynamic components of aqueous species, gases, and minerals, using equilibrium constants derived from the database SOLTHERM. These equilibrium constants are modifications of mineral thermodynamic data where log K's (saturation index based on dissolution reactions) were computed for cement minerals. The aqueous activity coefficients are determined by using the modified extended Debye-Hückel equation and gas fugacity coefficients (Tanger and Helgeson, 1988). A H^+ mass balance was applied to the brine solution composition measured at one atmosphere and 25^{o}C to calculate pH under: 1) base pH at neutral waters after the curing process, with a result of 11.8; 2) under CO_2 conditions yielding a pH of 3.0; and 3) CO_2-O_2 mixture conditions with a predicted pH of 3.95. The pH prediction for the solution enhanced the understanding of the pH gradients diffusing into the cement and identified specific conditions for mineral dissolution and precipitation.

The mineral saturation indices were calculated using the post-reacted brine chemical analysis. In both gas exposure experiments, the post-curing interval pH of 11.8 was reflected experimentally by the presence of the CH crystals on the cement cylinder surface, which produced a pH buffer during $CaCO_3$ precipitation. The pure CO_2 solutions were undersaturated in minerals, except for quartz, which was not observed. Modeling of the CO_2-O_2 mixture predicted precipitation of quartz and goethite, which was confirmed experimentally by XRD results of spalled material.

4.5.4. Corrosion of Stainless Steel Autoclaves

The experimental apparatus for the subject tests consisted of stainless steel (316 CrNiMo) autoclave vessels and fittings. Although CO_2 can be corrosive when dissolved in water, carbonic acid has no corrosive impact on stainless steel as confirmed in the pure-CO_2 experiments (Corrosion, 1963). However, the addition of O_2 led to corrosion due to chloride attack (pitting and/or crevice corrosion), particularly at higher temperature, and termination of the tests after ~ 2 months duration (Fig. 4-4). The mechanism is too complex for detailed discussion here, but the presence of hydrated iron oxides and lack of $FeCO_3$ in the corrosion products, as identified by XRD, confirms the deleterious role of Cl^- and oxygen in the degradation of stainless steel, which can be explained by the autocatalytic mechanism of pit growth (Ziomek-Moroz et al., 2010).

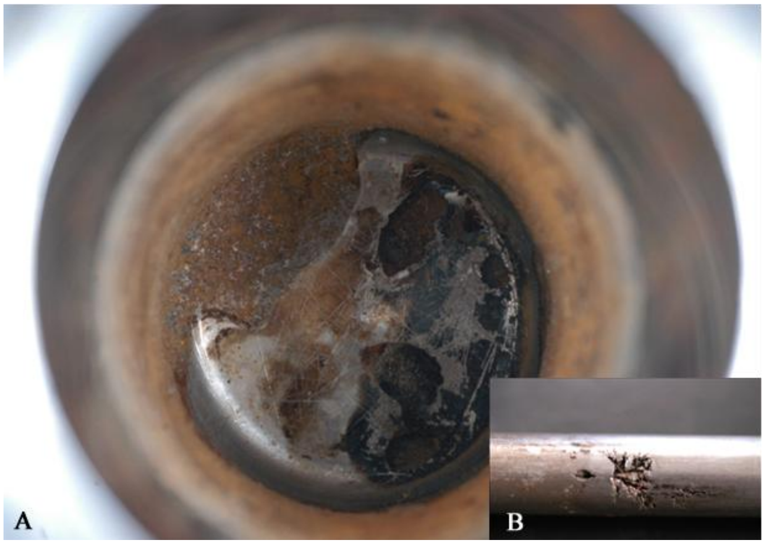

Figure 4-4. A) Chloride attack on stainless steel autoclave and B) thermocouple thermowell corrosion result of CO_2-O_2 exposure tests.

The CO_2-O_2 gas exposure tests were repeated using Teflon liners placed in the autoclave bodies to prevent further corrosion of the vessel. However, corrosion of the thermocouple thermowell, which extends down into the brine from the autoclave head, led to termination of the repeated tests after 73 days. Lessons learned from the corrosion experienced during these O_2-bearing gas exposure tests include 1) the use of protective liners and/or coatings (Teflon) on all stainless steel parts exposed to the high chloride brine during O_2-bearing gas exposure intervals, 2) curing of the cement cylinder specimens at pressure under argon as a substitute for hydraulic curing, to eliminate the exposure of all fittings in the head to the high chloride brine, and 3) minimization of local static environments created by improper alignment of parts and specimens in the autoclave, which can exacerbate corrosion issues. The corrosion experience and analysis garnered from these tests, while not part of the original test plan, provided valuable insight into the impact of O_2 addition to the gas injection stream. These results suggest that co-sequestration of O_2 may present a significant challenge to the integrity of both the well cement and well casing when injecting the gas mixture into high salinity and higher temperature saline formations.

4.6. Further Research

The effects of co-sequestration using a mixture of ~4% O_2, 1.5% SO_2, and balance $CO_{2.}$ will also be investigated and compared with the subject tests. The results of these experiments are intended to contribute to the evaluation of co-sequestration as a valid sequestration methodology. Flue gases containing SOx or sour hydrocarbon gas (H_2S) could potentially produce pyrite or other sulfur-bearing species in the cement via mineralization trapping. Additional research on the potential for DEF under these conditions is necessary.

4.7. Conclusions

The addition of 4% O_2 to the CO_2 gas injection stream during Class H portland cement exposure tests resulted in rapid formation of $CaCO_3$, enhanced cation diffusion, and mineralogical differences in the cement, compared to pure CO_2 exposure tests. In addition, secondary ettringite formation (possibly DEF), dicalcium silicate (C_2S) polymorphs, and hydrotalcite-like phase were observed in the CO_2-O_2 exposed cements. Modeling of this system suggests that the observed mineralogical changes were made possible by pH changes from the brine into the cement during exposure and extended hydration periods. The formation of delayed ettringite could potentially result in expansion and fracture formation; however, it is difficult to quantify any direct damage after the duration of subject tests. These observations suggest that the integrity of the wellbore is a concern with O_2 addition to the injected gas stream. Higher salinity and temperature affected the structure of C-S-H and hydration of the cement, which led to higher degradation rate and advanced degradation. Poor cement consolidation, poor bonding to the wellbore casing, or fracture development could lead to corrosion of the casing and degradation of the cement which could provide a leakage pathway along the wellbore for the injected gas (CO_2). The potential for corrosion of the steel casing in formations with high chloride brine concentrations was demonstrated, as corrosion of the experimental stainless steel autoclaves was observed in the subject tests.

CHAPTER V

BASALT AND SANDSTONE HOST ROCK WITH CLASS H PORTLAND CEMENT UNDER CO_2 SEQUESTRATION CONDITIONS

To be submitted to the Journal of Greenhouse Gas Control. In Chapter V, we compare the influence of basin specific brines under supercritical CO_2 conditions on the host rock Columbia River basalt and Mt. Simon Sandstone bonded to Class H cement. Experimental results are compared to modeling results. Please refer to Appendix C for SEM X-ray elemental maps and XRD data. Authors include: Circe Verba, William O'Connor, Gilbert Rush, and James Palandri.

5.1. Introduction

Geologic sequestration of CO_2 has the greatest potential in brine-bearing rock formations (DOE, 2007). Many candidate formations considered for CO_2 injection are exploration wells, natural gas wells, or oil, as well as the drilling new injection wells (e.g. Bergman & Winter, 1995; Bruant et al., 2002; DOE, 2007). Proposed CO_2 injection pilot tests in large sandstone-bearing formations in collaboration with the U.S. Department of Energy-National Energy Technology Laboratory (NETL) Phase III Regional Partnership (NATCARB, 2008). Injecting CO_2 into geologic formations initiates a sequence of geochemical reactions with the host formation and the resident aqueous solution. The composition of the fluid, pressure, and temperature of the formation all control the subsequent reactions. After CO_2 is injected, a separate free supercritical CO_2 phase can become trapped by impermeable rock formations such as shale. This is called *hydrodynamic trapping* and occurs because the CO_2 at sequestration depths is less dense than the brine and is not fully miscible in water. *Solubility trapping* occurs once the supercritical CO_2 dissolves into a solution. *Mineral trapping* is the final fate of dissolved CO_2 when it reacts with aqueous species or rock constituents, and precipitates out of solution. Mineral replacement is the most desirable of the three trapping mechanisms because the CO_2 is permanently stored and not subject to leakage (Bruant et al., 2002; White et al., 2003).

Duguid et al. (2011) examined a Class H cement embedded in sandstone and limestone and observed that the cement paste had a greater alteration depth when adjacent to sandstone with no significant alteration in the limestone-cement experiments. Furthermore, Rosenbauer et al. (2005) highlighted the need for understanding supercritical CO_2 reacting with limestone, as well as carbonate mineral formation in plagioclase-rich arkosic sandstone. Xu et al. (2005) modeled CO_2 mineral trapping within dawsonite and ankerite in a sandstone-shale model based on Gulf Coast sediments. A similar study in the Oriskany Formation sandstone in the Appalachian Basin could hold 0.36 Gt of dissolved CO_2 based on the aqueous geochemical model *PHREEQC* (Dilmore et al. (2008). The authors also speculated that it could hold 8.8 Gt of supercritical CO_2 if brine were displaced in the formation.

Flood basalts are a potential host rock for geologic sequestration owing to the ability of the basalts to store CO_2 by carbonate mineral precipitation (Reidel et al., 2002; McGrail et al., 2006). Mineralization experiments have shown that the reaction of basalt and supercritical CO_2 leads to the precipitation of carbonate minerals and thus basalt is a potential repository for storing CO_2 in a solid state (e.g. O'Connor, et al., 2003; McGrail et al., 2006; Schaef et al., 2009a,b; Verba et al., 2011). The Columbia River Basalt Group (CRBG) has an estimated 164,000 surface square miles spanning Idaho, Oregon and Washington with a volume of ~174,000 km^3. The CRBG is host to numerous aquifers with the potential to store >100 Gt of CO_2 (Reidel, 2005; McGrail et al., 2006). These basalts are heterogeneous in composition with variable amounts of augite, pigeonite, plagioclase, and trace amounts of ilmenite, orthopyroxene, or titaniferous magnetite (Reidel, 2005). In addition to the primary basalt minerals, secondary zeolite and limonite found within vesicles throughout the CRBG may react with dissolved or supercritical CO_2 to precipitate silica and magnesite-calcite (O'Connor, et al., 2002).

Portland cement paste is designed for a range of bore depths and subsurface environments to accommodate high pressure and temperature. Pumping cement slurry down the steel casing and back up the annulus seals the host rock to the casing (Nelson & Guillot, 2006). A cement plug is usually placed inside the steel casing after a well is abandoned. The terminology used herein where the term “cement paste” applies to both fresh and hardened hydrated cement. “Cement paste” is interchanged with “cement" and is distinct from “raw cement”, which refers to anhydrous constituents. Dry portland cement is mixed with water and forms metastable hydration products at various rates, depending on the temperature and pressure within the wellbore (Hewlet, 1998). The primary hydration products are a semi-amorphous gel known as calcium-silicate-hydrate (C-S-H, in cement nomenclature) and portlandite ($Ca(OH)_2$). The increase of temperature increases the rate of C-S-H network formation and the microstructure of the C-S-H changes from a network of semi-amorphous fibers to a more crystalline form (Bresson et al., 2002).

Portland cement is not thermodynamically stable and is susceptible to alteration by CO_2 that could lead to leakage by way of several pathways as discussed by Duguid et al. (2005, 2009). The dissolution and ion migration is promoted by supercritical CO_2 ($SCCO_2$) and may cause the cement seal between well casing and the formation rock to fail (Hitchon, 1996; Bruant et al., 2002; Gasda et al., 2004). The breakdown of hydrated cement paste or poor cement placement could also result in leakage of CO_2.

Previous experimental studies on wellbore Class H portland cement under simulated supercritical CO_2 and CO_2-saturated brine downhole conditions have shown that alteration and carbonation of the cement paste occurs (Duiguid et al., 2005; Barlet-Gouédard et al., 2009; Carey et al., 2007; Kutchko et al., 2007, 2008; Verba et al., 2012). The cement paste is highly reactive with dissolved CO_2 leading to calcium leaching and $CaCO_3$ replacement of the outermost exposed cement. Duguid et al. (2011) found that the wellbore environment of adjacent brine and host rock composition is important when considering long-term CO_2 sequestration. Furthermore Pruess and Müller (2009) suggest that salinity influences the rate of carbonation.

Previous experiments with cement alone have shown that the addition of CO_2 and its subsequent dissolution forms carbonic acid thus significantly lowering the pH of the solution (reaction 1, below). As the carbonic acid diffuses into the cement paste, $Ca(OH)_2$ dissolves (reaction 2) increasing the local porosity and fosters Ca^{2+} leaching out of the cement paste (Thaulow et al., 2001; Kutchko et al., 2008). Calcite precipitation results from Ca^{2+} diffusion out of the cement coupled with the infusion of carbonic acid into the cement (reaction 3). The resulting calcite provides a temporary, less permeable front blocking further carbonic acid attack. However, as the inward diffusion of carbonic acid continues, the outer edge of the calcite eventually dissolves and aqueous calcium bicarbonate forms (reaction 4). This bicarbonate can easily diffuse out of the cement paste leaving behind an amorphous silica gel zone (reaction 5).

$$CO_{2(gas)} + H_2O_{(aq)} \leftrightarrow H_2CO_{3\,(aq)} \tag{1}$$
$$Ca(OH)_{2(s)} + 2H^{+} \rightarrow Ca^{2+}_{(aq)} + 2OH^{-}_{(aq)} \tag{2}$$
$$Ca^{2+}_{(aq)} + HCO^{3-}_{(aq)} + OH^{-}_{(aq)} \rightarrow CaCO_{3(s)} + H_2O \tag{3}$$
$$H^{+}_{(aq)} + CaCO_{3(s)} \rightarrow Ca^{2+}_{(aq)} + HCO^{3-}_{(aq)} \tag{4}$$
$$2H^{+}_{(aq)} + C\text{-}S\text{-}H_{(s)} \rightarrow Ca^{2+}_{(aq)} + H_2O_{(aq)} + am\text{-}SiO_{2(s)} \tag{5}$$

There is a significant difference between the pH of the carbonated fluid (pH ~3) and the pore water in the unreacted cement matrix (pH ~13). This large pH gradient drives the transport of hydrogen ions into the cement paste while carbonate species diffuse inward due to the aqueous carbonate concentration gradient (Kutchko et al., 2007).

The most desirable sites for CO_2 sequestration are large sedimentary formations with high permeability that contain high salinity fluid and are topped with a confining caprock to prevent CO_2 escape. To evaluate such settings, this research focuses on determining the microstructural and chemical effects of carbonation upon the contact between hydrated cement paste and two host rocks, Grande Ronde basalt and Mt. Simon sandstone, both of which are saturated with natural fluids at downhole conditions.

5.2. Materials & Methods

The portland cement and formation rocks used in this study include the Grand Ronde Columbia River basalt and quartz-rich Mt Simon sandstone (Table 5-1). The first sequestration scenario consisted of portland Class H cement bonded to the Columbia River basalt and placed in a Pasco Basin brackish solution with <10,000 total dissolved solids (TDS) or 0.013 *M* (Table 5-2). The basalt sample was from a depth of 2,880 feet with a sample porosity of 20-30%. As a control, a basalt-only sample was submerged in brine and supercritical CO_2 to compare mineralogical effects without the cement reactions. The second sequestration scenario consisted of Mt. Simon sandstone encased in cement and placed in the Illinois basin brine, >50,000 TDS or 1.267 *M* (Table 5-2). The sandstone core was from depth of 4,105 feet with a sample porosity of 11.5%. As with the basalt, a sandstone-only sample submerged in brine and supercritical CO_2 in the absence of cement was examined.

Table 5-1. Initial solid composition (weight %) for the hydrated Class H cement paste, Grande Ronde Basalt, and Mt Simon Sandstone before subjected to supercritical CO_2.

Components	**LaFarge Cement**	**Grande Ronde Basalt**	**Mt Simon Sandstone**
SiO_2	17.95	50.19	94.13
Al_2O_3	2.4	14.21	1.14
Fe_2O_3	3.64	12.9	0.97
CaO	54.55	8.86	0.33
MgO	2.49	5.05	0.2
Na_2O	0.09	2.57	0.05
K_2O	0.1	1.01	0.78
Cr_2O_3	0.01	0.01	0.02
TiO_2	0.17	1.85	0.08
MnO	0.05	0.2	0.02
P_2O_5	0.113	0.258	0.025
SrO	0.08	0.04	0.01
BaO	0.05	0.05	0.01
* LOI [1]	16.85	2.71	0.45
Total	98.55	99.9	98.22
C [1]	1.65	0.08	0.12
CO_2	6.1	<0.2	0.4
SO_3	0.8	0.01	0.02
FeO	0.19	6.61	0.81
H_2O [2]	5.55	1.69	0.22

* LOI: Loss on Ignition, measured as the weight loss after 1 hour at 1000 C, in argon.

[1] Inorganic carbon

[2] Free moisture, measured as the weight loss after 1 hour at 105 C, in air.

The Class H portland cement was mixed to a 0.38 water-cement ratio and is made up of (estimated weight percent): 64.5% tricalcium silicate (Ca_3SiO_5); 11.77% dicalcium silicate (Ca_2SiO); 13.24% calcium aluminoferrite (Ca_4AlFeO_5); 2.94% MgO; 2.8% SO_4^{2-}; 0.16% total alkali; 0.62% free lime, and a loss on ignition (LOI) of 0.73. This type of cement contains no tricalcium aluminate ($Ca_3Al_2O_6$) making it resistant to sulfate attack as is required of oil wellbores.

Table 5-2. The initial composition of the solutions prior to cement curing or supercritical CO_2 *injection. Pasco brackish solution with 0.013 total mol/L being dominant with NaCl,* Na_2SO_4 *and NaF. Illinois Basin brine with 1.267 M dominated by NaCl,* $CaCl_2$*,* $MgCl_2$*, and* Na_2SO_4 *(source: Riedel (PNL), Illinois Geological Survey).*

Pasco Basin, WA Simulated Basalt Aquifer, salts	**Quantity, g/L**	**Mole/L**
$NaHCO_3$	0.097	0.001155
Na_2CO_3	0.03	0.000283
Na_2SO_4	0.207	0.001457
NaCl	0.41	0.007015
NaF	0.11	0.00262
KCl	0.0224	0.0003
Total	0.8764	0.013

Illinois Basin, Simulated Mt. Simon Sandstone Brine	**Quantity, g/L**	**Mole/L**
$NaHCO_3$	0.521	0.006202
NaCl	59.36	1.015691
$MgCl_2$	5.426	0.056989
Na_2SO_4	2.219	0.015622
$CaCl_2$	18.97	0.170926
$FeSO_4 \cdot 7H_2O$	0.353	0.00127
Total	86.849	1.267

In this study, 1x6-inch cores of formation rocks were cast in Class H cement within PVC forms (Figs. 5-1a & 5-2a). The autoclaves were purged with CO_2 to displace air, then heated to 35 °C and injected with CO_2 to obtain the final pressure of P_{co2}= 10 MPa. The samples were cured for 24 hours in the 1.2 L stainless steel (316 CrNiMo) static autoclave filled with 600 ml of reservoir fluid at 35 ^{o}C and ~10 MPa to simulate reservoir conditions. The absence of an extended cure does not allow normal hydration of the cement as would occur in a newly drilled and cemented well. The total CO_2 exposure duration was 84 days. In this study, we analyzed the initial hydrated cement, basalt, and sandstone for comparison to the cement and rock exposed to dissolved CO_2.

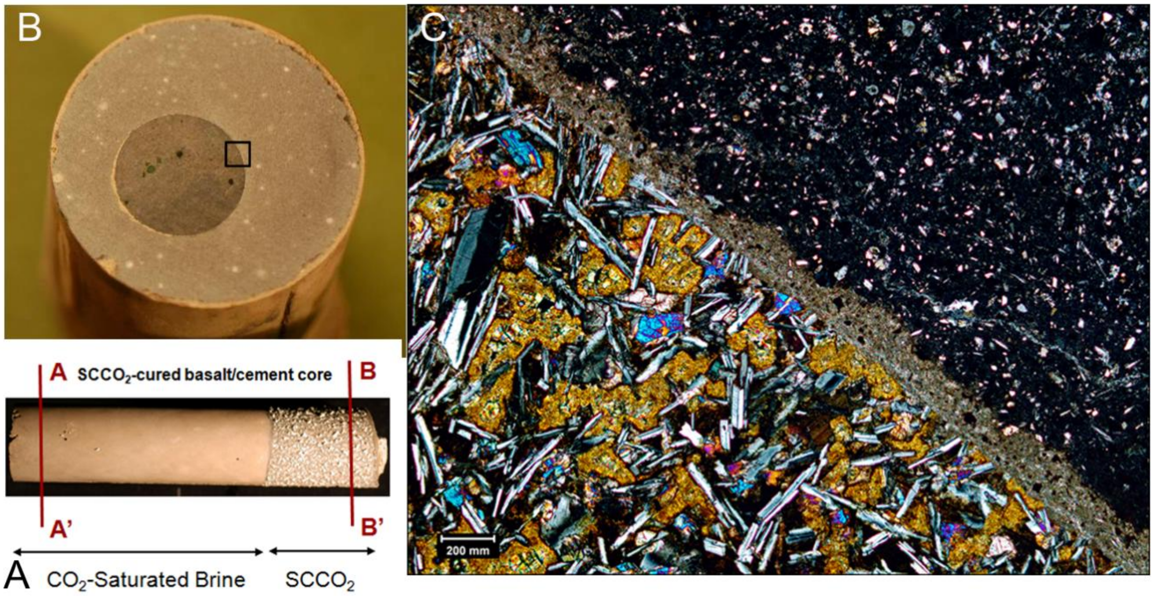

Figure 5-1. Basalt encased in cement after 84 days of exposure to supercritical CO_2. A) 2.54 x 152.4 mm (1"x 6") Grand Ronde basalt core in CO_2-saturated brine lacking surface crystals and supercritical CO_2 with portlandite crystals on the surface. A-A' and B-B' indicate where thin section were of the basalt in cement. B) Top surface of the cylinder. The white box is seen in (c); C) Transmitted polarized light microscopy of the interface between basalt (polymineralic and colorful) and cement (dark fine, grained) with grey calcium carbonation band of the basalt. The yellow-gold color indicates mineral replacement, primarily carbonation. Scale bar 200 µm.

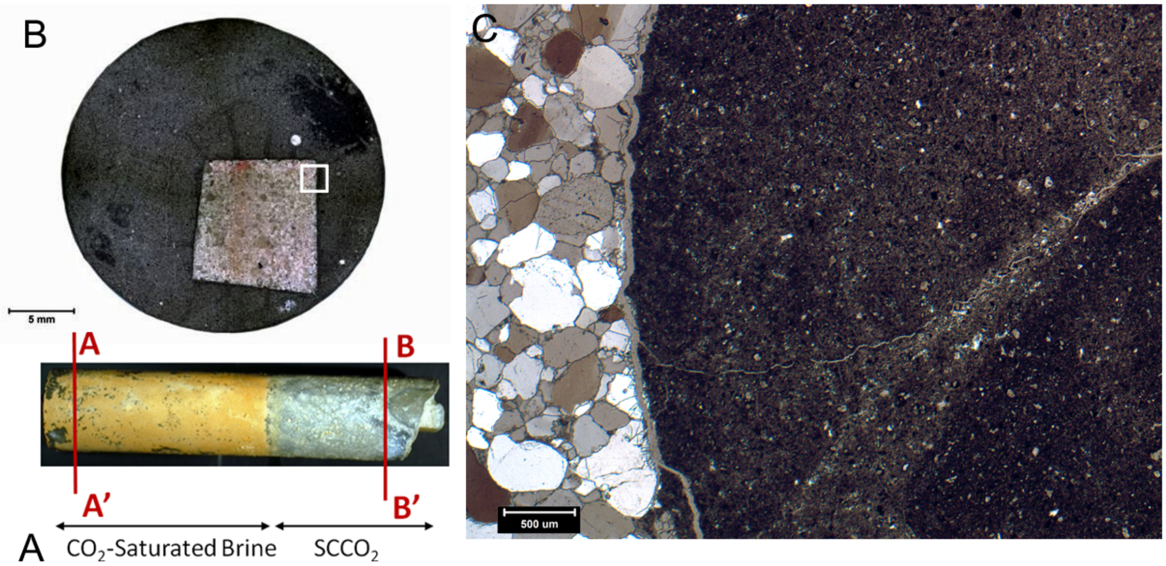

Figure 5-2. Sandstone encased in cement after 84 days of exposure to supercritical CO_2. A) 2.54 x 152.4 mm (1"x 6") Mt. Simon sandstone core in CO_2-saturated brine (reddish color) and supercritical CO_2 (gray). A-A' and B-B' shows where thin section were cut of the sandstone in cement. B) Top view of the cylinder with an approximate box to represent a close up of the boundary. C) Bottom cut of the cylinder. Transmitted polarized light microscopy of the interface between sandstone and cement with thin calcite band (gray) that has filled in a pre-existing fracture. Scale bar 500 µm.

5.2.1. Analytical Techniques

Samples were characterized using an optical microscope and an FEI Inspect F Scanning Electron Microscope (SEM) to generate backscattered electron images (BSE) and Energy Dispersive Spectroscopy (EDS) data, which was optimized with Ni and Cu standards for quantification. We obtained X-ray diffraction (XRD) pattern using a Rigaku Ultima III X-ray diffractometer with a 40KV/40mA Cu k-α source and a step speed of 1^{o}/min over a scan angle 2θ of 5^{o}-90^{o} to identify cementitious and reservoir rock minerals. Qualitative XRD analysis was performed using Jade v9.1.4 Plus software and the International Center for Diffraction Data (ICDD) pattern databases (ICDD, 2008).

All cement and rock compositions were determined by ALS Global Minerals, a commercial laboratory that specializes in solid rock analysis. Their methods described in Appendix D, include using an appropriate mixture of wet chemical, gravimetric and instrumental inductively coupled argon plasma spectroscopy (ICP-MS and ICP-AES) suited to determining all necessary components, as reported in Tables 5-1, 5-3 and graphed in Figures 5-5, 5-13. The Pasco solution and Illinois Basin brine (after 28-day curing period and after CO_2 injection) were analyzed by the ALS Geochemistry laboratory group with detection methods for metals (ICP) and inorganics (bicarbonate alkalinity as $CaCO_3$) as reported in Appendix D.

5.2.2. Geochemical Modeling

Geochemical calculations of the dissolved CO_2 reacting with the individual host rocks, and in the basalt-cement paste and sandstone–cement paste systems were carried out with program CHIM-XPT (Reed 1982; Reed, 1998). These three simulations examined phase relations among rocks, formation water, and the addition of CO_2 at subsurface conditions. CHIM-XPT computes the distribution of thermodynamic components among aqueous species, gases, and minerals using equilibrium constants at selected temperature and pressure tabulated in the SOLTHERM database (Reed and Palandri, 2013, and all data sources are referenced therein). Most of the equilibrium constants in SOLTHERM are computed using SUPCRT92 (Johnson et al., 1992), and modified to use internally consistent mineral thermodynamic data for silicates, oxides, hydroxides, carbonates, and gases from Holland and Powell (1998; available at URL: http://www.esc.cam.ac.uk/research/research-groups/holland/thermocalc). The model includes sulfide and other non-silicate mineral data from a revised SUPCRT92 data base, SLOP07 (Shock, et al., 1997, revised in 2007). Additional thermodynamic data for the cement paste minerals ettringite ($Ca_6Al_2(SO_4)_3(OH)_{12}\cdot 26H_2O$), jennite ($Ca_9Si_6O_{18}(OH)_6\cdot 8(H_2O)$), portlandite, Si-hydrogarnet and tobermorite ($Ca_{0.833}SiO_2(OH)_{1.667}(H_2O)_{0.5}$), from Matschei et al. (2007) were added to SOLTHERM. Shock et al. (1988, 1997) documents the thermodynamic data for water and aqueous species. CHIM-XPT computes aqueous activity coefficients using the extended Debye-Hückel equation of Helgeson, et al. (1981), as modified by Tanger and Helgeson (1988), and gas fugacities as discussed by Spycher and Reed (1988). To address the slow kinetics of dolomite and ankerite, these minerals were not allowed to form. Similarly, kinetics favors the precipitation of amorphous silica in low temperatures, but not quartz and its crystalline SiO_2 polymorphs. Therefore all SiO_2 phases, except amorphous silica, were suppressed (Reed and Palandri, 2013).

5.3. Results

5.3.1. XRD & Solid Composition

XRD measurements show that the Grande Ronde basalt contains augite ($FeCa_4Mg_3Si_8O_{24}$), trace amounts of olivine ($Mg_{1.8}Fe_{0.2}SiO_4$), and sodic plagioclase feldspar endmember ($Na_{0.5}Ca_{0.5}Al_{1.5}Si_{2.5}O_9$),. The amygdales in the basalt contained a mica, celadonite ($K(Fe, Mg, Al)_2Si_4O_{10}(OH)_2$ and zeolite heulundite ($CaAl_2Si_7O_{18}*6H_2O$). Table 5-1 shows the chemical compositions of the Grande Ronde basalt prior to supercritical CO_2 conditions. There were no carbonate species identified before supercritical CO_2 conditions.

Mt. Simon Sandstone is comprised of preposition quartz (96-98%), trace calcite, orthoclase ($KAlSiO_3$), and TiO_2. Table 5-1 shows the chemical compositions of the fresh Mt. Simon sandstone.

Table 5-1 can be compared to Table 5-3 which shows the initial compositions of the Class H cement paste prior to exposure to supercritical CO_2. XRD analysis of the unreacted cement paste identified the expected anhydrous cementitious phases of calcium silicate hydrates, such as haturite and larnite, calcium aluminoferrite (brownmillerite), and hydration products including $Ca(OH)_2$ and a significant broad rounded (amorphous) hump in the data.

Table 5-3. Solid composition for the Grande Ronde Basalt-Class H cement and Mt. Simon sandstone- cement after exposure to supercritical CO_2 (84 days).

Experimental Components	**1 Basalt/Cement Pasco Basin brin**	**2 Basalt/Cement Pasco Basin brine**	**4 SS/Cement Ill Basin brine**	**5 SS/Cement Ill Basin brine**
SiO_2	17.02	21.67	17.22	18.53
Al_2O_3	2.3	4.07	2.32	2.25
Fe_2O_3	3.63	5.09	3.58	3.54
CaO	50.96	43.06	53.14	51.97
MgO	2.26	2.58	2.42	2.36
Na_2O	0.03	0.41	0.01	0.01
K_2O	0.03	0.13	0.01	0.01
Cr_2O_3	0.01	0.01	0.01	0.01
TiO_2	0.17	0.43	0.19	0.17
MnO	0.05	0.07	0.05	0.05
P_2O_5	0.108	0.125	0.108	0.104
SrO	0.08	0.07	0.08	0.08
BaO	0.05	0.05	0.05	0.05
LOI *	21.8	20.5	19	19.1
Total	98.5	98.27	98.19	98.23
C [1]	2.58	2.85	1.98	2.16
CO_2	9	7.5	7	7.8
SO_3	0.74	0.64	0.88	0.9
FeO	0.19	0.75	0.37	0.38
H2O [2]	4.92	4.44	4.66	4.46
Net +CO2 [3]	2.7	1.2	0.5	1.3

wt %

* LOI: Loss on Ignition, measured as the weight loss after 1 hour at 1000 C, in argon.

[1] Inorganic carbon

[2] Free moisture, measured as the weight loss after 1 hour at 105 C, in air.

[3] Chemically-bonded water, measured as the difference between the LOI and all other volatiles (C, CO_2, and H_2O).

5.3.2. Grande Ronde Basalt-Pasco Solution

5.3.2.1. Effect of CO_2 on hydrated cement paste

The alteration on the exterior of the cement paste cylinder surrounding the basalt sample (Fig. 5-3) ranged from 325 μm to 2.6 mm with finely distributed carbonation revealed by Petrographic, SEM BSE observations and X-ray elemental maps. There is little remaining unaltered cement paste encased around the basalt cylinder. The replacement of $Ca(OH)_2$ and C-S-H by $CaCO_3$ is evident. The cement exterior showed increased porosity and relative enrichment in silica in SEM X-ray maps (Appendix C). In addition, SEM analysis shows that a remnant porous silica zone ranges in thickness from 200-500 μm, where the cement paste has lost its calcium. The elemental x-ray maps also depict the loss of elemental Mg, S, and Si of the exterior cement cylinder. Furthermore, the altered cement has a high concentration of elemental sulfur trapped within the gel-like C-S-H structure as seen in X-ray elemental mapping. The effect of CO_2 on cement paste combined with the low salinity of the Pasco solution resulted in complete and rapid alteration.

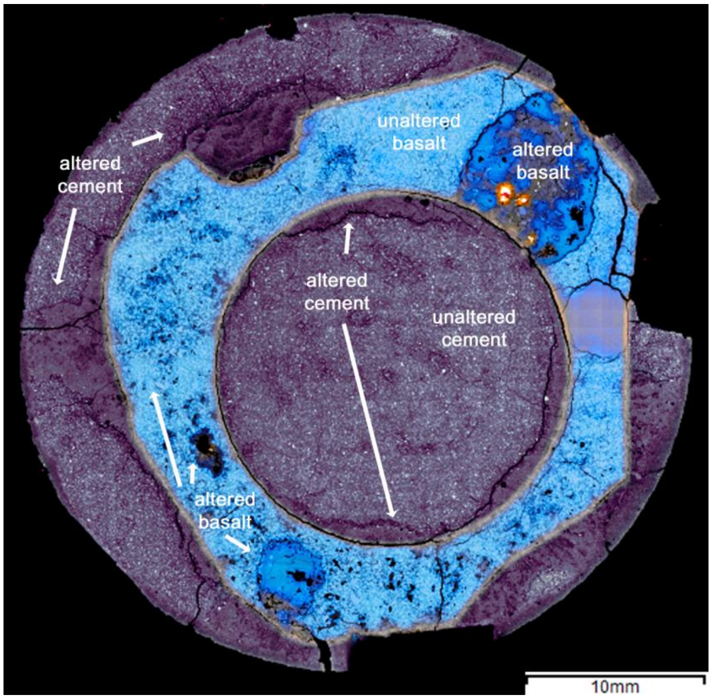

Figure 5-3. A SEM-BSE montage image of the Grande Ronde basalt/ portland cement interface with elemental (EDS-X-ray maps) overlays of Mg, Fe, Ca^{2+}, O. The purple hues: cement; blue hues basalt where the darker hues represent alteration. The thin orange rim is the (Ca, Fe, and Mg) carbonate band. Large pieces of the cement have broken are off after exposure to supercritical CO_2. Scale bar 10 mm.

5.3.2.2. Basalt-cement Interface

The interface between cement and basalt contains ~25 µm finely crystallized calcite band where the $Ca(OH)_2$ had been replaced as revealed by SEM-EDS calcium X-ray map and SEM point analysis (Figs. 5-1c and 5-4). The majority of cement alteration occurs with the amorphous silica zone with one band of carbonate followed by calcium depletion (Fig. 5-4). In extreme cases of alteration, a 6.7 mm long fracture along the cement-basalt interface has alteration up to ~900 µm extending into the cement. There is mineral replacement at the fractured interface extending into the cement with a series of four carbonated bands, each band followed by calcium depletion (upper left interface in Figs 5-3). This alteration along the basalt-cement paste interface suggests that CO_2 travelled along the pathway in areas of bonding weakness, as longitudinal diffusion along the interfaces, or along fractures.

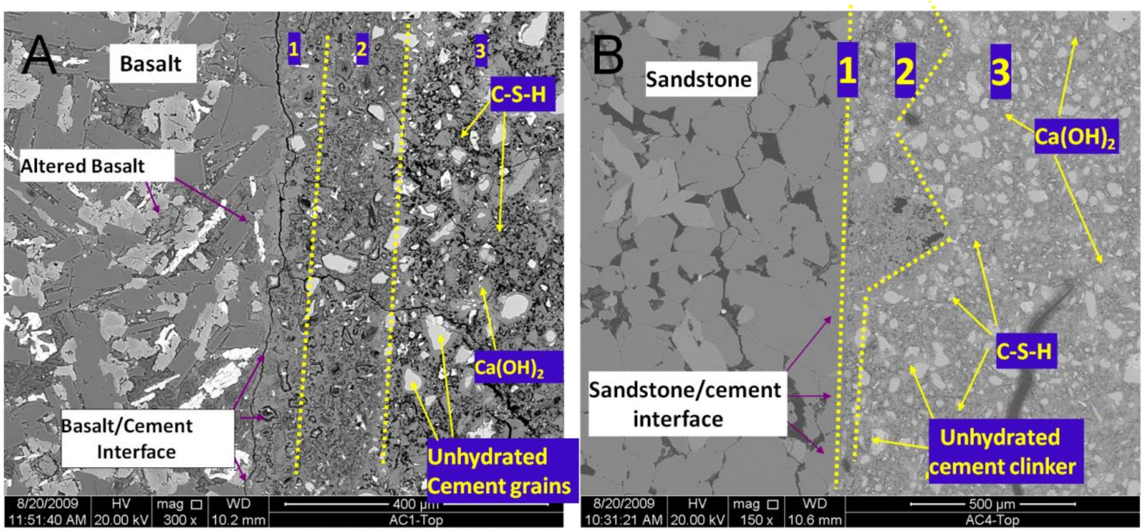

Figure 5-4. SEM BSE images A) Basalt-cement and B) Sandstone-cement samples exposed to supercritical CO_2 for 84 days. Dotted line indicates alteration boundaries: 1) porous silica zone, 2) $CaCO_3$ zone, 3) Ca-depleted cement.

The basalt-cement interface displays alteration of augite, magnetite, and olivine (Fig. 5-4A). Mineral dissolution may account for the increases in aqueous Fe^{2+} (46 mg/l) and aqueous Mg^{2+} (340 mg/l) once the basalt is exposed to supercritical CO_2, in comparison to the original solution (Fig. 5-5). The loss of Na^+ from plagioclase and K^+ from the groundmass, as seen by SEM EDS analyses, correlates to an increase of 320 mg/l of aqueous Na^+ and a 200 mg/l increase of K^+ in solution as shown in Figure 5-6. A small amount of Ti (2.2 mg/l) in the solution indicates the dissolution of ilmenite. In addition, basalt vesicles were filled with secondary precipitates of fine grained, magnesian calcite and semi-spherical amorphous silica nodules that were not present prior to CO_2 exposure (Fig. 5-6).

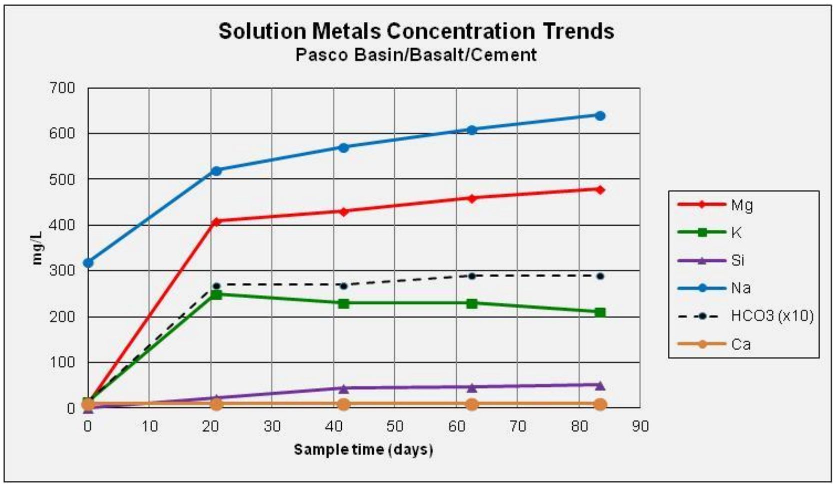

Figure 5-5. Changes in the solution composition of the CO_2-saturated Pasco Basin at 35°C and 10 MPa. Na^+, Mg^{2+}, and Si^{4+} increase in concentration from mineral dissolution. K^+ peaks at 21 days and begins to slowly decline. HCO_3^- slowly increases after CO_2 injection and the pH increases. No change in calcium (detection limit 10 mg/l) indicates $CaCO_3$ in the cement has not started to dissolve.

5.3.2.3. Basalt Core

The cylinder of basalt in the absence of cement paste was exposed to P_{CO2} =10 MPa and 35°C for 84 days immersed in the Pasco solution. SEM-EDS and petrographic analysis shows the precipitation of an intermixed iron-carbonate and magnesian-calcite formed primarily in the glassy groundmass and on the surface of augite and forsterite (Fig. 5-6). Furthermore, smaller vesicles were completely filled with calcite whereas larger vesicles, >100 μm in width, displayed depositional banding (Fig. 5-6). Polarized light microscopy revealed mineral replacement, particularly in augite and olivine, by brown and orange carbonates (Fig. 5-6A). A pre-existing glassy, semi-amorphous iron hydroxide that lined the vesicles, dissolved after 21 days and became an additional source of iron. These carbonates were identified as an iron-rich magnesite mixed with calcite and siderite. Some vugs were lined with semi-spherical amorphous silica. Vermiculite-kaolinite clay was also identified is the result of the carbonic acid fluid reaction with celadonite.

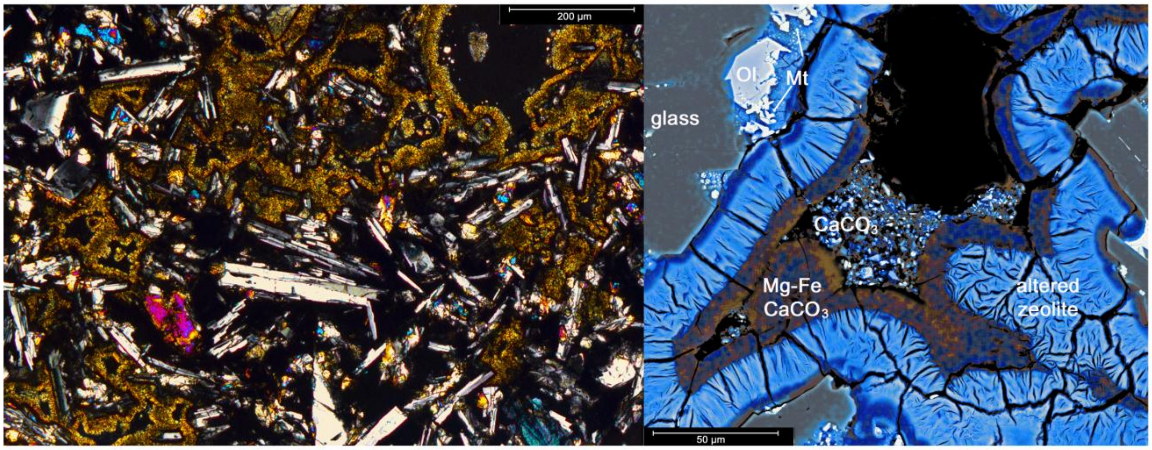

Figure 5-6. A) Transmitted polarized photomicrograph of the Grande Ronde basalt CO_2-exposure experimental test. Bright orange carbonate species infilling edges of zeolites within the basaltic vesicles. Scale bar 200 µm. B) SEM-BSE cameo image with Mg, Fe, Ca^{2+}, O EDS-X-ray maps overlaid. Reddish hue represents iron rich carbonate, dark blue represents carbonate (magnesite and calcite). Ol: altered olivine; Mt: magnetite. Scale bar 50 µm.

The reactions below (6-11) illustrate how augite, olivine, and plagioclase endmembers, based on XRD identified phases, react with carbonic acid as seen petrographically. Augite and olivine react to form mafic carbonates (reaction 6-11). The reactant plagioclase feldspar is 0.5 mole fraction albite and 0.5 mole fraction anorthite identified as labradorite ($Na_{0.5}Ca_{0.5}Al_{1.5}Si_{2.5}O_8$) which allows kaolinite and amorphous silica to precipitate. For the anorthite endmember, Ca^{2+} is released into solution which is applicable in reaction 9. For the albite endmember, the Na^+ is released in solution (Fig. 5-5) in accordance with the following reaction 10. Reaction 11 demonstrates a potential reaction of labradorite itself reacting under supercritical CO_2 conditions.

$$FeCa_4Mg_3Si_8O_{24\,(augite)} + 16H^+_{(acid)} + 8H_2O_{(aq)} \rightarrow 4Ca_{\,(aq)} + 3Mg_{\,(aq)} + Fe^{2+}_{(aq)} + 8H_4SiO_{4\,(aq)} \qquad (6)$$

$$(Ca,Mg,Fe)^{2+} + HCO_3^- \rightarrow (Ca, Mg, Fe)CO_3 + H^+ \qquad (7)$$

$$Mg_2SiO_{4\,(foresterite)} + 2CO_{2(aq)} \rightarrow 2MgCO_3 + SiO_{2(am.\ silica)} \qquad (8)$$

$$CaAl_2Si_2O_{8\,(anorthtite)} + H^+ + HCO_3^- + H_2O \rightarrow CaCO_3 + Al_2Si_2O_5(OH)_{4\,(kaolinite)} \qquad (9)$$

$$2NaAlSi_3O_{8\,(albite)} + 2H + H_2O \rightarrow Al_2Si_2O_5(OH)_{4\,(kaolinite)} + 4SiO_{2\,(am.\ silica)} + 2Na^+ \qquad (10)$$

$$\begin{aligned} &4Na_{0.5}Ca_{0.5}Al_{1.5}Si_{2.5}O_{8\,(labradorite)} + 2H_2CO_3^- + 3H_2O + 2H^+ \rightarrow \\ &\qquad 2CaCO_3 + 3Al_2Si_2O_5(OH)_{4\,(kaolinite)} + 4SiO_{2\,(am.\ silica)} + 2Na^+ \qquad (11) \end{aligned}$$

5.3.3. Mt. Simon Sandstone- Illinois Basin Brine

5.3.3.1. Effect of CO_2 on cement paste

The influence of CO_2 on the cement paste directly in contact with the Illinois brine resulted in a porous silica zone less than 300 µm in depth. Finely distributed calcite along the exterior of the cement cylinder extends an average of 100 µm thick, with a maximum alteration depth of 700 µm at fractured zones (Fig. 5-7). The majority of the cement is unaltered and contains clusters of unhydrated calcium alumino-ferrites as seen with SEM-EDS with high Mg (Fig. 5-7). These anhydrous ferrite cementitious grains have a thin layer of iron hydroxide. The Illinois Basin brine reacted less with the supercritical CO_2 resulting in less alteration of the cement bonded to sandstone (Fig. 5-7) in comparison the cement paste immersed in the Pasco solution (Fig. 5-4).

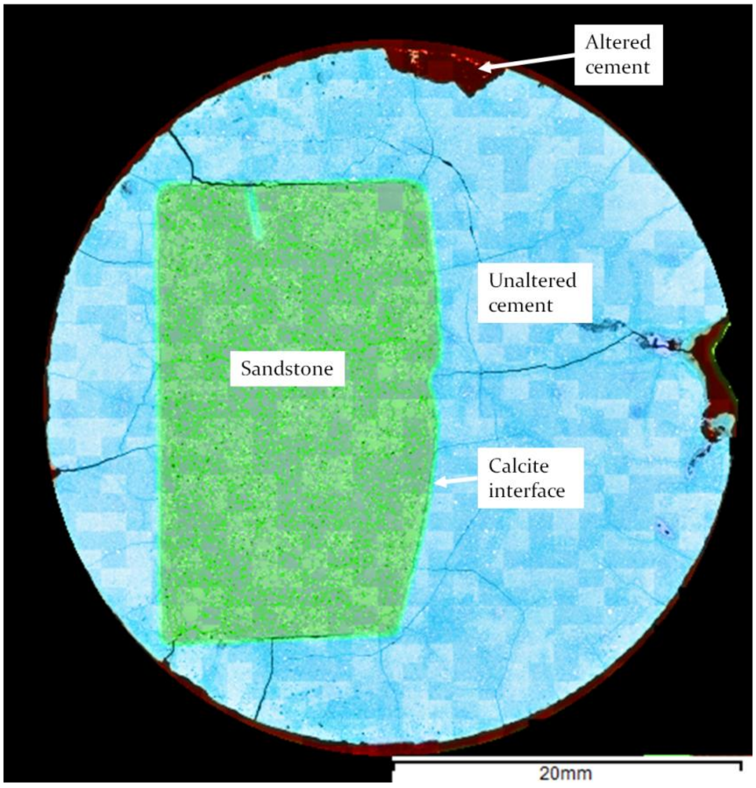

Figure 5-7. A SEM-BSE montage image of the Mt. Simon sandstone-Class H Portland cement in a CO_2-saturated Pasco Basin solution with Mg^{2+}, Fe^{2+}, Ca^{2+}, O^{2+} EDS-X-ray maps. Brown-red represents altered cement; the blue is unaltered cement. The blue-green rim which follows the entire interface is calcium carbonation. The dark green color represents the sandstone. The checkered pattern of light blue is an artifact of the scanning and stitching of BSE images. Scale bar 20 mm.

5.3.3.2. Interface between Mt. Simon Sandstone and cement paste

Petrographic examination of the sandstone-cement paste interface after exposure to CO_2 shows amorphous silica gel around the quartz grains and an adjacent ~20-30 μm thick, well crystallized band of $CaCO_3$ (Fig. 5-2C, zone 2 in Fig. 5-4). In addition, elemental X-ray mapping in Fig. 5-7 shows that the thin carbonation follows the entire cement-rock interface and fills previously existing fractures. Furthermore, x-ray mapping shows that the outermost carbonated zone has begun to lose calcium, leaving behind porous silica (Figs. 5-4B). Decalcification occurs in regions that provide a source of carbonic acid (i.e. near fractures) and where relic hydrated cement products have reacted, dissolving the calcium carbonate. Most of the reaction is localized leaving most of the cement paste unreacted in the Illinois Basin brine.

5.3.3.3. Sandstone Core

The influence of CO_2 on pure Mt. Simon sandstone is limited. There is a thin coating of $CaCO_3$ on quartz grains, with cubic halite (NaCl) no more than 50 μm in size, accompanied by tiny (<5 μm) sylvite (KCl) crystals (teal blue in Figs. 5-8). The boundaries of detrital quartz grains near fractures or crevices near the 1/2 mm exterior of the cylinder have precipitated amorphous silica as seen by SEM elemental analysis (Fig. 5-8). The Mt. Simon sandstone remains unaffected by the supercritical CO_2.

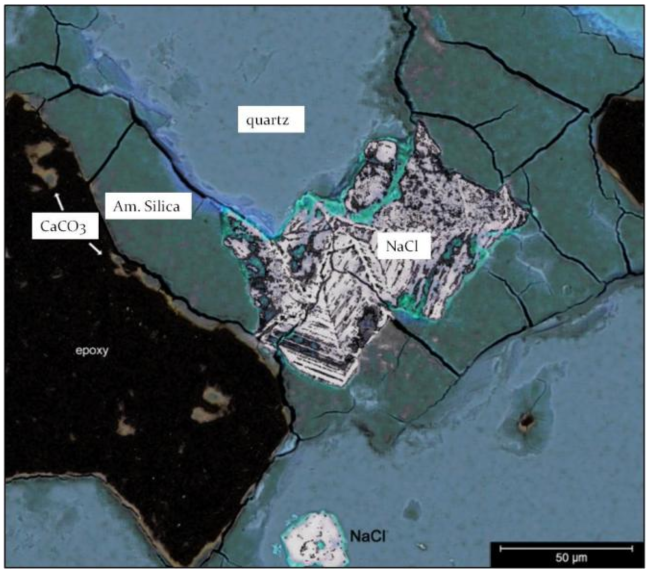

Figure 5-8. SEM BSE image with EDS X-ray map overlay of the Mt. Simon sandstone sample (no cement) exposed to CO_2 with amorphous silica surrounding quartz (qtz) grains, thin calcium carbonation covering with halite (white), and sylvite (bright teal) precipitation. Scale bar is 50 µm.

5.4. Geochemical Modeling

The purpose of geochemical modeling of the rock-cement-formation water system was to compare the laboratory experiments to the modeled results. We carried out four two-step titration calculations at 50°C in which the first step is the incremental titration of rock and/or cement paste into an initial mass of formation water, and recomputing equilibrium at each step. The titration continues until the desired water-rock ratio is reached. In the second step pure CO_2 is titrated incrementally into the fluid until the gas saturation pressure is equal to the predicted downhole pressure and a separate CO_2 phase forms. The change of pH reflects the mineral stability of carbonate minerals as CO_2 interacts with the host rock in the presence, or absence, of cement in their respective solutions.

5.4.1. Columbia River Basalt + Pasco Solution + CO_2

The first geochemical run was to examine the effect of supercritical CO_2 on the basalt alone. We examined two gas saturation pressures (102 and 306 bar) since more gas dissolves at the higher pressure. The two different pressures resulted in minor differences in the assemblages. The run at 306 bars yields a lower initial pH of 3.2 with a total of 166 g dissolved CO_2 in 1 kg of

Pasco Basin fluid. The run at 102 bars, the subsurface conditions expected in the Pasco basin, yields a higher pH of 3.7 with 50 g of dissolved CO_2 in 1 kg of Pasco Basin fluid and total of 28 kg of Grand Ronde basalt incrementally added (Fig 5-9). Total dissolved Ca^{2+}, and Fe^{2+} increased steadily until goethite (FeOOH) first formed and then kaolinite $Al_2Si_2O_5(OH)_4$ precipitated near a fluid pH of 3.2-3.25 and 0.003 fluid-rock ratio. As goethite dissolved, Na-nontronite formed. Amorphous silica (<1g) displayed short stability range where SiO_2 precipitated at pH of 3.44 and dissolved out at a pH of 4.48.

Increasing concentrations of calcium and sodium resulted in stilbite $NaCa_4(Si_{27}Al_9)O_{72}\cdot 28(H_2O)$ precipitation. The increase in pH and iron resulted in siderite ($FeCO_3$) precipitation at pH 3.56 once 0.4 g rock is added. Calcium concentration increased again after amorphous silica dissolved out. Magnesite ($MgCO_3$) precipitated at a pH of 4.7. The increase of pH to 5.39 allowed calcite and muscovite to precipitate despite the modest depletion of aqueous carbonate due to early precipitation of siderite. There is a maximum of 110 g of magnesite and a maximum of 200 g of siderite that precipitates in the run.

Magnesite and siderite both eventually dissolve out as bicarbonate, Fe^{2+} and Mg^{2+} decrease, but calcite persists until the end of the run. In this CO_2 dominated system, albite (modeled plagioclase feldspar) is stable at pH greater than 7.33, Fe-celadonite at 8.13 clinochlore at 8.5, and Fe-talc, 8.67 as siderite and magnesite dissolve. At 102 bars, a total of 28 kg of basalt was added to the system and the final pH was 12.23.

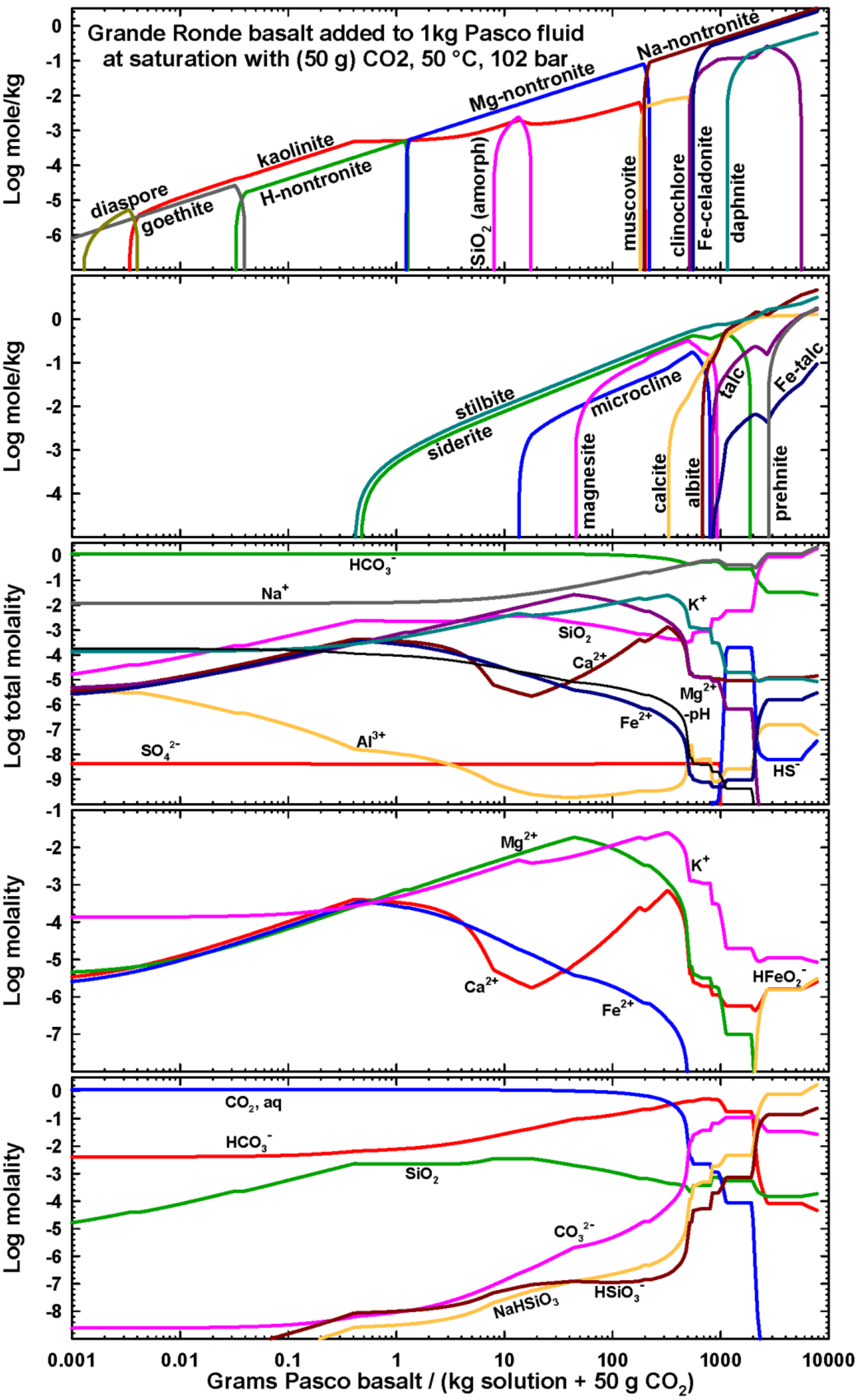

Figure 5-9. CHIM-XPT plot of the Grande Ronde Basalt immersed in Pasco Basin solution with 50 grams of CO_2 titrated until saturation pressure of 102 bars. Plot shows the change of mineral phases and chemical species with titrated basalt.

5.4.2. Columbia River Basalt +Cement paste + Pasco Solution + CO_2

The hydration of 125 g of dry cement powder produces ~161 g of cured cement. The initial cement paste composition contains less jennite and more portlandite than real cement. In the next step, 125 g of Grande Ronde Basalt was incrementally added to 1 kg of Pasco Basin fluid, and then CO_2 titrated until a saturation pressure of 102 bars.

The calculation results (Figure 5-10) are similar to the basalt-solution-gas run in the previous section, but allow for evaluation of a system containing both basalt and cement paste. The dominant mineral reactions are the replacement of portlandite by jennite, and once portlandite dissolves out, the replacement of jennite by tobermorite.

CO_2 addition causes tobermorite to dissolve in response to decreasing pH. Tobermorite provides calcium to form calcite and the silica to form celadonite. When tobermorite completely dissolves at 61 g of added CO_2, amorphous silica precipitates and 136 g of precipitates at a pH of ~7. Calcite dissolves only slightly over the remainder of the run in response to the falling pH. Pumpellyite dissolves once 60 g of gas is added, and stilbite becomes the second most abundant mineral in the assemblage after calcite. The initial source of Mg is in phlogopite (with a trace in chrysotile), which is replaced by talc, and then replaced by magnesite and Mg-nontronite ($Mg_{0.33}Fe_2Al_{0.33}Si_{3.67}O_{12}H_2$). Magnesite and Mg-nontronite remain unchanged. As goethite, Fe-celadonite, and Fe-talc dissolve, iron becomes available and siderite (11.2 g) replaces pyrite. The fluid pH continuously decreases over the calculation: the pH starts at 11.82 and ends at 4.52, with a large step from 11.1 to 7.65 as tobermorite dissolves out and calcite forms.

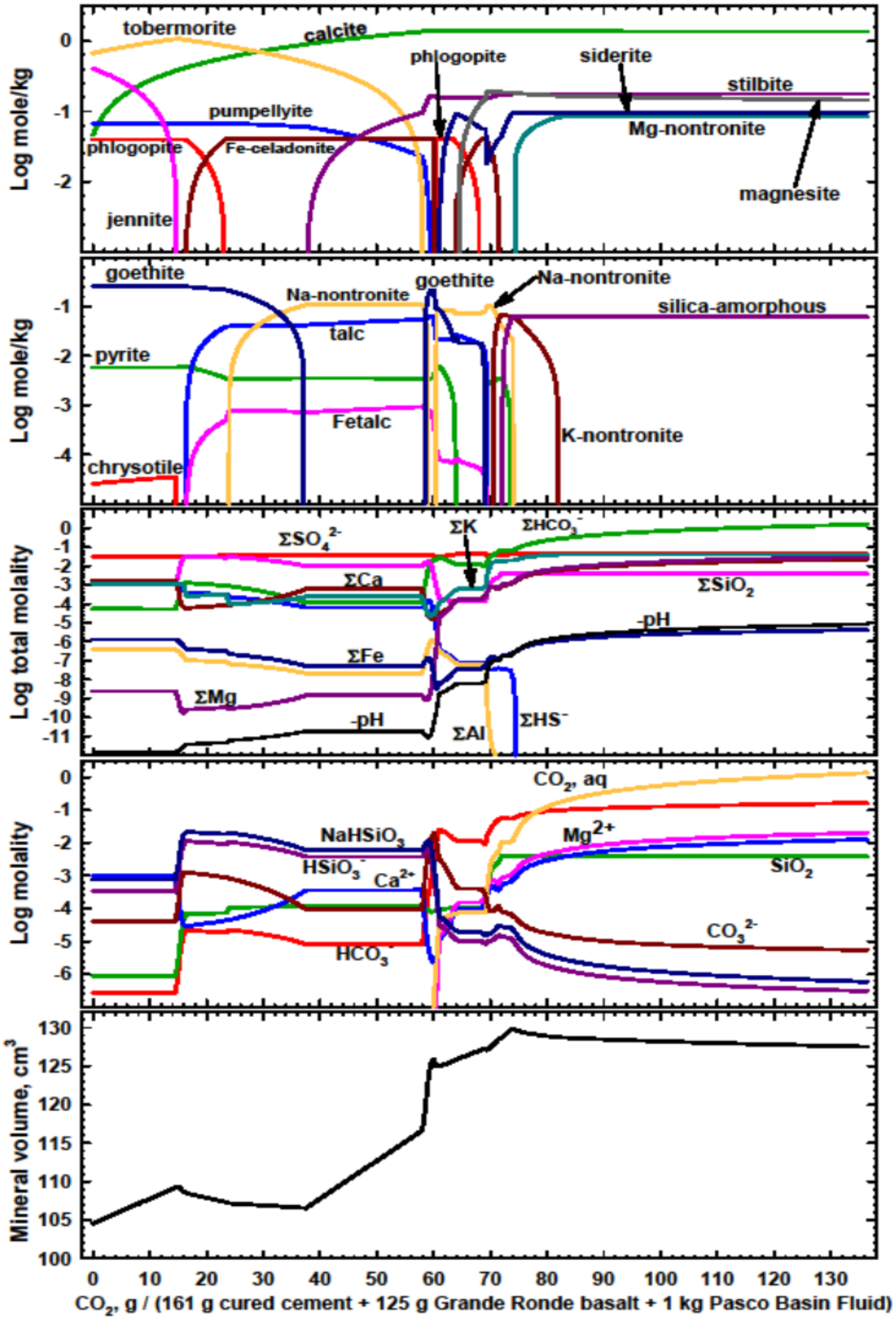

Figure 5-10. CHIM-XPT graph of CO_2 is titration into 161 g of cured cement and 125 g Grande Ronde Basalt in 1 kg of Pasco Basin fluid to a saturation pressure 102 bars. Plot shows the change of mineral phases and chemical species with titrated basalt.

5.4.3. Mt. Simon Sandstone + Illinois Brine + CO_2

This calculation is to examine the addition of supercritical $CO_2$with the Illinois brine and Mt. Simon sandstone. The Mt. Simon sandstone is dominated by quartz and the Illinois brine provides cations for reactions. Roughly 139 g of CO_2 gas was added to 1.04 kg of lab-simulated Illinois Basin brine (1 kg H_2O + 0.04 kg dissolved solutes) to bring the fluid to saturation with the gas. A total of 83 kg of Mt. Simon sandstone was added incrementally to the fluid-gas mixture in the final step (Fig. 5-11). Given that quartz dominated in the reactant sandstone, quartz would saturate early in the titration and subsequently precipitate with the addition of rock. However, silica from non-quartz detrital silicates reacting in the natural setting would likely supersaturate the system with respect to quartz at the low temperature of reaction, allowing aqueous silica to reach saturation with amorphous silica. To simulate this phenomenon, all quartz polymorphs were suppressed, except amorphous silica. We regard the quantity of precipitated SiO_2 (Fig. 5-11) as a summation of titrated quartz and amorphous silica.

Mt. Simon sandstone is Ca- and Mg-poor; calcite never precipitates and the amount of magnesite is an order of magnitude less than that of siderite. After the addition of 30 kg rock, dissolved CO_2 is depleted in the fluid and siderite makes up about 1.4 wt% of the rock. At the end of the run 80 kg of titrated sandstone is composed of 75,710 g amorphous silica/quartz, 516 g albite, 2,499 g Fe-celadonite, 58 g microcline, 21 g Mg-nontronite, and 264 g stilbite. The Mt. Simon sandstone contains only small amounts of components, such as CaO, to drive pH, consequently pH rises from initial pH of 4.77 to 5.8, but does not go higher.

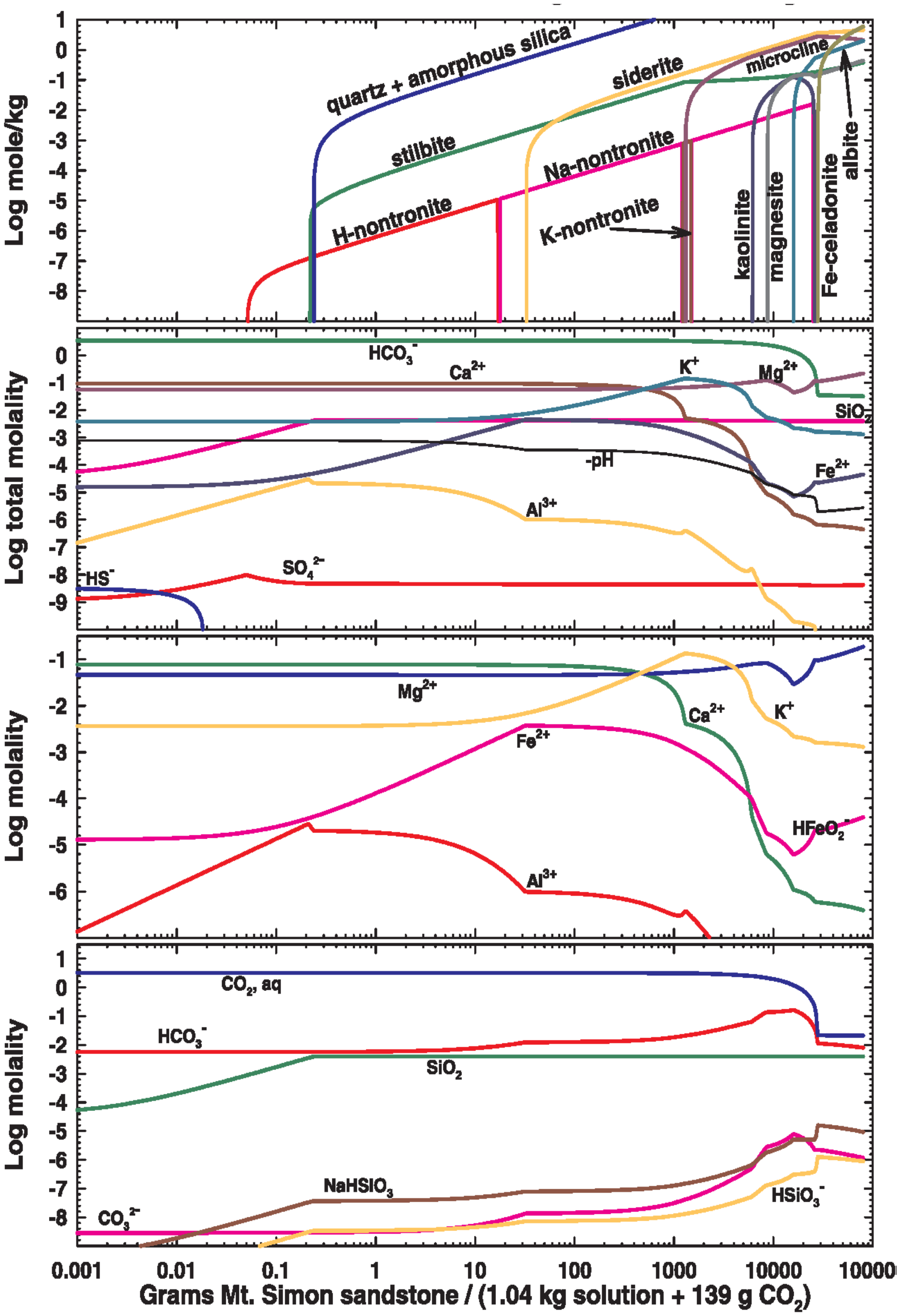

Figure 5-11. CHIM-XPT graph of Mt. Simon sandstone in 1.04 kg Illinois basin fluid and with 139 g CO_2 is titrated to 104 bars. Plot shows the change of mineral phases and chemical species with titrated sandstone.

5.4.4. Mt. Simon Sandstone + Cement paste+ Illinois Brine + CO_2

In the Mt. Simon sandstone-cement paste system, quartz is treated as an inert mass, and K_2O in the sandstone is assumed to be in microcline. First, 125 g of cured cement paste reacts with the Illinois Basin fluid, to produce 156 g of cured cement. The next step is adding 156 g of cured cement paste to Illinois basin fluid and adding equal amounts of 125 g Mt. Simon. Lastly, CO_2 is titrated into the system with results as shown in Fig. 5-12. Redox conditions are slightly reducing owing to FeO in sandstone as magnetite (Fe_3O_4). Magnetite is replaced by pyrite (FeS_2) containing sulfur from reduction of sulfate in the brine and in ettringite ($Ca_6Al_2(SO_4)_3(OH)_{12}\cdot 26H_2O$). Siderite replaces goethite when the pH decreases, dissolving goethite. In the cement paste, calcite replaces portlandite at a pH of ~11.3. Jennite ($Ca_9Si_6O_{18}(OH)_6\cdot 8(H_2O)$) and Si-hydrogarnet are replaced by tobermorite and yields a total of 138 g of calcite. Gypsum (2.2 g total) replaces ettringite, then buffers aqueous sulfate in concert with the large Ca^{2+} concentration. Other final minerals are 7.2 g of amorphous silica, 2.2 g magnesite, 13.6 g Mg-nontronite, and 21.3 g of stilbite, whereas Fe-celadonite, and talc dissolve out under the final acidic condition where the pH is 4.85.

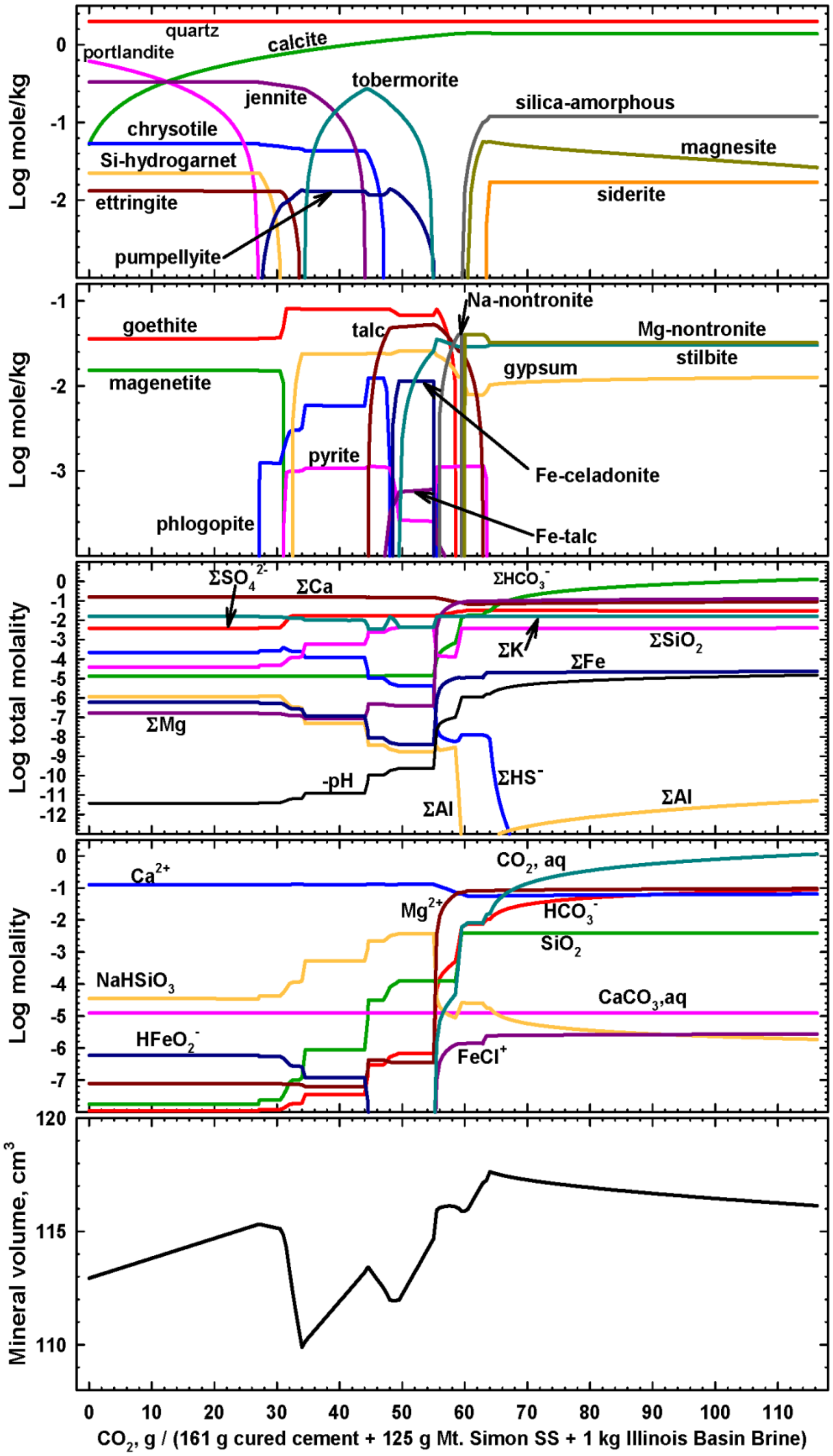

Figure 5-12. CHIM-XPT plot of cured cement with Illinois basin fluid and Mt. Simon sandstone with CO_2 is titrated into the system. Plot shows the change of mineral phases and chemical species with titrated sandstone. Quartz is shown as supersaturated, but is not involved in the reaction as it is treated as an inert mass.

5.5. Discussion

We conducted four different 84-day experiments under supercritical CO_2 conditions with the host rock as: 1) pure Grand Ronde basalt in Pasco Basin solution; 2) pure Mt. Simon sandstone immersed in Illinois Basin brine; as well as 3) basalt and 4) sandstone bonded to Class H portland cement under supercritical CO_2 conditions in their respective solution. The primary focus was to examine the interface between the cement and host rocks. For both rock types, the CO_2 permeated the interface between rock and cement where fractures formed due to poor bonding of cement to the rock. Petrographic analyses show that the well cement was corroded and weakened and CO_2 travelled along the interface of the cement paste and host rocks (Fig. 5-3). The Grande Ronde basalt was the most reactive to dissolved CO_2, resulting in mineral replacement of basaltic phenocrysts and glassy matrix by carbonate species. In addition, the cement paste was heavily altered (>50 wt%) and carbonated by CO_2 reaction. The intense of degradation of the cement in the basalt-cement experiment indicates that the low salinity of the Pasco solution resulted in an increased cation migration out of the cement, likely due to higher CO_2 solubility, discussed in section 5.5.2. On the other hand, the Mt Simon sandstone displayed little carbonation or alteration at the interface, although the cement paste surrounding the cement did react in the Illinois Basin brine.

5.5.1. Grande Ronde Aqueous Phase Chemical Analysis

The measured solution concentrations in the Pasco Basin solution (mg/l) under acidic conditions reflect the dissolution of the basalt and cement paste as a function of time (Fig. 5-6). The basalt has a ready source of Ca^{2+}, Fe^{2+}, and Mg^{2+} cations available and is reactive to the CO_2. CO_2 mineral trapping is the dominant sequestration process where the basalt exchanges cations and carbonate minerals precipitate. XRD microanalysis found degradation products of heulundite and celadonite zeolites, identified as montmorillonite-vermiculite clay and trace amounts of kaolinite clay lining the vugs. These vesicles provide access to glassy groundmass for supercritical fluid, which allowed for further dissolution of the glass matrix and phenocrysts.

Solution analyses indicated that basalt components leached into the solution. The dissolution of augite, olivine, and plagioclase phenocrysts and glassy groundmass increased aqueous K^+, Mg^{2+}, Na^+, and silica concentrations (Fig. 5-5). For example, the Mg^{2+} increased to forty times the original concentration in solution. As seen in SEM-EDS X-ray maps, after 28 days of supercritical CO_2 exposure, aqueous K^+ initially increased by 250 mg/l as the K_2O in the basaltic glassy groundmass dissolved. Sylvite (KCl) precipitated lowering aqueous K^+ concentrations to 210 mg/l. After CO_2 injection, HCO_3^- immediately increased in solution as seen in Figure 5-5. The increase of HCO_3^-, with no change of aqueous calcium concentrations, suggests that $CaCO_3$ had not yet begun to dissolve.

5.5.2. Mt Simon Sandstone Aqueous Phase Chemical Analysis

The Illinois Basin brine is more complex than the Pasco Basin solution. In contrast to the Pasco formation water, the high salinity Illinois Basin brine (1.267 *M*) had little interaction with the sandstone and cement paste until ~42 days of exposure to supercritical CO_2 (Fig. 5-13). The increase in aqueous species (Ca, Na, Mg, etc) is limited by what is available in the sandstone (mostly quartz) and is leached from the cement paste. After injecting CO_2 into the system, there was an initial drop in Ca^{2+} from 3200 to 2500 mg/l and a slight decrease of Si (16 mg/l) concentrations. This indicates that the calcium from the brine contributes to $CaCO_3$ precipitation in the cement paste. The decrease of aqueous silica is presumably owing to the precipitation of amorphous silica gel surrounding the quartz grains as seen by electron microscopy (Fig. 5-8). Figure 5-13 also shows that HCO_3^- concentrations are highest (>400 mg/l) at ~64 days followed by an increase in aqueous Ca^{2+} to concentrations that exceed initial brine levels. This point of the experiment marks the depletion of portlandite within the exterior of the cement and that the calcite has begun to dissolve. Lastly, the potassium increases from 480 to 710 mg/l and then plummets to 180 mg/l after 63 days. Although, XRD did not identify KCl, the K^+ decrease is likely due to precipitation of a K-mineral, such as KCl. The presence of halite supports the conclusion that other salts may have precipitated within the hydrated cement (Fig. 5-8).

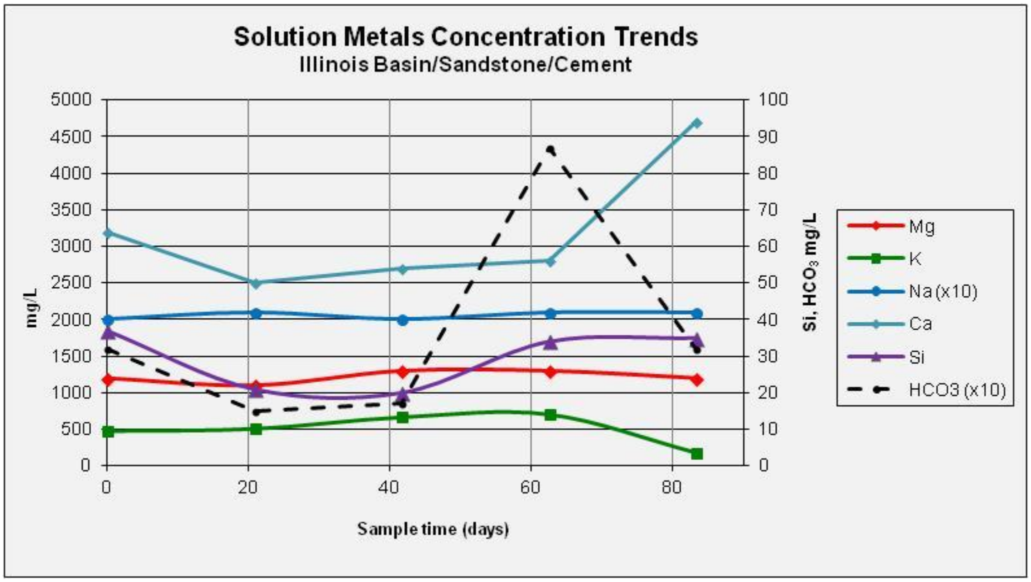

Figure 5-13. Trend of aqueous species between the cured cement-basalt-Illinois basin brine. Changes in the solution composition of the CO_2-saturated Illinois Basin brine at 35°C and 10 MPa. Right-hand side Y-axis applies to aqueous Si^+ and HCO_3^-; left Y-axis all other species. Na^+ and Mg^{2+} concentration fluctuates. Si solution initially decreases and then returns to initial levels. HCO_3 spikes at 63 days, marking the depletion of portlandite in the cement. The actual concentrations of Na^+ and HCO_3^- were multiplied by 0.1 for plotting.

The exterior of the cement paste cylinder that encases the sandstone sample showed little carbonation (Fig. 5-7). The lower degree of alteration may be a consequence of decreased CO_2 solubility of the Illinois Basin Brine. The alteration of the cement that encases the sandstone appears to have a limited CO_2 solubility as there is a lack of calcium carbonate formation. In addition, carbonate minerals or silica gel fills fractures and gaps surrounding the silicic clasts in the sandstone in the supercritical CO_2 environment as seen in Figures 5-2C and 5-7. The formation of calcite and silica gel inhibits diffusion, and thus limits further alteration. Based on these results, we can conclude that sequestering CO_2 in higher salinity brines and silicic formations is advantageous and there is less risk of cement seal.

5.5.3. Laboratory Experiments and Modeling Comparison

The geochemical reactions models of the host rock were developed using CHIM-XPT (Figs. 5-9 to 5-13) are compared to experimental observations. These calculations also provided favored mineral reactions and pH conditions during supercritical CO_2 conditions. Metastable jennite and Si-hydrogarnet are typical phases in all the CHIM-XPT runs; jennite is replaced by a crystalline C-S-H, tobermorite. CHIM-XPT also calculated that ettringite precipitates, indicating that sulfate would be found in a semi-stable form rather than bonding to the semi-amorphous gel C-S-H in the cement. Ettringite is unlikely in Class H cement and previously not seen in these experimental cement CO_2 immersion studies. Instead, SEM-EDS X-ray mapping shows that sulfur inclusions of unhydrated gypsum and elemental sulfur are trapped in the C-S-H structure of the cement. Additional unlikely phases that were computed by CHIM-XPT were Fe-celadonite and talc at the same time portlandite was dissolving. Talc is unlikely to precipitate, whereas celadonite is a pre-existing phase before CO_2-exposure.

Another difference between the calculated and experimental minerals in the basalt is that CHIM-XPT determined that the dominant zeolite was stilbite instead of heulundite actually found. The thermodynamic database, SOLTHERM, does not contain data for Na- or K-bearing zeolites, and instead uses albite, paragonite, microcline, and muscovite as proxies for zeolites. Clays such as montmorillonite-based smectites precipitated in the experimental simulations. Therefore, clinochlore (Mg-chlorite), acts as a proxy for these clay minerals identified in XRD after CO_2 injection in the basalt samples. However, Al^{3+} and Mg^{2+} in the real world would precipitate in poorly crystallized clay minerals or amorphous solids.

CHIM-XPT calculates the reaction at different downhole locations during CO_2 sequestration. This study divided the simulations into two categories: 1) basalt formation water-gas reactions to represent the formation away from the wellbore (Fig. 5-8) and 2) basalt-cement paste reactions to water-gas to replicate conditions at the wellbore (Fig. 5-9). The modeling reactions showed that the formerly dissolved CO_2 resides in the basalt primarily as calcite. Depending on the absence or presence of cement, there were key differences in the pH of the Pasco solution after CO_2 was injected. In the basalt-only run (without cement), the final pH was 12.23, whereas the basalt-cement paste in Pasco brine run was still acidic at pH of 4.52. Both experimental and modeling results indicate that basalt has high capacity to convert CO_2 into minerals, but the integrity of the cement paste seal may be compromised.

The first CHIM-XPT run with the basalt reacting with only cement and Pasco brine at high P_{CO2} =102 bars resulted in a range of pH (11.4-4.52) and carbonate mineral assemblages of siderite, siderite-magnesite, siderite-magnesite-calcite, siderite-calcite, and lastly calcite. The basalt-cement paste that reacted with CO_2 resulted in 136 g CO_2 consumed per 1 kg Pasco solution, and an estimated 322 g solid produced with a volume of 128 cm^3. By the end of the CHIM-XPT simulation, the cement paste has undergone significant alteration, with both the basalt and cement paste showing mineral replacement; this resembles what is observed petrographically (Figures 5-1c, 5-3, and 5-4). The greater amount of carbonate is indicative of both the cement and basalt carbonate. In comparison, the CHIM-XPT run modeling basalt-only shows that 50 g of CO_2 gas dissolved in 1 kg of the Pasco solution at 102 bars and 166 g at 306 bars and there were high concentrations of magnesite, calcite, and trace amounts of siderite precipitated. From these results, we infer that in the Columbia River basalts with injected CO_2 gas would locally mineralize in the form of physical trapping.

In the CHIM-XPT simulation of Mt. Simon Sandstone-Illinois Brine under supercritical CO_2, quartz was omitted from the initial calculation to allow amorphous silica to precipitate. These runs were divided into two categories to replicate experiments: 1) A sandstone-brine-P_{CO2} simulation to represent the formation beyond the wellbore (Fig. 5-12); and 2) sandstone-cement paste-brine at high P_{CO2} at the wellbore (Fig. 5-13). The pure sandstone CHIM-XPT run consumed 115.7g CO_2 and produced 186.65 g solid products with a final volume of 70.71 cm^3.

However, the CHIM-XPT calculation sandstone-brine-gas reaction shows that reacted CO_2 formed 37 g magnesite and 526 g of siderite. The precipitation of siderite in the model is entirely dependent on the complete reaction of FeO, magnetite, and goethite in the. XRD analysis did not confirm whether goethite and magnetite occur in real sandstone. In addition, we found no calcite microscopically or by XRD in this system, even though the brine contained a significant amount of calcium (Table 5-2).

By comparison, in the sandstone-cement paste-brine and CO_2 system, CHIM-XPT calculates that when 139 g of CO_2 is added. Calcite is the dominant carbonate with trace amounts of gypsum, magnesite, and siderite; this calculation was confirmed petrographically (Figs. 5-2 and 5-7). Essentially, the presence of cement makes no difference in total CO_2 consumption. In addition, siderite in the experiments may be too minor to detect in sandstone by XRD, although the CHIM-XPT calculations predict its presence. Whether cement is in the system or not, the pH of the Mt. Simon brine is acidic at 4.77 to 5.8 after supercritical CO_2 saturation to intended pressure. Based on experimental analysis and modeling, we conclude that sandstone formations could store dissolved and supercritical CO_2 without rapid degradation of the cement interface.

5.6. Conclusion

The reaction of supercritical CO_2 with Class H portland cement and two different formation rocks was examined at a microstructural level. Sequestration of CO_2 in formation fluids is dependent on brine composition, pressure, and temperature. The experiments of formation rocks immersed in the respective basin brines were as follows: 1) The Columbia River Grande Ronde basalts immersed in Pasco Basin brackish solution (0.013 *M*) and 2) the Mt. Simon Sandstone in Illinois basin brine (1.28 *M*). Experimental samples were subjected to 35°C and P_{CO2}= 10 MPa for 84 days. Both host rocks bonded to cement paste showed some level of carbonate precipitation, primarily calcite or siderite, from the interaction of the cement paste with CO_2. The basalt was more reactive with CO_2 than the sandstone.

Due to the low salinity solution and inferred high CO_2 solubility, the basalt-cement displayed significant alteration depth (~1 mm) at the interface and substantial alteration in the cement paste. Much of the cement paste bonded to the basalt is highly altered which mirrors the response to the decrease in pH of the Pasco solution. Dissolution of magnetite, olivine and the glassy groundmass of the basalt provided aqueous Fe^{2+}, K^+, Mg^{2+} to precipitate ferron magnesite, magnesite, and calcite. The sandstone-cement sample on the other hand, had a relatively thin, well-crystallized calcite band inhibited acid attack in the sandstone-cement sample and there was little alteration of the cement paste compared to the cement bonded to basalt. The pH of the Illinois basin brine with the Mt. Simon sandstone varied little from the original solution and limited the permeability of CO_2 into the cement.

Geochemical modeling conducted with CHIM-XPT was used to determine pH and potential mineral phases at sequestration conditions. There was an estimated consumption of 50 g of $CO_{2\ (g)}$ at 102 bars and 161 g at 306 bars in 1 kg of Pasco solution. The addition of cement paste and basalt immersed in Pasco solution displayed a fluctuating pH over the course calculation, starting with a pH of 11.82 ending at 6.97. The basalt-cement run resulted in 136 g $CO_{2\ (g)}$ consumed in 1 kg of Pasco solution at 102 bars and precipitated of calcite, magnesite, and siderite. In contrast, the pH of the Illinois Basin brine after CO_2 injection was calculated to never exceed a pH of 5.8. An estimated 139 g of CO_2 was consumed indicating the system can dissolve some CO_2 and not degrade the cement.

Based on a comparison of the experimental analysis and modeling of host rock, we conclude that basalt has a high capacity to convert CO_2 into carbonate minerals; however, there may be risk to the integrity of the hydrated cement seal or bonding surface. The Mt. Simon sandstone formation has high capacity to store aqueous and supercritical CO_2 with a lower risk of alteration to hardened cement paste.

The next chapter, Chapter VI discusses the structural integrity of cement which is driven by changes in cement composition and hydration. The cement paste strength is controlled by factors of the brine composition under supercritical CO_2 higher pressure and temperature conditions.

CHAPTER VI

GEOMECHANICAL STRENGTH TESTS FOR PORTLAND CEMENT FOR SEQUESTRATION PURPOSES

Chapter VI will be submitted as an internal Technical Progress Report (TPR) for the Department of Energy, National Energy Technological Laboratory. Co-authored material is included. Authors are Circe Verba, Mark Reed, Jason Ideker, and Barbara Kutchko. This paper is written by myself, with editorial assistance from my coauthors. John Logan assisted in the experimental set-up.

6.1. Introduction:

In Chapter II, cement types and cement hydration are discussed. In this study, oil-well cements were subjected to high pressures and temperatures under carbon sequestration conditions. Class H portland cement as defined by the American Petroleum Institute (API) standards has high sulfate resistance and is intended for use at 2.5 km without admixtures (API, 1997). This type of cement hydrates well under the high pressures and high temperatures characteristic of deep rock formation sequestration conditions.

We examine the pore pressure, physical properties, and stress of wellbore cement under simulated CO_2 sequestration conditions. Rock and cement properties such as density, permeability, porosity, and thickness contribute to geomechanical constraints in sequestration conditions. The experimental conditions are based on NETL Phase II injection sites which typically occur at depths from 2.29 to 3.35 km, pressures from 24.1 MPa to 32 MPa, and temperatures from 69 ^{o}C to 125^{o}C. The effect of carbonate expansion and secondary minerals, especially ettringite formation at simulated wellbore conditions, is highly debated in the current literature. This study identifies changes in cement integrity under continuous exposure to CO_2-rich fluid by measuring cement physical strength.

6.1.1. Cement Chemical Constituents & Hydration Response

A combination of calcium (e.g. limestone or seashells) and silica (e.g. clays or shale) produces raw cement when heated in a kiln to calcining, clinkering temperature (~1450°C). The major components of portland cement are tricalcium silicate (Ca_3SiO_5), dicalcium silicate (Ca_2SiO_3), tricalcium aluminate ($Ca_3Al_2O_6$), and calcium aluminoferrite (Ca_4AlFeO_5). Gypsum ($CaSO_4 \cdot 2H_2O$) is added and integrated with the clinker to prevent instantaneous flash set. Sulfate-resistant cements intended for sequestration are typically low in the aluminate phases (i.e. $Ca_3Al_2O_6$ and Ca_4AlFeO_5).

Hydration products form when the calcium silicates of portland cement are mixed with water. Depending on the pressure and temperature, these products form at different rates (Hewlet, 1998). Hydration temperature is a particularly important factor in the stability and morphology of the mineral products. The hydration of Ca_3SiO_5 is responsible for the initial set and early strength development, while the hydration of Ca_2SiO_3 is crucial to the cement's final strength. The hydration of both calcium silicates is an exothermic process and requires approximately the same amount of water (Taylor, 1997; Nelson, 1990). Increasing the temperature ($T > 23°C$) increases the initial rate of hydration, thereby affecting the microstructure and ultimately reduces the overall long-term strength of the cement paste.

The typical hydration products of ordinary portland cement form a network of a semi-amorphous gel, calcium-silicate-hydrate (Ca_xSi_x*xH_2O, abbreviated cement nomenclature as C-S-H) and portlandite, or calcium hydroxide ($Ca(OH)_2$) around the calcium silicates (reactions 1 and 2). The hydration reactions from Nelson (1990) in oxide notation are as follows:

$$2Ca_3SiO_5 + 6H \rightarrow Ca_3Si_2 \cdot 3H_2O + 3Ca(OH)_2 \quad (1)$$
$$2Ca_2SiO_3 + 4H \rightarrow Ca_3Si_2 \cdot 3H_2O + Ca(OH)_2 \quad (2)$$

The hydration pressure and temperature, play an important role in chemical behavior (Nelson, 1990). The crystalline morphology of cement paste is one factor with greatest impact on chemical behavior. As temperatures increase to >40^{o}C, C-S-H becomes more fibrous and crystalline, and is ultimately unstable above 110^{o}C (Le Saout et al., 2004; Nelson, 1990). The dendritic, crystalline network of C-S-H impacts the initial rate of hydration and can impede the formation of other hydration products, such as $Ca(OH)_2$, and the final strength of the cement.

Although pressure alone does not greatly affect cement formation, it is an important contributor in combination with increasing temperatures during the curing process and as the cement paste sets (Bresson et al., 2002). The early stages of hydration of the Ca_3SiO_5 influence final cement porosity during curing which contributes to the structure of C-S-H (i.e. Bresson and Zanni, 1998; Bentur et al., 1979). Depending on the starting water to cement (w/c) ratio, increased temperatures expedite cement hydration by enhancing the nucleation of hydration products resulting in early setting (Zhang et al., 2010). Bresson et al., (2002) found that Ca_2SiO_3 dissolution increased under pressure led to rapid C-S-H and $Ca(OH)_2$ precipitation. In addition, the transition of non-crystalline to crystalline phases may be impacted. For example, Bresson and Zanni (1998) found that hydrogrossular $CaO_3Al_2O_3(SiO_2)_{3-x}(H_2O)_{2(0-3)}$ replaced ettringite in a sample cured at high temperature (~80^{o}C) and high pressure (1,015 psi). At temperatures above 160^{o}C or pressures above 5,000 psi, the C-S-H structure begins to polymerize into a crystalline structure similar to that found in hillebrandite ($Ca_2Si_3[OH]_2$), jaffeite ($Ca_6[Si_2O_7][OH]_6$), or tobermorite-like ($Ca_5Si_6O_{16}[OH]_2{\cdot}4H_2O$ or $Ca_5Si_6[O,OH]_{18}{\cdot}5H_2O$) (Bresson et al., 2002; Bresson and Zanni, 1998). Therefore, in addition to increased temperature, pressure is a factor in cement hydration. The formation of cement will likely have higher degradation rates at higher pressures and temperatures. Conditions downhole, including temperature and pressure, may impact cement hydration before the influence of environmental geochemical factors. Future studies must address these factors in determining the strength and structure of the cement.

6.1.2. CO_2 Sequestration & Challenges

Large quantities of carbon dioxide, a greenhouse gas, are emitted during coal-base energy production. Technologies are being developed to mitigate the accumulation of CO_2 in the atmosphere. Due to their high storage capacity, brine-bearing formations have the greatest potential for long-term (>1,000 years) geologic sequestration of CO_2. (e.g. Bergman & Winter, 1995; Bruant et al., 2002; DOE, 2007). An ideal deep saline candidate consists of a brine solution (>50,000 TDS) topped by an impermeable top caprock, typically shale, that would prevent leakage or contamination into freshwater aquifers. Existing wellbores from oil, natural gas reservoirs, and exploration wells can be converted to provide a suitable saline formation for CO_2 storage (Fig 6-1).

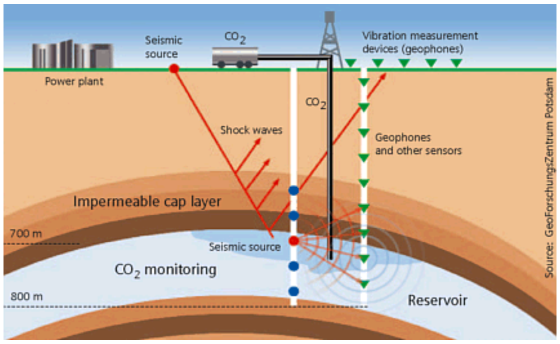

Source: GeoForschungsZentrum Potsdam

Figure 6-1. Geologic sequestration from CO_2 production to CO_2 injection into a reservoir with a caprock (DOE, 2007).

Portland cement is metastable in a supercritical CO_2 environment. The integrity of the wellbore seal is a concern because CO_2 could leak back into the atmosphere, for instances, leakage could occur between the cement and the steel casing or formation rock (Duiguid & Scherer, 2009; Rimmelé et al., 2008). In brief, CO_2 could dissolve into a saline aquifer as a consequence of supercritical CO_2 reacting with Ca-rich alkaline compounds. This generates carbonic acid (H_2CO_3) that could degrade the cement paste. Previous studies have found that the effects of pure supercritical CO_2 and CO_2-saturated brine on wellbore seals at simulated downhole conditions result in cement alteration and calcium carbonate precipitation (e.g. Duiguid et al., 2005; Barlet-Gouédard et al., 2006; Kutchko et al., 2007, 2008, 2009). In addition, Kutchko et al. (2008) conducted an immersion study where Class H cement was exposed to CO_2 for nine days, resulting in a 220 µm alteration thickness around the cement cylinder. Monte Carlo and Elovich diffusion modeling showed that the 220 micron depth extrapolates to ~1 mm after 20 years of exposure to CO_2.

In CO_2-enhanced oil recovery (EOR) injection sites, both the durability of cement paste and the importance of wellbore depth have been examined (Carey et al., 2007; Crow et al., 2009; Scherer et al., 2011). Analysis of cement cores from EOR operations in the SACROC unit in Texas yielded results comparable to those obtained in the laboratory (Carey et al., 2007). Crow et al. (2009) studied that cement cores from a natural CO_2 reservoir in Colorado and Bachu and Watson (2009) studied 79 wells in Alberta, Canada where CO_2 was used for EOR operations and acid gas (H_2S and CO_2 mixture). In all cases, converted wells failed at higher rates than wells specifically used for injection. Scherer et al. (2011) found significant differences in the altered states of the cement samples, which they attributed to changes in salinity and host rock at different depths. However, neither these static experiments nor any of the laboratory studies have examined the effects of CO_2 on the strength of the cement paste itself. This study examines the effect of [co]-sequestered gases on cement paste strength.

6.1.3. Formation of $CaCO_3$

Calcium hydroxide is one of the primary calcium hydration products found within the cement and is stable at pH of 12-13, the C-S-H is stable at a pH of ~10-11, and any unhydrated ferrite are stable in a pH range of 4-7 (Lecolier et al., 2006). Pressurized CO_2 produces carbonic acid yielding a pH of ~2-4 in the pore solution and so the carbonic acid reacts with the cement and leaches calcium from $Ca(OH)_2$ and C-S-H (e.g. Kutchko et al., 2007). Diffusion of Ca^{2+} forms a calcium carbonate zone and leaves behind a porous, amorphous silica gel zone (as outlined by Kutchko et al., 2007 and demonstrated in Fig. 6-2).

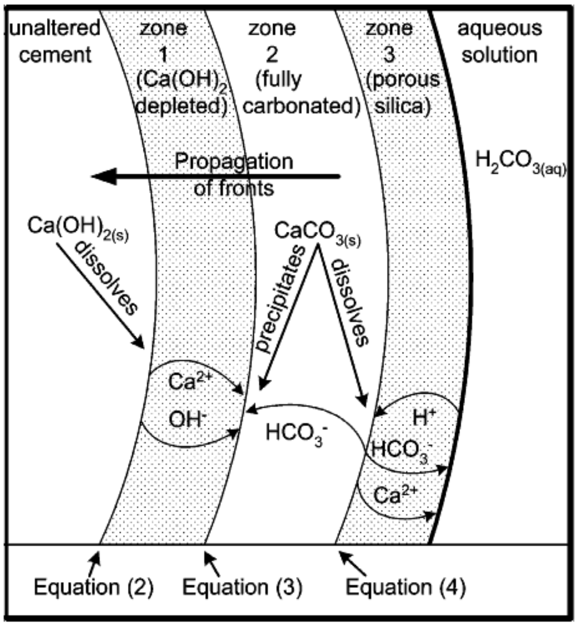

Figure 6-2. Schematic displaying calcium migration and dissolution in the formation of alteration fronts (from Kutchko et al., 2007).

$CaCO_3$ initially increases the cement's compressive strength and reduces its permeability. However, microfractures may form in the carbonated zone due to volume expansion (Johannesson et al., 2001). It is not certain if expansion will occur under the confined stress conditions found within the wellbore as it does in atmospheric conditions. However the continuous contact of the cement with acidic fluid will eventually cause $CaCO_3$ to dissolve and lead to cement degradation. The $CaCO_3$ becomes unstable at lower pH levels and bicarbonate (HCO_3^-) begins to dominate the system (Thaulow et al., 2001). As the $CaCO_3$ becomes increasingly unstable, carbonated fluid begins to diffuse inwardly and Ca^{2+} ions diffuse outward into solution. When the amorphous silica gel forms, the cement volume decreases, which in turn increases cement permeability (Shen, 1989). The diffusion either stabilizes in a static system or the cement continues to degrade with continued injection of CO_2.

6.1.4. Mineral Precipitation & Expansion

Another concern is the expansion of the cement due to secondary mineral precipitation and potential degradation after the cement paste has hardened. The formation of $CaCO_3$ and the secondary [delayed] ettringite formation (DEF) may result in cement degradation. The extent to which secondary ettringite is responsible for cement degradation is still under debate. Assessment of cement wellbore seal integrity depends on several factors including the expected downhole conditions and gases captured with sequestration. A strength study examining a pure-CO_2, CO_2-O_2-mixture, and CO_2-O_2-H_2SO_4 after exposure to supercritical CO_2 environments was undertaken.

6.1.4.1. Carbonation of Cement

As discussed by Verba et al. (2012a), the primary interaction between cement and the supercritical CO_2 environment generates carbonation of the portland cement paste. The total carbonation thickness of all CO_2-influenced samples was 200-800 µm. In a pure supercritical CO_2 environment, the total average alteration extends concentric to cylinder surface to a depth of 1.25 mm (1 *M*) and 0.836 mm (2.17 *M*) after exposure to gas. In comparison, the cement paste exposed to CO_2-O_2 had average alteration depths of 1.6 mm at 85°C and 0.7 mm at 50°C for 1 *M*, whereas the 2.17 *M* solution alteration depths averaged 1.69 mm (Verba et al., 2012a).

The impact of carbonation on cement strength with continuous gas injection is unknown. The alteration of specific cement samples may impact the integrity of only the cement exterior rather than the cement paste sample as a whole. The formation of carbonate increases the cement surface density which reduces surface porosity and may reduce chloride ion permeability. As carbonated water diffuses into the cement matrix, $CaCO_3$ forms. The compressive strength initially increases and cement permeability decreases as a result of volume expansion of the $CaCO_3$ (Shen, 1989). Calcite has a higher molar volume (36.9 cm^3/mol) than that of $Ca(OH)_2$ (33.1 cm^3/mol) (Glasser et al., 2008). The volumetric expansion of calcite may cause microfractures that could provide a pathway for further interaction with the carbonic acid. The carbonation processes itself may not negatively affect the cement as suggested by Glasser et al. (2008), however cement stress is not well documented in the literature. A study by Chi et al.

(2002) demonstrated that the carbonation of concrete may increase mechanical strength as measured in compressive strength determined by ASTM C39 testing.

6.1.4.2. Delayed Ettringite

Portland Class H cement is limited in aluminate phases thus limiting precipitation of ettringite, a hydration product common in ordinary cements. However, secondary ettringite formation occurs in co-sequestration settings under oxidizing conditions. Although these ettringite-type reactions are limited initially to hydration in this cement type, the reactions that do occur are important in secondary mineral precipitation. In typical OPC, ettringite forms when calcium and sulfate ions from gypsum react with the aluminate and hydroxyl ions from the $Ca_3Al_2O_6$ and form a calcium trisulfoaluminate hydrate [$Ca_6Al_2(SO_4)_3(OH)_{12}\cdot 26H_2O$]. Ettringite formation in plastic-state hydrating cement paste does not cause physical degradation (Taylor et al., 2001).

Through expansion and fracturing, secondary ettringite formation may weaken the hardened cement paste. Secondary ettringite could be the result of internal sulfate attack, which can occur during the hydration of the cement paste when cured at temperatures above 70^{o}C (Hewlett, 1998). Another study found that ettringite is stable only up to 100^{o}C (Glasser, 1996). Expansion of secondary sulfate phases may increase confined crystallization pressure in the cement paste pores (Glasser, 1996; Flatt & Scherer, 2008). Studies from Johansen et al. (1993) and Taylor (2001) suggest that as expansion occurs, opportunistic ettringite and $Ca(OH)_2$ precipitate in the void. Recrystallization around anhydrous cement grains can then cause fractures.

One theory postulates that an ettringite precursor may exist in some amorphous form (Glasser, 1996; Mehta, 1992). Fu et al. (1993) found that sulfate ions are slow to release from the C-S-H phase in high temperature steam-cured concretes. Colleparadi (2003) also suggested that sulfate released late from C-S-H was related to internal sulfate attack. When exposed to pure

CO_2, sulfate appears to be contained within the C-S-H phase and no ettringite or other sulfate minerals formed (Verba et al., 2012ab).

In addition to temperature, the pore solution's pH plays an important role in ettringite formation. Stark and Bollard (1999) compared data published on the stability of ettringite and concluded that ettringite is found where the local pH ranges from 9 to 13.4. The addition of supercritical CO_2 will decrease the pH in cement pores and provides semi-favorable conditions for the formation of secondary ettringite crystals. Verba et al. (2012a) identified secondary ettringite in cement paste after exposure to CO_2-O_2 conditions at environmental temperatures of 50^oC and 85^oC. The ettringite is not present in the carbonated zone, due to increased pH, but ettringite is present in unaltered cement paste. Within the pore solution, dissolved CO_2 also lowers pH, which leaches sulfate from bound C-S-H. Typically, ettringite does not precipitate because Class H cement has little or no calcium-aluminate content and Al^{3+} is fairly immobile in Ca_4AlFeO_5.

Secondary ettringite precipitates within the cement paste due to oxidation of the calcium-aluminoferrite and the ingress of deleterious species (acid and chlorides). In the CO_2-O_2 exposed cement paste samples, X-ray Diffraction (XRD) showed an increase (~13 wt% of total cement alteration) of ettringite after exposure to supercritical sequestration gases (Verba et al., 2012a). Scanning electron microscopy showed pores filled with ettringite with microfractures ranging in width from 0.5-3 µm propagating toward the least resistant pathway around the mineral grains (Fig. 6-3). These fractures are not interpreted as an artifact of sample preparation due to the small fracture sizes because fractures induced during sample preparation often cut across mineral grains and stem into larger fractures. The presence of these fractures indicates that the integrity of the cement paste may be compromised if acidic fluid continues to degrade the surrounding cement.

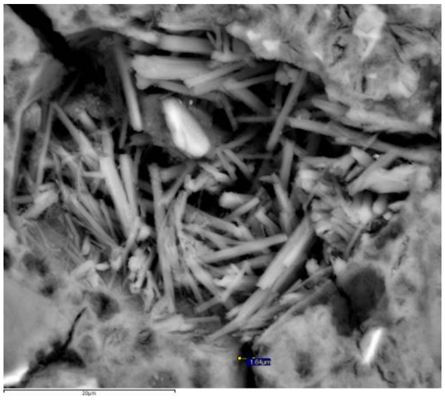

Figure 6-3. Close up of cement paste pore space filled with secondary ettringite needles extending into fractures.

Ettringite formation is therefore proposed to precipitate primarily from the unhydrated calcium-aluminoferrite grains, the only source of Al^{3+} present in the cement paste. Examination of the Fe-replacement in alumino-ferrite grains with the addition of O_2 may influence the Fe^{2+} present. Meller et al. (2004) suggested 10% impurities in calcium-aluminoferrite (brownmillerite is the "mineral equivalent") with a variable Al/Fe ratio. As the cement interacts with the supercritical CO_2, iron (II) oxidizes with the anhydrous cement grains enabling the precipitation of secondary ettringite. The reactions below demonstrate a potential, simplified process for combining sequestration conditions with secondary ettringite. As the substituted calcium-aluminoferrite oxidizes and forms iron hydroxide, it releases aqueous aluminum (reaction 3). Concurrently, CO_2 reactions bring about the dissolution of portlandite and decalcification of C-S-H; aqueous calcium is present in the pores, providing a calcium source within the cement pores (equations 4-6) (Verba et al., 2012ab). The diffusion of calcium and hydroxide ions from CO_2 reactions are available to react with sulfate from gypsum and secondary ettringite precipitates (reaction 7).

$$Ca_2Fe^{2}{+}Al^{4+}O_5 + O_2^{+}\ 11H^{+} \rightarrow Fe(OH)_3 + Al^{3+}{}_{(aq)} + Ca^{2+}{}_{(aq)} + 4H_2O \qquad (3)$$
$$CO_2 + H_2O \rightarrow H_2CO_3 \rightarrow 2H^{+} + HCO_3^{-} \qquad (4)$$
$$CO_3^{2-} + H_2O \rightarrow HCO_3^{-} + OH^{-} \qquad (5)$$
$$Ca(OH)_2 + H^{+} \rightarrow Ca^{2+} + 2OH^{-} \qquad (6)$$
$$6Ca^{2+} + 2Al^{3+} + 12OH^{-} + 3SO_4^{2-} + 26H_2O \rightarrow Ca_6Al_2(OH)_{12}(SO_4)_3{*}26H_2O \qquad (7)$$

6.2. Materials & Methods

6.2.1. Cement and CO_2 Conditions

This study used cement pastes composed of portland Class H well cement manufactured by Lafarge. A Bogue calculation from oxide content was used to extrapolate the composition of the initial powder analysis of the cement (in weight percent). The majority of the cement is $Ca_3SiO_{5,}$ with no trace of $Ca_3Al_2O_6$. The composition was 64.5% tricalcium silicate (Ca_3SiO_5), 11.77% dicalcium silicate (Ca_2SiO_3), 13.24% calcium aluminoferrite ($4CaO\cdot Al_2O_3\cdot Fe_2O_3$), 0% tricalcium aluminate ($Ca_3Al_2O_6$), 2.94% MgO, 2.8% SO_4^{2-}, 0.16% total alkali content (Na_2O), 0.62% free lime, and had a loss on ignition (LOI) of 0.73. The samples had a w/c ratio of 0.38 based on practices recommended by the American Petroleum Institute (API) (API, 1997).

The brine used in to cure and submerge the cements under P_{CO2} was a 1 *M* mixed brine. The brine consisted of 0.16 mole/l $CaCl_2$, 0.02 mole/l $MgCl_2$, and 0.82 mole/l NaCl.

We cast the cement slurry into 25 mm x 152 mm PVC-pipe forms and cured the samples for 28 days at 50^{o}C or 85^{o}C, respectively, and 28.9 MPa in brine-filled autoclaves. Immediately after curing, the cement samples were placed vertically into 1.2 L stainless steel (316 CrNiMo) static autoclave vessels filled with 600 ml of brine. CO_2 was used to displace air and purge the autoclaves; the autoclaves were then brought up to temperature and injected with gaseous CO_2 (or mixed gas) to final conditions of 50^{o}C or 85^{o}C and 28.9 MPa. After the desired exposure period, samples designated for strength tests were removed and cut with ethanol as cutting fluid, into 25 cm slices and stored in vacuum-sealed mylar bags.

6.2.2. Sulfuric Acid Conditions

To imitate exposure to sulfur-dioxide dissolved in brine, a gas composition of 94.5% CO_2, 4% O_2, and 1.5% SO_2 was used to simulate a proxy. The geochemical model CHIM-XPT (not discussed in depth here) calculated that the addition of SO_2 to the CO_2-O_2 stream disproportionates to sulfuric acid, along with the formation of carbonic acid, and an excess of supercritical CO_2 and O_2. We used 7% H_2SO_4 brine solution as a proxy to represent hydrated cement samples in mixed gas conditions. Cement cylinders were cured at 50°C and 85°C at 28.9 MPa for 28 days and then exposed to CO_2-O_2 conditions for 28 days. The cement samples were subsequently submerged for 7 days at room temperature and pressure in sulfuric acid until evidence of spalling occurred.

6.2.3. Strength Applications

Both tensile and compressive tests would indicate whether carbonation and delayed ettringite formation are detrimental or beneficial to cement well integrity. The formation of ettringite after curing provides valuable insight into the potential effects of [co]-sequestering gases such as O_2 or SO_2 with CO_2. Quantifying the change in compressive strength could provide analytical data for any strength loss due to secondary mineral precipitation or acid attack.

ASTM Standard C496 has a standard test method for splitting tensile strength of concrete specimens such as molded cylinders. Unfortunately, no cement paste standards are available for measuring tensile strength as a point load and the standards for measuring compressive strengths vary (cubic, prism, or cylindrical). As there is no set point load tensile test standard, we utilized a point load test that hydraulically compresses the cement sample between two steel spheres until failure occurs. A pressure gauge (gauge load) measures the applied load and calculates the apparent strength using the cylinder samples' thickness and diameter. The equivalent uniaxial tensile strength was determined by applying Nigel's correction.

Compressive strength was determined by applying an axially directed force to the point of deformation, and failure occurred at the limit of compressive strength when the cement was crushed. Cement strength was calculated by dividing the maximum load at failure by the load dispersed over the cross-sectional area. Strength tests from the American Standard for Testing and Materials (ASTM) were used for quality control. To determine acceptable concrete and cement in-place strength, several testing parameters must be considered. ASTM C 349:

Compressive Strength of Hydraulic Cement Mortars (Using Portions of Prisms Broken in Flexure) and ASTM C 873-94: the Standard Test Method for Compressive Strength of Concrete Cylinders Cast In Place in Cylindrical Molds. Kim et al. (1998) used the latter method found that 28 day-old cylindrical OPC cement at 40^{o}C with a w/c=0.35 and cured for 7 days had a compressive strength of 51.7 MPa. The compressive strengths determined in this study were comparable to those obtained using the methodology of Kim et al. (1998), and ASTM C 873-94 and ASTM C150, respectively.

The cement cylinders were encased in heat-treated polyolefin shrink jacket to simulate semi-confined settings. The primary method to measure the physical change in the cylinders was to test 1) compressive strength of cement paste cylinders roughly 2.54 x 2.54 mm in size (1:1 size ratio), and 2) tensile strength on 1.27 x 2.54 mm (1:2 size ratio) cement prior and post-exposure to sequestration conditions. Several sample types were examined: 1) A marble sample for relative loads, 2) hydrated cement, and 3) hydrated cement exposed to different gas types to replicate [co]-sequestration conditions. The uniaxial compressive strength can be measured by calculating the load and stress at cement cylinder failure in an unconfined within the hydraulic press.

6.3. Results and Discussion

The precipitation of secondary minerals (carbonates, ettringite, or gypsum) may cause the cement to expand slightly during gas exposure (Glasser, 1996; Hewlett, 1998). These results provide initial strength comparisons to quantify any direct damage of secondary mineral precipitation after the subject tests. However, the number of samples must be increased to establish experimental validity and determine if these tensile strength differences are significant.

6.3.1. Alteration from Sulfuric Acid

To study cement strength near a conventional sour gas stream (SO_2) or acid-waste stream in sequestration settings, this study exposed cement pastes to CO_2-O_2 and sulfuric acid. Figure 6-4A shows the cement sample following exposure to sulfuric acid under atmospheric conditions with different stages of hydrating sulfates (gypsum, bassanite, and anhydrite) precipitated as confirmed by wet XRD analysis. The combination of curing the cement in higher temperature (85^{o}C) and sulfuric acid resulted in spalled material. Cement spalling is likely due to hydration at a higher temperature, which resulted in a more crystalline C-S-H, such as tobermorite. The loss of cement occurred in the calcium-depleted zone where $Ca(OH)_2$ was replaced by calcite. The sulfuric acid attack on the cement resulted in non-cohesive gypsum in the bottom of the glass beaker. In addition, the unaltered cement cured at the higher temperature (85^{o}C) lost 2 mm (4 mm diameter) on the sides of the cylinders. Conversely, the sample exposed to lower temperature (50^{o}C) had pure crystalline gypsum precipitate where the cylinder increased ~4 mm in diameter and 5.5 mm in width (Fig. 6-4B). Furthermore, depending on the hydration temperature, this gas mixture may degrade the cement structure to the point it is completely unstable for sequestration purposes, as simulated with 7% H_2SO_4 at atmospheric conditions. The newly precipitated minerals impact the structural integrity of the cement as determined by the compressive and tensile tests.

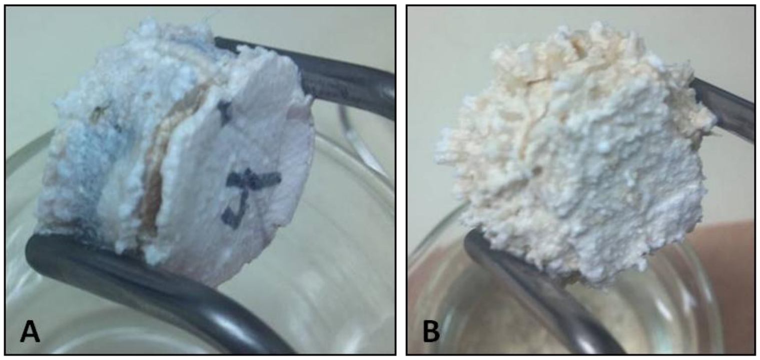

Figure 6-4. Alteration of hydrated portland cement exposed to CO_2-O_2 under sequestration conditions and then atmospheric conditions with 7% sulfuric acid for 7 days. A) Degradation of cement paste core cured with minor gypsum precipitation at 85^{o}C and B) Crystalline precipitation of gypsum on portland cement exposed to CO_2-O_2 at cured 50^{o}C.

6.3.2. Tensile Point Load Tests

Point load tests (Table 6-1) were performed on the following samples: 1) portland cement cured for 28 days in 1 *M* (Ca-Mg-Na-Cl) brine, but not exposed to any gases; 2) cured cement samples exposed to CO_2; 3) cured cement samples exposed to CO_2-O_2; and 4) cured cement samples exposed to CO_2-O_2 and sulfuric acid leach. A marble sample is representative of natural cemented limestone that has undergone higher pressure and temperature conditions was tested to compare its tensile strength of that of the hydrated cement; the tensile strength of the marble sample was 5.67 MPa.

Table 6-1. Point load test data to determine tensile strength of 1) marble, cement paste cured in 1 M NaCl, $CaCl_2$, and $MgCl_2$, brine (no exposure to gas), 2) CO_2, 3) CO_2-O_2 exposed cement, and then 4) submerged in H_2SO_4.

Sample ID	Core Diameter (in)	Thickness (in)	Load (lbs) on Failure	K-Geometry factor	Tensile Strength (psi)	Nigels Correction	Average Tensile (psi)	(Mpa)
Marble	0.98	0.58	503.75	1.18	1038.62	823.15	**652.83**	**5.67**
Brine (surrogate) cured cement pre-exposure								
1	1.03	0.47	310.00	1.53	977.10	774.39	**751.84**	**5.18±.55**
2	1.04	0.48	271.25	1.51	823.03	652.28		
3	1.04	0.43	271.25	1.69	1031.06	817.15		
4	1.02	0.46	279.00	1.56	938.00	743.40		
5	1.04	0.50	348.75	1.47	995.22	788.75		
6	1.03	0.44	294.50	1.62	1041.58	825.50		
7	0.98	0.47	319.30	1.47	1032.12	817.99		
8	1.03	0.43	193.75	1.67	728.43	577.31		
9	1.05	0.46	286.75	1.60	955.79	757.50		
10	1.02	0.52	372.00	1.38	964.19	764.16		
Brine (surrogate) cured cement CO_2 exposure								
1B	1.03	0.37	124.00	1.93	1008.308	799.12	**840.09**	**5.79±0.93**
[1]2B	1.04	0.28	775.00	2.63	7122.48	5644.85		
3B	1.06	0.31	135.63	2.40	999.04	791.78		
4B	1.04	0.32	124.00	2.25	832.84	660.06		
5B	1.02	0.50	449.50	1.42	1246.79	988.13		
6B	1.03	0.48	399.13	1.50	1213.02	961.36		
Brine cured, CO_2-O_2 gas exposed								
1A	1.02	0.52	271.25	1.38	707.33	560.59	**621.34**	**4.14±.57**
2A	1.02	0.54	251.88	1.32	599.91	475.45		
3A	1.01	0.42	201.50	1.68	797.81	632.29		
4A	1.02	0.47	271.25	1.51	850.69	674.21		
5A	1.01	0.44	228.63	1.62	829.01	657.03		
Brine cured cement, CO_2-O_2 H_2SO_4 exposure								
sample 1 (50°C)	1.06	0.50	342.55	1.49	971.34	769.82	**620.418**	**4.99±0.45**
sample 2 (50°C)	1.16	0.67	550.25	1.21	854.82	677.48		
sample 3 (85°C)	1.21	0.70	503.75	1.21	710.82	563.35	**593.677**	**3.38±0.71**
sample 4 (85°C)	1.01	0.50	191.43	1.41	526.82	417.53		

[1] Excluded from data (sample did not fail)

The average brine-cured tensile strength was 5.18 MPa, and the CO_2 exposed samples had an average tensile strength of 5.79 MPa. The average tensile strength for samples exposed to CO_2-O_2 cured at 50°C was 4.14 MPa. The sulfuric acid leached samples averaged a tensile strength 4.99 MPa at 50°C and 3.38 MPa cured at 85°C. The cement exposed to CO_2 had a slightly higher tensile strength than the unexposed (brine cured) samples by an average of 11.7%. The deviation in strength falls within the range of cured cement strength indicates that carbonation may or may not effect cement paste strength. Regardless, samples exposed to mixed gas were weaker than both the unexposed and CO_2-exposed cement as Figure 6-5 displays.

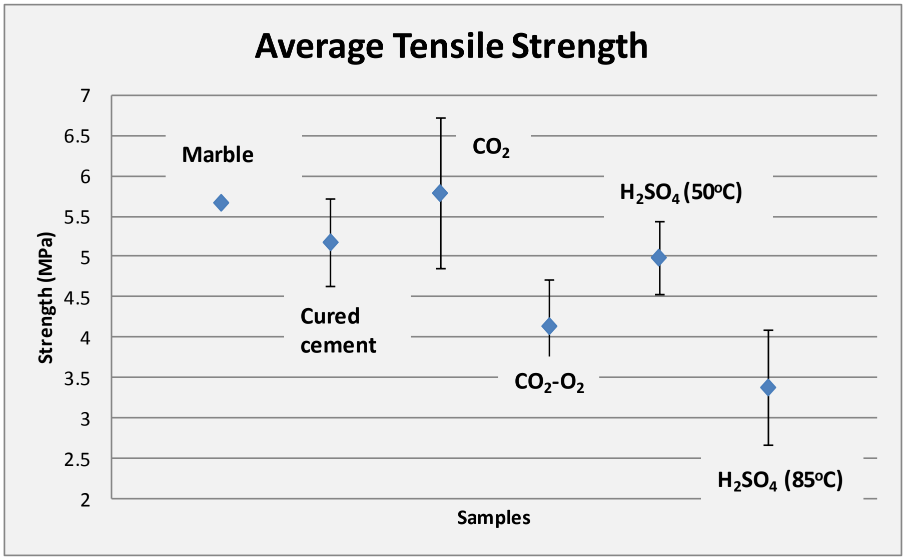

Figure 6-5. Average tensile strength for cured portland cement samples exposed to CO_2; cured cement samples exposed to CO_2-O_2; CO_2-O_2 and sulfuric acid leach, and a marble sample used for high pressure and natural temperature.

These test results indicate that CO_2-O_2 may decrease the tensile strength of cement. The cement paste strength decreased 1 MPa (20% loss) at 50°C, which could be due to secondary ettringite precipitation combined with cement carbonation.

Alternatively, the cement submerged in sulfuric acid displayed a ~2 MPa (34.7%) strength loss in the higher 85°C temperature cylinder. Combined with the influence of hydration temperature and secondary mineral precipitation, the cement paste exposed to sulfuric acid had the lowest tensile strength. At 50^{o}C, the cement paste sample had a 3.7% loss compared to the hydrated cement paste. The addition of sulfur to the system after the exposure to CO_2-O_2 gas appears to have increased the strength at lower temperatures. This increase in strength may be due to the expansion and infilling of gypsum, which slightly improved the tensile strength of the cement cylinder. However, based on this study, it is unclear if longer exposure, beyond 7 days, to sulfuric acid would decrease the final strength at the lower temperature.

6.3.3. Compression Tests

Compressive strength values for 28-day cured cement paste, CO_2-O_2- exposed, and CO_2-O_2- gas and sulfuric acid leach are presented Table 6-2 and Fig. 6-6.

Table 6-2. Compressive tests on hydrated portland cement cured in a 1 M NaCl, $CaCl_2$*, and* $MgCl_2$*, brine, then cement samples exposed to* CO_2-O_2 *at 50*^{o}*C and 85*^{o}*C, and then samples submerged in sulfuric acid at 50*^{o}*C and 85*^{o}*C.*

Sample	Compressive strength[1] (psi)	Compressive Strength (MPa)
hydrated cement 1	4720	32.54
hydrated cement 2	4872	33.59
hydrated cement 3	4817	33.21
hydrated cement 4	5420	37.37
CO_2-O_2 1 (50^{o}C)	4033	27.81
CO_2-O_2 2 (50^{o}C)	4226	29.14
CO_2-O_2 3 (85^{o}C)	3206	22.11
CO_2-O_2 4 (85^{o}C)	3676	25.34
H_2SO4 (50^{o}C)	3704	25.54
H_2SO4 (85^{o}C)	2946	20.31

[1] factored to cross sectional area

Samples exposed to pure CO_2 were not analyzed for compressive strength because there were too few samples to determine statistical significance. This study shows a clear reduction in the cement paste's compressive strength when subjected to high P_{CO2} gas co-sequestered gases compared to that of unaltered hydrated cement.

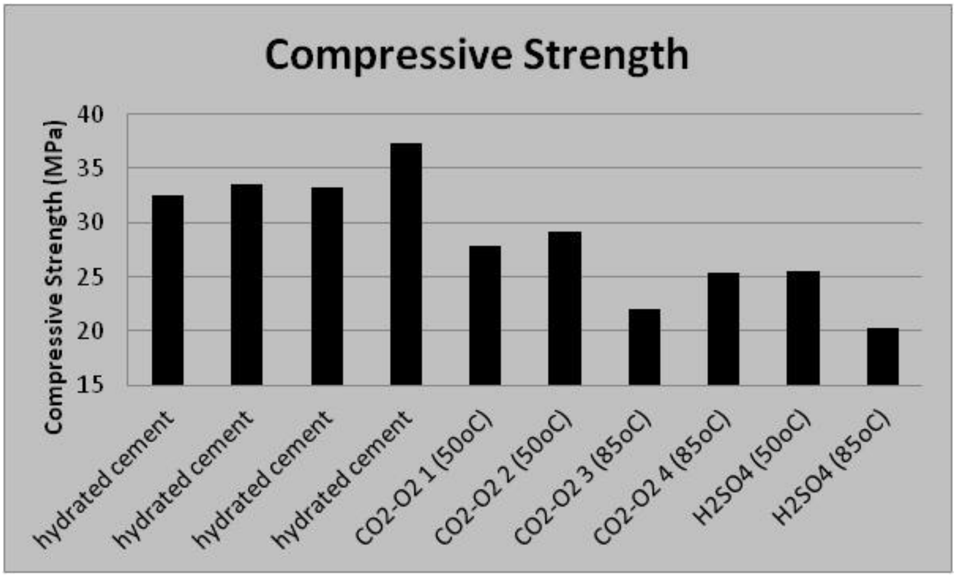

Figure 6-6. Compressive strength of cement samples comparing cured cement at 50°C, co-sequestered simulated, CO_2-O_2 mixed gas for 56 days at both 50°C and 85°C, and sulfuric acid submerged cement cured at both 50°C and 85°C.

The hydrated cement samples cured in brine for 28 days had an average compressive strength of 34.18 MPa. In addition, petrography analysis showed that much of the paste remained unhydrated. Next, this study compares the cured hydrated cement samples to the cement paste samples after gas exposure. In this study, the values for the hydrated cement paste were not as high (51.7 MPa at 40°C w/c=0.35 for 7 days and aged 28 days) as those found by Kim et al. (1998), however the measurements do indicate moderate strength after curing.

It is difficult to determine if the addition of CO_2 causes a real increase in compressive strength, however initial results indicate all cement samples do deviate from the values of the cured cement paste. Cement paste samples exposed to only CO_2-O_2 mixed gas for 56 days at 50°C had an average compressive strength of 28.5 MPa at 50°C and 23.73 MPa at 85°C. After submersion in sulfuric acid, the cement showed reduced strength of 25.5 MPa at 50°C and 20.3 MPa at 85°C.

One significant observation was that of the influence of temperature on compressive strength. All cement samples cured at 85°C showed a clear reduction in compressive strength when immersed in acidic fluids. Under high pressure and temperature, the C-S-H became more crystalline which decreases the cement strength while under acidic conditions. At higher temperature, the rate of hydration increased and compressive strength developed earlier. The influence of temperature ultimately compromised the integrity of the cement.

It is important to note the study examined only two samples under the influence of sulfuric acid. These results showed that the cement paste sample with gypsum crystals cured at 50°C had a slightly higher compressive strength than that of the sample cured at 85°C. Cement samples exposed to CO_2-O_2 conditions and then submerged in sulfuric acid had a 10 to 15 MPa decrease in strength in comparison to the cured hydrated cement.

6.4. Conclusions

This study sought to further our understanding of the impact of supercritical CO_2 and to determine if secondary mineral precipitation influences the strength of cement paste. Oil-well cements subjected to high temperatures and pressures in saline formations are a potential method to mitigate to rising atmospheric CO_2 levels. Variables such as pH, pressure, salinity, and temperature have a large impact on the stability of the cement. Pressure and temperature significantly influences the hydration of cement which is vital for cement strength and durability.

[Co]-sequestration of CO_2, CO_2-O_2, and CO_2-O_2-SO_2 may precipitate secondary minerals, specifically secondary ettringite formation or gypsum, which appears to weaken the cement paste. The tensile strength of cement may increase slightly when exposed to CO_2. However, the addition of O_2 to the gas injection weakens the cement and is most likely due to secondary development of ettringite. In addition, dissolved SO_2 gas in formation water, results in sulfuric acid and reacts with the cement to form gypsum and weakens cement's compressive strength. The combination of higher temperature (85^{o}C) during hydration and gas exposure appears to be detrimental because the material spalled. It is an important to note that cement strength measurements were after high pressure and temperatures, rather than under *in-situ* confined conditions. To better gauge whether cement exposed to CO_2 and co-sequestration gases is a viable option to mitigate CO_2 emissions, further studies should address confined conditions to investigate the mechanical and physical properties of wellbore cements.

The next chapter, Chapter VII concludes and discusses the entire dissertation.

CHAPTER VII

CONCLUSIONS

7.1. Summary

The purpose of this dissertation was to characterize the influence of supercritical CO_2 on Class H portland cement submerged in mixed brines. Wellbores are likely sites for CO_2 geological sequestration however they are also very likely to permit leakage of the sequestered CO_2. The dissolution of CO_2 in water forms carbonic acid which is known to alter wellbore cement sheaths and thus compromise the wellbore itself. This dissertation combines civil engineering and geochemistry to examine the geochemical interactions of the application of cement, cement paste hydration, the influence of chlorides, and secondary mineral precipitation.

The project has four main objectives: 1) to investigate pure CO_2 sequestration conditions and the ensuing cement alteration; 2) to measure cement alteration immersion in brine to stimulate co-sequestration; 3) to analyze the influence of basin-specific brine on the formation rock-cement interface; and 4) to determine the compressive and tensile strength of the cements described above. To meet the first objective, cement samples were exposed to pure CO_2 at 50^oC and P_{CO2}=28.9 MPa for 84 days while submerged in mixed chloride content (NaCl, $CaCl_2$, $MgCl_2$). Brine composition was based on the NETL Phase III Regional Sequestration Partnerships CO_2 injection sites. The second objective was met by using a mixed CO_2-O_2 gas to simulate the potential for co-sequestration and analyzing cement/brine immersion tests. The C-S-H becomes crystalline at higher temperatures and making the cement less resistance to acid attack. Therefore, during the immersion tests high temperatures were used to investigate the impact these temperatures would have on the primary cement structure under sequestration conditions. The third objective was to determine the influence of basin-specific brine on the interface between the bonded cement and host rock was met by encasing Columbia River Basalt and Mt. Simon sandstone in portland cement with their respective basin solutions at 35°C and PCO_2= 10 MPa for up to 84 days.

The final objective to measure the compressive and tensile strength of the cements after exposure to CO_2, CO_2-O_2, and CO_2-O_2-SO_2 . The rationale for this is objective is that cement hydration is influenced by variables such as pH, pressure, salinity, and temperature. Portland cement is not stable in the acidic conditions which exist during sequestration and results in $Ca(OH)_2$ and C-S-H dissolution, carbonation, and leaves remnant amorphous silica. The [co]-sequestration of CO_2, CO_2-O_2, and CO_2-O_2-SO_2 gas mixtures precipitates secondary minerals, specifically secondary ettringite formation, which may influence cement strength.

In support of the experimental work, a thermodynamic geochemical model (CHIM-XPT) was utilized to calculate mineral phase saturation and pH solution. The calculations were based on experimental data for solutions from the immersion tests of portland cement exposed to supercritical CO_2, CO_2-O_2 mixed gas, CO_2 -O_2-SO_2, as well as conditions for the host rock-cement experiment basin solutions.

7.2. Immersion Test Conclusions

7.2.1. Pure CO_2:

Class H portland cement paste samples were subjected to supercritical CO_2 at 50°C and 28.9 MPa to simulate downhole CO_2 sequestration conditions in brine-bearing formations. The effects of distilled water and various Na-Mg-Ca-Cl brine compositions and salinities (1–2.17 *M*) were investigated. After exposure to simulated sequestration conditions, portland cement developed distinct zones of alteration: 1) a calcium-depleted, porous, amorphous silica zone, 2) a well crystallized $CaCO_3$ band, 3) a subtle calcium-depleted zone, and 4) a distinct chloride-enriched zone, which had not been previously identified in sequestration studies. The addition of CO_2 into the complex brine influences the pH and controls the mineral stability and the rate of degradation. This pH gradient drives the diffusion of calcium species, which further degrades the cement paste. Pore fluids migrate within the cement matrix and drive the gradient boundary, a propagation front, further into the unaltered cement. The cement exposed to the lower salinity brine (1 *M*) had a larger alteration depth of 1.25 mm compared to the cement exposed to the higher salinity brine (2.2 *M*) with an alteration depth of 0.836 mm. This experiment also showed that distilled water should not be used to cure nor store cement because distilled water initiates cement degradation prior to gas injection.

Titanium isocon analysis from electron microprobe (EMPA) was use for semi-quantification of elemental concentrations in each alteration zone. In contrast to other studies, our results lead us to the conclusion that there was no true calcium depletion front propagating into the unaltered cement paste based on the average Ti concentration. The absence of a dissolution front is likely due to the ingress of calcium from the brine solution into the cement matrix. Instead remnant amorphous silica zone would be present where the majority of ions have been lost, and a carbonated zone with an increase of calcium in weight percent from the solution.

7.2.2. Co-Sequestration:

CO_2-O_2-cement exposure tests showed alteration depths of 1.6 mm at 85^oC and 0.7 mm at 50^oC for 1 *M* and the cement was depleted in $CaCO_3$ and Ca^{2+} depletion indication changes in its mineralogy. The exposure experiments also corroded the stainless steel (316 CrNiMo) of the autoclave and this was likely due to the addition of O_2. After exposure to mixed gases, the secondary minerals ettringite [$Ca_6Al_2(SO_4)_3(OH)_{12}\cdot 26H_2O$] and hydrotalcite [$Mg_6Al_2(CO_3)(OH)_{16}\cdot 4H_2O$] formed. The ettringite may be the result of Fe^{2+} replacement in aluminoferrite grains and occurs in hardened cement paste above 70^oC and leading to the loss of cement paste integrity, including degradation, expansion, and fracturing under atmospheric conditions. The mineralization of ettringite coupled with the formation of microfractures suggests that detrimental DEF could be initiated at higher wellbore temperatures, as seen in 85^oC immersion tests.

7.2.3. Host rock-cement-brine interaction:

The long-term experiments of the host rock-cement-brine demonstrate that brine composition influences cement alteration. Experimental cement-rock-brine combinations were carried out at 35°C and P_{CO2}= 10 MPa for up to 84 days, conditions under which the fluids are CO_2-saturated. The Grande Ronde basalt-cement immersed in Pasco solution had a greater alteration depth (~1 mm) at the interface with the cement than the interface of the cement-sandstone (20-30 μm). In addition, the CO_2 interaction with the basalt resulted in the conversion of CO_2 as permanent mineral trapping. The Mt. Simon sandstone formation-cement immersed in Illinois brine, on the other hand, showed little mineral replacement or alteration to the cement, but has a high capacity to store supercritical and dissolved CO_2.

The low salinity of the Pasco solution played a significant role in the alteration of the hydrated cement. The dissolution of magnetite, olivine and sodic plagioclase (Fe^{2+}, Mg^{2+}, Na^{+}) was seen in the basalt when exposed to supercritical CO_2. Ca^{2+} leaching from portlandite and C-S-H in the cement was also apparent. These reactions resulted in the precipitation of calcite, magnesite, and fine Fe-carbonate. Dissolution of heulundite ($CaAl_2Si_7O_{18}*6H_2O$) and celadonite ($K(Fe,Mg,Al)_2Si_4O_{10}(OH)_2$) resulted in the formation of a poorly crystalline clay.

The quartz-dominated Mt. Simon Sandstone had a thin, well-crystallized, calcite band (~20-30 μm) at the interface between the sandstone and cement after CO_2 exposure. The formation of silica gel and the carbonate inhibited further acid attack in the sandstone. Furthermore, only 100-700 μm of the cement paste was altered. The Illinois Basin brine demonstrates higher resistance to alteration when subjected to supercritical CO_2.

7.3. Geochemical Modeling Conclusions

Geochemical modeling of the effects of supercritical CO_2 on cement and brine was done using CHIM-XPT methods as outlined by Reed and Spycher (1982) and Reed (1998). CO_2 was titrated incrementally to saturation pressure based on the respective downhole pressures of the wellbores. Basin specific brines were used with subsurface conditions of 50^{o}C and PCO_2=28.9 MPa for the cement gas exposure tests and 35^{o}C and P_{CO2}= 10 MPa for the host rock samples.

In the cement tests, after curing the equilibrated cement-brine had a pH of 11.8 and in pure CO_2 conditions, CHIM-XPT calculated a pH of 3.0 at 1 *M* and 3.85 at 2.17 *M*. Once CO_2 was introduced into the system, the brine became more acidic. The mineral assemblages in the pure CO_2 solutions were undersaturated, except for quartz, which was not observed experimentally. Modeling the CO_2-O_2 gas mixture determined a pH of 3.96 at 1 *M* and 3.85 at 2.17 *M*. Mineral saturations in the CO_2-O_2 mixture calculated the precipitation of quartz and goethite. Modeling of a simple (*Surrogate*) brine combined with a gas mixture of 95.5% CO_2+ 4% O_2+ 1.5% SO_2 resulted in a solution of pH = 4.34. The model also predicted an excess of 31% O_2 under those conditions and calculated that H_2S from SO_2 disproportionation is oxidized to sulfate. We determined that 5.7 ml of sulfuric acid (7%) would simulate the desired conditions. Additional reactions would likely precipitate anhydrite, calcite, gypsum, and dolomite, all of which were verified experimentally.

Geochemical modeling was also conducted with CHIM-XPT to determine saturated mineral phases and pH at *in-situ* conditions of the basalt and sandstone host rock formations. There was an estimated 50 g of $CO_{2\ (g)}$ consumed at 102 bars and 161 g at 306 bars in 1 kg of Pasco solution and Columbia River basalt. The Columbia River basalt encased in cement combined with Pasco brine displayed a fluctuating pH over the course of the calculation, starting at 11.82 and finishing at 6.97. There was an estimated 136 g of $CO_{2(g)}$ dissolved in the Pasco solution at 102 bars with precipitation of magnesite, calcite and siderite. The pH of the Illinois Basin brine and Mt. Simon sandstone [and cement paste] was acidic and retained 139 g of CO_2 with an end pH of 5.8.

7.4. Tensile and Compression Conclusions

Point load tests tensile tests were performed on 1) portland cement cured for 28 days in a 1 *M* ($CaCl_2$, $MgCl_2$, NaCl) brine, but not exposed to any gases; 2) cured cement samples exposed to CO_2; 3) cured cement samples exposed to CO_2-O_2; and 4) cured cement samples CO_2-O_2 that were submerged in sulfuric acid. All cement samples were cured and subjected to gas exposure at 50^{o}C or 85^{o}C and 28.9 MPa. [Co]-Sequestration of CO_2, CO_2-O_2, and CO_2-O_2-SO_2 resulted in the precipitation of calcium carbonate, ettringite, and gypsum which influenced the strength of the cement paste. To better gauge whether cement exposed to CO_2 and co-sequestration gases are viable options to mitigate CO_2 emissions, subsequent studies should address confined conditions to further investigate the mechanical and physical properties of wellbore cements.

The CO_2 exposed samples slightly increased cement strength by 11.7% in comparison to the brine-cured cement. The addition of O_2 to the gas injection weakened the cement by ~20% likely due to microfractures from the development of ettringite. The average tensile strength for the sulfuric acid exposed cement at 50^{o}C was reduced by only ~ 4%, whereas in the higher temperature (85^{o}C) sample tensile strength was reduced by 34.7%. The higher temperature (85^{o}C) during hydration and subsequent gas exposure had a detrimental effect on cement.

The compressive strength was measured for each of condition: 1) cured cement paste prior to any gas exposure, 2) cement exposed to CO_2-O_2, and 3) cement immersed in CO_2-O_2-sulfuric acid. The hydrated cement samples cured in brine for 28 days had a moderate compressive strength of 34.18 MPa when compared to API and ASTM standards. Cement samples exposed to a CO_2-O_2 mixed gas for 56 days at 50^{o}C had an average compressive strength of 26.1 MPa, whereas the H_2SO_4 immersed samples had a compressive strength <26 MPa. This study shows that there is a significant difference in compressive strength of high PCO_2 gas exposed cement paste in comparison to unexposed hydrated cement.

APPENDIX A

CLASS H CEMENT EXPOSED TO SUPERCRITICAL CO_2

Scanning Electron Microscopy Backscatter and X-ray Elemental Maps

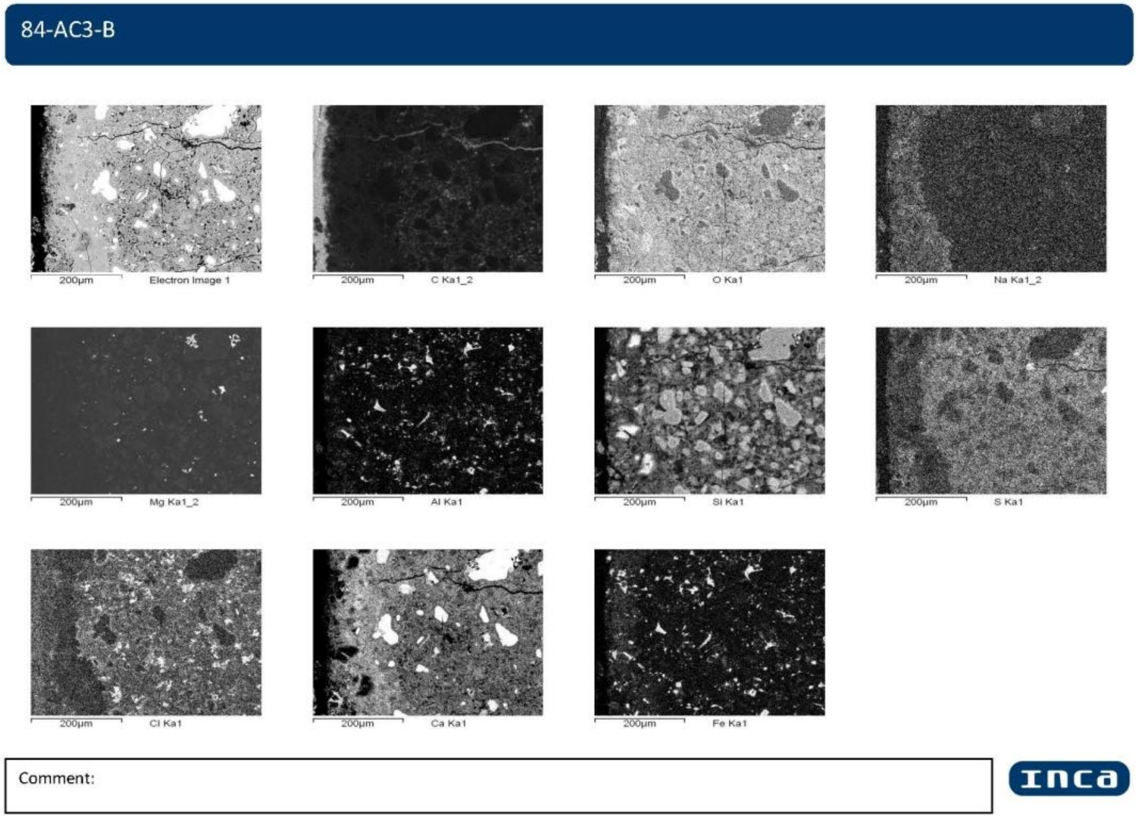

84-AC3-B

Comment:

84-AC3-B

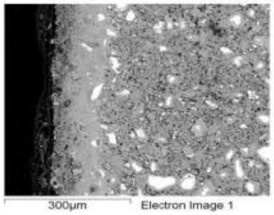

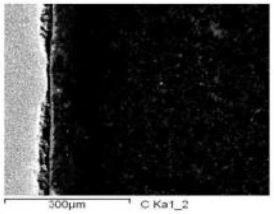

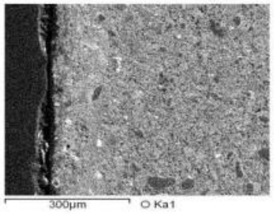

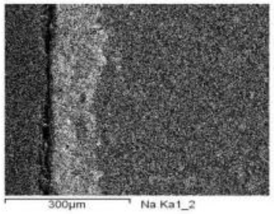

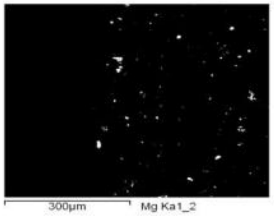

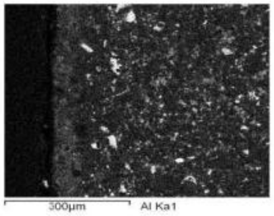

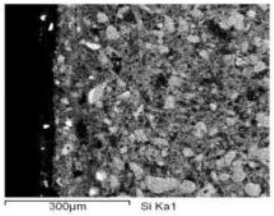

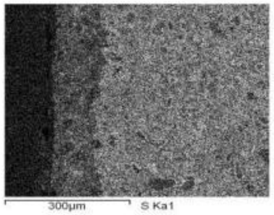

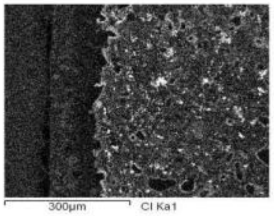

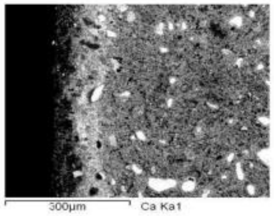

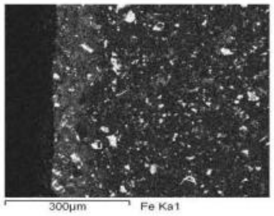

Comment:

28-AC5-B

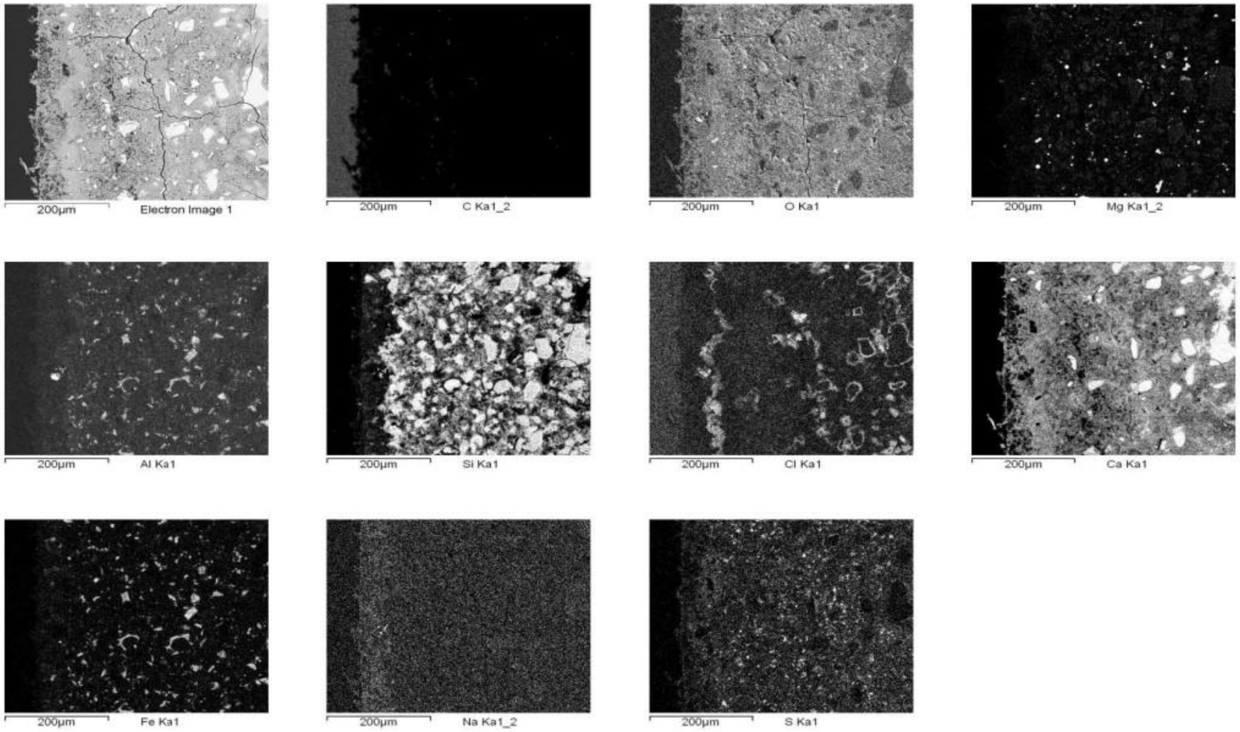

Comment:

84-AC5-B

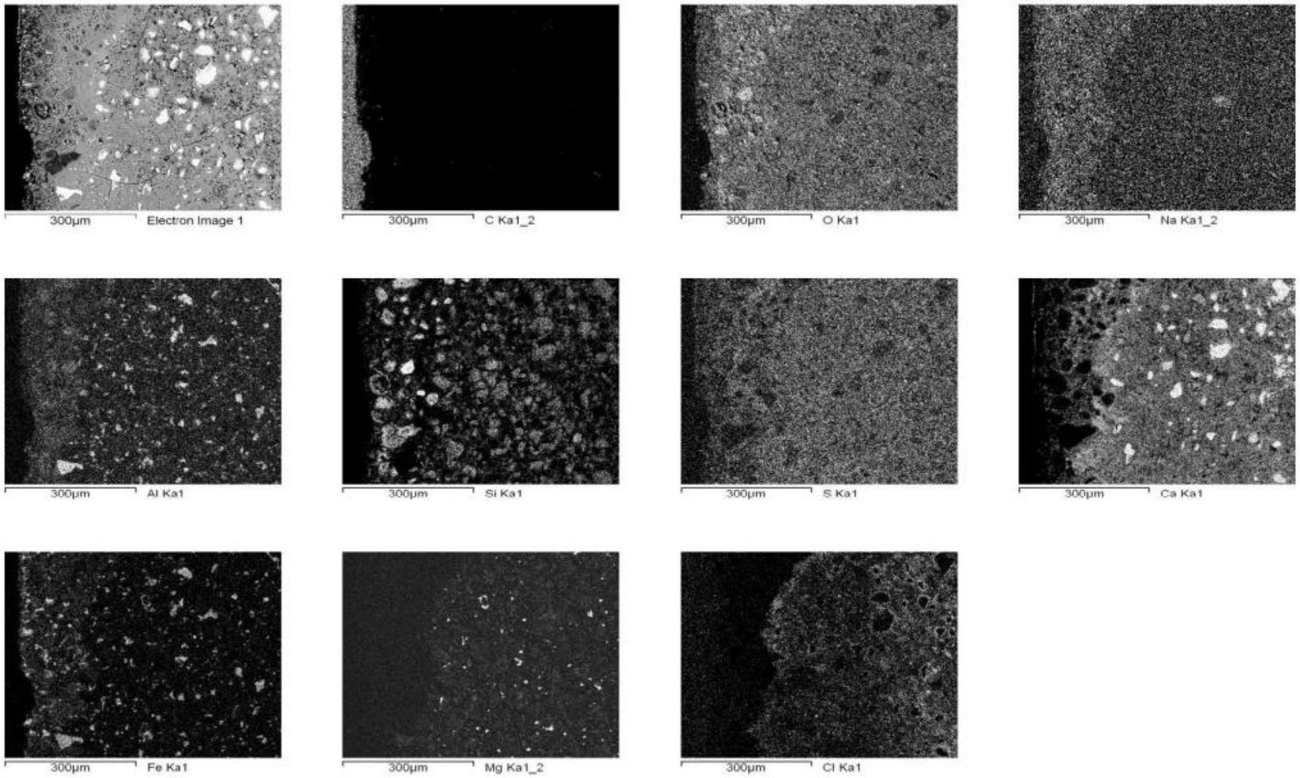

Comment:

84-AC5-B

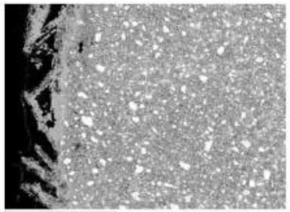

Electron Image 1

C Ka1_2

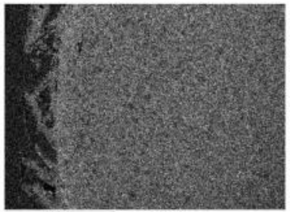

O Ka1

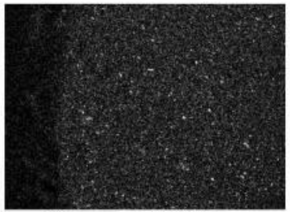

Mg Ka1_2

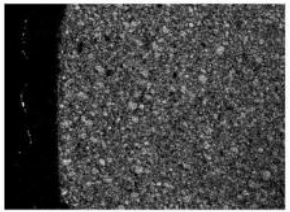

Si Ka1

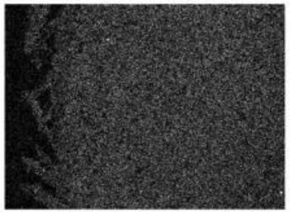

S Ka1

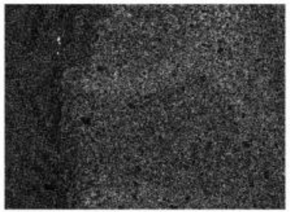

Cl Ka1

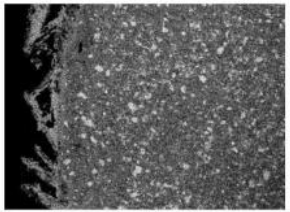

Ca Ka1

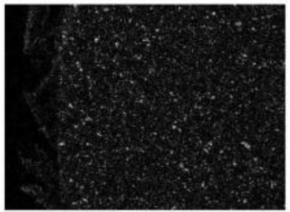

Fe Ka1

Na Ka1_2

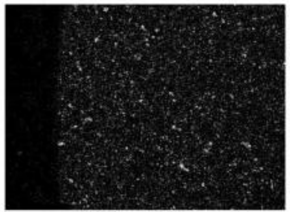

Al Ka1

Comment:

84-AC5-B

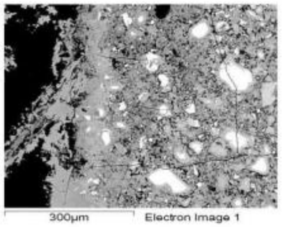

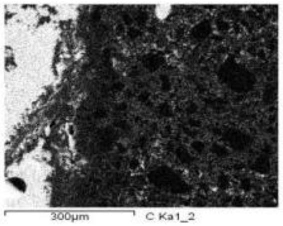

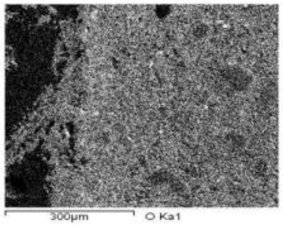

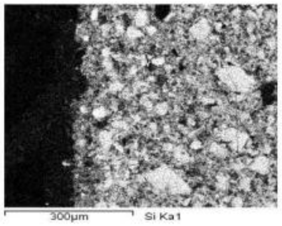

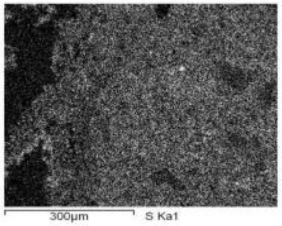

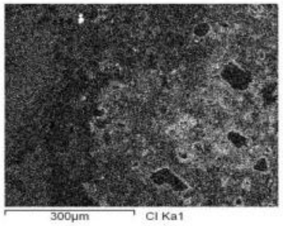

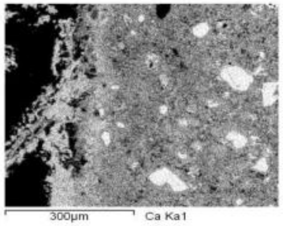

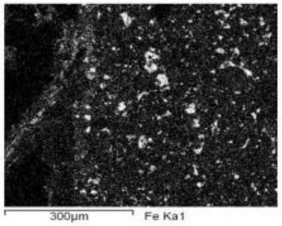

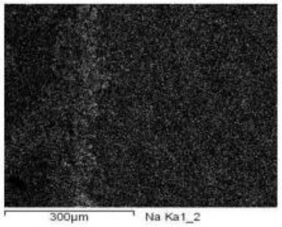

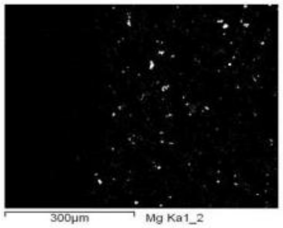

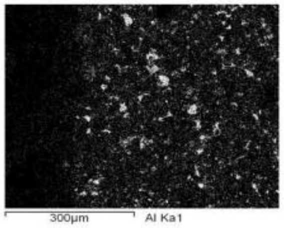

Comment:

84-AC5-B

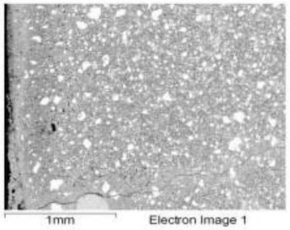

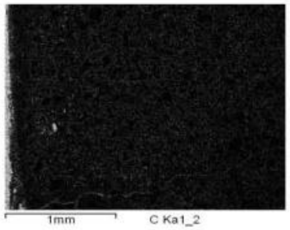

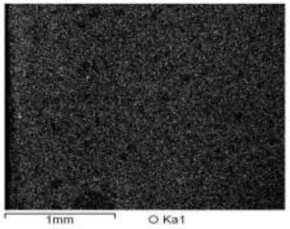

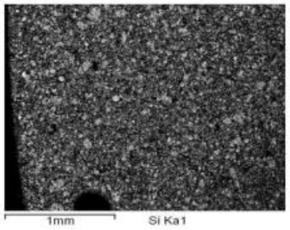

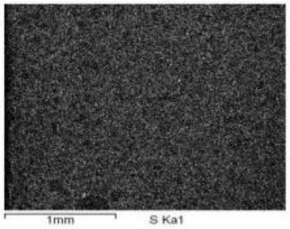

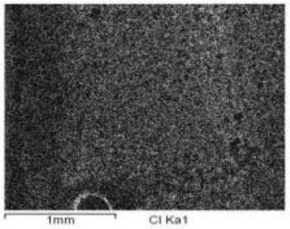

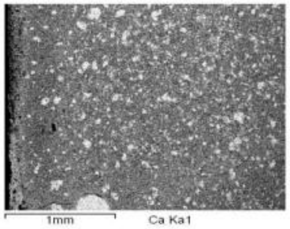

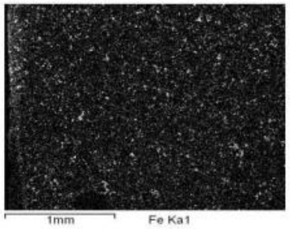

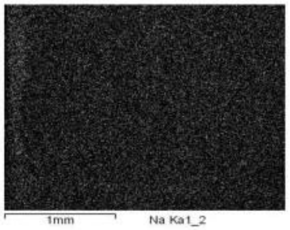

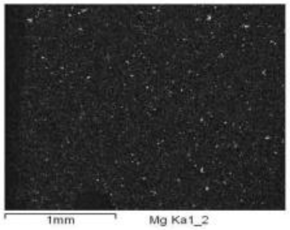

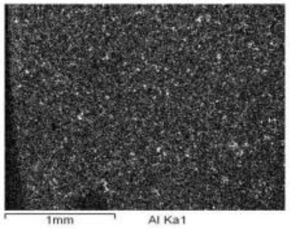

Comment:

84-AC5-B

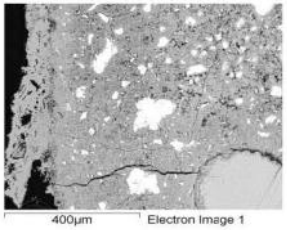

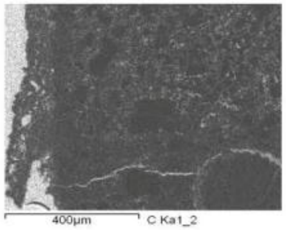

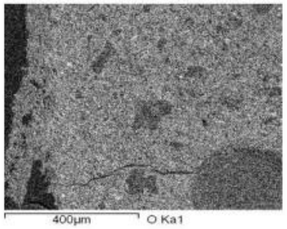

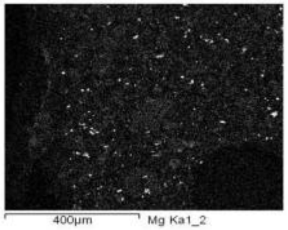

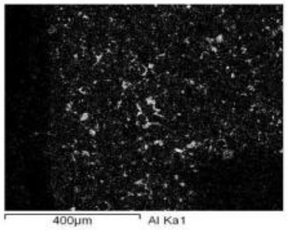

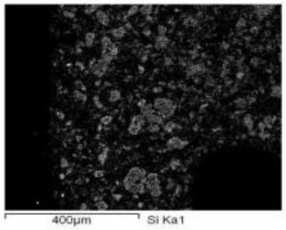

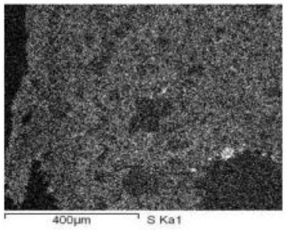

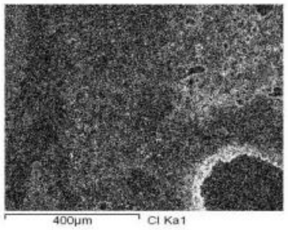

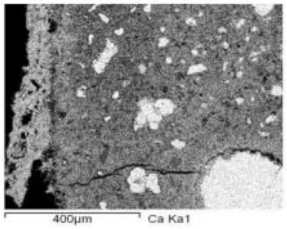

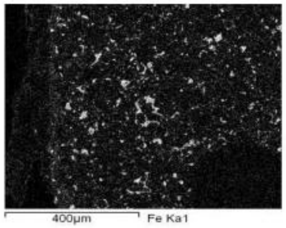

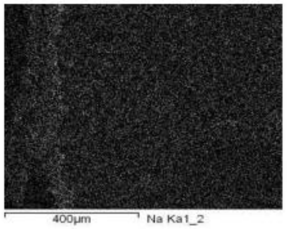

Comment:

84-AC4-B

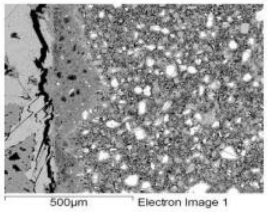

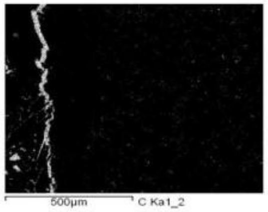

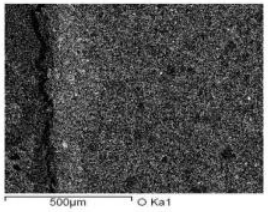

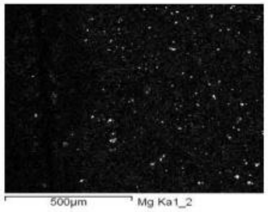

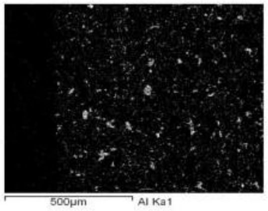

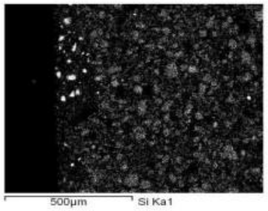

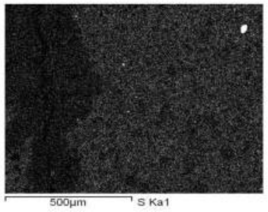

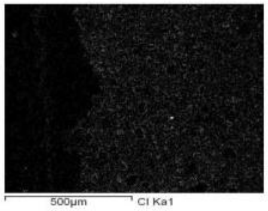

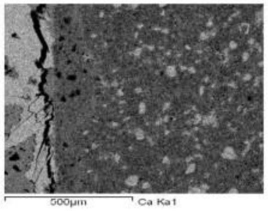

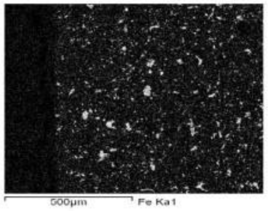

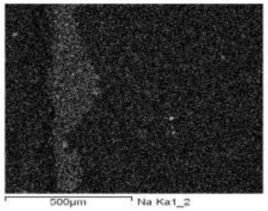

Comment: 250x of location 3 with portlandite crystals; interesting boundary (missing Si porous region)

84-AC4-B

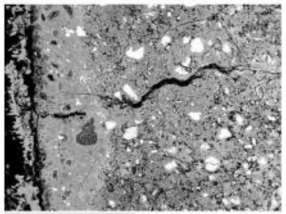

400µm Electron Image 1

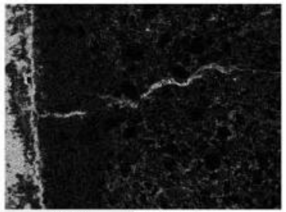

400µm C Ka1_2

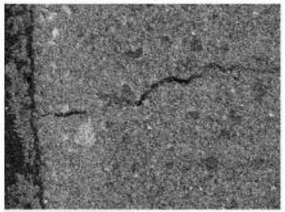

400µm O Ka1

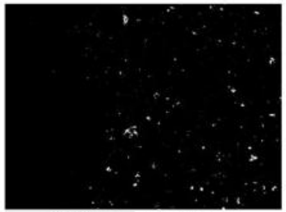

400µm Mg Ka1_2

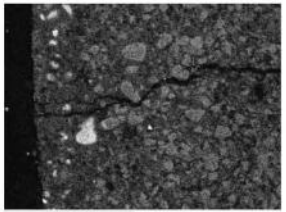

400µm Si Ka1

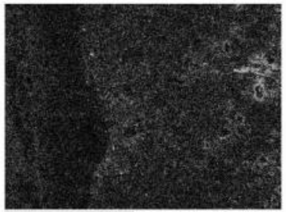

400µm Cl Ka1

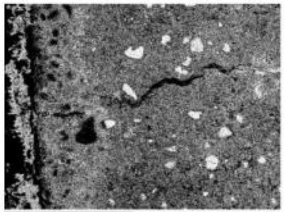

400µm Ca Ka1

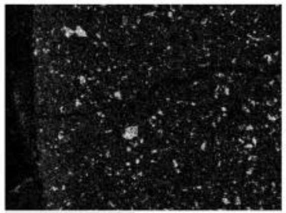

400µm Fe Ka1

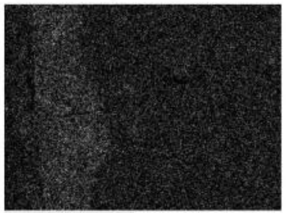

400µm Na Ka1_2

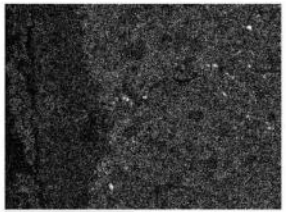

400µm S Ka1

Comment:

84-AC4-B

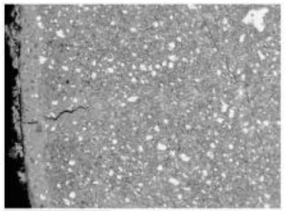

1mm Electron Image 1

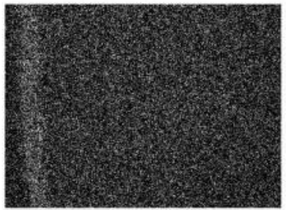

1mm Na Ka1_2

1mm Mg Ka1_2

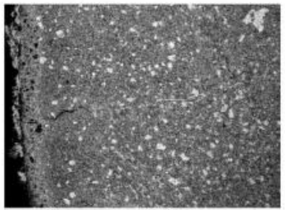

1mm Ca Ka1

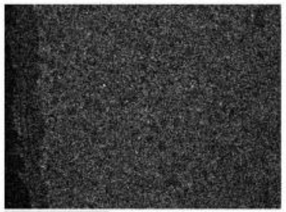

1mm S Ka1

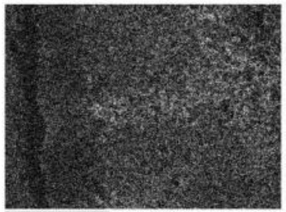

1mm Cl Ka1

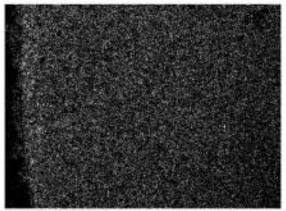

1mm O Ka1

1mm C Ka1_2

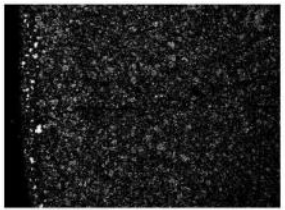

1mm Si Ka1

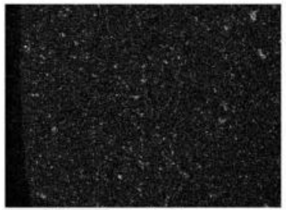

1mm Al Ka1

Comment:

84-AC4-B

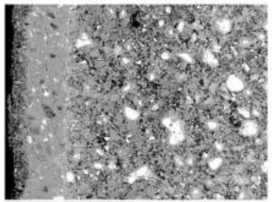

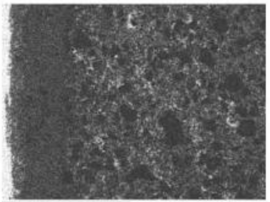

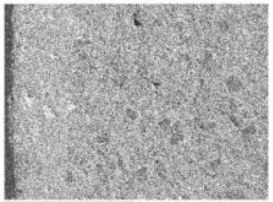

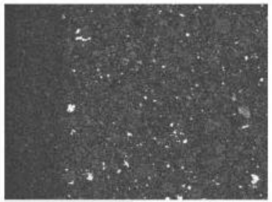

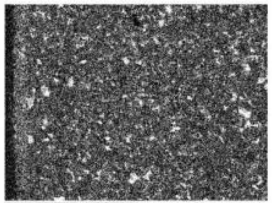

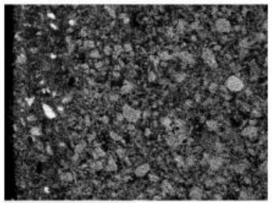

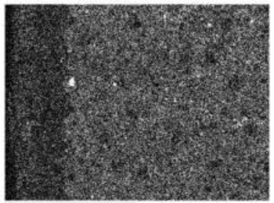

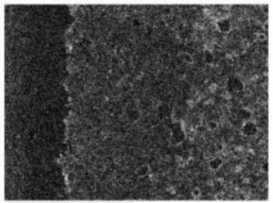

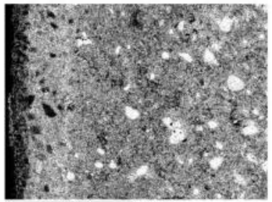

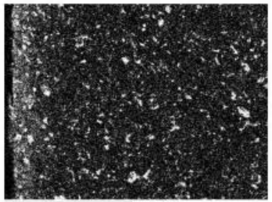

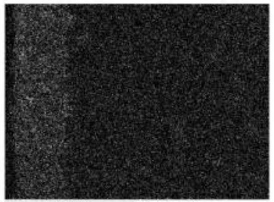

Comment:

84-AC4-B

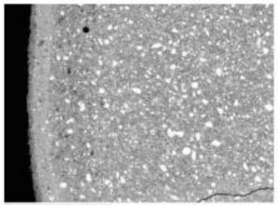

Electron Image 1

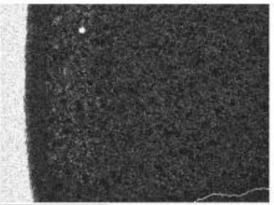

C Ka1_2

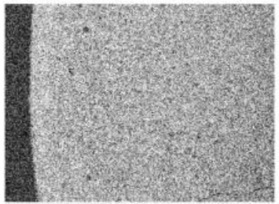

O Ka1

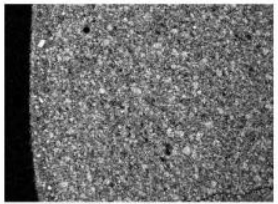

Si Ka1

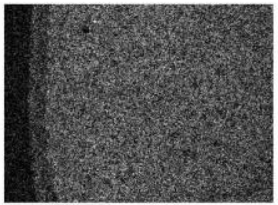

S Ka1

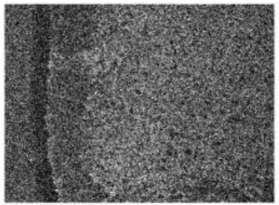

Cl Ka1

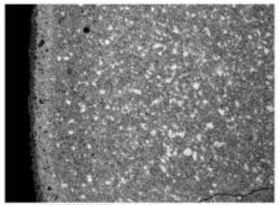

Ca Ka1

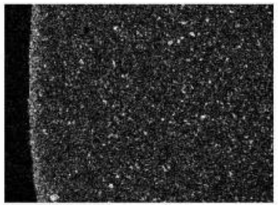

Fe Ka1

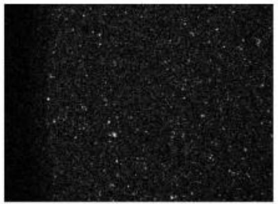

Mg Ka1_2

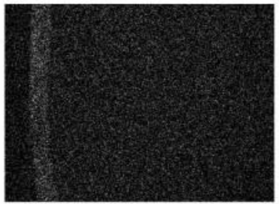

Na Ka1_2

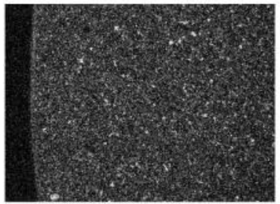

Al Ka1

Comment:

84-AC2-B

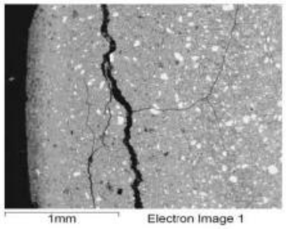

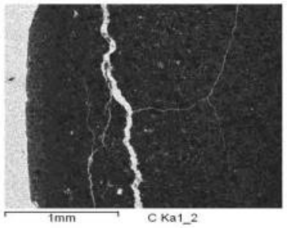

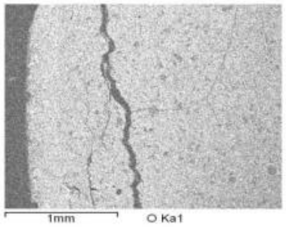

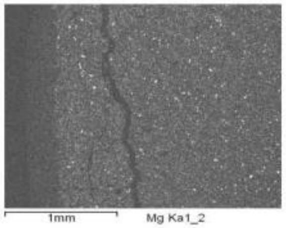

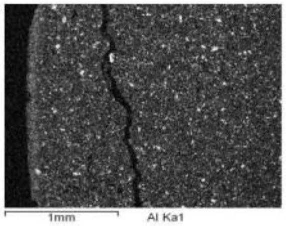

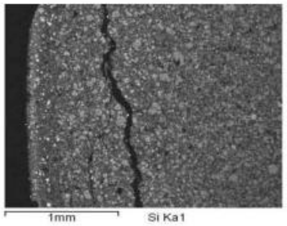

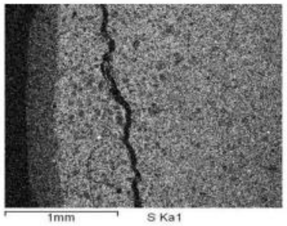

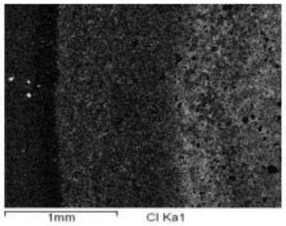

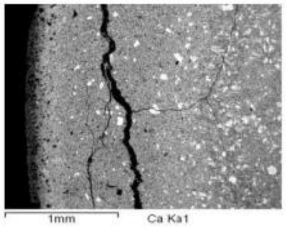

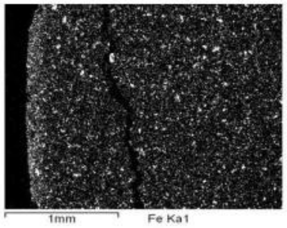

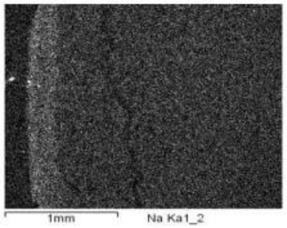

Comment: 84-AC2-B(3)

84-AC2-B

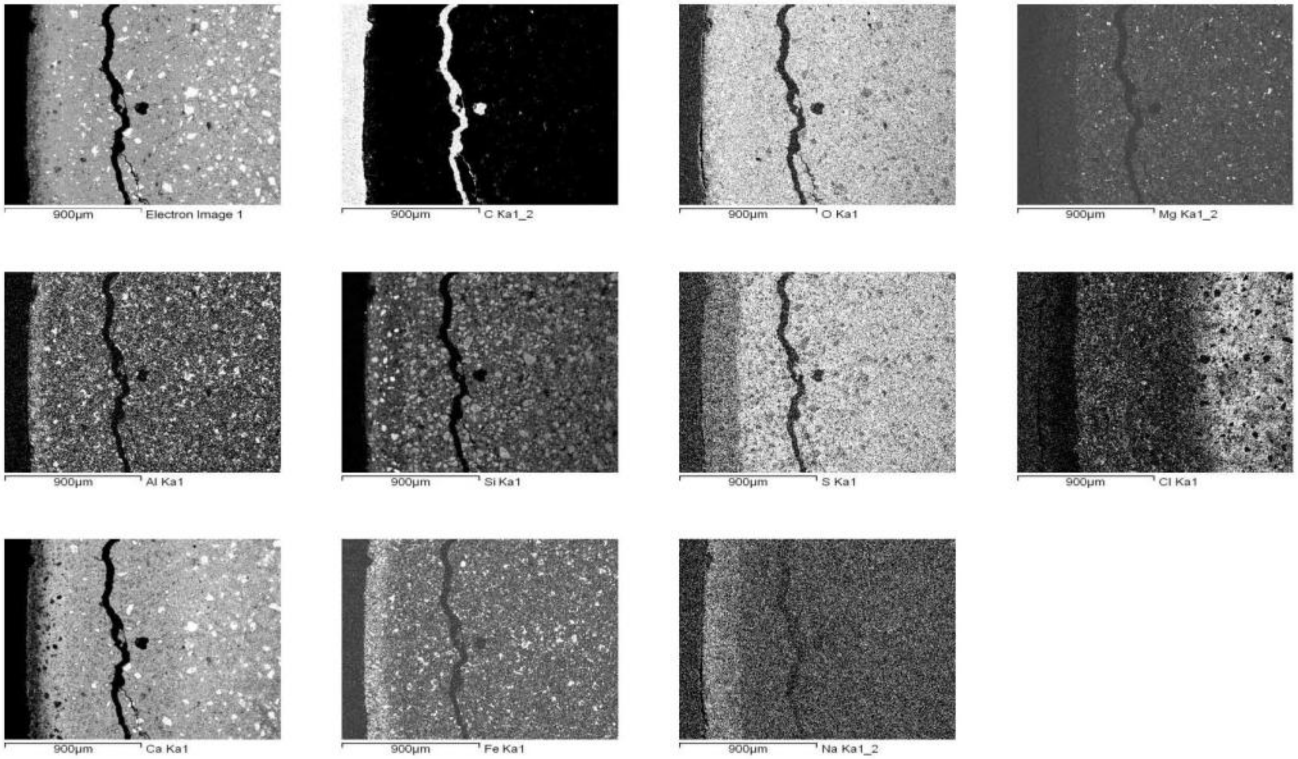

Comment: 84-AC2-B(1)

84-AC2-B

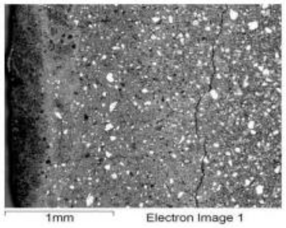

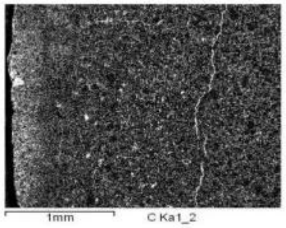

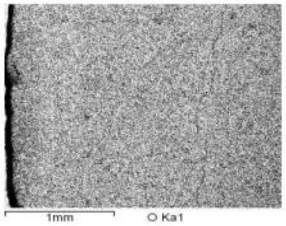

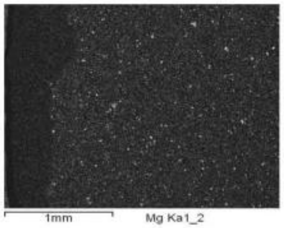

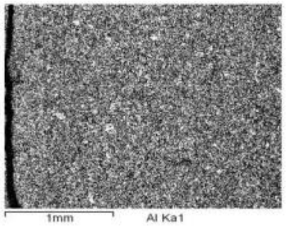

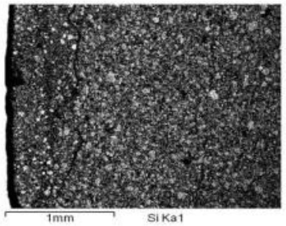

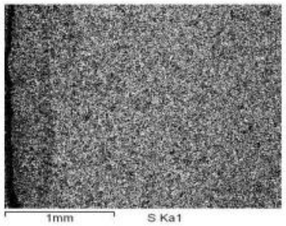

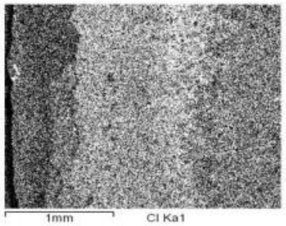

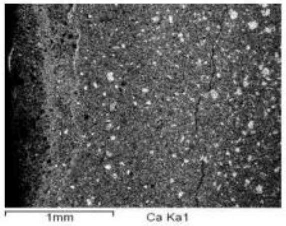

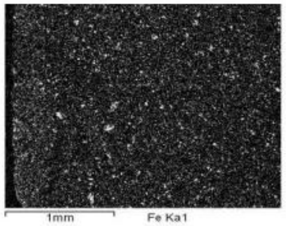

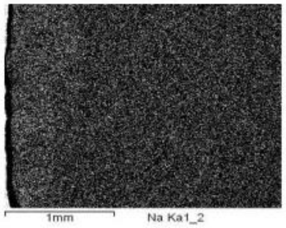

Comment:

82-AC3-B

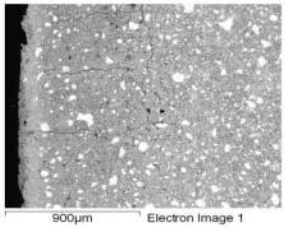

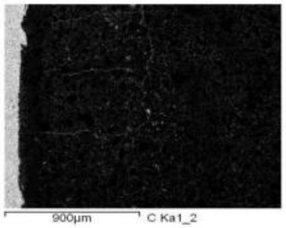

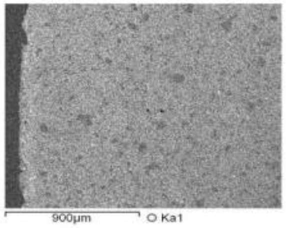

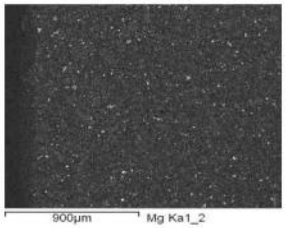

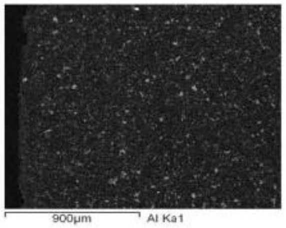

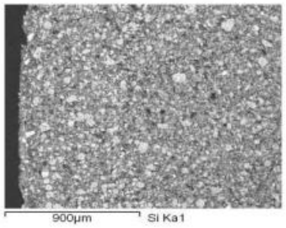

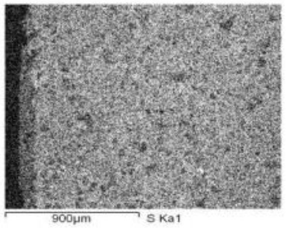

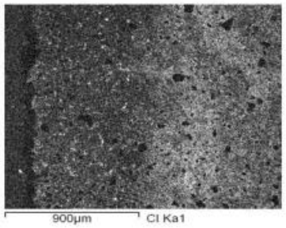

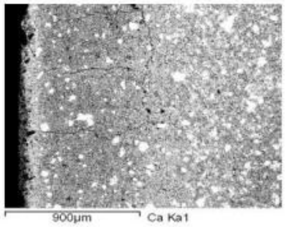

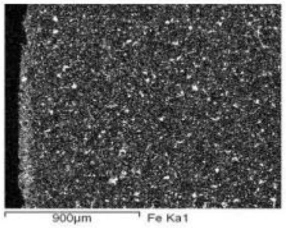

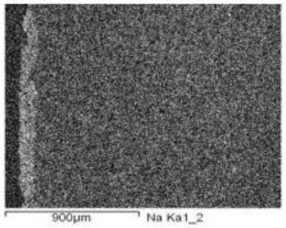

Comment: 84-AC3-B(2)

84-AC1-B

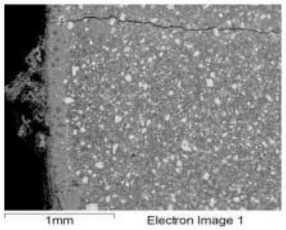

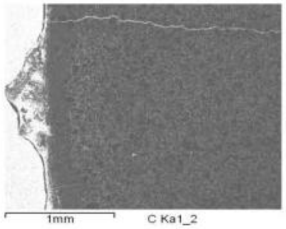

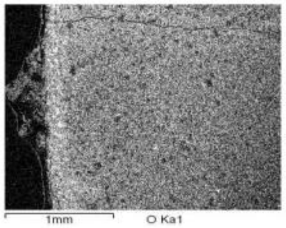

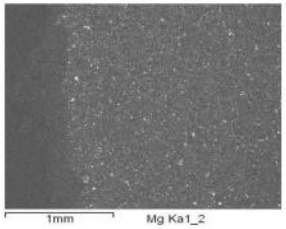

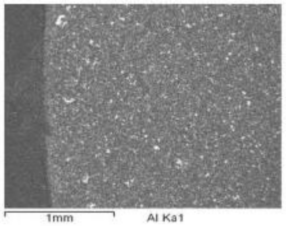

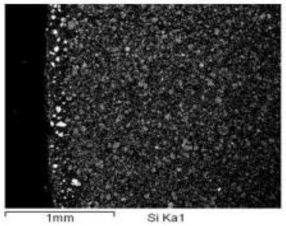

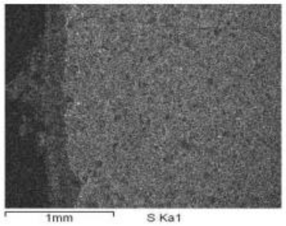

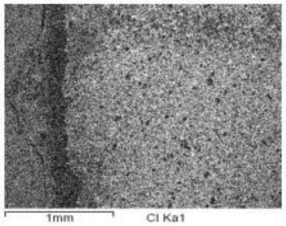

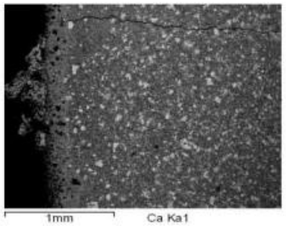

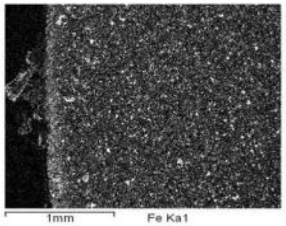

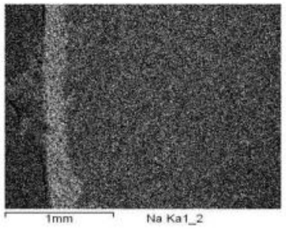

Comment:

84-AC1-B

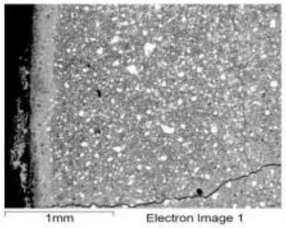

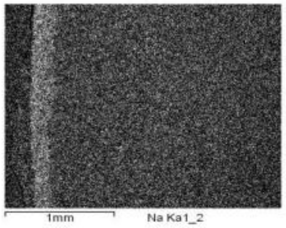

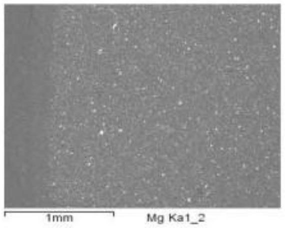

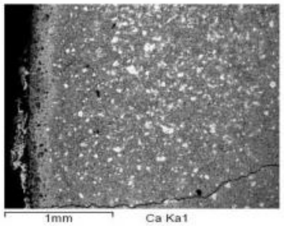

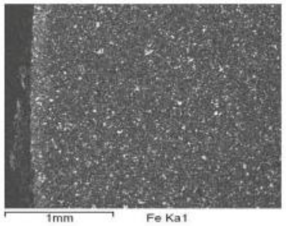

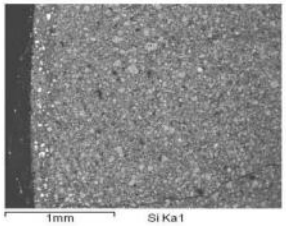

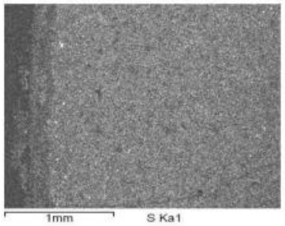

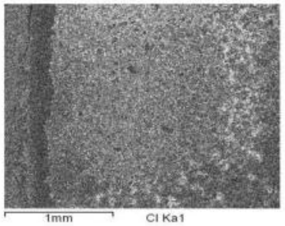

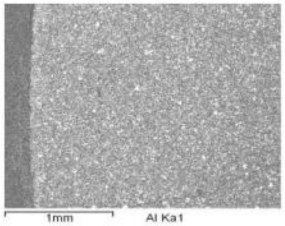

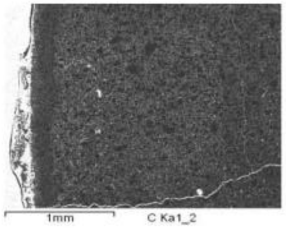

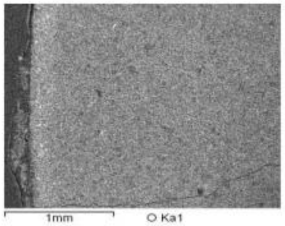

Comment:

84-AC1-B

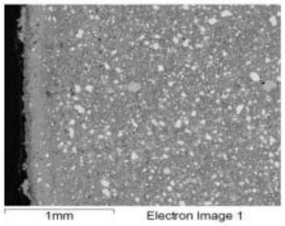

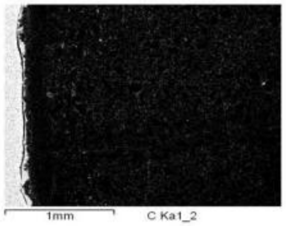

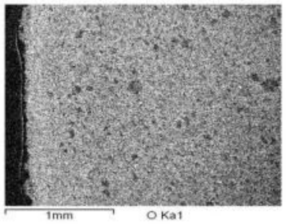

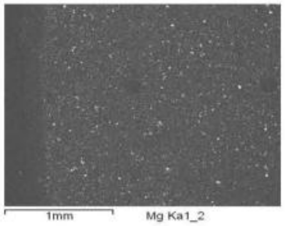

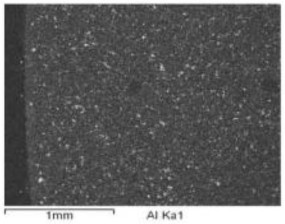

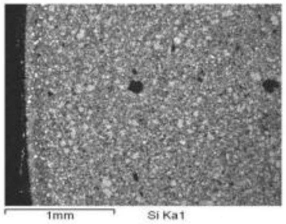

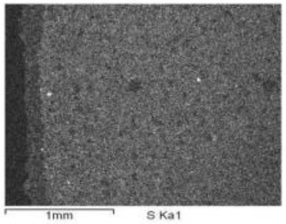

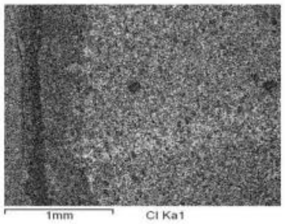

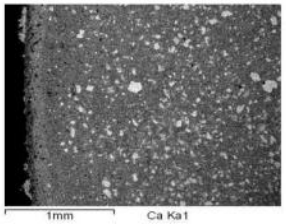

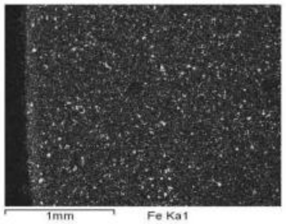

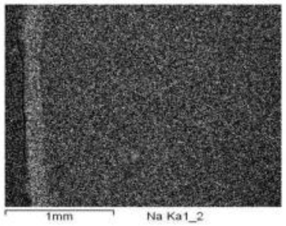

Comment:

84-AC1-B

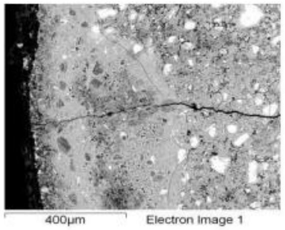

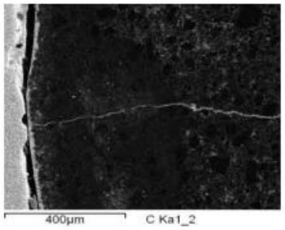

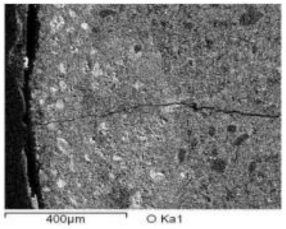

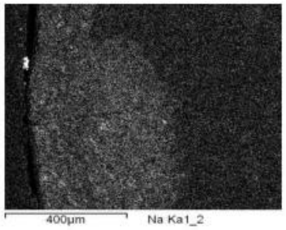

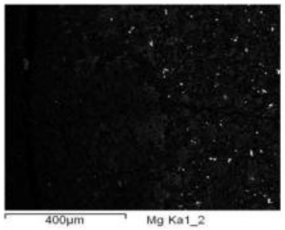

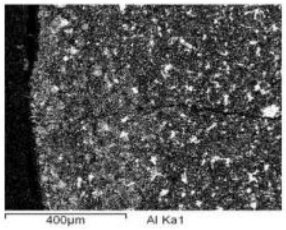

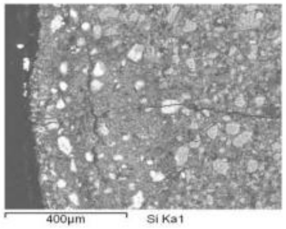

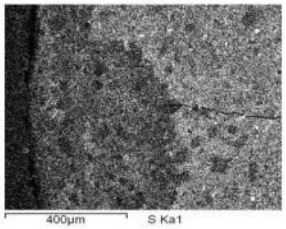

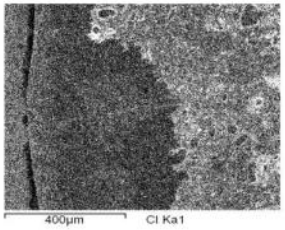

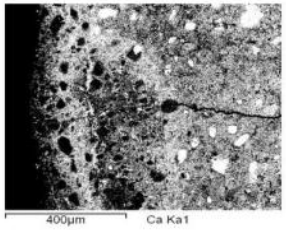

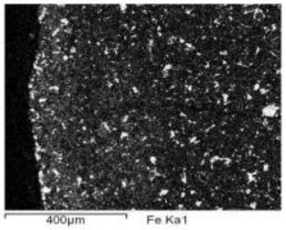

Comment: 84-AC1-B(3)

84-AC1-B

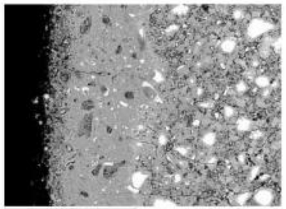

Electron Image 1

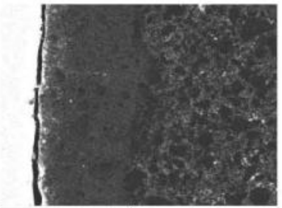

C Ka1_2

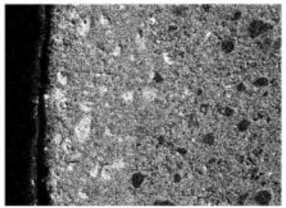

O Ka1

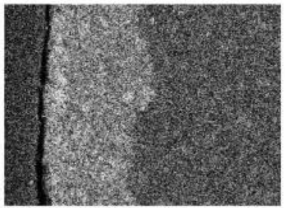

Na Ka1_2

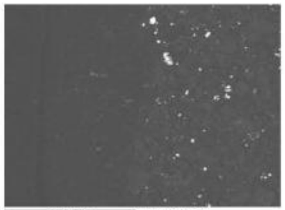

Mg Ka1_2

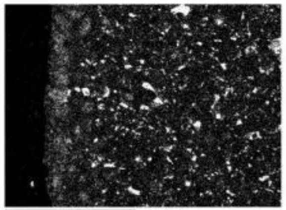

Al Ka1

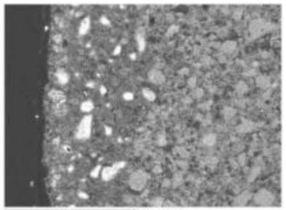

Si Ka1

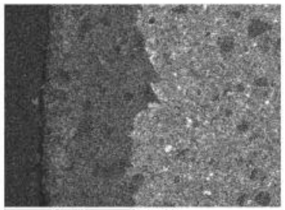

S Ka1

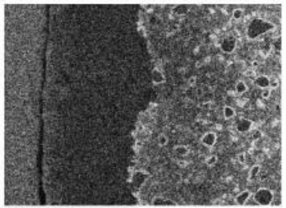

Cl Ka1

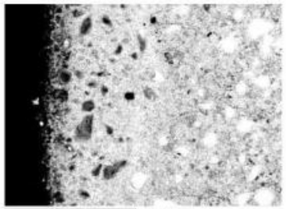

Ca Ka1

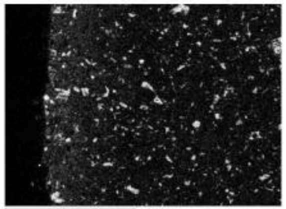

Fe Ka1

Comment: 84-AC1-B(2)

84-AC1-B

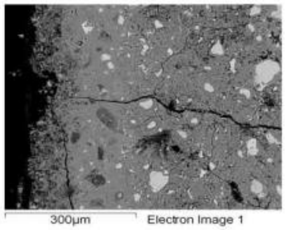

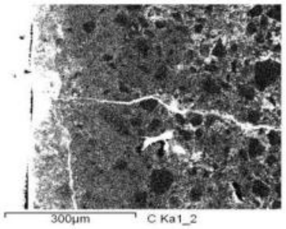

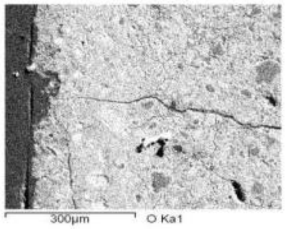

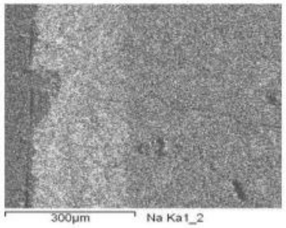

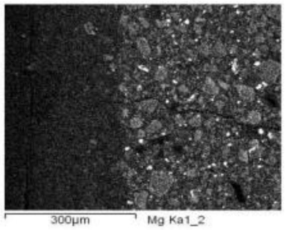

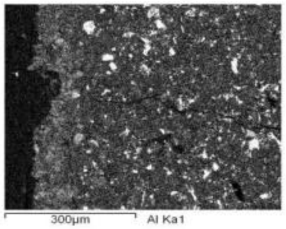

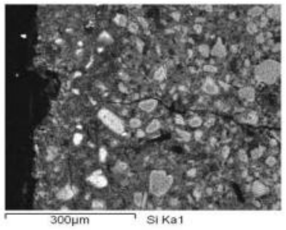

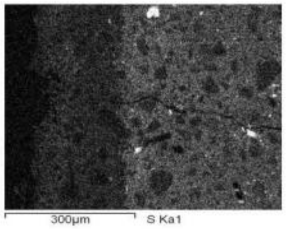

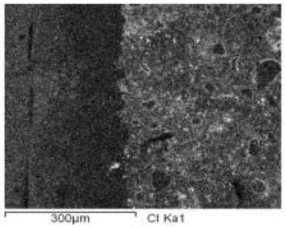

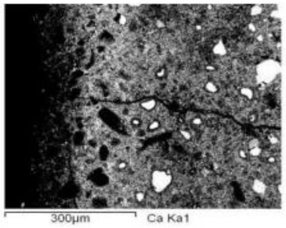

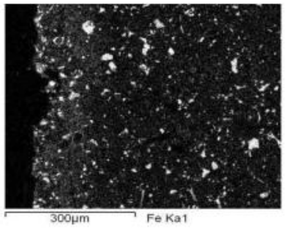

Comment: 84-AC1-B(1)

84-AC2-B

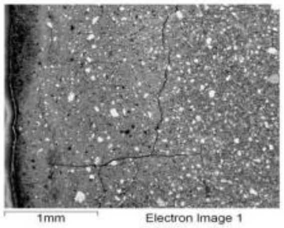

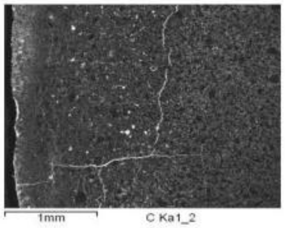

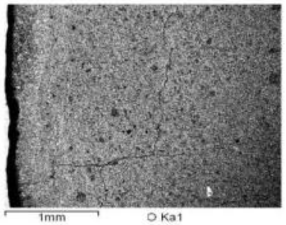

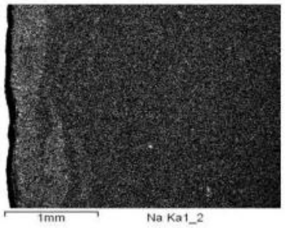

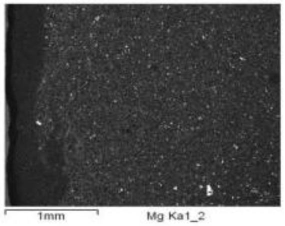

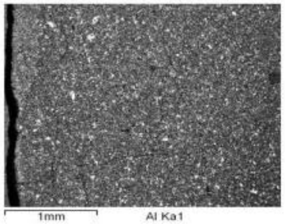

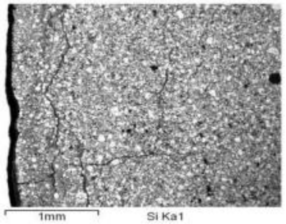

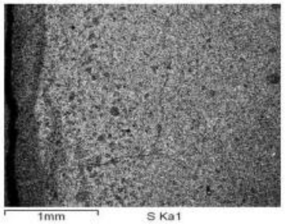

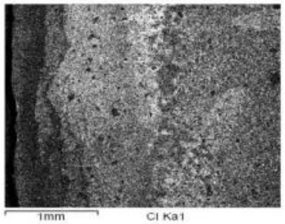

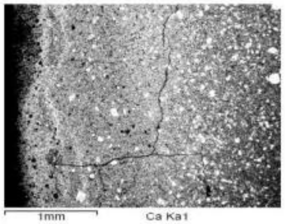

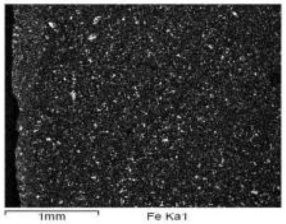

Comment:

84-AC2-B

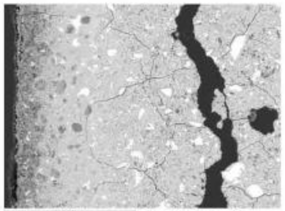

Electron Image 1

C Ka1_2

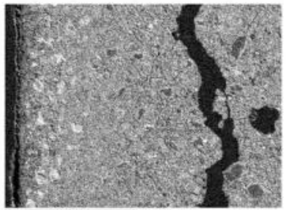

O Ka1

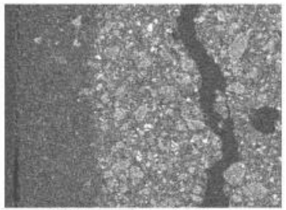

Mg Ka1_2

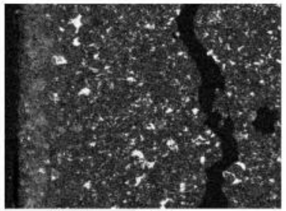

Al Ka1

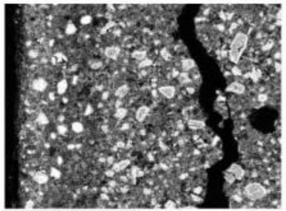

Si Ka1

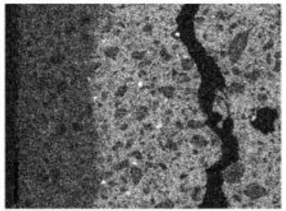

S Ka1

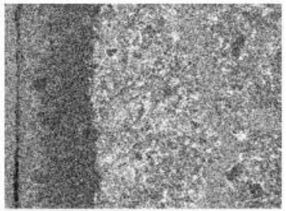

Cl Ka1

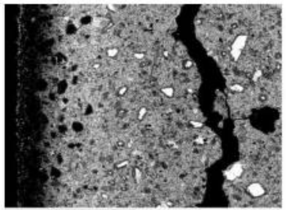

Ca Ka1

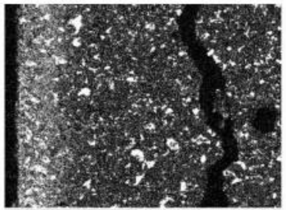

Fe Ka1

Comment:

84-AC3-B

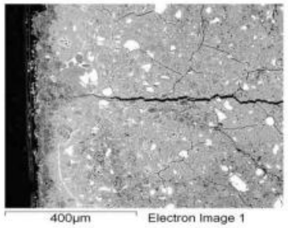

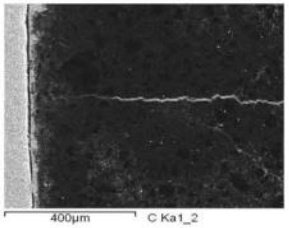

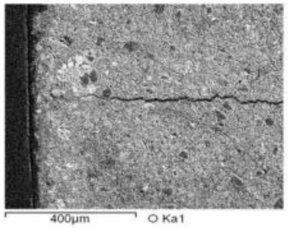

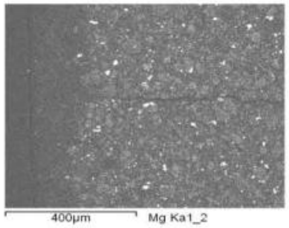

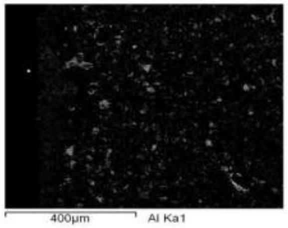

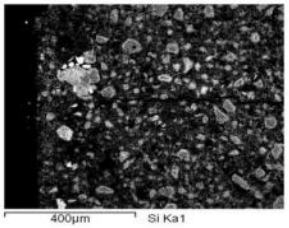

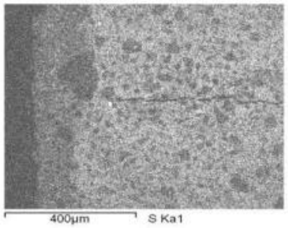

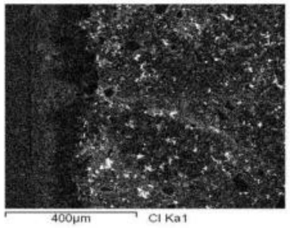

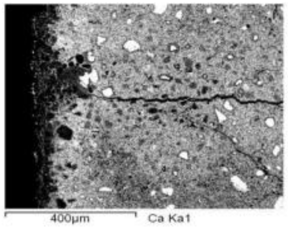

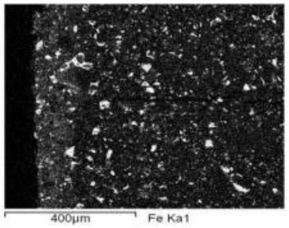

Comment:

X-ray Diffraction Patterns Class H Cement Exposed To Supercritical CO2

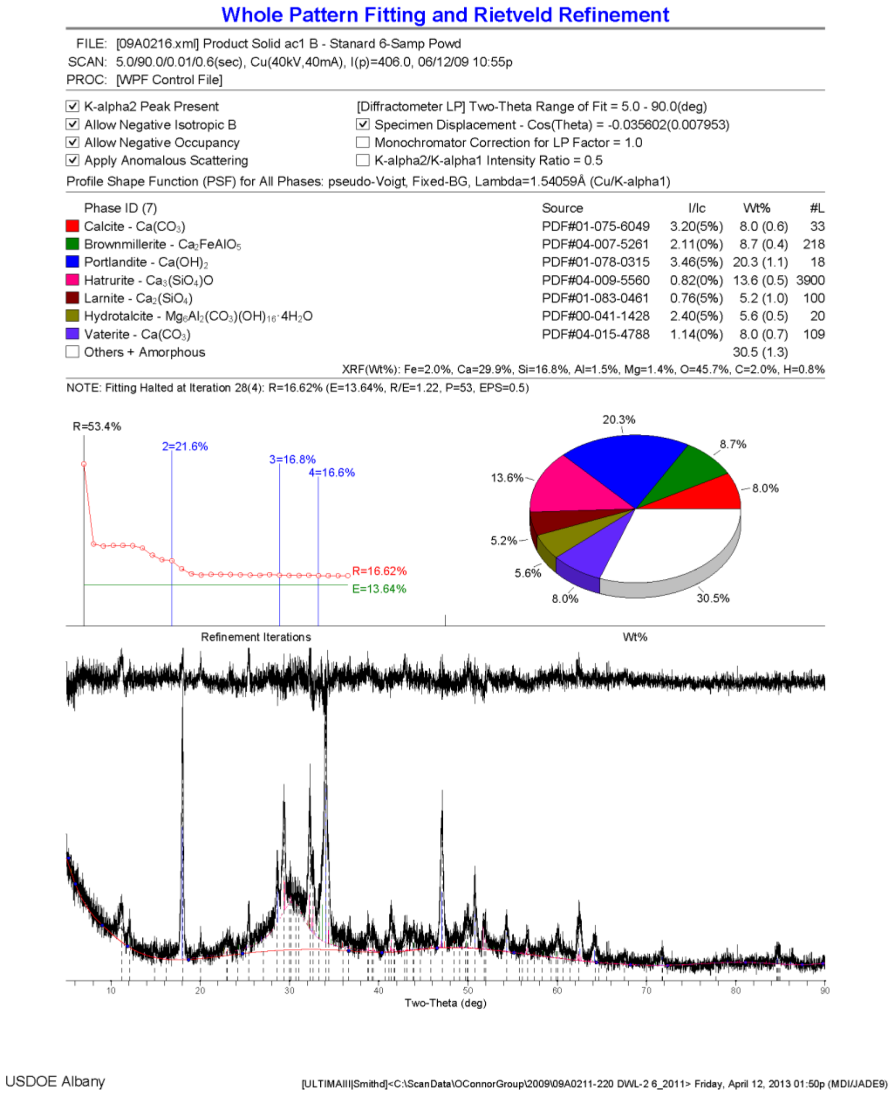

Whole Pattern Fitting and Rietveld Refinement

FILE: [09A0216.xml] Product Solid ac1 B - Stanard 6-Samp Powd
SCAN: 5.0/90.0/0.01/0.6(sec), Cu(40kV,40mA), I(p)=406.0, 06/12/09 10:55p
PROC: [WPF Control File]

☑ K-alpha2 Peak Present
☑ Allow Negative Isotropic B
☑ Allow Negative Occupancy
☑ Apply Anomalous Scattering

[Diffractometer LP] Two-Theta Range of Fit = 5.0 - 90.0(deg)
☑ Specimen Displacement - Cos(Theta) = -0.035602(0.007953)
☐ Monochromator Correction for LP Factor = 1.0
☐ K-alpha2/K-alpha1 Intensity Ratio = 0.5

Profile Shape Function (PSF) for All Phases: pseudo-Voigt, Fixed-BG, Lambda=1.54059Å (Cu/K-alpha1)

Phase ID (7)	Source	I/Ic	Wt%	#L
🟥 Calcite - $Ca(CO_3)$	PDF#01-075-6049	3.20(5%)	8.0 (0.6)	33
🟩 Brownmillerite - Ca_2FeAlO_5	PDF#04-007-5261	2.11(0%)	8.7 (0.4)	218
🟦 Portlandite - $Ca(OH)_2$	PDF#01-078-0315	3.46(5%)	20.3 (1.1)	18
■ Hatrurite - $Ca_3(SiO_4)O$	PDF#04-009-5560	0.82(0%)	13.6 (0.5)	3900
🟫 Larnite - $Ca_2(SiO_4)$	PDF#01-083-0461	0.76(5%)	5.2 (1.0)	100
■ Hydrotalcite - $Mg_6Al_2(CO_3)(OH)_{16} \cdot 4H_2O$	PDF#00-041-1428	2.40(5%)	5.6 (0.5)	20
🟪 Vaterite - $Ca(CO_3)$	PDF#04-015-4788	1.14(0%)	8.0 (0.7)	109
☐ Others + Amorphous			30.5 (1.3)	

XRF(Wt%): Fe=2.0%, Ca=29.9%, Si=16.8%, Al=1.5%, Mg=1.4%, O=45.7%, C=2.0%, H=0.8%

NOTE: Fitting Halted at Iteration 28(4): R=16.62% (E=13.64%, R/E=1.22, P=53, EPS=0.5)

USDOE Albany

[ULTIMAIII|Smithd]<C:\ScanData\OConnorGroup\2009\09A0211-220 DWL-2 6_2011> Friday, April 12, 2013 01:50p (MDI/JADE9)

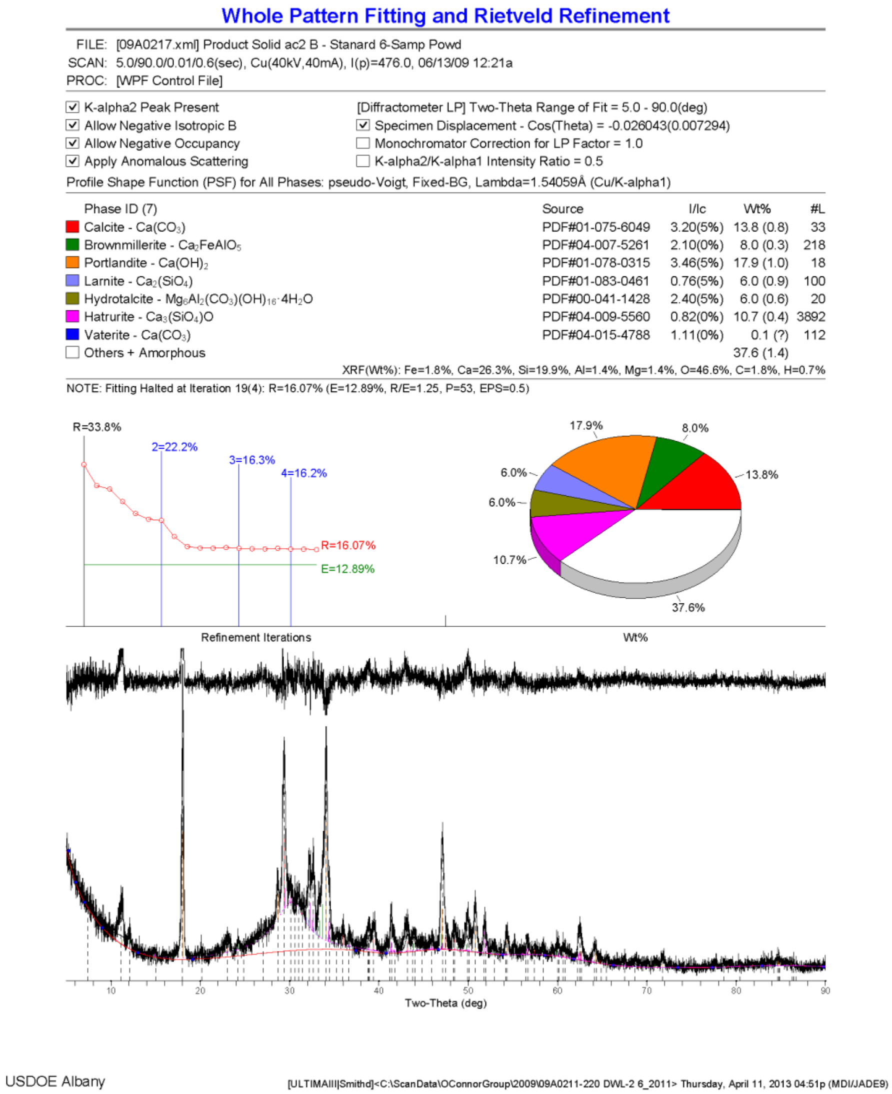

Whole Pattern Fitting and Rietveld Refinement

FILE: [09A0217.xml] Product Solid ac2 B - Stanard 6-Samp Powd
SCAN: 5.0/90.0/0.01/0.6(sec), Cu(40kV,40mA), I(p)=476.0, 06/13/09 12:21a
PROC: [WPF Control File]

☑ K-alpha2 Peak Present
☑ Allow Negative Isotropic B
☑ Allow Negative Occupancy
☑ Apply Anomalous Scattering

[Diffractometer LP] Two-Theta Range of Fit = 5.0 - 90.0(deg)
☑ Specimen Displacement - Cos(Theta) = -0.026043(0.007294)
☐ Monochromator Correction for LP Factor = 1.0
☐ K-alpha2/K-alpha1 Intensity Ratio = 0.5

Profile Shape Function (PSF) for All Phases: pseudo-Voigt, Fixed-BG, Lambda=1.54059Å (Cu/K-alpha1)

	Phase ID (7)	Source	I/Ic	Wt%	#L
🟥	Calcite - $Ca(CO_3)$	PDF#01-075-6049	3.20(5%)	13.8 (0.8)	33
🟩	Brownmillerite - Ca_2FeAlO_5	PDF#04-007-5261	2.10(0%)	8.0 (0.3)	218
🟧	Portlandite - $Ca(OH)_2$	PDF#01-078-0315	3.46(5%)	17.9 (1.0)	18
🟪	Larnite - $Ca_2(SiO_4)$	PDF#01-083-0461	0.76(5%)	6.0 (0.9)	100
🟫	Hydrotalcite - $Mg_6Al_2(CO_3)(OH)_{16}\cdot4H_2O$	PDF#00-041-1428	2.40(5%)	6.0 (0.6)	20
🟪	Hatrurite - $Ca_3(SiO_4)O$	PDF#04-009-5560	0.82(0%)	10.7 (0.4)	3892
🟦	Vaterite - $Ca(CO_3)$	PDF#04-015-4788	1.11(0%)	0.1 (?)	112
☐	Others + Amorphous			37.6 (1.4)	

XRF(Wt%): Fe=1.8%, Ca=26.3%, Si=19.9%, Al=1.4%, Mg=1.4%, O=46.6%, C=1.8%, H=0.7%

NOTE: Fitting Halted at Iteration 19(4): R=16.07% (E=12.89%, R/E=1.25, P=53, EPS=0.5)

USDOE Albany

[ULTIMAIII|Smithd]<C:\ScanData\OConnorGroup\2009\09A0211-220 DWL-2 6_2011> Thursday, April 11, 2013 04:51p (MDI/JADE9)

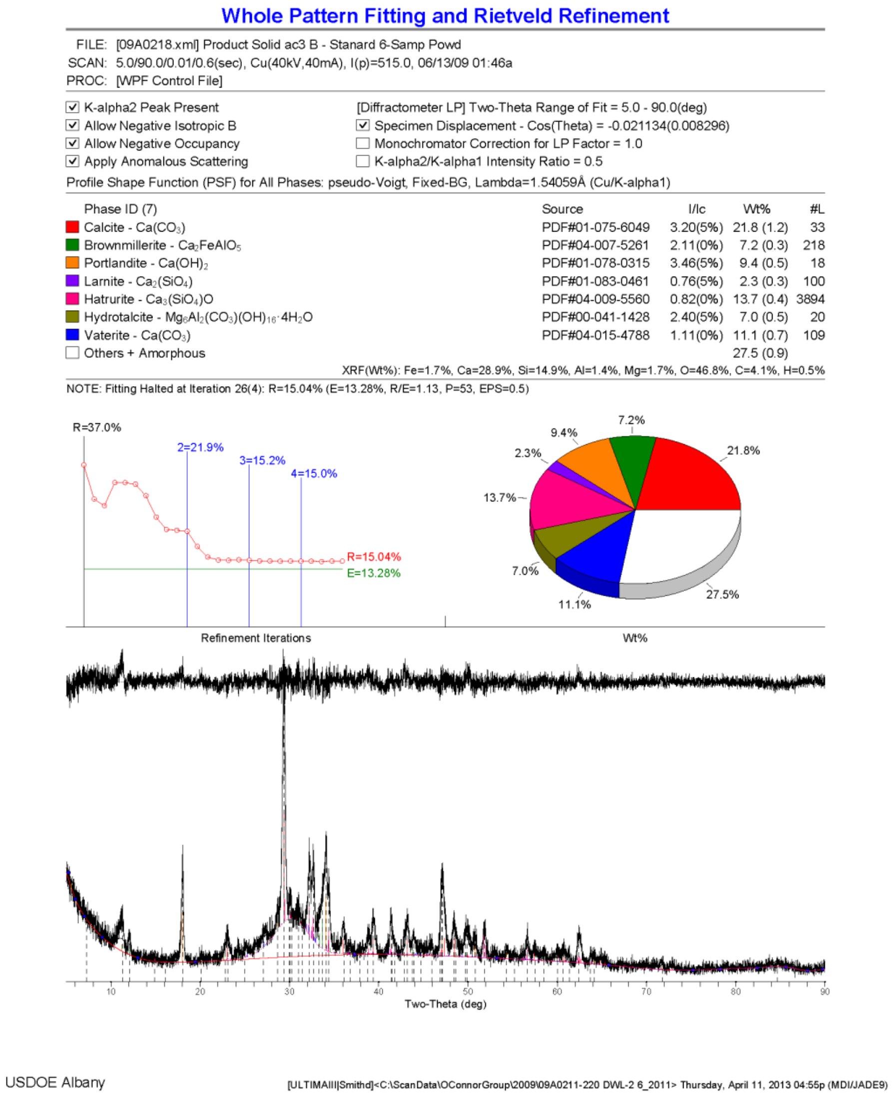

Whole Pattern Fitting and Rietveld Refinement

FILE: [09A0218.xml] Product Solid ac3 B - Stanard 6-Samp Powd
SCAN: 5.0/90.0/0.01/0.6(sec), Cu(40kV,40mA), I(p)=515.0, 06/13/09 01:46a
PROC: [WPF Control File]

- ☑ K-alpha2 Peak Present
- ☑ Allow Negative Isotropic B
- ☑ Allow Negative Occupancy
- ☑ Apply Anomalous Scattering

[Diffractometer LP] Two-Theta Range of Fit = 5.0 - 90.0(deg)
- ☑ Specimen Displacement - Cos(Theta) = -0.021134(0.008296)
- ☐ Monochromator Correction for LP Factor = 1.0
- ☐ K-alpha2/K-alpha1 Intensity Ratio = 0.5

Profile Shape Function (PSF) for All Phases: pseudo-Voigt, Fixed-BG, Lambda=1.54059Å (Cu/K-alpha1)

	Phase ID (7)	Source	I/Ic	Wt%	#L
🟥	Calcite - $Ca(CO_3)$	PDF#01-075-6049	3.20(5%)	21.8 (1.2)	33
🟩	Brownmillerite - Ca_2FeAlO_5	PDF#04-007-5261	2.11(0%)	7.2 (0.3)	218
🟧	Portlandite - $Ca(OH)_2$	PDF#01-078-0315	3.46(5%)	9.4 (0.5)	18
🟪	Larnite - $Ca_2(SiO_4)$	PDF#01-083-0461	0.76(5%)	2.3 (0.3)	100
■	Hatrurite - $Ca_3(SiO_4)O$	PDF#04-009-5560	0.82(0%)	13.7 (0.4)	3894
■	Hydrotalcite - $Mg_6Al_2(CO_3)(OH)_{16}\cdot 4H_2O$	PDF#00-041-1428	2.40(5%)	7.0 (0.5)	20
🟦	Vaterite - $Ca(CO_3)$	PDF#04-015-4788	1.11(0%)	11.1 (0.7)	109
☐	Others + Amorphous			27.5 (0.9)	

XRF(Wt%): Fe=1.7%, Ca=28.9%, Si=14.9%, Al=1.4%, Mg=1.7%, O=46.8%, C=4.1%, H=0.5%

NOTE: Fitting Halted at Iteration 26(4): R=15.04% (E=13.28%, R/E=1.13, P=53, EPS=0.5)

USDOE Albany

[ULTIMAIII|Smithd]<C:\ScanData\OConnorGroup\2009\09A0211-220 DWL-2 6_2011> Thursday, April 11, 2013 04:55p (MDI/JADE9)

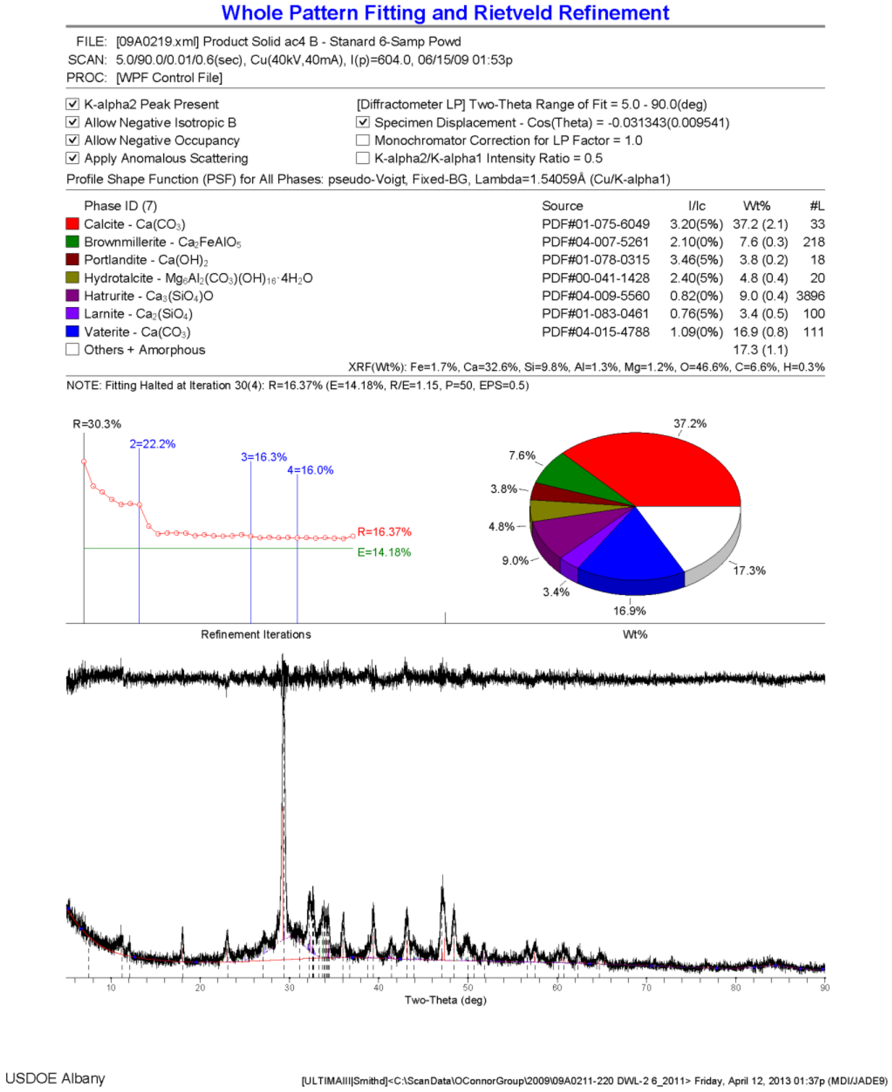

Whole Pattern Fitting and Rietveld Refinement

FILE: [09A0219.xml] Product Solid ac4 B - Stanard 6-Samp Powd
SCAN: 5.0/90.0/0.01/0.6(sec), Cu(40kV,40mA), I(p)=604.0, 06/15/09 01:53p
PROC: [WPF Control File]

☑ K-alpha2 Peak Present
☑ Allow Negative Isotropic B
☑ Allow Negative Occupancy
☑ Apply Anomalous Scattering

[Diffractometer LP] Two-Theta Range of Fit = 5.0 - 90.0(deg)
☑ Specimen Displacement - Cos(Theta) = -0.031343(0.009541)
☐ Monochromator Correction for LP Factor = 1.0
☐ K-alpha2/K-alpha1 Intensity Ratio = 0.5

Profile Shape Function (PSF) for All Phases: pseudo-Voigt, Fixed-BG, Lambda=1.54059Å (Cu/K-alpha1)

Phase ID (7)	Source	I/Ic	Wt%	#L
🟥 Calcite - $Ca(CO_3)$	PDF#01-075-6049	3.20(5%)	37.2 (2.1)	33
🟩 Brownmillerite - Ca_2FeAlO_5	PDF#04-007-5261	2.10(0%)	7.6 (0.3)	218
🟫 Portlandite - $Ca(OH)_2$	PDF#01-078-0315	3.46(5%)	3.8 (0.2)	18
🟨 Hydrotalcite - $Mg_6Al_2(CO_3)(OH)_{16}\cdot 4H_2O$	PDF#00-041-1428	2.40(5%)	4.8 (0.4)	20
🟪 Hatrurite - $Ca_3(SiO_4)O$	PDF#04-009-5560	0.82(0%)	9.0 (0.4)	3896
🟪 Larnite - $Ca_2(SiO_4)$	PDF#01-083-0461	0.76(5%)	3.4 (0.5)	100
🟦 Vaterite - $Ca(CO_3)$	PDF#04-015-4788	1.09(0%)	16.9 (0.8)	111
☐ Others + Amorphous			17.3 (1.1)	

XRF(Wt%): Fe=1.7%, Ca=32.6%, Si=9.8%, Al=1.3%, Mg=1.2%, O=46.6%, C=6.6%, H=0.3%

NOTE: Fitting Halted at Iteration 30(4): R=16.37% (E=14.18%, R/E=1.15, P=50, EPS=0.5)

USDOE Albany

[ULTIMAIII|Smithd]<C:\ScanData\OConnorGroup\2009\09A0211-220 DWL-2 6_2011> Friday, April 12, 2013 01:37p (MDI/JADE9)

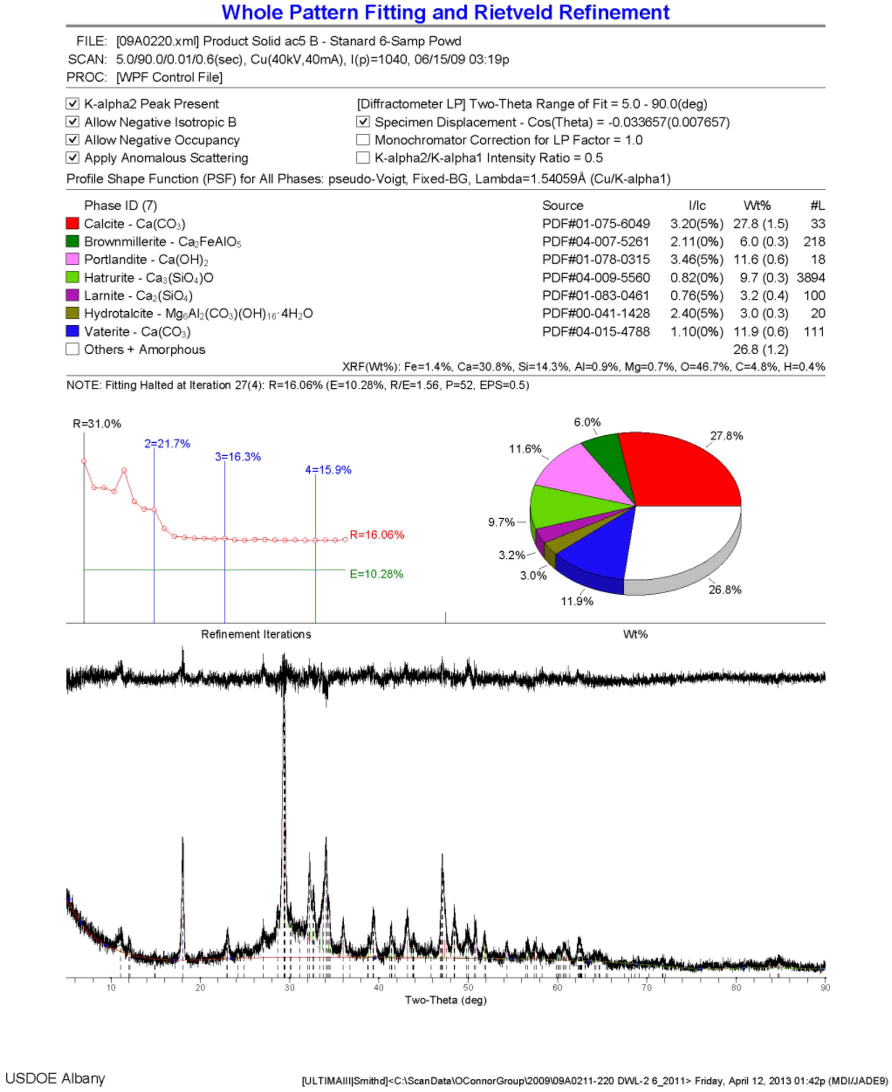

Whole Pattern Fitting and Rietveld Refinement

FILE: [09A0220.xml] Product Solid ac5 B - Stanard 6-Samp Powd
SCAN: 5.0/90.0/0.01/0.6(sec), Cu(40kV,40mA), I(p)=1040, 06/15/09 03:19p
PROC: [WPF Control File]

- ☑ K-alpha2 Peak Present
- ☑ Allow Negative Isotropic B
- ☑ Allow Negative Occupancy
- ☑ Apply Anomalous Scattering

[Diffractometer LP] Two-Theta Range of Fit = 5.0 - 90.0(deg)
- ☑ Specimen Displacement - Cos(Theta) = -0.033657(0.007657)
- ☐ Monochromator Correction for LP Factor = 1.0
- ☐ K-alpha2/K-alpha1 Intensity Ratio = 0.5

Profile Shape Function (PSF) for All Phases: pseudo-Voigt, Fixed-BG, Lambda=1.54059Å (Cu/K-alpha1)

Phase ID (7)	Source	I/Ic	Wt%	#L
🟥 Calcite - Ca(CO_3)	PDF#01-075-6049	3.20(5%)	27.8 (1.5)	33
🟩 Brownmillerite - Ca_2FeAlO_5	PDF#04-007-5261	2.11(0%)	6.0 (0.3)	218
🟪 Portlandite - $Ca(OH)_2$	PDF#01-078-0315	3.46(5%)	11.6 (0.6)	18
🟩 Hatrurite - $Ca_3(SiO_4)O$	PDF#04-009-5560	0.82(0%)	9.7 (0.3)	3894
🟪 Larnite - $Ca_2(SiO_4)$	PDF#01-083-0461	0.76(5%)	3.2 (0.4)	100
🟫 Hydrotalcite - $Mg_6Al_2(CO_3)(OH)_{16}\cdot 4H_2O$	PDF#00-041-1428	2.40(5%)	3.0 (0.3)	20
🟦 Vaterite - Ca(CO_3)	PDF#04-015-4788	1.10(0%)	11.9 (0.6)	111
☐ Others + Amorphous			26.8 (1.2)	

XRF(Wt%): Fe=1.4%, Ca=30.8%, Si=14.3%, Al=0.9%, Mg=0.7%, O=46.7%, C=4.8%, H=0.4%

NOTE: Fitting Halted at Iteration 27(4): R=16.06% (E=10.28%, R/E=1.56, P=52, EPS=0.5)

USDOE Albany

[ULTIMAIII|Smithd]<C:\ScanData\OConnorGroup\2009\09A0211-220 DWL-2 6_2011> Friday, April 12, 2013 01:42p (MDI/JADE9)

APPENDIX B

CLASS H CEMENT EXPOSED TO SUPERCRITICAL CO_2-O_2

Scanning Electron MicroscopyBackscatter and X-ray Elemental Maps

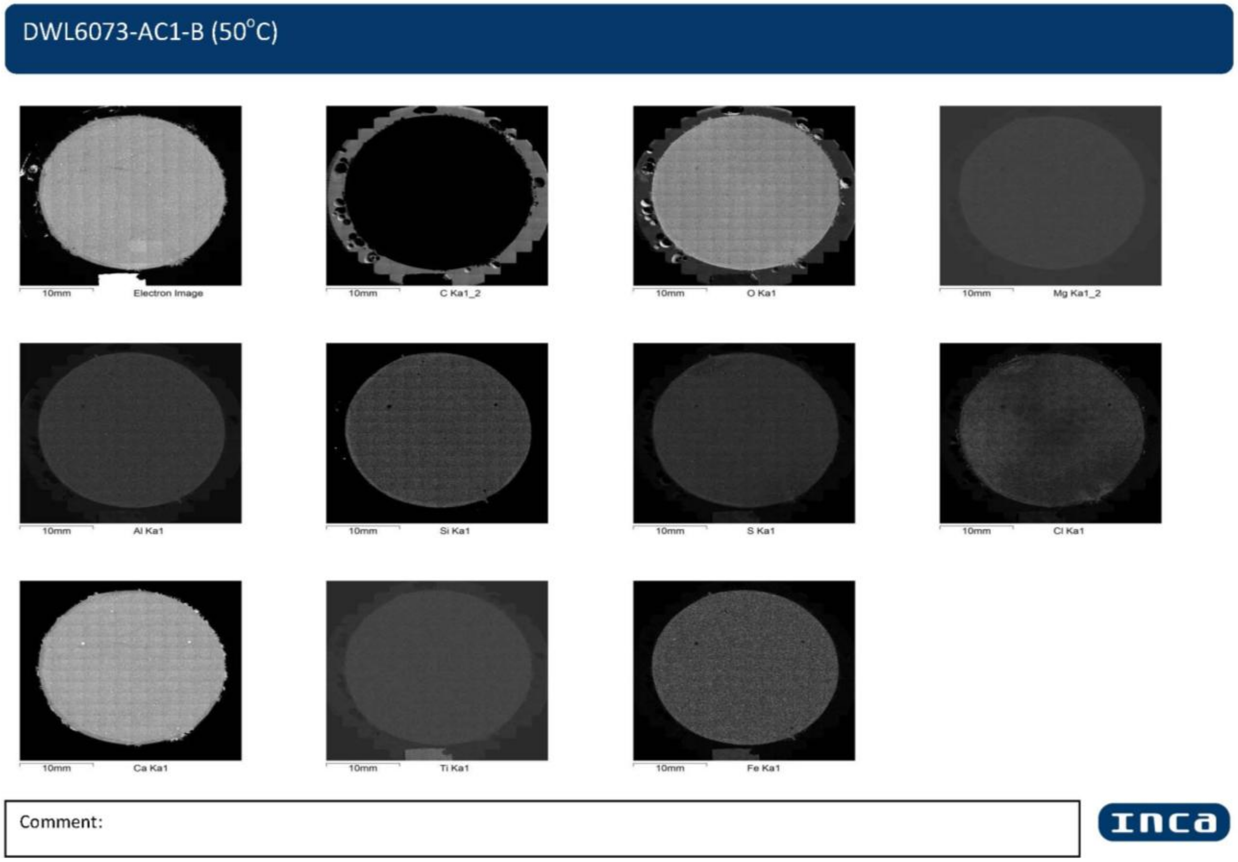

DWL6073-AC1-B (50°C)

Comment:

DWL6-73-AC1-B CO2-O2 50°C

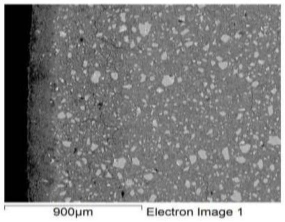

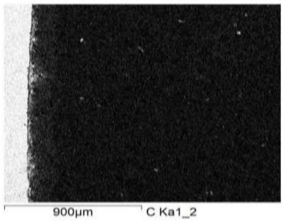

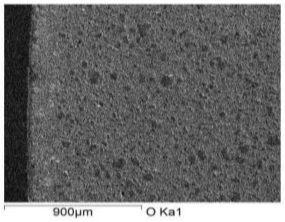

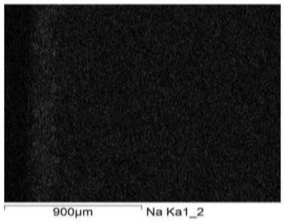

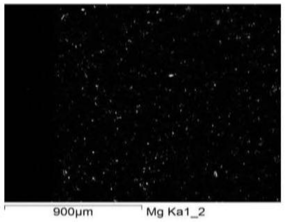

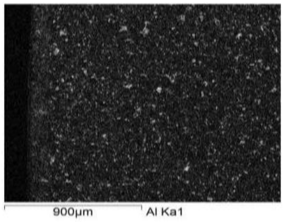

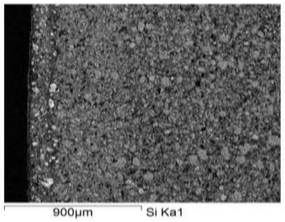

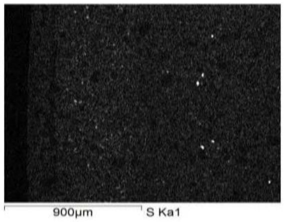

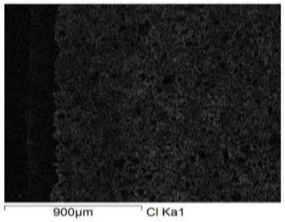

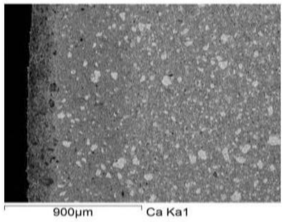

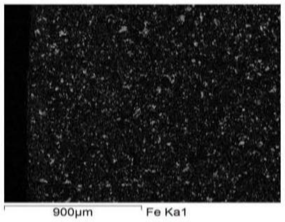

Comment:

DWL5-53-AC1-B 85°C

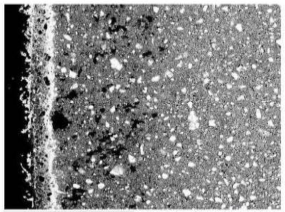

Electron Image 1

C Ka1_2

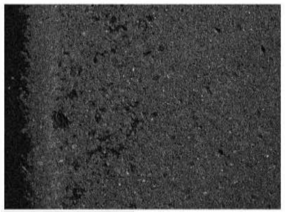

O Ka1

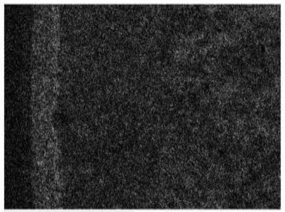

Na Ka1_2

Mg Ka1_2

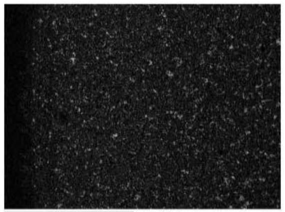

Al Ka1

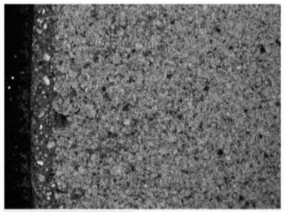

Si Ka1

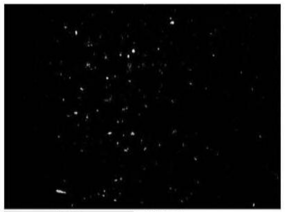

S Ka1

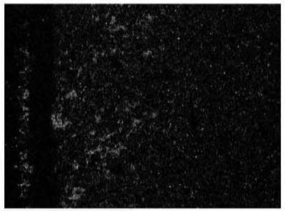

Cl Ka1

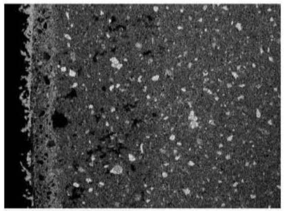

Ca Ka1

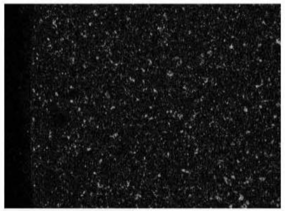

Fe Ka1

Comment:

DWL5-53-AC1-B

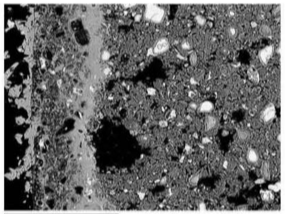

Electron Image 1

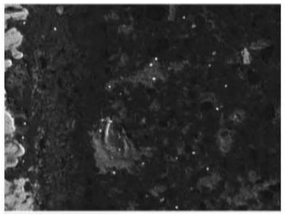

C Ka1_2

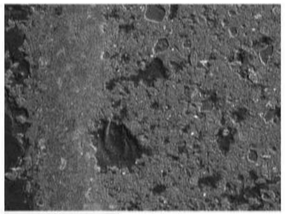

O Ka1

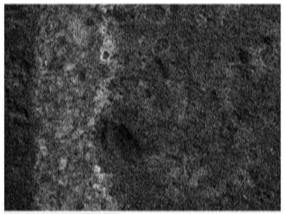

Na Ka1_2

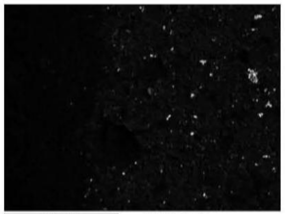

Mg Ka1_2

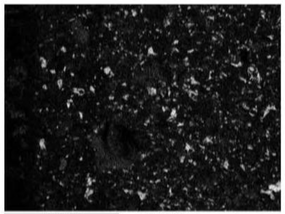

Al Ka1

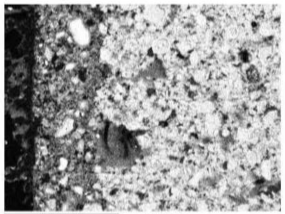

Si Ka1

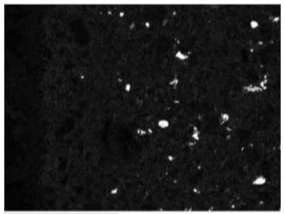

S Ka1

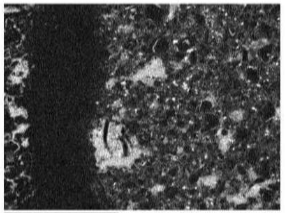

Cl Ka1

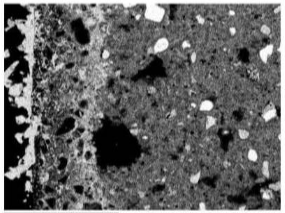

Ca Ka1

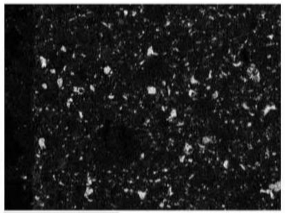

Fe Ka1

Comment:

DWL-3-28-AC5-B(4) CO2/O2

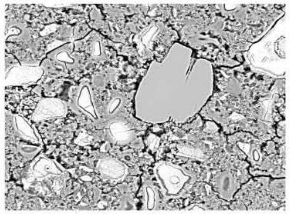
Electron Image 1

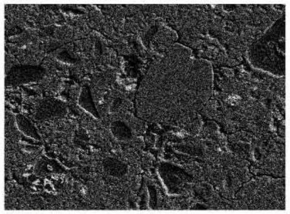
O Ka1

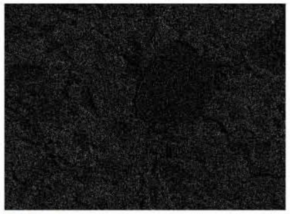
Na Ka1_2

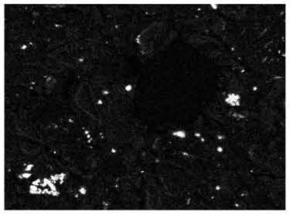
Mg Ka1_2

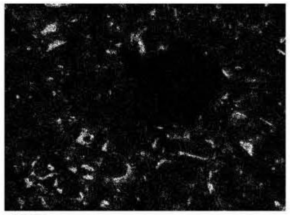
Al Ka1

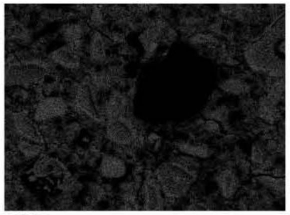
Si Ka1

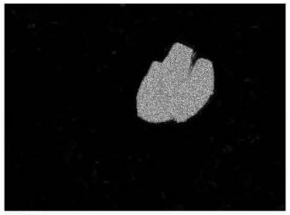
S Ka1

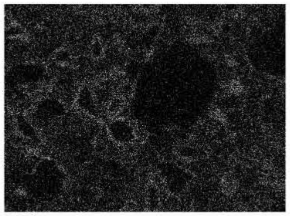
Cl Ka1

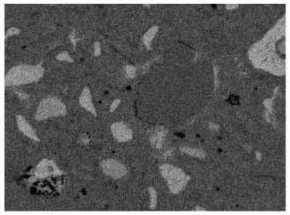
Ca Ka1

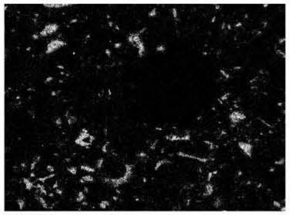
Fe Ka1

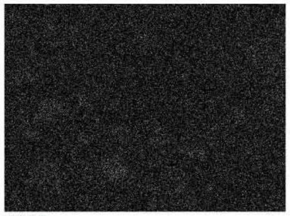
K Ka1

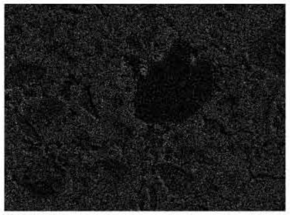
C Ka1_2

Comment:

DWL-3-AC1-B(2) CO2/O2

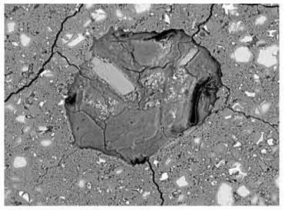
Electron Image 1


O Ka1

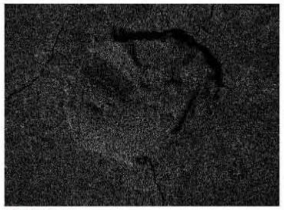
Na Ka1_2


Mg Ka1_2

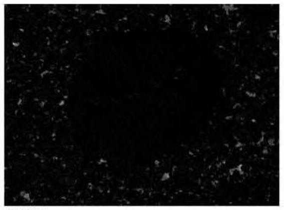
Al Ka1

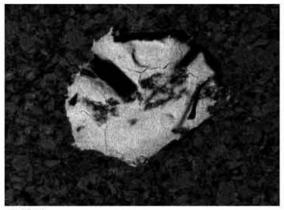
Si Ka1

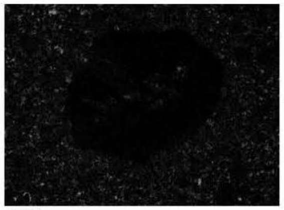
S Ka1

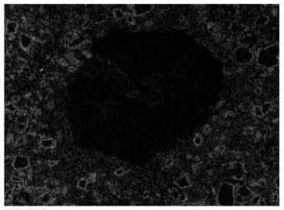
Cl Ka1

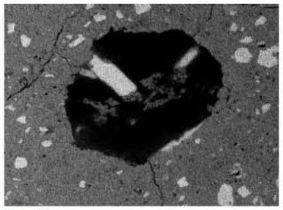
Ca Ka1

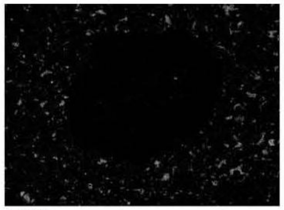
Fe Ka1

Comment:

DWL-3-28-AC5-B(2)

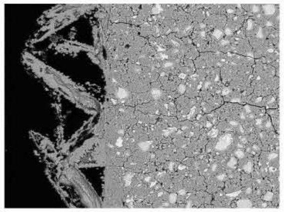
Electron Image 1


C Ka1_2

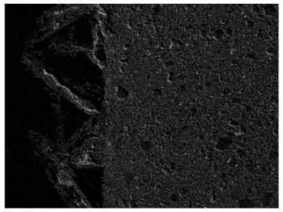
O Ka1

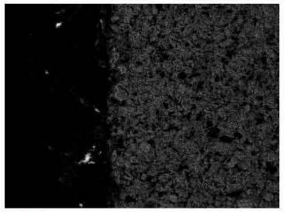
Si Ka1

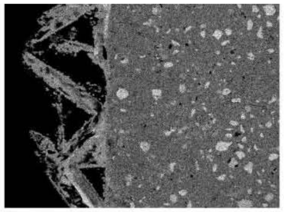
Ca Ka1

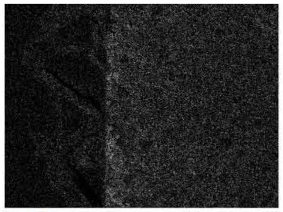
Na Ka1_2

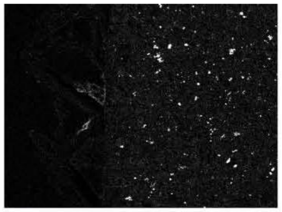
Mg Ka1_2


K Ka1


S Ka1

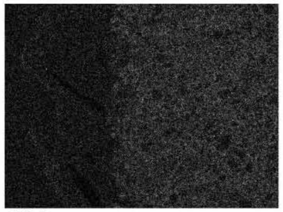
Cl Ka1

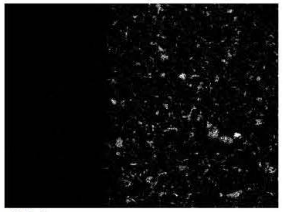
Al Ka1

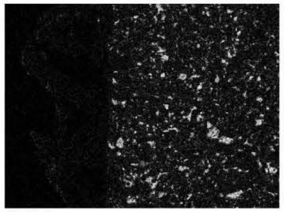
Fe Ka1

Comment:

DWL6-73-AC2-T

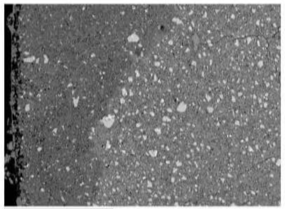

Electron Image 1


C Ka1_2

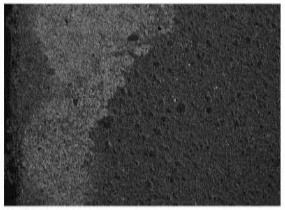
O Ka1


Na Ka1_2

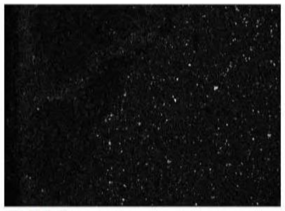
Mg Ka1_2

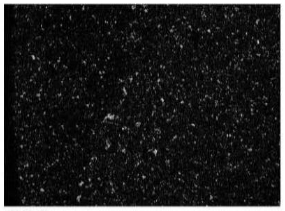
Al Ka1

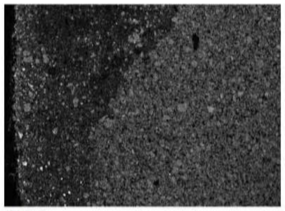
Si Ka1

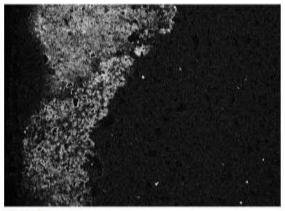
S Ka1

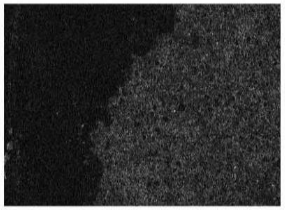
Cl Ka1

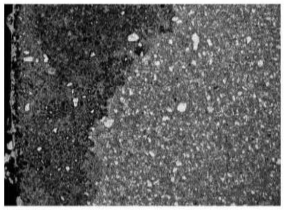
Ca Ka1

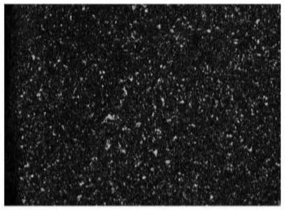
Fe Ka1

Comment:

DWL6-73-AC2-T

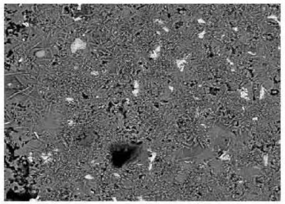
100µm Electron Image 1

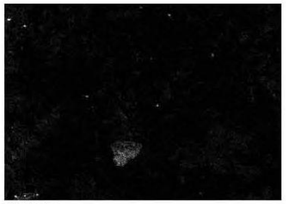
C Ka1_2


O Ka1

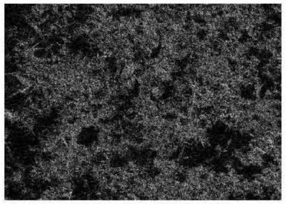
Na Ka1_2

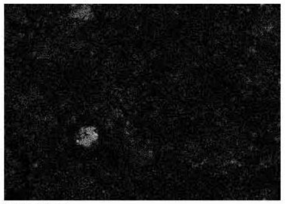
Mg Ka1_2

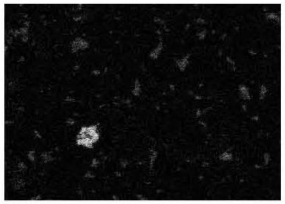
Al Ka1

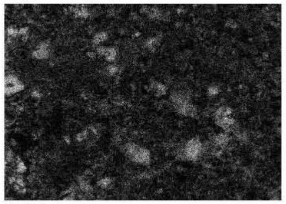
Si Ka1

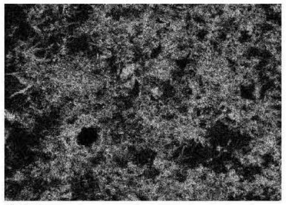
S Ka1

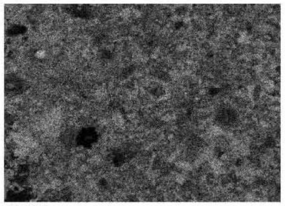
Ca Ka1

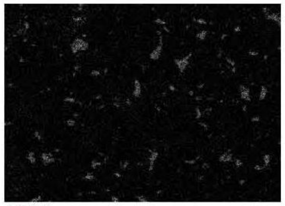
Fe Ka1

Comment:

X-ray Diffraction Patterns: Class H Cement Exposed To Supercritical CO_2-O_2

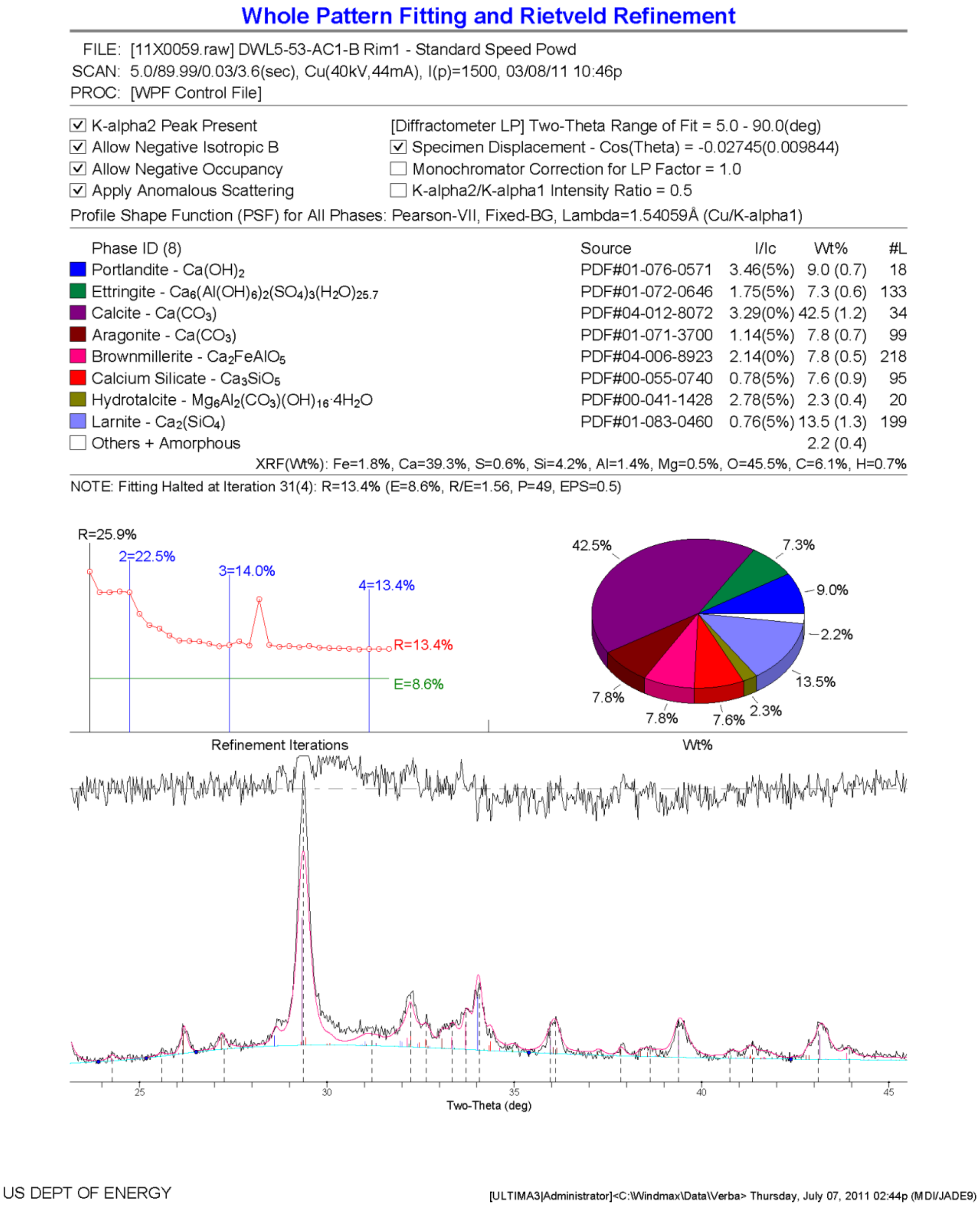

Whole Pattern Fitting and Rietveld Refinement

FILE: [11X0059.raw] DWL5-53-AC1-B Rim1 - Standard Speed Powd
SCAN: 5.0/89.99/0.03/3.6(sec), Cu(40kV,44mA), I(p)=1500, 03/08/11 10:46p
PROC: [WPF Control File]

☑ K-alpha2 Peak Present
☑ Allow Negative Isotropic B
☑ Allow Negative Occupancy
☑ Apply Anomalous Scattering

[Diffractometer LP] Two-Theta Range of Fit = 5.0 - 90.0(deg)
☑ Specimen Displacement - Cos(Theta) = -0.02745(0.009844)
☐ Monochromator Correction for LP Factor = 1.0
☐ K-alpha2/K-alpha1 Intensity Ratio = 0.5

Profile Shape Function (PSF) for All Phases: Pearson-VII, Fixed-BG, Lambda=1.54059Å (Cu/K-alpha1)

Phase ID (8)	Source	I/Ic	Wt%	#L
■ Portlandite - $Ca(OH)_2$	PDF#01-076-0571	3.46(5%)	9.0 (0.7)	18
■ Ettringite - $Ca_6(Al(OH)_6)_2(SO_4)_3(H_2O)_{25.7}$	PDF#01-072-0646	1.75(5%)	7.3 (0.6)	133
■ Calcite - $Ca(CO_3)$	PDF#04-012-8072	3.29(0%)	42.5 (1.2)	34
■ Aragonite - $Ca(CO_3)$	PDF#01-071-3700	1.14(5%)	7.8 (0.7)	99
■ Brownmillerite - Ca_2FeAlO_5	PDF#04-006-8923	2.14(0%)	7.8 (0.5)	218
■ Calcium Silicate - Ca_3SiO_5	PDF#00-055-0740	0.78(5%)	7.6 (0.9)	95
■ Hydrotalcite - $Mg_6Al_2(CO_3)(OH)_{16}{\cdot}4H_2O$	PDF#00-041-1428	2.78(5%)	2.3 (0.4)	20
■ Larnite - $Ca_2(SiO_4)$	PDF#01-083-0460	0.76(5%)	13.5 (1.3)	199
☐ Others + Amorphous			2.2 (0.4)	

XRF(Wt%): Fe=1.8%, Ca=39.3%, S=0.6%, Si=4.2%, Al=1.4%, Mg=0.5%, O=45.5%, C=6.1%, H=0.7%

NOTE: Fitting Halted at Iteration 31(4): R=13.4% (E=8.6%, R/E=1.56, P=49, EPS=0.5)

US DEPT OF ENERGY

[ULTIMA3|Administrator]<C:\Windmax\Data\Verba> Thursday, July 07, 2011 02:44p (MDI/JADE9)

Whole Pattern Fitting and Rietveld Refinement

FILE: [11X0061.raw] DWL5-66-AC3-B Rim - Standard Speed Powd
SCAN: 5.0/89.99/0.03/3.6(sec), Cu(40kV,44mA), I(p)=647.0, 03/09/11 04:27a
PROC: [WPF Control File]

☑ K-alpha2 Peak Present	[Diffractometer LP] Two-Theta Range of Fit = 5.0 - 90.0(deg)
☑ Allow Negative Isotropic B	☑ Specimen Displacement - Cos(Theta) = -0.026534(0.008295)
☑ Allow Negative Occupancy	☐ Monochromator Correction for LP Factor = 1.0
☑ Apply Anomalous Scattering	☐ K-alpha2/K-alpha1 Intensity Ratio = 0.5

Profile Shape Function (PSF) for All Phases: Pearson-VII, Fixed-BG, Lambda=1.54059Å (Cu/K-alpha1)

	Phase ID (9)	Source	I/Ic	Wt%	#L
🟦	Portlandite - $Ca(OH)_2$	PDF#01-076-0571	3.46(5%)	12.0 (0.7)	18
🟩	Ettringite - $Ca_6(Al(OH)_6)_2(SO_4)_3(H_2O)_{25.7}$	PDF#01-072-0646	1.75(5%)	12.0 (0.7)	133
🟪	Calcite - $Ca(CO_3)$	PDF#04-012-8072	3.28(0%)	8.9 (0.4)	34
🟫	Aragonite - $Ca(CO_3)$	PDF#01-071-3700	1.14(5%)	4.4 (1.0)	98
🟦	Vaterite - $Ca(CO_3)$	PDF#04-010-6864	1.21(0%)	10.5 (0.9)	30
🟥	Brownmillerite - Ca_2FeAlO_5	PDF#04-006-8923	2.15(0%)	5.3 (0.3)	218
🟥	Calcium Silicate - Ca_3SiO_5	PDF#00-055-0740	0.78(5%)	10.0 (0.8)	95
🟫	Hydrotalcite - $Mg_6Al_2(CO_3)(OH)_{16}\cdot 4H_2O$	PDF#00-041-1428	2.78(5%)	3.5 (0.3)	20
🟦	Larnite - $Ca_2(SiO_4)$	PDF#01-083-0460	0.76(5%)	2.7 (0.5)	199
☐	Others + Amorphous			30.7 (1.3)	

XRF(Wt%): Fe=1.2%, Ca=26.6%, S=0.9%, Si=16.0%, Al=1.4%, Mg=0.8%, O=49.0%, C=2.9%, H=1.1%

NOTE: Fitting Halted at Iteration 27(4): R=10.95% (E=8.73%, R/E=1.25, P=53, EPS=0.5)

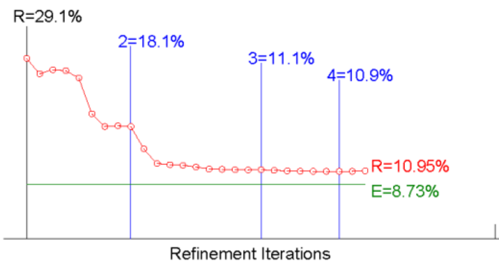

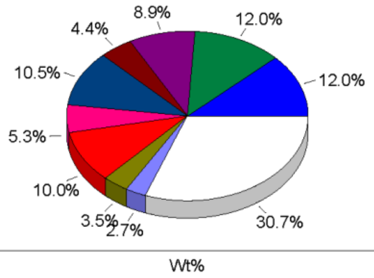

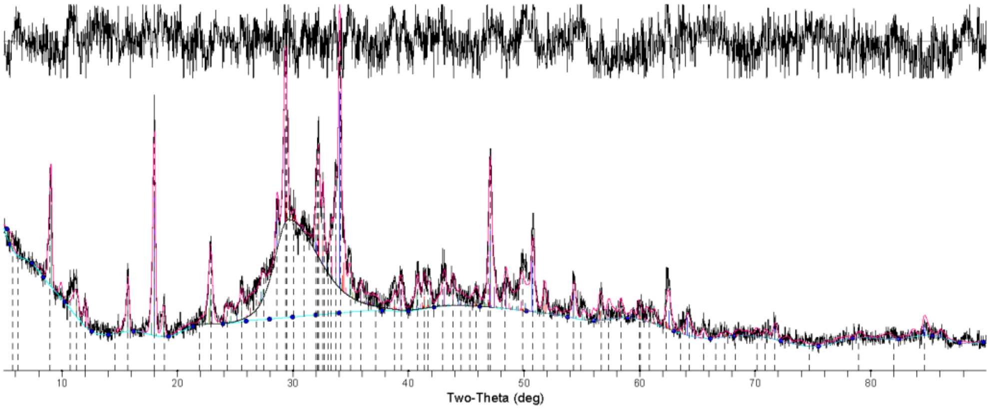

US DEPT OF ENERGY

[ULTIMA3|Administrator]<C:\Windmax\Data\Verba> Thursday, July 07, 2011 03:25p (MDI/JADE9)

APPENDIX C

MT. SIMON SANDSTONE & GRANDE RONDE BASALT BONDED TO CLASS H CEMENT EXPOSED TO SUPERCRITICAL CO_2

Scanning Electron MicroscopyBackscatter and X-ray Elemental Maps

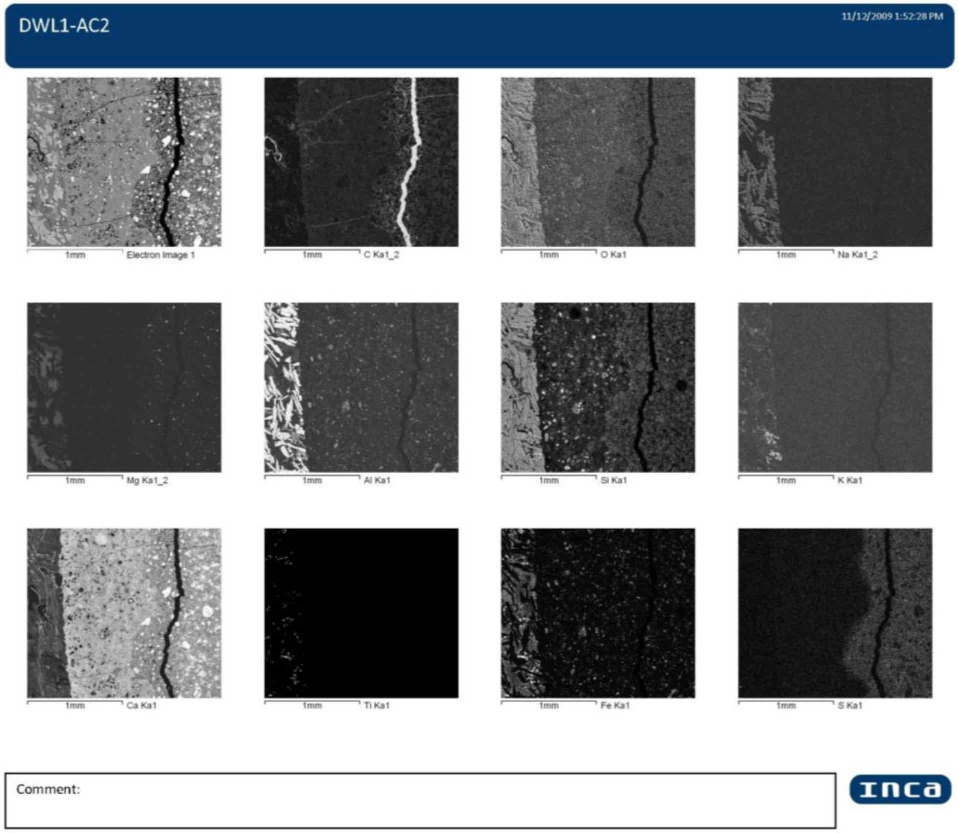

DWL-1-AC1-B

11/2/2009 3:44:59 PM

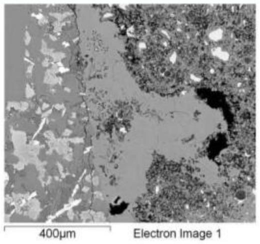

Electron Image 1

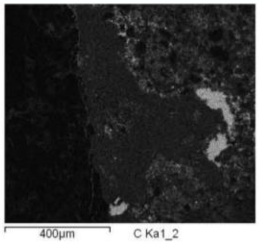

C Ka1_2

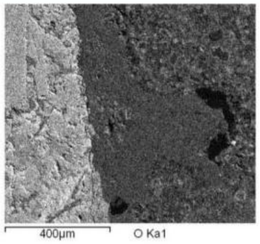

O Ka1

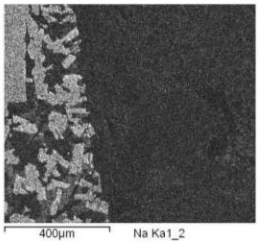

Na Ka1_2

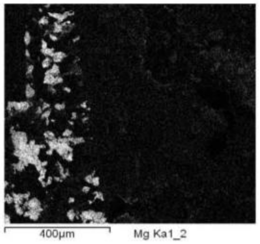

Mg Ka1_2

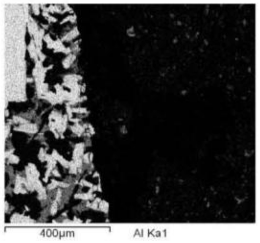

Al Ka1

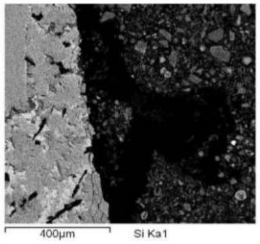

Si Ka1

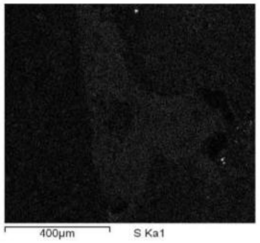

S Ka1

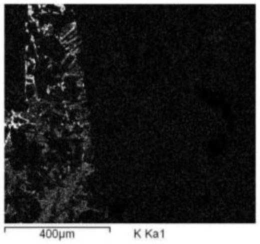

K Ka1

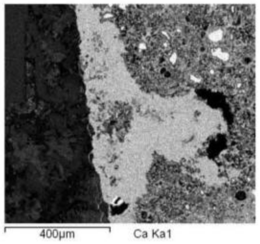

Ca Ka1

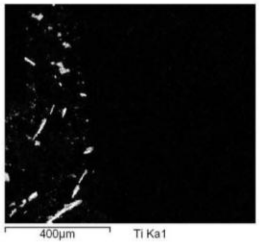

Ti Ka1

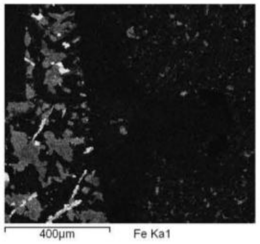

Fe Ka1

Comment:

DWL-1-AC1-B

11/2/2009 4:56:11 PM

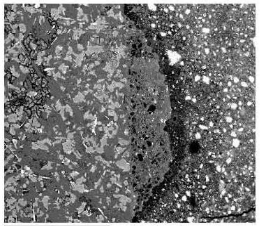

Electron Image 1

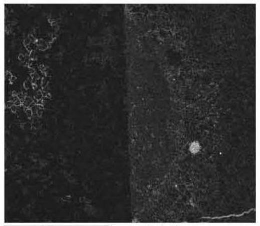

C Ka1_2

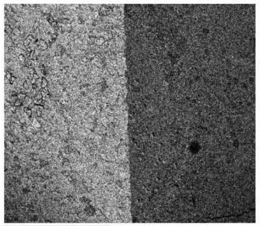

O Ka1

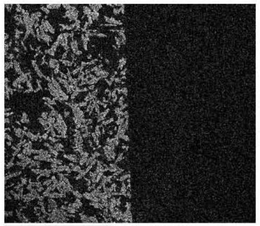

Na Ka1_2

Mg Ka1_2

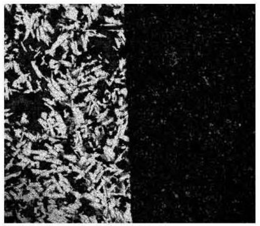

Al Ka1

Si Ka1

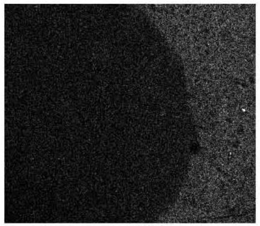

S Ka1

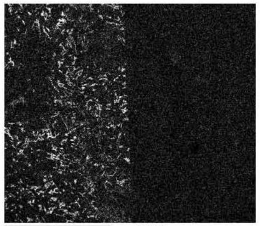

K Ka1

Ca Ka1

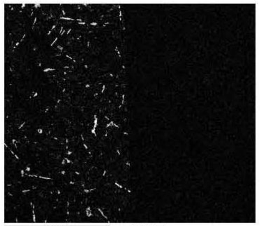

Ti Ka1

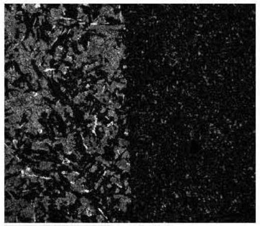

Fe Ka1

Comment:

Project 1

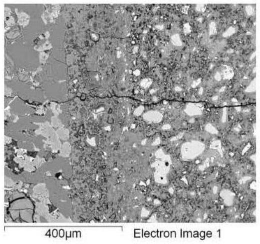

Electron Image 1

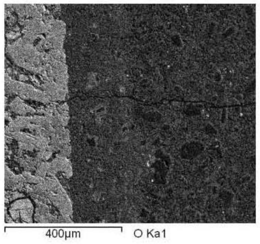

O Ka1

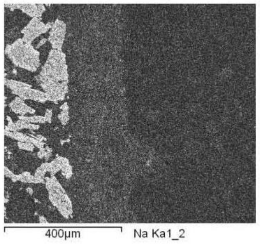

Na Ka1_2

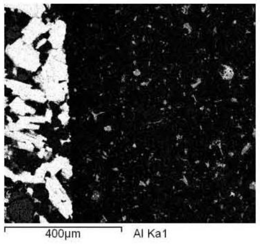

Al Ka1

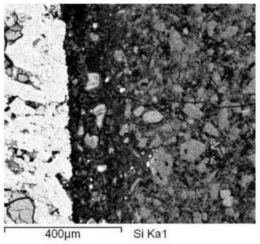

Si Ka1

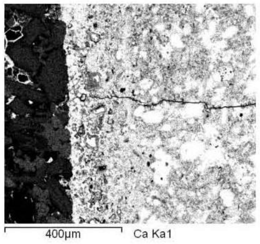

Ca Ka1

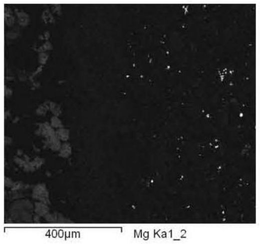

Mg Ka1_2

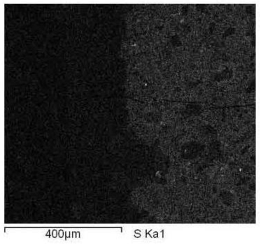

S Ka1

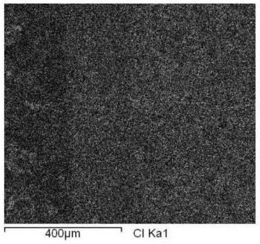

Cl Ka1

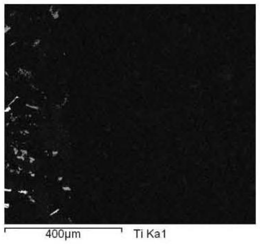

Ti Ka1

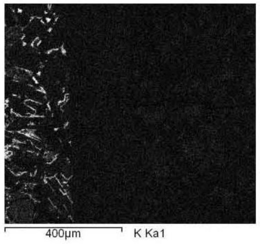

K Ka1

Comment:

DWL1-AC1-Tr

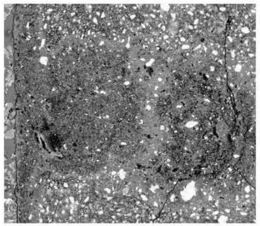

Electron Image 1

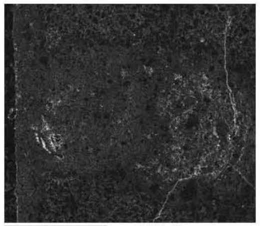

C Ka1_2

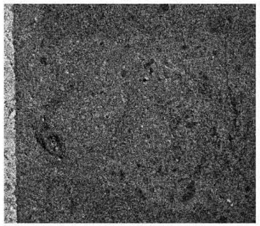

O Ka1

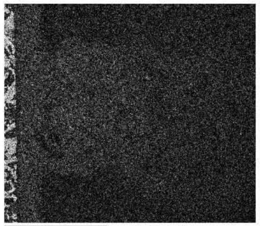

Na Ka1_2

Mg Ka1_2

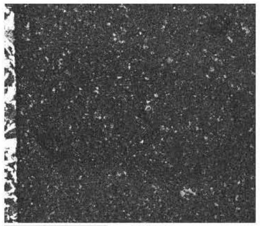

Al Ka1

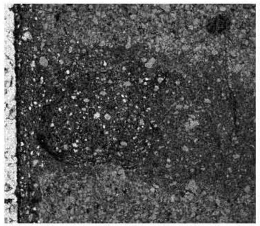

Si Ka1

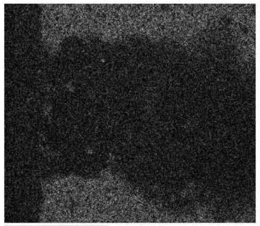

S Ka1

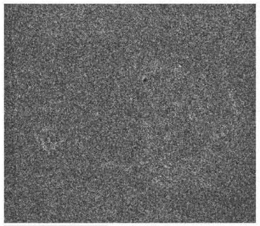

Cl Ka1

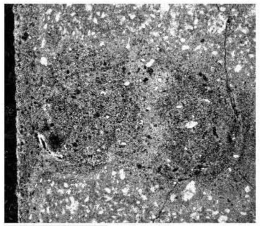

Ca Ka1

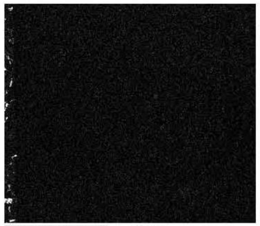

Ti Ka1

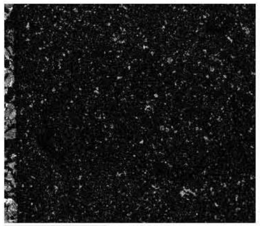

Fe Ka1

Comment:

DWL1-AC2

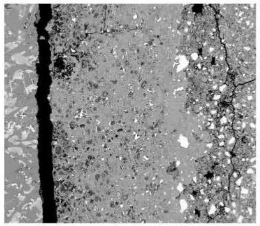

Electron Image 1

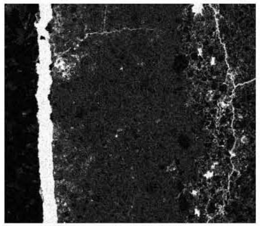

C Ka1_2

O Ka1

Mg Ka1_2

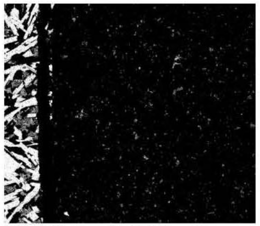

Al Ka1

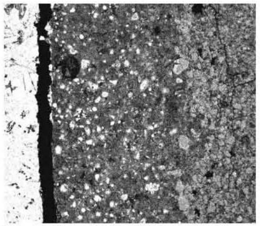

Si Ka1

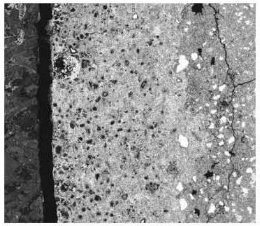

Ca Ka1

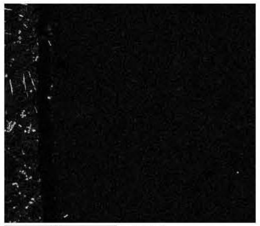

Ti Ka1

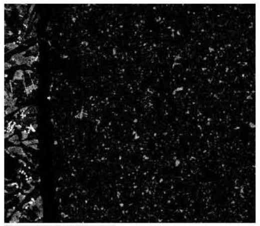

Fe Ka1

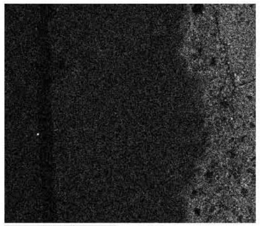

S Ka1

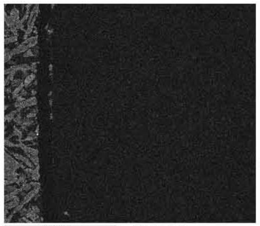

Na Ka1_2

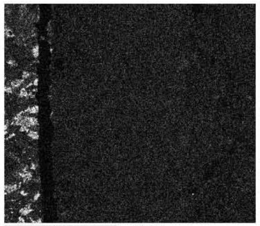

K Ka1

Comment:

DWL1-AC4

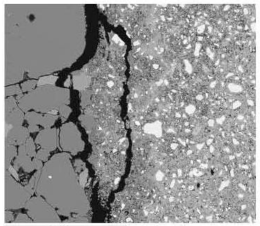

Electron Image 1

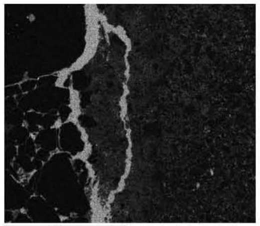

C Ka1_2

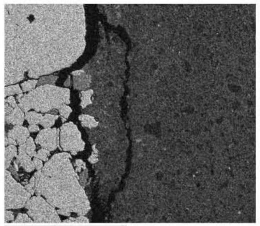

O Ka1

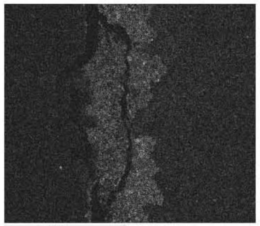

Na Ka1_2

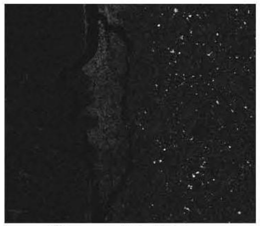

Mg Ka1_2

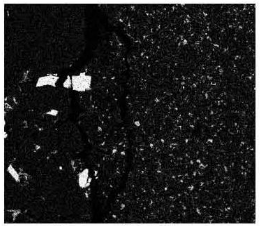

Al Ka1

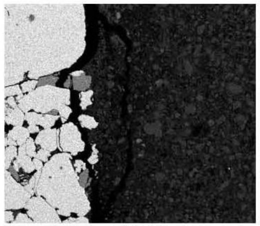

Si Ka1

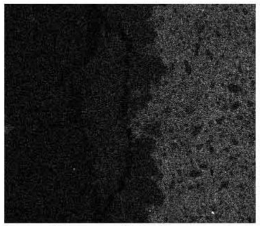

S Ka1

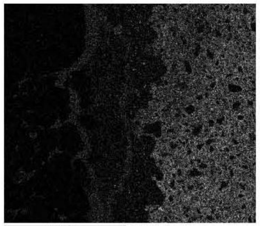

Cl Ka1

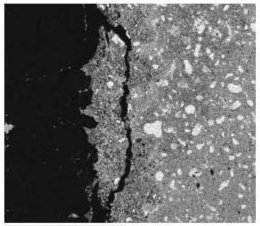

Ca Ka1

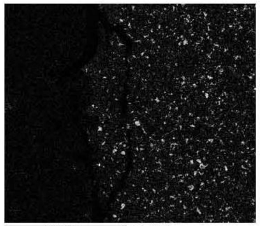

Fe Ka1

Comment:

DWL1-AC4

11/9/2009 5:57:36 PM

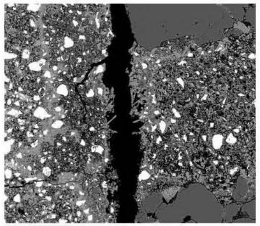

Electron Image 1

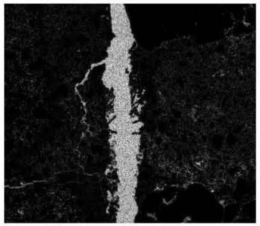

C Ka1_2

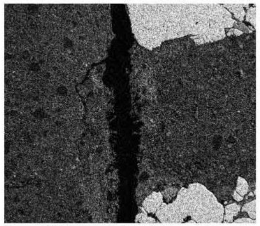

O Ka1

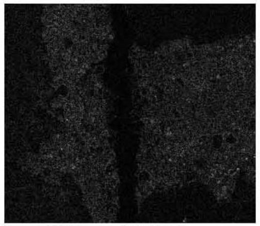

Na Ka1_2

Mg Ka1_2

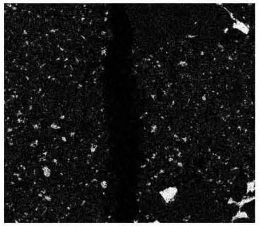

Al Ka1

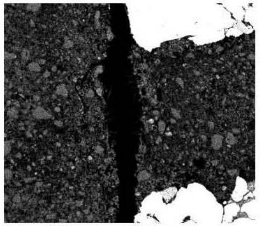

Si Ka1

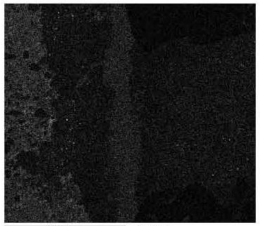

Cl Ka1

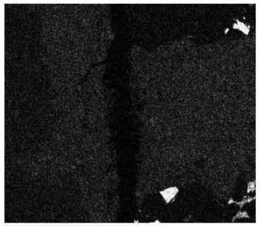

K Ka1

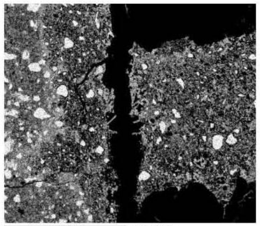

Ca Ka1

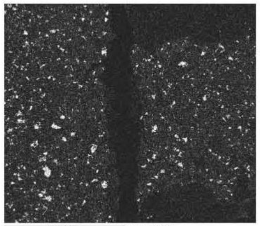

Fe Ka1

Comment:

INCA

DWL1-AC4

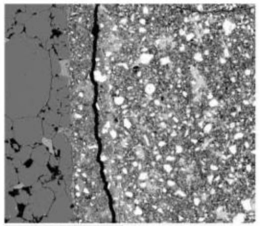

Electron Image 1

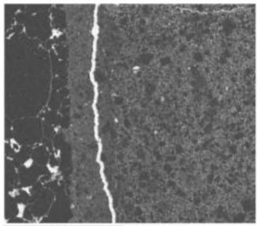

C Ka1_2

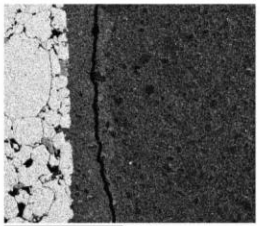

O Ka1

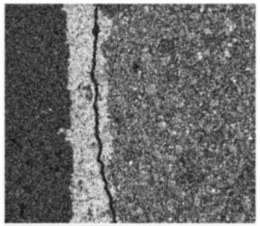

Mg Ka1_2

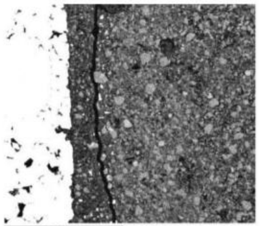

Si Ka1

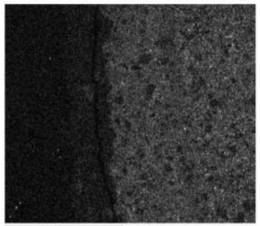

S Ka1

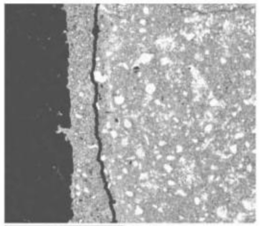

Ca Ka1

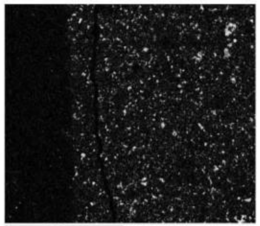

Fe Ka1

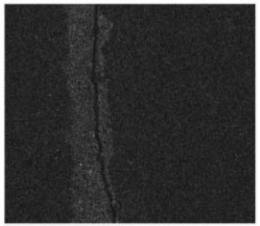

Na Ka1_2

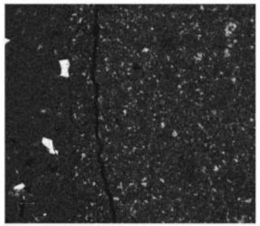

Al Ka1

Comment:

DWL1-AC4

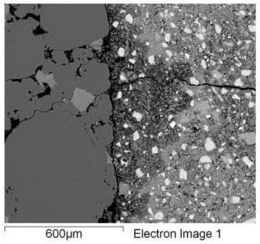
600µm Electron Image 1

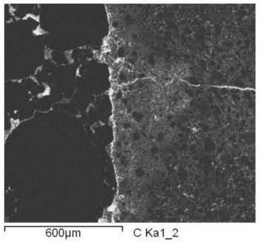
600µm C Ka1_2

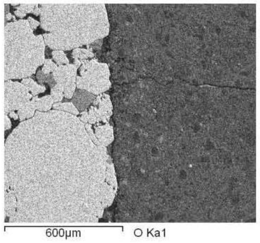
600µm O Ka1

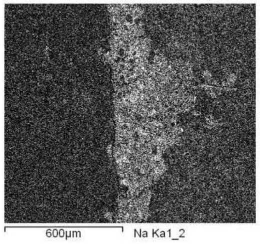
600µm Na Ka1_2

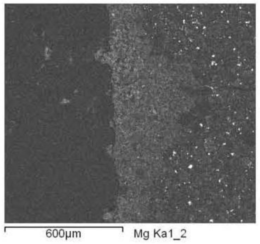
600µm Mg Ka1_2

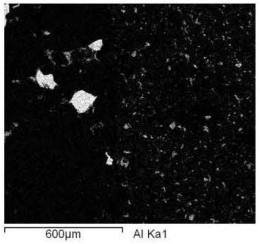
600µm Al Ka1

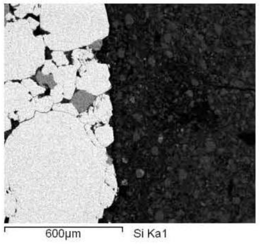
600µm Si Ka1

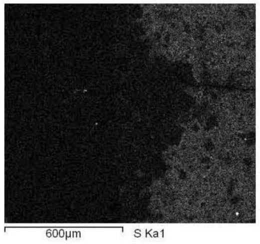
600µm S Ka1

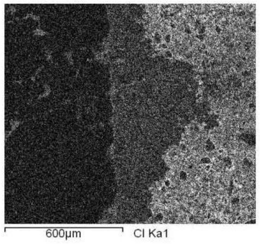
600µm Cl Ka1

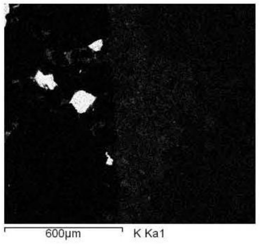
600µm K Ka1

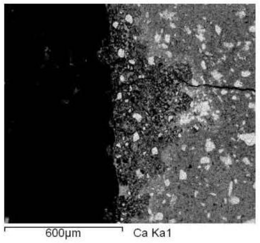
600µm Ca Ka1

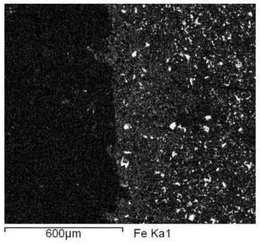
600µm Fe Ka1

Comment:

DWL1-AC4

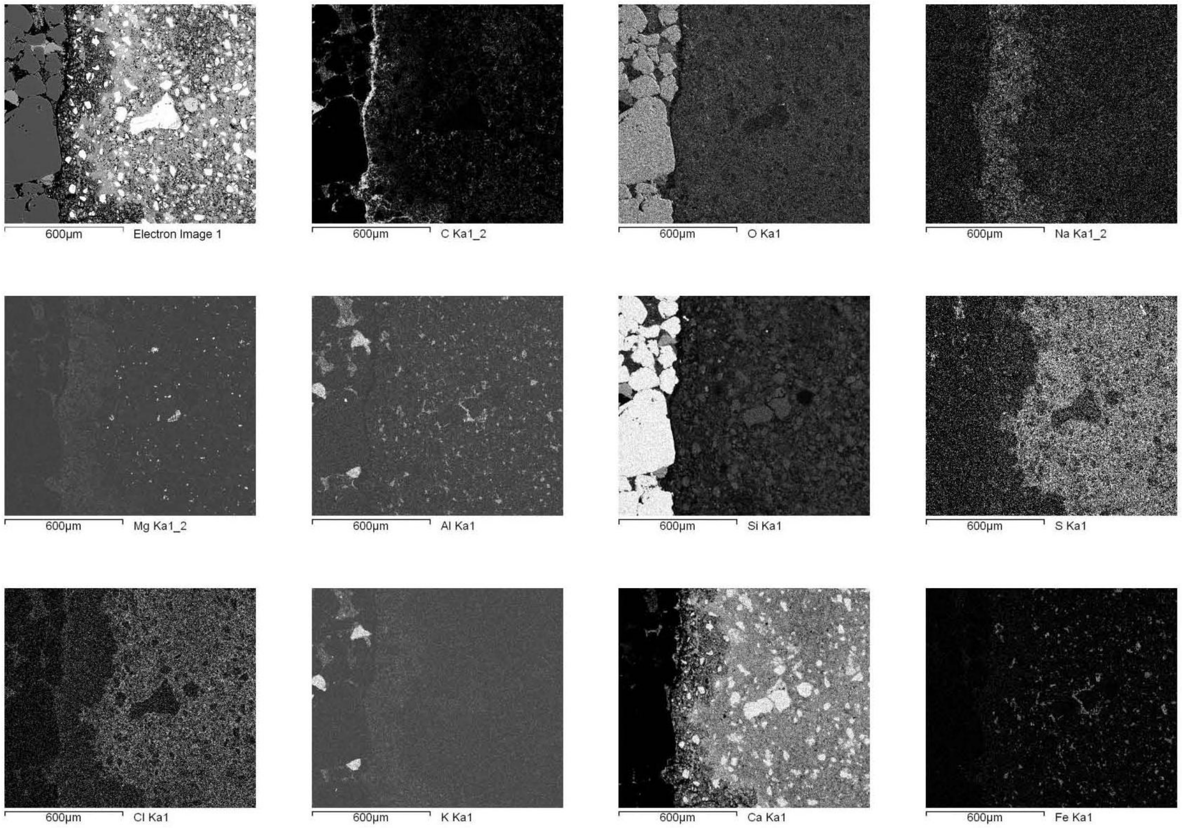

Comment:

DWL1-AC5

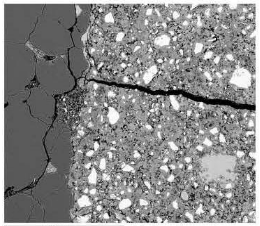

Electron Image 1

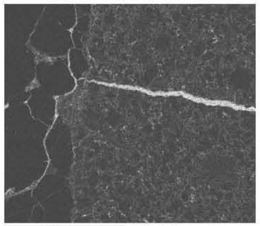

C Ka1_2

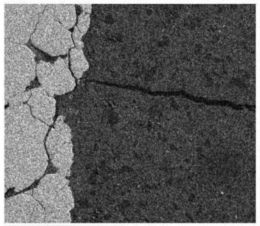

O Ka1

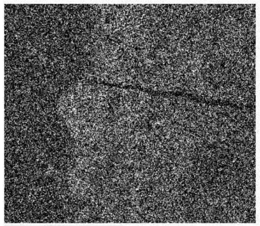

Na Ka1_2

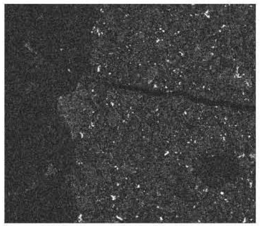

Mg Ka1_2

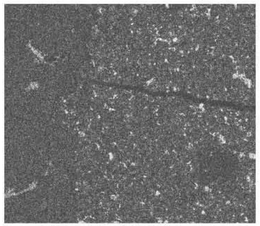

Al Ka1

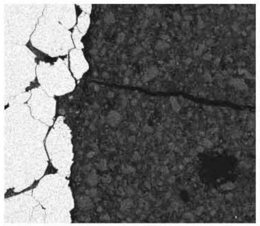

Si Ka1

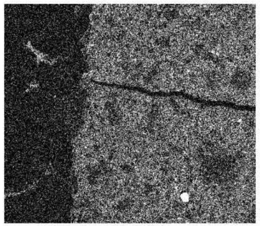

S Ka1

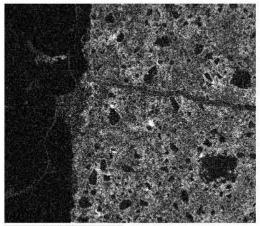

Cl Ka1

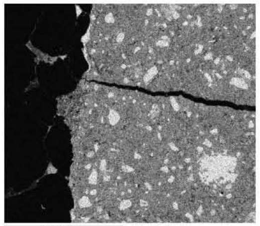

Ca Ka1

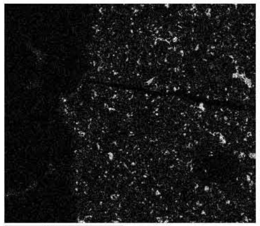

Fe Ka1

Comment:

DWL1-AC5

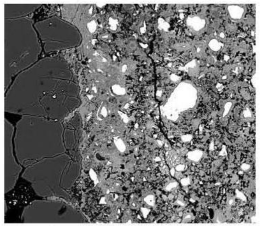

Electron Image 1

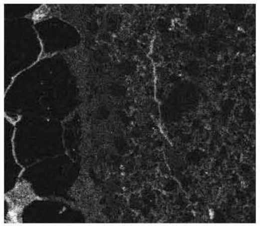

C Ka1_2

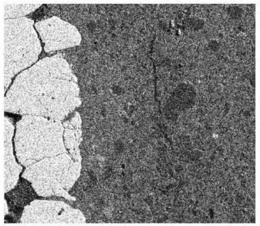

O Ka1

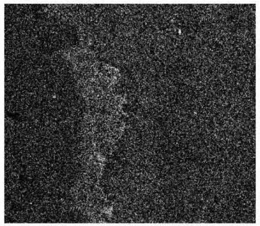

Na Ka1_2

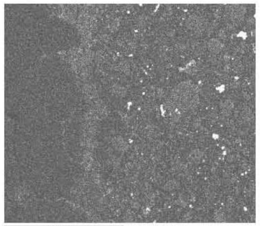

Mg Ka1_2

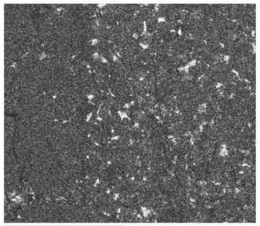

Al Ka1

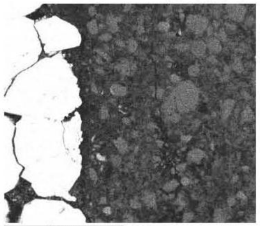

Si Ka1

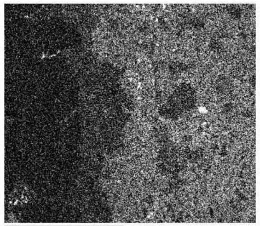

S Ka1

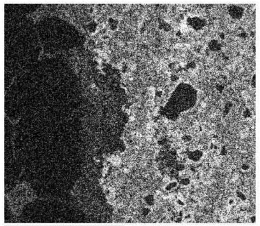

Cl Ka1

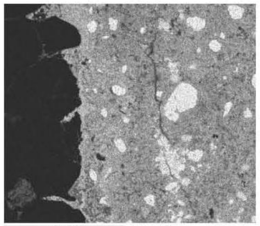

Ca Ka1

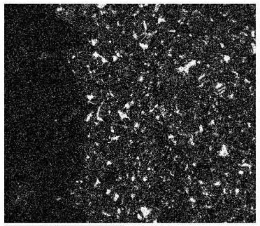

Fe Ka1

Comment:

X-ray Diffraction Patterns: Mt. Simon Sandstone & Grande Ronde Basalt Bonded To Class H Cement Exposed To Supercritical CO_2

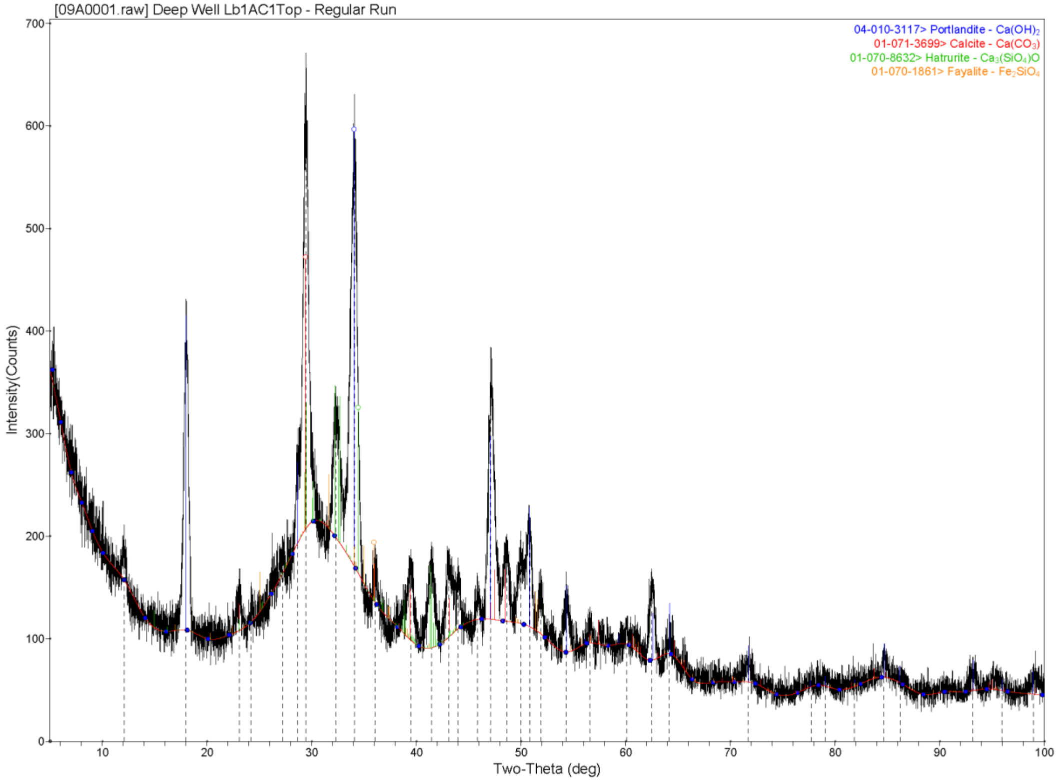

National Energy Technology Laboratory

[SMITH-WXP|Smithd]<Y:\OConnorGroup\2009> Tuesday, April 19, 2011 05:51p (MDI/JADE9)

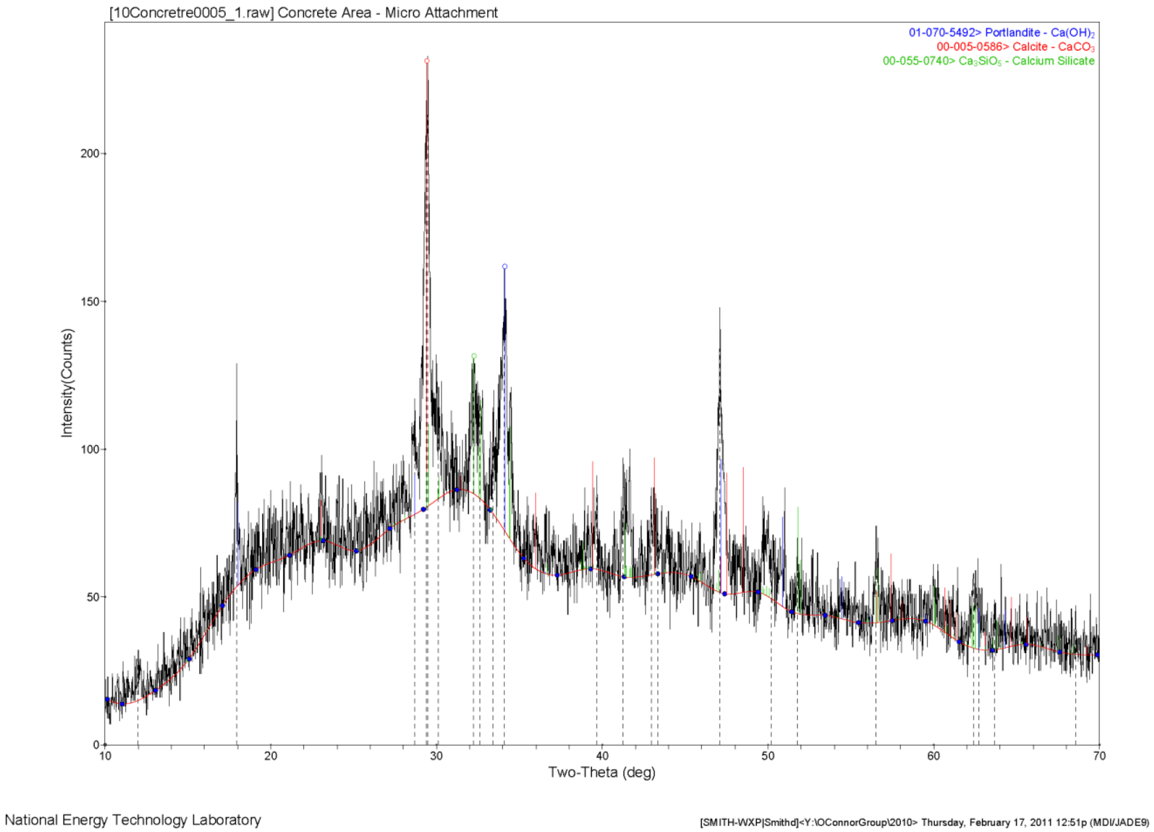
[10Concretre0005_1.raw] Concrete Area - Micro Attachment
01-070-5492> Portlandite - $Ca(OH)_2$
00-005-0586> Calcite - $CaCO_3$
00-055-0740> Ca_3SiO_5 - Calcium Silicate
Intensity(Counts)
200
150
100
50
0
10
20
30
40
50
60
70
Two-Theta (deg)
National Energy Technology Laboratory
[SMITH-WXP|Smithd]<Y:\OConnorGroup\2010> Thursday, February 17, 2011 12:51p (MDI/JADE9)

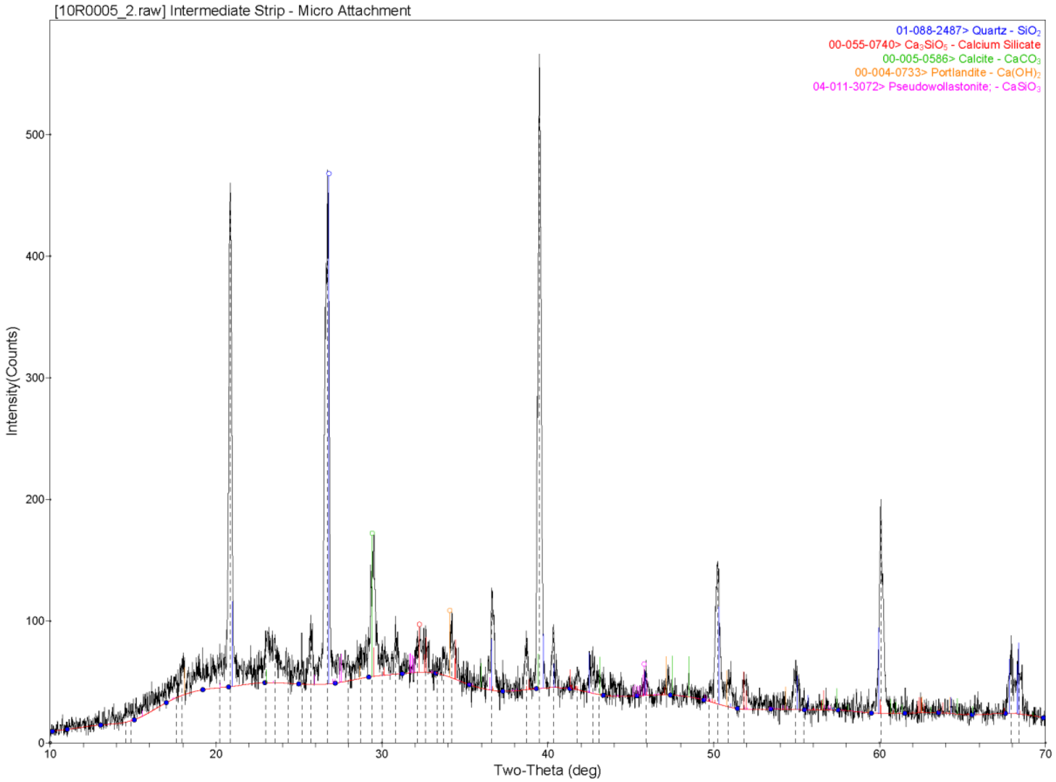

National Energy Technology Laboratory

[SMITH-WXP|Smithd]<Y:\OConnorGroup\2010> Thursday, February 17, 2011 12:48p (MDI/JADE9)

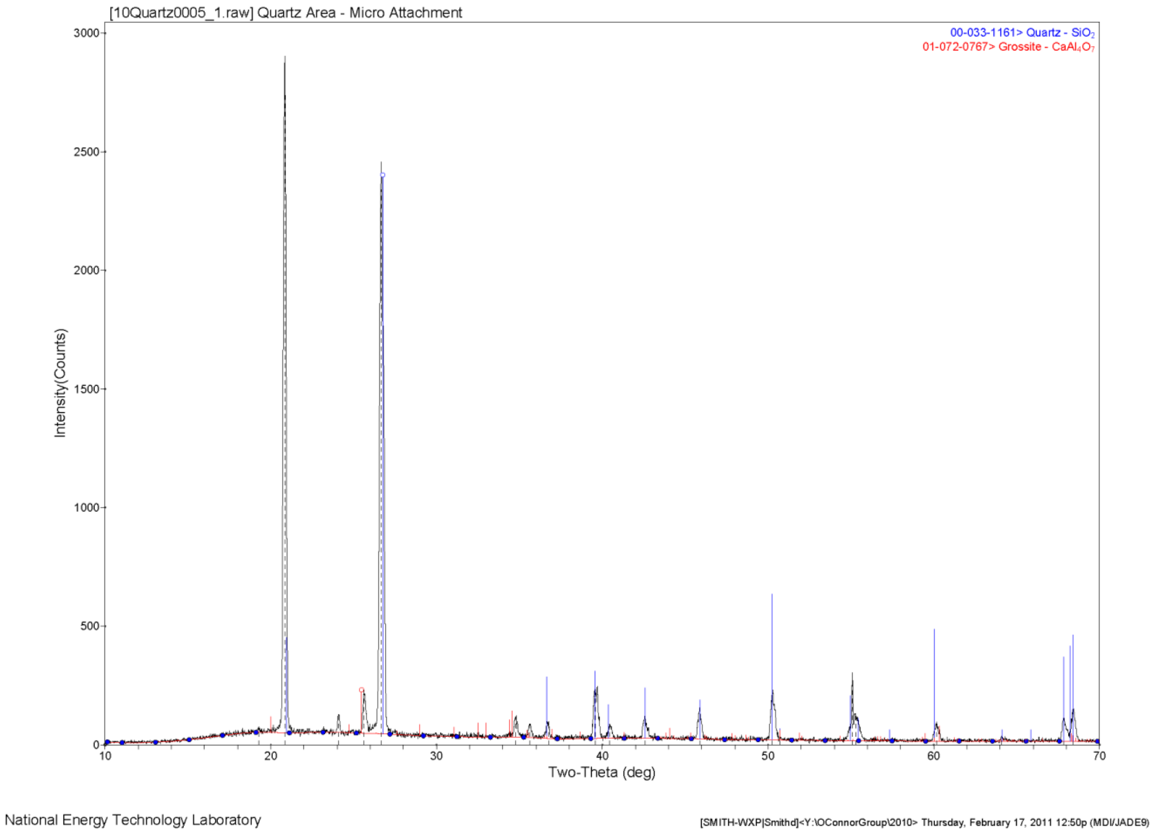
[10Quartz0005_1.raw] Quartz Area - Micro Attachment
00-033-1161> Quartz - SiO_2
01-072-0767> Grossite - $CaAl_4O_7$
Intensity(Counts)
3000
2500
2000
1500
1000
500
0
10
20
30
40
50
60
70
Two-Theta (deg)
National Energy Technology Laboratory
[SMITH-WXP|Smithd]<Y:\OConnorGroup\2010> Thursday, February 17, 2011 12:50p (MDI/JADE9)

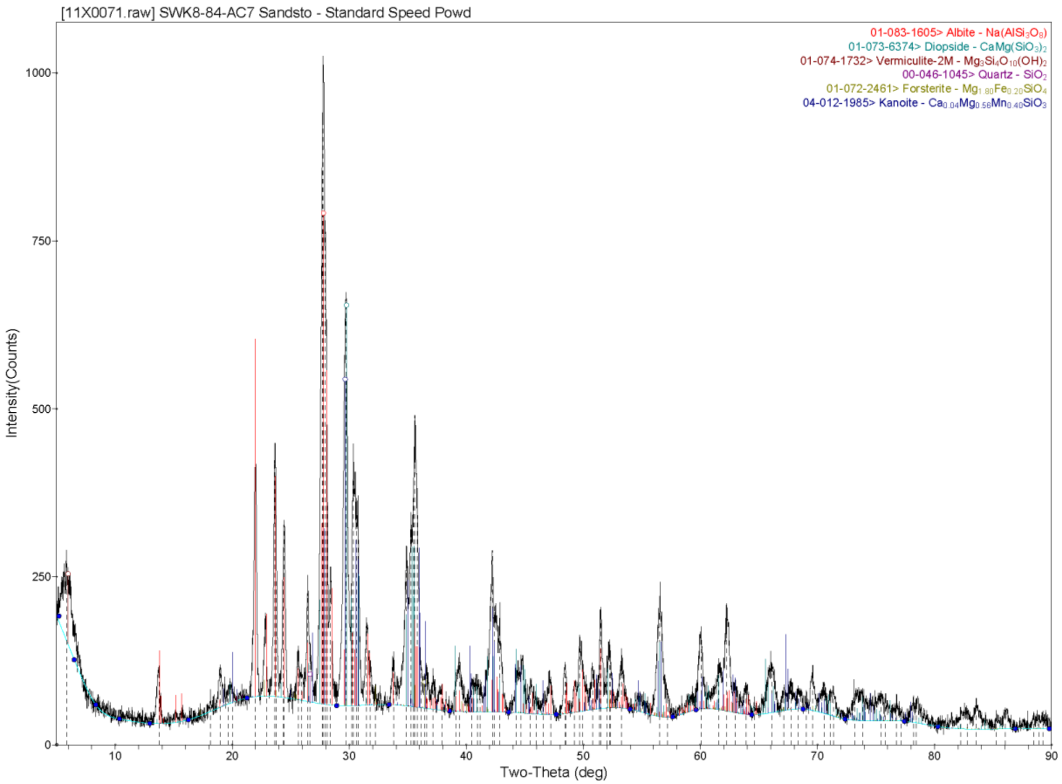

US DEPT OF ENERGY

[ULTIMA3|Administrator]<C:\Windmax\Data\Verba> Monday, March 28, 2011 04:29p (MDI/JADE9)

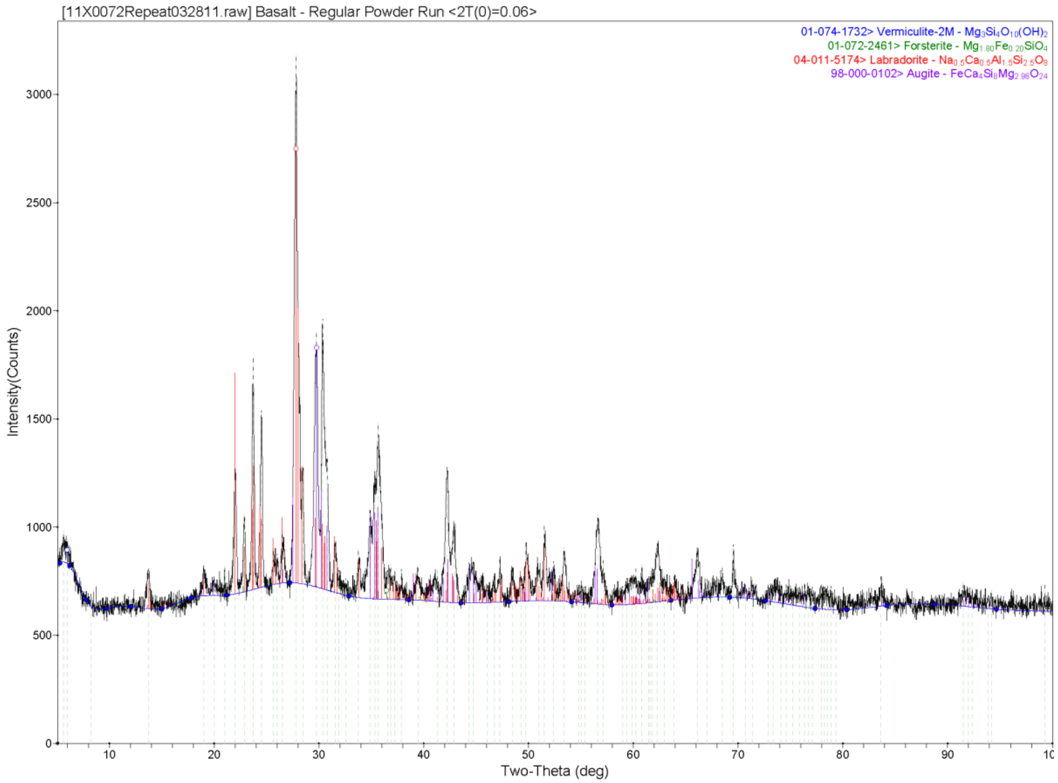

NETL

[PN0000032258|disenhoc]<F:\XRD\Circe\CD work> Wednesday, April 06, 2011 01:47p (MDI/JADE9)

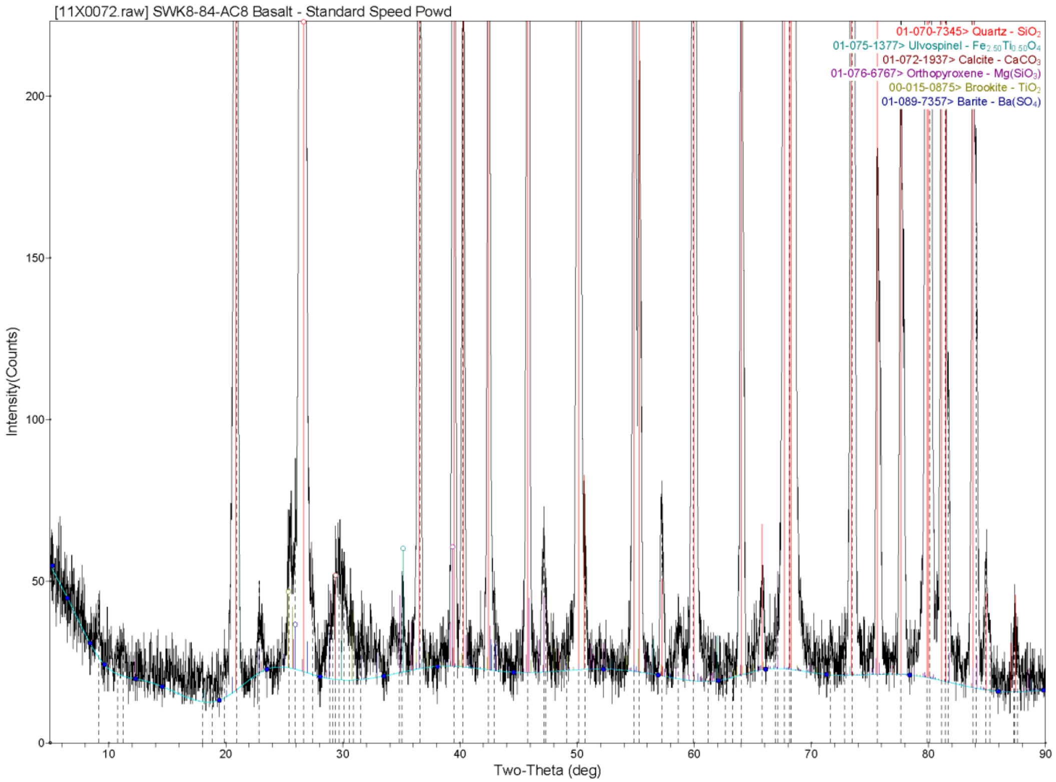

US DEPT OF ENERGY

[ULTIMA3|Administrator]<C:\Windmax\Data\Verba> Monday, March 28, 2011 02:48p (MDI/JADE9)

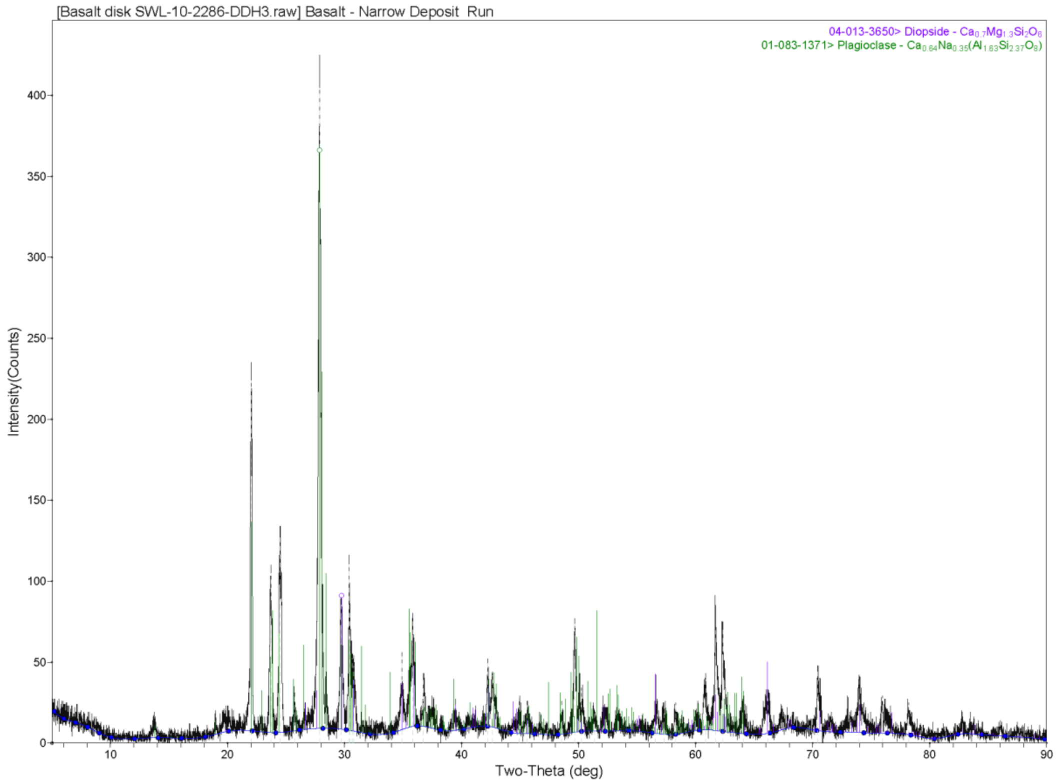

NETL

[PN0000032258|disenhoc]<M:\Basalt Data - Sequestration\XRD Basalt\SWL-10-2286-DDH3> Wednesday, July 20, 2011 12:00p (MDI/JADE9)

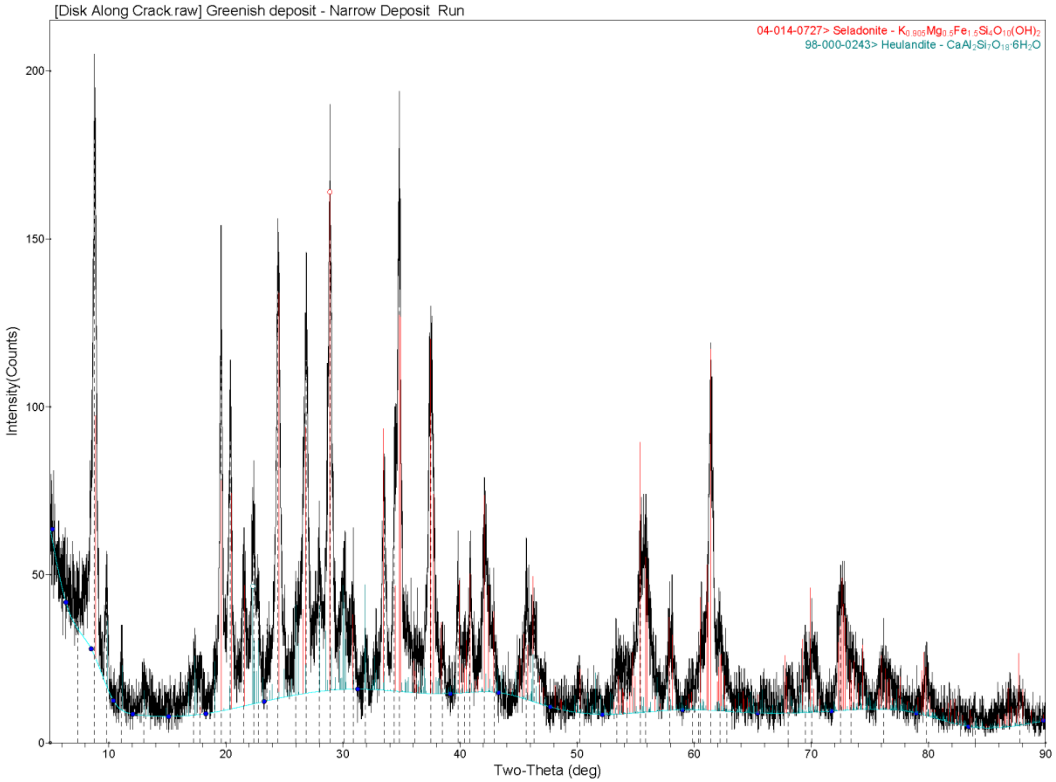

US DEPT OF ENERGY

[ULTIMA3|Administrator]<C:\Windmax\Data\Disenhof> Friday, May 06, 2011 11:22a (MDI/JADE9)

Whole Pattern Fitting and Rietveld Refinement

FILE: [11X0072.raw] SWK8-84-AC8 Basalt - Standard Speed Powd
SCAN: 5.0/90.0/0.02/2.4(sec), Cu(40kV,44mA), I(p)=15104, 03/04/11 04:23a
PROC: [WPF Control File]

☑ K-alpha2 Peak Present
☑ Allow Negative Isotropic B
☑ Allow Negative Occupancy
☑ Apply Anomalous Scattering

[Diffractometer LP] Two-Theta Range of Fit = 5.0 - 90.0(deg)
☑ Specimen Displacement - Cos(Theta) = -0.013974(0.005373)
☐ Monochromator Correction for LP Factor = 1.0
☐ K-alpha2/K-alpha1 Intensity Ratio = 0.5

Profile Shape Function (PSF) for All Phases: pseudo-Voigt, Fixed-BG, Lambda=1.54059Å (Cu/K-alpha1)

	Phase ID (5)	Source	I/Ic	Wt%	#L
🟦	Quartz - SiO_2	PDF#01-070-7345	3.06(5%)	97.9 (7.0)	29
🟩	Ulvospinel - $Fe_{2.50}Ti_{0.50}O_4$	PDF#01-075-1377	4.91(5%)	0.1 (0.0)	18
🟥	Calcite - $CaCO_3$	PDF#01-072-1937	3.23(5%)	1.1 (0.2)	32
🟧	Orthopyroxene - $Mg(SiO_3)$	PDF#01-076-6767	0.55(5%)	0.8 (0.3)	134
🟫	Brookite - TiO_2	PDF#04-003-0844	1.53(0%)	0.1 (0.1)	105

XRF(Wt%): Fe=0.0%, Ti=0.1%, Ca=0.4%, Si=46.0%, Mg=0.2%, O=53.1%, C=0.1%

NOTE: Fitting Halted at Iteration 26(4): R=41.0% (E=8.73%, R/E=4.69, P=29, EPS=0.5)

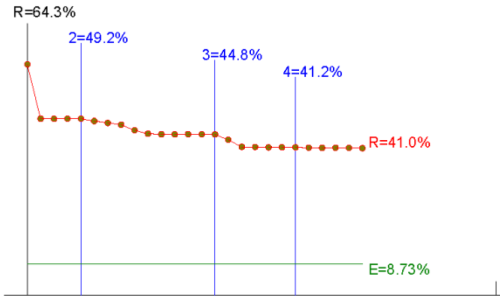

Refinement Iterations

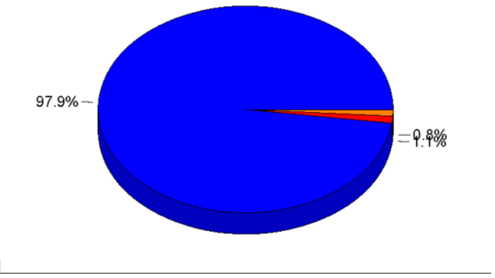

Wt%

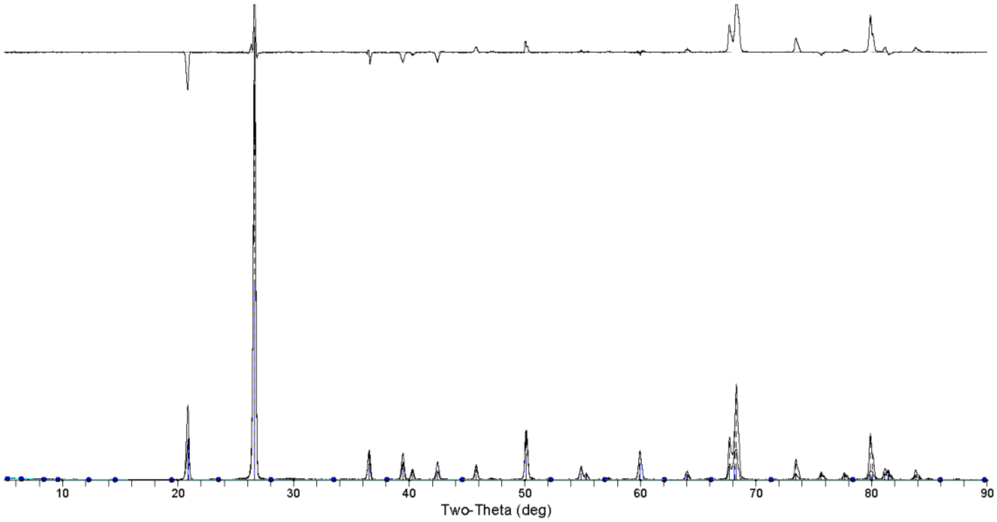

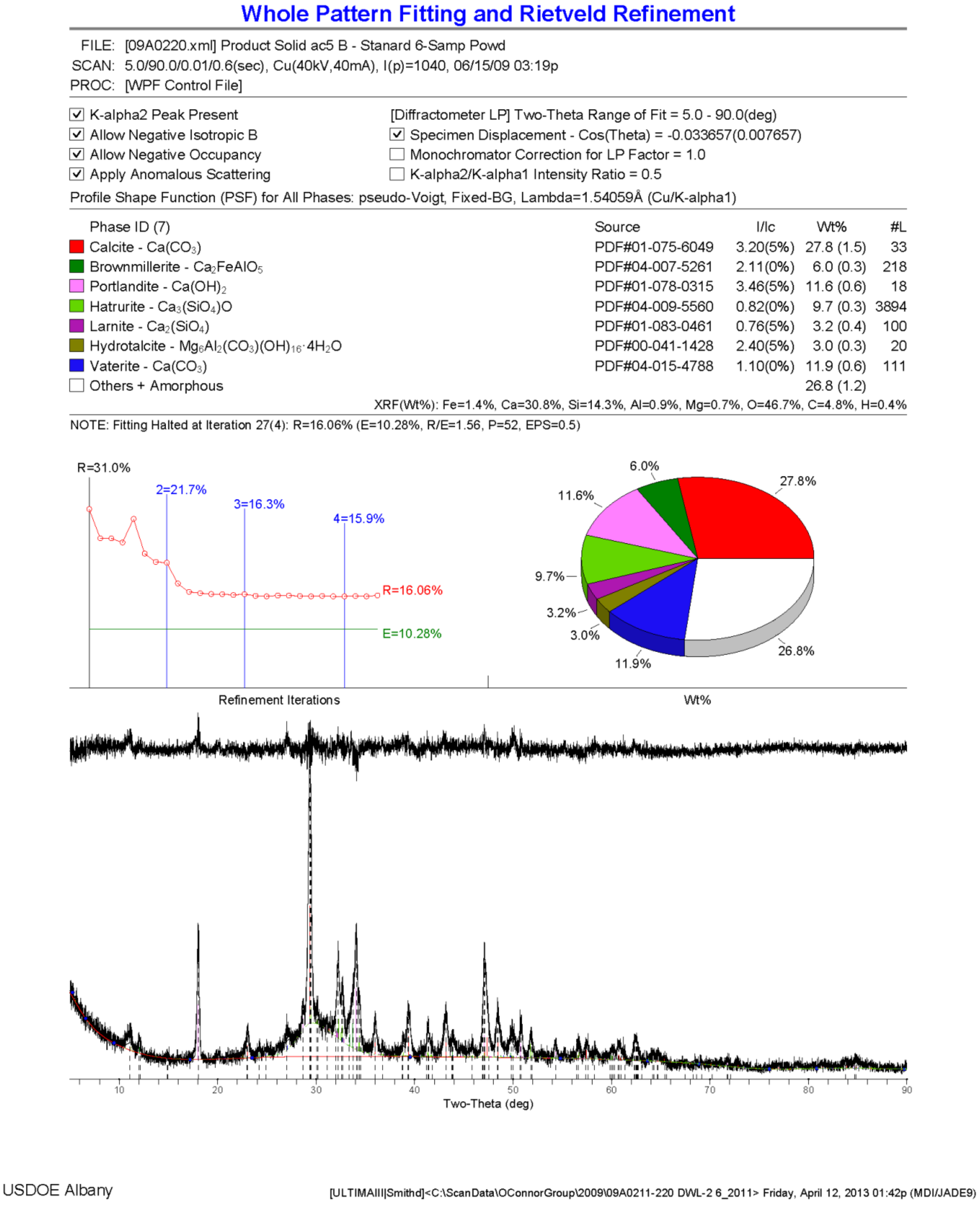

Whole Pattern Fitting and Rietveld Refinement

FILE: [09A0220.xml] Product Solid ac5 B - Stanard 6-Samp Powd
SCAN: 5.0/90.0/0.01/0.6(sec), Cu(40kV,40mA), I(p)=1040, 06/15/09 03:19p
PROC: [WPF Control File]

- ☑ K-alpha2 Peak Present
- ☑ Allow Negative Isotropic B
- ☑ Allow Negative Occupancy
- ☑ Apply Anomalous Scattering

[Diffractometer LP] Two-Theta Range of Fit = 5.0 - 90.0(deg)
- ☑ Specimen Displacement - Cos(Theta) = -0.033657(0.007657)
- ☐ Monochromator Correction for LP Factor = 1.0
- ☐ K-alpha2/K-alpha1 Intensity Ratio = 0.5

Profile Shape Function (PSF) for All Phases: pseudo-Voigt, Fixed-BG, Lambda=1.54059Å (Cu/K-alpha1)

Phase ID (7)	Source	I/Ic	Wt%	#L
🟥 Calcite - Ca(CO_3)	PDF#01-075-6049	3.20(5%)	27.8 (1.5)	33
🟩 Brownmillerite - Ca_2FeAlO_5	PDF#04-007-5261	2.11(0%)	6.0 (0.3)	218
🟪 Portlandite - $Ca(OH)_2$	PDF#01-078-0315	3.46(5%)	11.6 (0.6)	18
🟩 Hatrurite - $Ca_3(SiO_4)O$	PDF#04-009-5560	0.82(0%)	9.7 (0.3)	3894
🟪 Larnite - $Ca_2(SiO_4)$	PDF#01-083-0461	0.76(5%)	3.2 (0.4)	100
🟫 Hydrotalcite - $Mg_6Al_2(CO_3)(OH)_{16}\cdot 4H_2O$	PDF#00-041-1428	2.40(5%)	3.0 (0.3)	20
🟦 Vaterite - Ca(CO_3)	PDF#04-015-4788	1.10(0%)	11.9 (0.6)	111
☐ Others + Amorphous			26.8 (1.2)	

XRF(Wt%): Fe=1.4%, Ca=30.8%, Si=14.3%, Al=0.9%, Mg=0.7%, O=46.7%, C=4.8%, H=0.4%

NOTE: Fitting Halted at Iteration 27(4): R=16.06% (E=10.28%, R/E=1.56, P=52, EPS=0.5)

USDOE Albany

[ULTIMAIII|Smithd]<C:\ScanData\OConnorGroup\2009\09A0211-220 DWL-2 6_2011> Friday, April 12, 2013 01:42p (MDI/JADE9)

Whole Pattern Fitting and Rietveld Refinement

FILE: [09A0216.xml] Product Solid ac1 B - Stanard 6-Samp Powd
SCAN: 5.0/90.0/0.01/0.6(sec), Cu(40kV,40mA), I(p)=406.0, 06/12/09 10:55p
PROC: [WPF Control File]

☑ K-alpha2 Peak Present
☑ Allow Negative Isotropic B
☑ Allow Negative Occupancy
☑ Apply Anomalous Scattering

[Diffractometer LP] Two-Theta Range of Fit = 5.0 - 90.0(deg)
☑ Specimen Displacement - Cos(Theta) = -0.035602(0.007953)
☐ Monochromator Correction for LP Factor = 1.0
☐ K-alpha2/K-alpha1 Intensity Ratio = 0.5

Profile Shape Function (PSF) for All Phases: pseudo-Voigt, Fixed-BG, Lambda=1.54059Å (Cu/K-alpha1)

Phase ID (7)	Source	I/Ic	Wt%	#L
🟥 Calcite - $Ca(CO_3)$	PDF#01-075-6049	3.20(5%)	8.0 (0.6)	33
🟩 Brownmillerite - Ca_2FeAlO_5	PDF#04-007-5261	2.11(0%)	8.7 (0.4)	218
🟦 Portlandite - $Ca(OH)_2$	PDF#01-078-0315	3.46(5%)	20.3 (1.1)	18
■ Hatrurite - $Ca_3(SiO_4)O$	PDF#04-009-5560	0.82(0%)	13.6 (0.5)	3900
🟫 Larnite - $Ca_2(SiO_4)$	PDF#01-083-0461	0.76(5%)	5.2 (1.0)	100
🟨 Hydrotalcite - $Mg_6Al_2(CO_3)(OH)_{16}\cdot 4H_2O$	PDF#00-041-1428	2.40(5%)	5.6 (0.5)	20
🟪 Vaterite - $Ca(CO_3)$	PDF#04-015-4788	1.14(0%)	8.0 (0.7)	109
☐ Others + Amorphous			30.5 (1.3)	

XRF(Wt%): Fe=2.0%, Ca=29.9%, Si=16.8%, Al=1.5%, Mg=1.4%, O=45.7%, C=2.0%, H=0.8%

NOTE: Fitting Halted at Iteration 28(4): R=16.62% (E=13.64%, R/E=1.22, P=53, EPS=0.5)

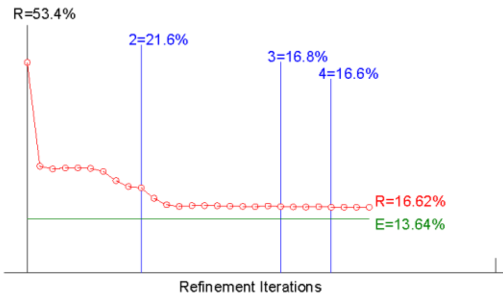

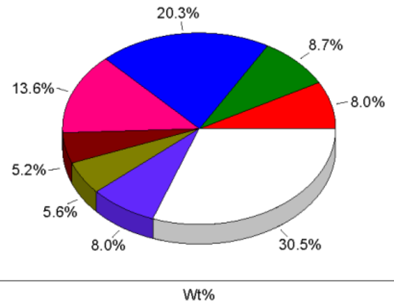

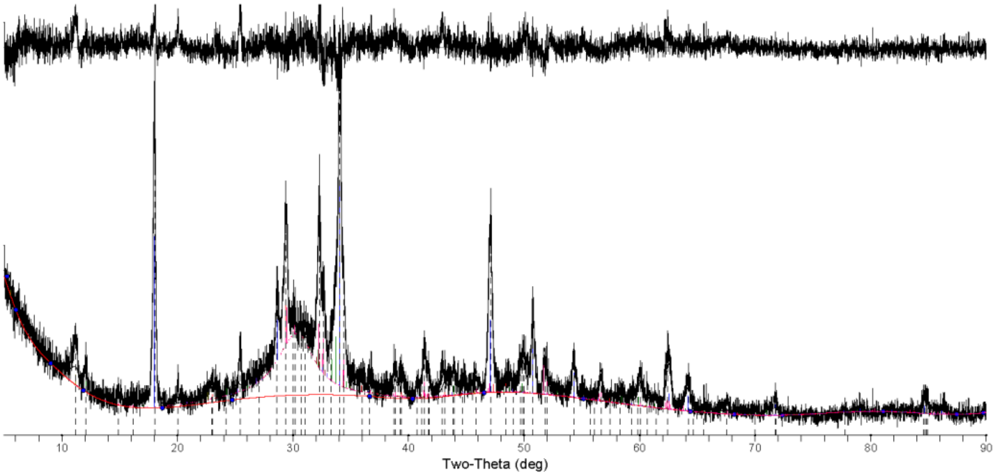

Whole Pattern Fitting and Rietveld Refinement

FILE: [09A0217.xml] Product Solid ac2 B - Stanard 6-Samp Powd
SCAN: 5.0/90.0/0.01/0.6(sec), Cu(40kV,40mA), I(p)=476.0, 06/13/09 12:21a
PROC: [WPF Control File]

☑ K-alpha2 Peak Present
☑ Allow Negative Isotropic B
☑ Allow Negative Occupancy
☑ Apply Anomalous Scattering

[Diffractometer LP] Two-Theta Range of Fit = 5.0 - 90.0(deg)
☑ Specimen Displacement - Cos(Theta) = -0.026043(0.007294)
☐ Monochromator Correction for LP Factor = 1.0
☐ K-alpha2/K-alpha1 Intensity Ratio = 0.5

Profile Shape Function (PSF) for All Phases: pseudo-Voigt, Fixed-BG, Lambda=1.54059Å (Cu/K-alpha1)

	Phase ID (7)	Source	I/Ic	Wt%	#L
🟥	Calcite - Ca(CO_3)	PDF#01-075-6049	3.20(5%)	13.8 (0.8)	33
🟩	Brownmillerite - Ca_2FeAlO_5	PDF#04-007-5261	2.10(0%)	8.0 (0.3)	218
🟧	Portlandite - $Ca(OH)_2$	PDF#01-078-0315	3.46(5%)	17.9 (1.0)	18
🟪	Larnite - $Ca_2(SiO_4)$	PDF#01-083-0461	0.76(5%)	6.0 (0.9)	100
🟫	Hydrotalcite - $Mg_6Al_2(CO_3)(OH)_{16}\cdot 4H_2O$	PDF#00-041-1428	2.40(5%)	6.0 (0.6)	20
🟪	Hatrurite - $Ca_3(SiO_4)O$	PDF#04-009-5560	0.82(0%)	10.7 (0.4)	3892
🟦	Vaterite - Ca(CO_3)	PDF#04-015-4788	1.11(0%)	0.1 (?)	112
☐	Others + Amorphous			37.6 (1.4)	

XRF(Wt%): Fe=1.8%, Ca=26.3%, Si=19.9%, Al=1.4%, Mg=1.4%, O=46.6%, C=1.8%, H=0.7%

NOTE: Fitting Halted at Iteration 19(4): R=16.07% (E=12.89%, R/E=1.25, P=53, EPS=0.5)

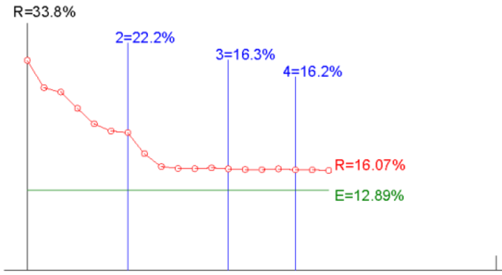

Refinement Iterations

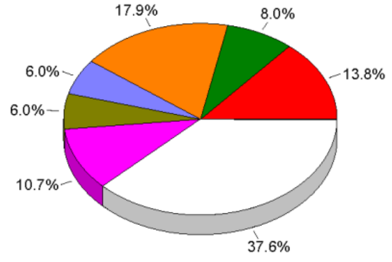

Wt%

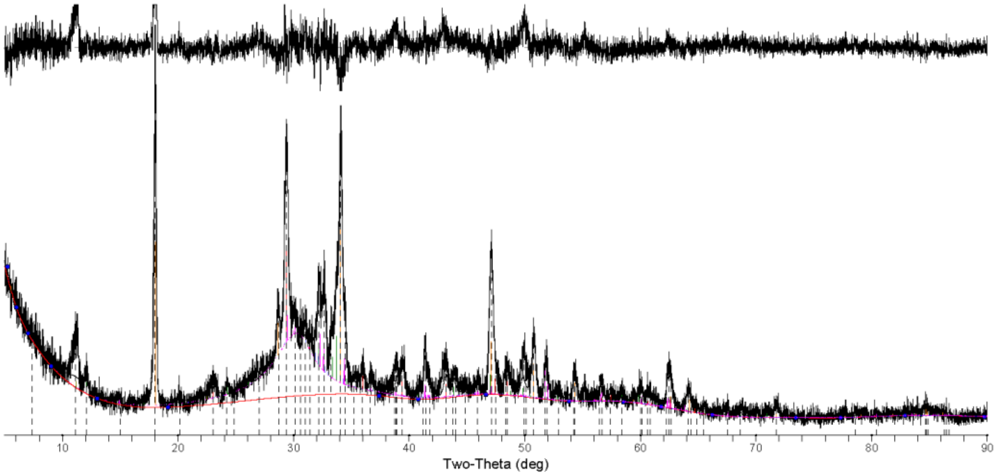

USDOE Albany

[ULTIMAIII|Smithd]<C:\ScanData\OConnorGroup\2009\09A0211-220 DWL-2 6_2011> Thursday, April 11, 2013 04:51p (MDI/JADE9)

Whole Pattern Fitting and Rietveld Refinement

FILE: [09A0218.xml] Product Solid ac3 B - Stanard 6-Samp Powd
SCAN: 5.0/90.0/0.01/0.6(sec), Cu(40kV,40mA), I(p)=515.0, 06/13/09 01:46a
PROC: [WPF Control File]

☑ K-alpha2 Peak Present
☑ Allow Negative Isotropic B
☑ Allow Negative Occupancy
☑ Apply Anomalous Scattering

[Diffractometer LP] Two-Theta Range of Fit = 5.0 - 90.0(deg)
☑ Specimen Displacement - Cos(Theta) = -0.021134(0.008296)
☐ Monochromator Correction for LP Factor = 1.0
☐ K-alpha2/K-alpha1 Intensity Ratio = 0.5

Profile Shape Function (PSF) for All Phases: pseudo-Voigt, Fixed-BG, Lambda=1.54059Å (Cu/K-alpha1)

Phase ID (7)	Source	I/Ic	Wt%	#L
🟥 Calcite - Ca(CO$_3$)	PDF#01-075-6049	3.20(5%)	21.8 (1.2)	33
🟩 Brownmillerite - Ca$_2$FeAlO$_5$	PDF#04-007-5261	2.11(0%)	7.2 (0.3)	218
🟧 Portlandite - Ca(OH)$_2$	PDF#01-078-0315	3.46(5%)	9.4 (0.5)	18
🟪 Larnite - Ca$_2$(SiO$_4$)	PDF#01-083-0461	0.76(5%)	2.3 (0.3)	100
🟥 Hatrurite - Ca$_3$(SiO$_4$)O	PDF#04-009-5560	0.82(0%)	13.7 (0.4)	3894
🟫 Hydrotalcite - Mg$_6$Al$_2$(CO$_3$)(OH)$_{16}$·4H$_2$O	PDF#00-041-1428	2.40(5%)	7.0 (0.5)	20
🟦 Vaterite - Ca(CO$_3$)	PDF#04-015-4788	1.11(0%)	11.1 (0.7)	109
☐ Others + Amorphous			27.5 (0.9)	

XRF(Wt%): Fe=1.7%, Ca=28.9%, Si=14.9%, Al=1.4%, Mg=1.7%, O=46.8%, C=4.1%, H=0.5%

NOTE: Fitting Halted at Iteration 26(4): R=15.04% (E=13.28%, R/E=1.13, P=53, EPS=0.5)

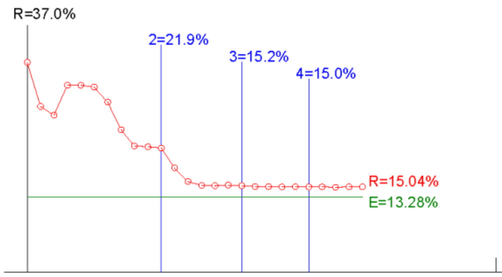

Refinement Iterations

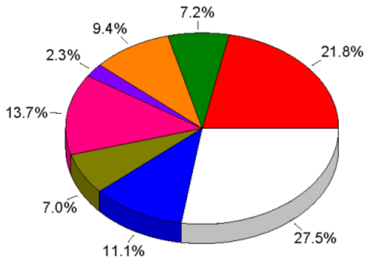

Wt%

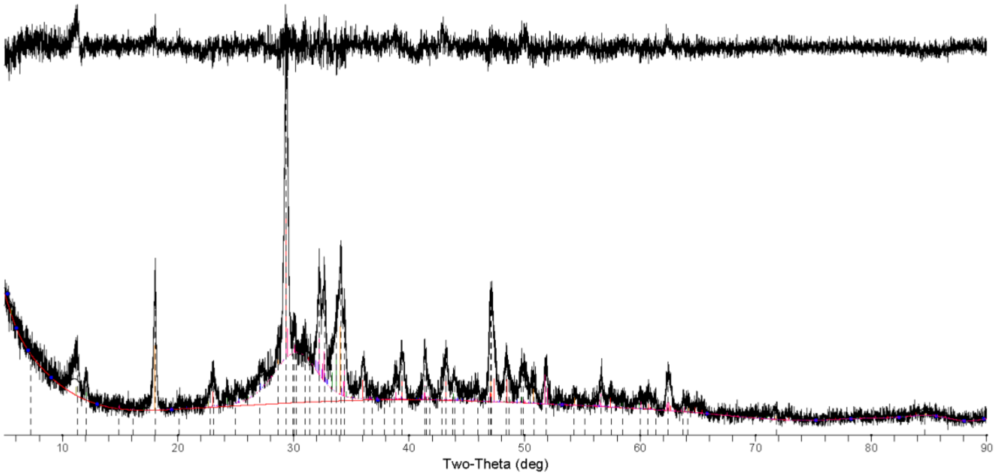

Whole Pattern Fitting and Rietveld Refinement

FILE: [09A0219.xml] Product Solid ac4 B - Stanard 6-Samp Powd
SCAN: 5.0/90.0/0.01/0.6(sec), Cu(40kV,40mA), I(p)=604.0, 06/15/09 01:53p
PROC: [WPF Control File]

☑ K-alpha2 Peak Present	[Diffractometer LP] Two-Theta Range of Fit = 5.0 - 90.0(deg)
☑ Allow Negative Isotropic B	☑ Specimen Displacement - Cos(Theta) = -0.031343(0.009541)
☑ Allow Negative Occupancy	☐ Monochromator Correction for LP Factor = 1.0
☑ Apply Anomalous Scattering	☐ K-alpha2/K-alpha1 Intensity Ratio = 0.5

Profile Shape Function (PSF) for All Phases: pseudo-Voigt, Fixed-BG, Lambda=1.54059Å (Cu/K-alpha1)

	Phase ID (7)	Source	I/Ic	Wt%	#L
🟥	Calcite - Ca(CO$_3$)	PDF#01-075-6049	3.20(5%)	37.2 (2.1)	33
🟩	Brownmillerite - Ca$_2$FeAlO$_5$	PDF#04-007-5261	2.10(0%)	7.6 (0.3)	218
🟫	Portlandite - Ca(OH)$_2$	PDF#01-078-0315	3.46(5%)	3.8 (0.2)	18
🟨	Hydrotalcite - Mg$_6$Al$_2$(CO$_3$)(OH)$_{16}$·4H$_2$O	PDF#00-041-1428	2.40(5%)	4.8 (0.4)	20
🟪	Hatrurite - Ca$_3$(SiO$_4$)O	PDF#04-009-5560	0.82(0%)	9.0 (0.4)	3896
🟪	Larnite - Ca$_2$(SiO$_4$)	PDF#01-083-0461	0.76(5%)	3.4 (0.5)	100
🟦	Vaterite - Ca(CO$_3$)	PDF#04-015-4788	1.09(0%)	16.9 (0.8)	111
☐	Others + Amorphous			17.3 (1.1)	

XRF(Wt%): Fe=1.7%, Ca=32.6%, Si=9.8%, Al=1.3%, Mg=1.2%, O=46.6%, C=6.6%, H=0.3%

NOTE: Fitting Halted at Iteration 30(4): R=16.37% (E=14.18%, R/E=1.15, P=50, EPS=0.5)

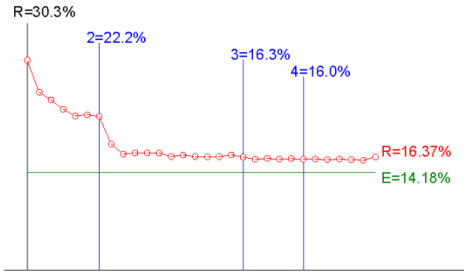

Refinement Iterations

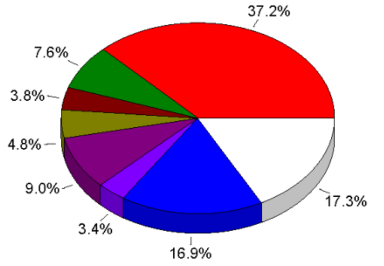

Wt%

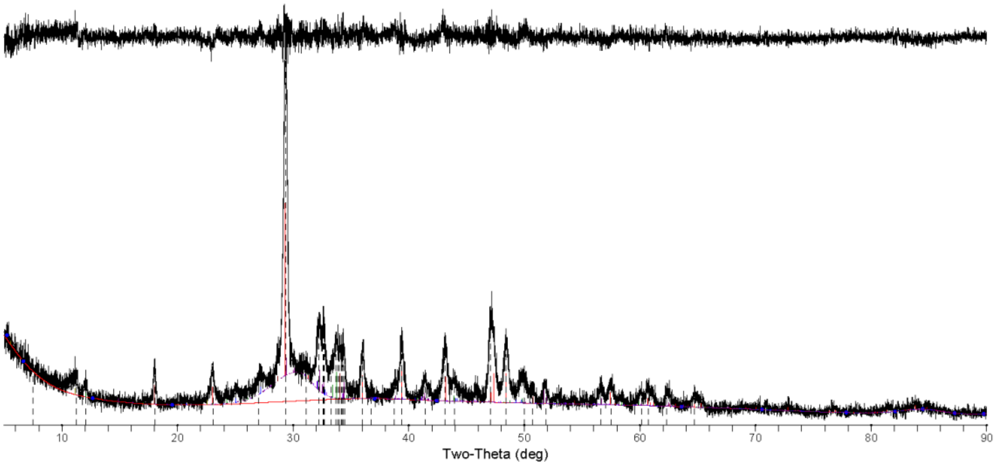

APPENDIX D

ALS Laboratories Mineral And Solution Chemical Data And Analytical Errors

ALS Laboratory Group: Minerals

The composition of basalt, cement, and sandstone as analyzed from ALS Geochemistry Laboratory: H_2SO_4-HF acid digestion and volumetric titration finish to determine solid FeO, carbonate leach and gravimetric analysis for SO_4, thermal decomposition by LECO for total sulfur and carbon, trace metals from ICP-MS (lithium metaborate fusion), and ICP-AES for inorganic metals. The duplicate error is the duplicate tolerance when the solid sample was rerun for comparison to the laboratory's standard.

ALS Global- solid geochemical methods

Method	Short Description	Analyte(s)	Units	DL	UL	Duplicate	Std. Error %
S-IR08	Total Sulphur (Leco)	S	%	0.01	50	5	3.5
C-IR07	Total Carbon (Leco)	C	%	0.01	50	5	3.5
ME-MS81	Lithium Borate Fusion ICP-MS	Ultra trace metals	ppm	0.01-10*	1000	10	10
ME-ICP06	Whole Rock Package - ICP-AES	inorganic oxide metals	%	0.01	100	5	5
ME-MS42	Up to 34 elements by ICP-MS	Trace metals	ppm	0.01	250	10	10
OA-GRA05	Loss on Ignition at 1000C	Whole sample	%	0.01	100	5	5
Fe-VOL01	Ferrous Iron	FeO	%	0.01	100	3.54	2.5
C-Gas06	Carbonate Carbon	C	%	0.05	14	10	7.07
OA-GRA10	Moisture	H2O	%	0.01	100	5	3.54
ME-4ACD81	Base and trace elements, 4-acid digestion, ICP finish	Transition metals	ppm	0.5-2*	10000	10	10

*lower limit ranges dependent on element

ALS Laboratory Group: Analytical Chemistry and Testing Services for Solution

Case Narrative: Inorganics
Brine Solutions -- 100824-2

1. This report consists of liquid samples.

2. The samples were prepared for analysis based on Methods for the Chemical Analysis of Waters and Wastes (MCAWW), May 1994 procedures, Environmental Monitoring Systems Laboratory (EMSL) Rev 2.1 procedures, and Standard Methods for the Examination of Water and Wastewater, 20th Edition 1998 procedures.

3. The samples were analyzed following MCAWW, EMSL, and Standard Method procedures for the following methods:

Analyte	Method	SOP #
Alkalinity	310.1	1106 Rev 8
Bicarbonate	310.1	1106 Rev 8
Carbonate	310.1	1106 Rev 8
Free Carbon Dioxide	ASTM 4500-CO2 D	
pH	150.1	1126 Rev 17
Bromide	300.0 Revision 2.1	1113 Rev 11
Chloride	300.0 Revision 2.1	1113 Rev 11
Fluoride	300.0 Revision 2.1	1113 Rev 11
Sulfate	300.0 Revision 2.1	1113 Rev 11

4. All standards and solutions were used within their recommended shelf life.

5. The samples were prepared and analyzed within the established hold time for each analysis except pH. The samples were analyzed outside of the standard ALS holding time.
All in house quality control procedures were followed, as described below.

6. General quality control procedures.

- A preparation (method) blank and laboratory control sample (LCS) were prepared and analyzed with the samples in each applicable preparation batch. There were not more than 20 samples in each preparation batch.
- The method blank associated with each applicable batch was below the reporting limit for the requested analytes. This indicates that no contaminants were introduced to the samples during preparation and analysis.
- The LCS was within the acceptance limits for each applicable analysis.
- All initial and continuing calibration blanks (ICB/CCB) associated with each applicable analytical batch were below the reporting limit for the requested analytes.
- All initial and continuing calibration verifications (ICV/CCV) associated with each analytical batch were within the acceptance criteria for the requested analytes. This indicates a valid calibration and stable instrument conditions.

7. Matrix specific quality control procedures.
Sample 1009194-1 was designated as the quality control sample for the alkalinity, bicarbonate, and carbonate analysis. Sample 1009194-5 was designated as the quality control sample for the

pH analysis. Per method requirements, matrix QC was performed for the bromide, chloride, fluoride, and sulfate analysis. Since a sample from this order number was not the selected quality control (QC) sample, matrix specific QC results are not included in this report. Similarity of matrix and therefore relevance of the QC results should not be automatically inferred for any sample other than the native sample selected for QC.

- A sample duplicate was prepared and analyzed with the alkalinity, bicarbonate, carbonate, and pH batches. All guidance criteria for precision were met.
- For pH, the difference between the pH of the sample and its duplicate must be less than or equal to 0.2 pH units to be in control. RPD is not calculated for this analysis.

8. Electrical conductivity screening indicated that the concentration of dissolved salts was high in the samples. Therefore, it was necessary to dilute the samples prior to injection into the ion chromatograph in order to minimize the amount of salts loaded into the analytical column.

It was necessary to further dilute the samples in order to bring the chloride concentrations into the analytical range of the ion chromatograph (IC).

Reduced aliquots were taken of the samples for the alkalinity, bicarbonate, and carbonate analysis. The samples had limited sample volume. Reporting limits were elevated accordingly.

9. Manual integrations are performed when needed to provide consistent and defensible data following the guidelines in SOP 939 Revision 3.

Target Analyte	**Spike Added**	**LCS Result**	**Reporting Limit**	**Result Qualifier**	**LCS % Rec.**	**Control Limits**
FLUORIDE	2.5	2.45	0.1		98	90 - 110%
CHLORIDE	5	5.08	0.2		102	90 - 110%
BROMIDE	5	5.26	0.2		105	90 - 110%
SULFATE	25	24.5	1		98	90 - 110%
TOTAL ALKALINITY AS CaCO3	100	99	5		99	85 -115

*LCS= Laboratory control sample

++ Free Carbon Dioxide is derived from Total Alkalinity and pH results for a given sample via Standard Methods SM4500- CO_2 D. pH was determined via SW846 method 9040 and Alkalinity was determined via EPA method 310.1.

Derived Carbon Dioxide Results Are Not Valid For Samples That Contain More Than 500 Mg/L Of Total Dissolved Solids (TDS)

A. Bicarbonate Alkalinity:
HCO_3^- as mg $CaCO_3$/L= $T - 5.0 * 10(^{pH - 10})/1 + 0.94 * 10(^{pH - 10})$
Where T = total alkalinity, mg $CaCO_3$/L

Free Carbon Dioxide Where A = bicarbonate alkalinity, from A:
mg CO_2/L= $2.0 * A * 10(^{6 - pH})$

Case Narrative: Metals
Brine Solutions -- 100824-2

1. The samples were prepared for analysis based on SW-846, 3rd Edition procedures.

For analysis by Trace ICP, the samples were digested following method 3010A and SOP 806 Rev. 14.

2. The samples were analyzed following SW-846, 3rd Edition procedures.

Analysis by Trace ICP followed method 6010B and SOP 834 Rev. 7.
The relationship between intensity and concentration for each element is established using at least four standards, one of which is a blank solution.

During sample analysis concentrations are computed by the software and the results are printed in mg/L. The instrument software does not provide a printout which gives both intensity and concentration. The validity of the calibration equation is tested by analyzing the following solutions: a blank, a low level check solution with concentrations near the reporting limit, an Initial Calibration Verification (ICV) standard from a 2nd source standard solution with concentrations near the middle of the analytical range, a Continuing Calibration Verification (CCV) standard with concentrations at two times those in the ICV, and a readback of the highest calibration standard.

These solutions provide verification that the calibration equations are functioning properly throughout the analytical range of the instrument. During sample analysis dilutions are made for analytes found at concentrations above the highest calibration standard. No results are taken from extrapolations beyond the highest standard.

3. All standards and solutions are NIST traceable and were used within their recommended shelf life.
4. The samples were prepared and analyzed within the established hold times.

All in house quality control procedures were followed, as described below.

5. General quality control procedures.
    - A preparation (method) blank laboratory control sample and laboratory control sample duplicate were digested and analyzed with the samples in this digestion batch. There were not more than 20 samples in this digestion batch.
    - The preparation (method) blank associated with this digestion batch was below the
    - reporting limit for the requested analytes.
    - The laboratory control samples associated with this digestion batch were within the acceptance limits for the requested analytes. This indicates complete digestion according to the method.
    - All initial and continuing calibration blanks associated with this analytical batch were below the practical quantitation limits for the requested analytes.

- All initial and continuing calibration verifications associated with this analytical batch were within the acceptance criteria for the requested analytes, with the exception of CCV16 for phosphorus. All samples were below the reporting limit for phosphorus, no
    - further action was taken.

- The interference check samples and high standard readbacks associated with Method
- 6010B were within acceptance criteria.

6. Matrix specific quality control procedures. Due to limited sample volume matrix QC was limited to an LCS and LCSD.
7. All samples required dilutions to bring nickel and/or sodium into the analytical range of the Trace ICP.

CASNO	Target Analyte	Spike Added	LCSD Result	Reporting Limit	LCSD % Rec.	RPD Limit	Reporting error %
7429-90-5	ALUMINUM	100	97	10	97	20	1
7440-36-0	ANTIMONY	25	22.7	1	91	20	2
7440-38-2	ARSENIC	100	95.1	0.5	95	20	1
7440-39-3	BARIUM	100	95.3	5	95	20	1
7440-41-7	BERYLLIUM	2.5	2.32	0.25	93	20	1
7440-69-9	BISMUTH	50	55.8	1	112	20	1
7440-42-8	BORON	50	46.6	5	93	20	2
7440-43-9	CADMIUM	2.5	2.42	0.25	97	20	1
7440-70-2	CALCIUM	2000	1860	50	93	20	2
7440-47-3	CHROMIUM	10	9.28	0.5	93	20	1
7440-48-4	COBALT	25	23.2	0.5	93	20	1
7440-50-8	COPPER	12.5	11.7	0.5	94	20	1
7439-89-6	IRON	50	44.7	5	89	20	1
7439-92-1	LEAD	25	23.6	0.15	94	20	1
7439-93-2	LITHIUM	25	23.6	0.5	95	20	2
7439-95-4	MAGNESIUM	2000	1920	50	96	20	2
7439-96-5	MANGANESE	25	23.6	0.5	94	20	1
7439-98-7	MOLYBDENUM	50	48.1	0.5	96	20	1
7440-02-0	NICKEL	25	23	1	92	20	1
7723-14-0	PHOSPHORUS	500	501	10	100	20	1
7440-09-7	POTASSIUM	2000	1820	50	91	20	2
7782-49-2	SELENIUM	100	92	0.25	92	20	1
7440-21-3	SILICON	100	91.9	2.5	92	20	1
7440-22-4	SILVER	5	4.69	0.5	94	20	1
7440-23-5	SODIUM	2000	1830	50	91	20	2
7440-24-6	STRONTIUM	25	24	0.5	96	20	1
7440-28-0	THALLIUM	100	99.1	0.5	99	20	2
7440-31-5	TIN	25	25.1	2.5	100	20	2
7440-32-6	TITANIUM	25	23.8	1	95	20	1
7440-61-1	URANIUM	500	487	10	97	20	2
7440-62-2	VANADIUM	25	23.7	0.5	95	20	1
7440-66-6	ZINC	25	23	1	92	20	1

REFERENCES CITED

Allen, D. E., Strazisar, B. R., Soong, Y., and Hedges, S. W. (2005). Modeling carbon dioxide sequestration in saline aquifers: Significance of elevated pressures and salinities. Fuel Processing Technology, 86.

Andac, *M*., and Glasser, F. P. (1999). Long-term leaching mechanisms of Portland cement-stabilized municipal solid waste flyash in carbonated water. Cement and Concrete Research, 29, 179-186.

API. (1997). Recommended practice for testing well cements. API Recommended Practice 10B, p. 133. Washington, DC.

ASTM C 109, (1998) "Test Method for Compressive Strength of Hydraulic Cement Mortars (Using 2-in or [50-mm] Cube Specimens),"Annual Book of ASTM Standards, vol. 04.01, ASTM West Conshohocken, PA.

ASTM C 150 compressive strength specifications

ASTM C 873-94, "Test Method for Compressive Strength of Concrete Cylinders Cast in Place in Cylindrical Molds."

Bachu, S.,Watson,T.L. (2009). Review of failures for wells used for CO2 and acid gas injection in Alberta, Canada, Energy Procedia. 1,3531–3537.

Bachu, S., and Adams, J. J. (2003). Sequestration of CO_2 in geological media in response to climate change: Capacity of deep saline aquifers to sequester CO_2 in solution. Energy Conversion and Management, 44, 3151-3175.

Bachu, W. D. Gunter, and Perkins, E. H. (1994). Aquifer disposal of CO_2: Hydrodynamic and mineral trapping. Energy Conservation and Management, 35(4), 269–279.

Barlet-Gouedard, V., Rimmele, G., Goffe, B., and Porcherie, O. (2007). Well technologies for CO_2 geological storage: CO_2-resistant cement. Oil and Gas Science and Technology, 62, 325–334.

Barlet-Gouedard, V., Rimmele, G., Porcherie, O., Quisel, N, and Desroches, J. A. (2009). Solution against well cement degradation under CO_2 geological storage environment. International Journal of Greenhouse Gas Control, 3, 206–216.

Barron, A. (2009) Application of Portland cement in the energy services industry. Connexions Project.

Bearden, W. G. (1959). Effect of temperature and pressure on the physical properties of cement. Oil-Well Cementing Practices in the United States (pp. 49-59). New York: API.

Beaudoin, J. J., Ramachandran, V. S., and Feldman, R. F. (1990). Interaction of chloride and C-S-H. Cement and Concrete Research, 20, 833–875.

Bennion, D. B., and Bachu, S. (2008). Dependence on temperature, pressure, and salinity of the IFT and relative permeability displacement characteristics of CO_2 injected in deep saline aquifers. In Proceedings from SPE Annual Technical Conference and Exhibition. SPE 102138. San Antonio, Texas.

Bentur et al. (1979). Structural properties of calcium silicate pastes: II, Effect of curing temperature. Journal of American Ceramic Society, 62(7-8), 362-366.

Bergman, P. D., and Winter, E. *M*. (1995). Disposal of carbon dioxide in the U.S. Energy Conversion Mgmt., 36, 523-526.

Bertolini, L., Bernhard, E., Pedeferri, P., and Polder, R. (2004). Transport processes in concrete. In Corrosion of steel in concrete. ISBN: 3-527-30800-8 (pp. 21-32). Wiley-VCH Verlag Gmbh & Co. KGaA, Weinheim.

Birnin-Yauri, U. A., and Glasser, F. P. (1998). Friedel's salt, Ca2 Al(OH)6 (Cl, OH) 2H2O: Its solid solutions and their role in chloride binding. Cement and Concrete Research, 28(12), 1713–1723

Bresson, B., and Zanni, H. (1998). Pressure and temperature influence on tricalcium silicate hydration. A 1H and 29Si NMR study. J. Chim. Phys., 95, 327-331.

Bresson, B., Meducin, F., and Zanni, H. (2002). Hydration of tricalcium silicate (C3S) at high temperature and high pressure. Journal of Materials Science, 37, 5355-5365.

Bruant, R. G., Guswa, A. J., Celia, *M*. A., and Peters, C. A. (2002). Safe storage of CO_2 in deep saline aquifers. Environ. Sci. Technol., 36, 240-245.

Bruckdorfer, R. A. (1986). Carbon dioxide corrosion in oilwell cements. SPE 15176.

Campbell, D. H. (1986/1999). Microscopical examination and interpretation of Portland cement and clinker. Portland Cement Association.

Carey, J. W., Wigand, *M*., Chipera, S. J., Wolde Gabriel, G., Pawar, R., Lichtner, P. C., Wehner, S. C., Raines, *M*. A., and Guthrie, G. D. (2007). Analysis and performance of oil well cement with 30 years of CO_2 exposure from the SACROC unit, West Texas, U.S.A. Intl. J. Greenhouse Gas Control, 1(1), 75-85.

Chi, J.M., Huang, R., & Yang, C.C. (2002). Effect of carbonation on mechanical properties of concrete using accelerated testing method. *Journal of Marine Science and Technology* 10(1): 14-20.

Cody, R. D., Cody, A. *M*., Spry, P. G., and Gan, G. (1996). Experimental deterioration of highway concrete by chloride deicing salts. Environmental & Engineering Geoscience, II(4), 575-588.

Colleparadi, *M*. (2003). A state-of-the-art review on delayed ettringite attack on concrete. Cement & Concrete Composites, 25, 401-407.

Collepardi, *M*. (1999). Damage by delayed ettringite formation. Concrete International, 69-74.

Colston et al. (In press). An in situ energy-dispersive diffraction study of the hydration of oilwell cement systems under high temperature/autoclave conditions up to 130˚C. Cement and Concrete Research.

Crandell, L. E., Ellis, B. R., and Peters, C. A. (2010). Dissolution potential of SO2 Co-injected with CO_2 in geologic sequestration. Environ. Sci. Technol., 44, 349-355.

Crow, W., Williams, B., Carey, J.W., Celia, M., Gasda, S., 2009, Wellbore integrity analysis of a natural CO_2 producer. Proc. 9th Int. Conf. Greenhouse Gas Control Technologies, Washington DC, USA.

Csizmadia, J., Balázs, G., and Tamás, F. D. (2001). Chloride ion binding capacity of aluminoferrites. Cement and Concrete Research, 31, 577–588.

Davidson, J., Freund, P., and Smith, A. Putting carbon back into the ground. IEA Greenhouse Gas R&D Programme (IEA GHG) Report, ISBN1 898373 28 0.

Department of Energy. (2007). Carbon sequestration technology roadmap and program plan. Washington, DC: U.S. Department of Energy.

Diamond, S. (1996). Delayed ettringite formation — processes and problems. Cement and Concrete Composites, 18, 205-215.

Diamond, S., Ong S., and Bonen, D. (1994). Characteristics of secondary ettringite deposited in steam cured concrete undergoing ASR. In Proceedings.

Dilmore, R.M., Allen, D.E., McCarthy Jones, J.R., Hedges, S.W., and Soong, Y., 2008, Sequestration of dissolved CO_2 in the Oriskany Formation: Environmental Science and Technology, v. 42, p. 2760-2766.

Duan ZH, Sun R, Zhu C, et al. (2006) An improved model for the calculation of CO2 solubility in aqueous solutions containing Na+, K+, Ca2+, Mg2+, Cl-, and SO42-. Marine Chem., 98 (2-4): 131-139.

Duan, Z., and Sun, R. (2003). An improved model calculating CO_2 solubility in pure water and aqueous NaCl solutions from 257 to 533 K and from 0 to 2000 bar. Chem. Geol., 193, 257–271.

Duguid, A., and Scherer, G. (2009). Degradation of oilwell cements due to exposure to carbonated brine. Int. J. Greenhouse Gas Control, 4(3), 546-560.

Duguid, A., Radonjic, *M*., and Scherer, G. (2005). Degradation of well cements exposed to carbonated brine. Proceedings from the 4th Annual Conference on Carbon Capture and Sequestration, May 2-5, at Monitor and Exchange Publications and Forum, Washington D.C.

Duguid, A., Radonjic, *M*., and Scherer, G. W. (2011). Degradation of cement at the reservoir/ cement interface from exposure to carbonated brine. International Journal of Greenhouse Gas Control, 5(6), 1413-1428.

Fabbri, A., Corvisier, J., Schubnel, A., Brunet, F., Goffe, B., Rimmele, G., and Barlet-Gouedard, V. (2009). Effect of carbonation on the hydro-mechanical properties of portland cements. Cement and Concrete Research, 39(12), 1156-1163.

Famy, C., and Taylor, H. F. W. (2001). Ettringite in hydration of Portland cement concrete and its occurrence in mature concretes. ACI Mater. J., 98(4), 350-356.

Feldman, R. F., and Ramachandran, V. S. (1966) Character of Hydration of 3CaO•Al2O3, *J. Amer. Cer. Soc*, v. 49 pp. 268–273

Flatt, R. Scherer, G.W. (2008). Thermodynamics of crystallization stresses in DEF. Cement and Concrete Research (38): pp. 325-336.

Fu, Y., and Beauidoin, J. J. (1996). Mechanism of delayed ettringite formation in Portland cement system. ACI Mater J., 327–33.

Ghods, P., Isgor, O. B., McRae, G., and Miller, T. (2009). The effect of concrete pore solution composition on the quality of passive oxide films on black steel reinforcement. Cem. Concr. Compos., 31(1), 2–11.

Glasser, F. P. (2001). The role of Ca(OH)2 in Portland cement concretes. In J. Skalny, J. Gebauer, and I. Odler (Eds.), Calcium Hydroxide in Concrete. The American Ceramic Society (pp. 11-36). Westerville, Ohio.

Grant, J.A., 1986, The isocon diagram--a simple solution to Gresens' equation for metasomatic alteration. Economic Geology, v. 81, p. 1976-1982.

Grant, J.A., 2005, Isocon analysis: a brief review of the method and applications. Physics and Chemistry of the Earth Special Issue.

Helgeson, H. C., Kirkham, D. H., and Flowers, G. C. (1981). Theoretical prediction of the thermodynamic behavior of aqueous electrolytes at high pressures and temperatures: IV. Calculation of activity coefficients, osmotic coefficients, and apparent molal and standard and relative partial molal properties to 600°C and 5 kbar. Amer. J. Sci., 281, 1249-1516.

Herzog, H., Drake, E., and Adams, E. (1997). CO2 capture, reuse, and storage technologies for mitigating global climate change. DOE Order No. DE-AF22-96PC01257.

Hewlett, P.C. (Ed) (1998). Lea's Chemistry of Cement and Concrete. 4th Ed, Arnold, London pp 299-342.

Hitchon, B. (1996). Aquifer Disposal of Carbon Dioxide. Sherwood Park, Alberta Resource Council: Geoscience Publishing Ltd.

Hitchon, B. et al. (1999). Sedimentary basins and greenhouse gases: A serendipitious association. Energy Conversion & Management, 40, 825-843.

Hobbs, D. W. (1999). Expansion and cracking in concrete associated with delayed ettringite formation. In B. Erlin (Ed.), Ettringite – The Sometimes Host of Destruction. ACI Report SP-177. (Reported in Keith Quillin, 2001).

Holloway, S. (2005). Underground sequestration of carbon dioxide – A viable greenhouse gas mitigation option. Energy, 30, 2318-2333.

http://www.cement.ca/cement.nsf/0/4366443DA425F3C3852568A8007B9157?OpenDocument.

International Centre for Diffraction Data. (2008). Powder Diffraction File Update: PDF-2.

International Nickel Company, Inc. (1963). Corrosion resistance of the austenitic chromium-nickel stainless steels in chemical environments.

Jacquemet, N., Pironon, J., and Saint-Marc, J. (2008). Mineralogical changes of a well cement in various H2S-CO_2(-brine) fluids at high pressure and temperature. Environmental Science & Technology, 42, 282-288.

Johannesson, B., and Utgenannt, P. (2001). Microstructural changes caused by carbonation of cement mortar. Cement and Concrete Research, 31, 925–931.

Johansen, V., Thaulow, N., and Skalny, J. (1993). Adv. Cem. Res., 5 (17), 23.

Johnson, J. W., Oelkers, E. H., and Helgeson, H. C. (1992). SUPCTR92: A software package for calculating the standard molal thermodynamic properties of minerals, gases, aqueous species, and reactions from 1 to 5000 bar and 0 to 1000 8C. Comput. Geosci., 7, 899-947.

Keith, D. W., Giardina, J. A., Morgan, M. G., and Wilson, E. J. (2005). Regulating the underground injection of CO2. Environmental Science and Technology, 39(24), 499A-505A.

Kim, J. K., Moon, Y. H., and Eo, S. H. (1998). Compressive strength development of concrete with different curing time and temperature. Cem. Concr. Res., 28, 1761–1773.

Krilov, Z., Loncaric, B., and Crosco, Z. M. (2000). Investigation of a long-term cement deterioration under a high-temperature gas downhole environment. SPE 58771.

Kutchko, B. G., Strazisar, B. R., Lowry, G. V., Dzombak, D. A., and Thaulow, N. (2008). Rate of CO2 attack on hydrated class H well cement under Geologic Sequestration Conditions. Environ. Sci. Technol., 42(16), 6237-6242.

Kutchko, B. G., Strazisar, B. R., Lowry, G. V., Dzombak, D. A., and Thaulow, N. (2008). Rate of CO_2 attack on hydrated class H well cement under Geologic Sequestration Conditions. Environ. Sci. Technol., 42(16), 6237-6242.

Kutchko, B. G., Strazisar, B. R., Dzombak, D. A., Lowry, G. V., and Thaulow, N. (2007). Degradation of well cement by CO_2 under geologic sequestration conditions. Environ. Sci. Technol., 13(41), 4787–4792.

Kutchko, B., Strazisar, B., Hawthorn S., Lopano, C., Miller, D., Hakala, A., and Guthrie, G. (2011). H2S-CO_2 reaction with hydrated class H well cement: Acid-gas injection and CO_2 co-sequestration. Environmental Science and Technology. 5(4), 880-888.

Lawrence, B., Moody, E., Guillemette, R., and Carrasquillo, R. (1999). Evaluation and mitigating measures for premature concrete distress in Texas, Department of Transportation Concrete Elements. Journal of Cement, Concrete and Aggregates (CCA), 21(1), 73-81.

Le Saout, G. et al. (2013). Chemical structure of cement aged at normal and elevated temperatures and pressures. Part I. Class G oilwell cement. Cement and Concrete Research.

Le Saout, G. et al. (2004). Study of oilwell cements by solid-state NMR. C.R. Chimie, 7, 383-388.

Lécolier, E., Rivereau, A., Ferrer, N., Audibert, A. and Longaygue, X. (2006). Durability of oilwell cement formulations aged in H2S-containing fluids. IADC/SPE 99105, IADC/SPE Drilling Conference, Miami, Florida, USA, 21-23 February.

Locher, F. W., Richartz, W., and Sprung, S. (1976). Setting of cement – Part I: Reaction and development of structure. ZKG Intern., 29(10), 435-442.

Lorenz, S., and Müller, W. (2003). Modeling of halite formation in natural gas storage aquifers. Paper presented at TOUGH Symposium, Lawrence Berkeley Natl. Lab., Berkeley, California.

Matschei, T., Lothenbach, B., and Glasser, F. P. (2007). Thermodynamic properties of Portland cement hydrates in the system CaO-Al2O3-SiO2-CaSO4-$CaCO_3$-H2O. Cem. Concr. Res., 37, 1379-1410.

Matteo, E. N., and Scherer, G. W. (2012). Experimental study of the diffusion-controlled acid degradation of class H Portland cement. International Journal of Greenhouse Gas Control, 7, 181–191.

McGrail, B. P., Schaef, H. T., Ho, A. *M*., Chien, Y. J., Dooley, J. J., and Davidson, C. L. (2006). Potential for carbon dioxide sequestration in flood basalts. Journal of Geophysical Research, 111, B12201.

Meducin, F. et al. (2001). Oilwell cements: NMR contribution to establish the phase diagram pressure/temperature of the mixture H2O/Ca3SiO5. C.R. Acad. Sci.Paris, Chimie/ Chemsitry, 4, 801-804.

Méducin, F. et al. (2002). Complementary analyses of a tricalcium silicate sample hydrated at high pressure and temperature. Cement and Concrete Research, 32, 65-70.

Meller, N., Hall,C., Jupe, A.C., Colston, S.L.,Jacques, S.D.M., Barnes, P., Phipps, J. (2004). The paste hydration of brownmillerite with and without gypsum: a time resolved synchrotron diffraction study at 30, 70, 100 ,and 150 ◦C. Journalof Materials Chemistry 14,428–435.

Mehta, P., and Monteiro, P. (2006). Concrete: Microstructure, properties, and materials. 3rd ed., McGraw Hill.

Milestone, N. B., Sugama, T., Kubacka, L. E., and Carciello, N. (1986). Carbonation of geothermal grouts – Part 1: CO_2 attack at 150˚C. Cement and Concrete Research, 16, 941-950.

NATCARB Database. NatCarb: 2008 version. http://www.natcarb.org.

Nelson, E. B. (1990). Well cementing. Sugar Land, TX: Schlumberger Educational Services.

Neville, A. (1995). Chloride attack of reinforced concrete: an overview. Materials and Structures, 28, 63-70.

O'Connor, W. K., Dahlin, D. C., Rush, G. E., Dahlin, C. L., and Collins, W. K. (2002). Carbon dioxide sequestration by direct mineral carbonation: Process mineralogy of feed and products. Miner. Metall. Processes, 19, 95–101.

Onan, D. D. (1984). Effects of supercritical carbon dioxide on well cements. SPE 12593.

Palandri, J. L., and Kharaka, Y. K. (2005). Ferric iron-bearing sediments as a mineral trap for CO2 sequestration: Iron reduction using sulfur-bearing waste gas. Chemical Geology, 217, 351-364.

Plummer, L. N., and Busenberg, E. (1982). The solubilities of calcite, aragonite and vaterite in CO_2–H2O solutions between 0 and 90 °C, and an evaluation of the aqueous model for the system $CaCO_3$–CO_2. Geochimica et Cosmochimica Acta, 46, 1011–1040.

Pourbaix, *M*. (1974). Atlas of Electrochemical Equilibria in Aqueous Solutions. National Association of Corrosion Engineers, Houston, TX, USA.

Pruess, K., and Müller, N. (2009). Formation dry-out from CO_2 injection into saline aquifers: 1. Effect of solids precipitation and their mitigation. Water Resource. Res., 45, W03402, doi:10.1029/2008WR007101.

Reed, *M*. H. (1982). Calculation of multicomponent chemical equilibria and reaction processes in systems involving minerals, gases, and an aqueous phase. Geochimica Cosmochimica Acta, 46, 513-528.

Reed, *M*. H. (1998). Techniques in hydrothermal ore deposits geology. Reviews in Economic Geology, 10, 109-124. Richards and P. Larson (Eds.).

Reed, *M*. H., and Spycher, N. F. (1984). Calculation of pH and mineral equilibria in hydrothermal water with application to geothermometry and studies of boiling and dilution. Geochim. Cosmochim. Acta, 48, 1479-1490.

Reed, *M*., and Palandri, J. (2013). SOLTHERM.H08, A database of equilibrium constants for minerals and aqueous species. Eugene, Oregon: University of Oregon.

Reidel, S. P. (2005). A lava flow without a source. The Cohassett flow and its compositional components, Sentinel Bluffs member, Columbia River Basalt Group. J. Geol., 113, 1-21.

Reidel, S. P., Johnson, V. G., and Spane, F. A. (2002). Natural gas storage in basalt aquifers of the Columbia Basin, Pacific Northwest USA: A guide to site characterization. Richland, WA: Pacific Northwest National Laboratory.

Richards, L. A. (1931). Capillary conduction of liquids through porous mediums. Physics, 1(5), 318–333. Bibcode 1931Physi...1..318R. doi:10.1063/1.1745010.

Ridgwell, A., and Zeebe, R. (2005). The role of the global carbonate cycle in the regulation and evolution of the Earth system. Earth Planet. Sci. Lett., doi:10.1016/j.epsl.2005.03.006.

Rimmelé, G., Barlet-Gouédard, V., Porcherie, O., Goffé, B., and Brunet, F. (2008). Heterogeneous porosity distribution in Portland cement exposed to CO_2-rich fluids. Cem. Concr. Res., 38, 1038-1048.

Rosenbauer, R. J., Koksalan, T., and Palandri, J. L. (2005). Experimental investigation of CO_2-brine-rock interactions at elevated temperature and pressure: Implications for CO_2 sequestration in deep-saline aquifers. Fuel Processing Technology, 86, 1581-1597.

Rumpf, B., Nicolaisen H., Ocal C., and Maurer, G. (1994). Solubility of carbon dioxide in aqueous solutions of sodium chloride: Experimental results and correlation. J. Sol. Chem., 23, 431–448.

Schaef, H. T., and McGrail, B. P. (2009b). Dissolution of columbia river basalt under mildly acidic conditions as a function of temperature: Experimental results relevant to the geological sequestration of carbon dioxide. Applied Geochemistry, 24(5), 980-987.

Schaef, H. T., McGrail, B. P., and Owen, A. T. (2009a). Basalt-CO_2-H2O interactions and variability in carbonate mineralization rates. In Energy Procedia, 9th International Conference on Greenhouse Gas Control Technologies, 1(1), 4899-4906. Amsterdam, Netherlands: Elsevier.

Scherer, G. W. (1999). Crystallisation in pores. Cement and Concrete Research, 29(8), 1347-1358.

Scherer, G. W. (2004). Stress from crystallization of salt. Cement and Concrete Research, 34(9), 1613–24.

Scherer, G. W., Kutchko, B., Thaulow, N., Duguid, A., and Mook, B. (2011). Characterization of cement from a well at Teapot Dome Oil Field: Implications for geologic sequestration. Int. J. Greenhouse Gas Control, 5, 115–1240.

Scherer, G. W., Zhang, J., Weissinger, E. A., and Peethamparan, S. (2010). Early hydration and setting of oil well cement. Cement Concr. Res., 40, 1023–1033.

Scrivener, K., and Skalny P. (2005). Conclusions of the international RILEM TC 186-ISA workshop on internal sulfate attack and delayed ettringite formation. Materials and Structures, 38(280), 659-663.

Shen, J. C. 1989. Effects of CO_2 attack on cement in high-temperature applications. SPE 18618.

Shock, E. L. et al. (1998). SLOP98.dat (computer data file). http://geopig.asu.edu/supcrt92_data/slop98.dat, accessed on 2005-11-05. Current location: http://geopig.asu.edu/sites/default/files/slop98.dat.

Spycher, N., and Pruess, K. (2005). CO_2-H2O mixtures in the geological sequestration of CO_2. II. Partitioning in chloride brines at 12–100 °C and up to 600 bar. Geochimica et Cosmochimica Acta,69(13), 3309-3320.

St. John, D. A., Poole, A. W., and Sims, I. (1998). Concrete petrography: A handbook of investigative techniques. London: Arnold.

Stark, J., and Bollmann, K. (1999). Ettringite formation in concrete pavements. ACI Spring Convention, Seattle 1997, Special Publication ACI Journal.

Stark, J., and Ludwig, H.-*M*. (1995). The influence of the type of cement on the freeze-thaw and freeze-deicing-salt-resistance of concrete. Intern. Conf. on Concrete under Severe Conditions CONSEC. Sapporo/Japan.

Stutzman, P. (2004). Scanning electron microscopy imaging of hydraulic cement microstructure. Cement and Concrete Composites, 26, 957-966.

Stutzman, P. E. (2001). Scanning electron microscopy in concrete petrography. In J. Skalny, J. Gebauer, and I. Odler, (Eds.), Materials Science of Concrete Special Volume: Calcium Hydroxide in Concrete. The American Ceramic Society (pp. 59-72).

Stutzman, P. E., and Clifton, J. R. (April 1999). Specimen preparation for scanning electron microscopy. In Proceedings of the twenty-first international conference on cement microscopy, eds. L. Jany and A. Nisperos, Las Vegas, Nevada, pp. 10-22.

Sweatman, R. E., Santra, A., Kulakofsky, D. S., and Calvert, D. G. J. (2009). Effective zonal isolation for CO_2 sequestration wells. In SPE International Conference on CO_2 Capture, Storage, and Utilization, SPE Paper 126226. San Diego, California.

Tanger IV, J. C., and Helgeson, H. C. (1998). Calculation of the thermodynamic and transport properties of aqueous species at high temperatures and pressures: Revised equations of state for the standard and partial molal quantities of ions and electrolytes. Am. J. Sci. V., 288, 19– 98.

Taylor, H. F. W. (1997). Cement chemistry. New York: Academic Press.

Taylor, H. F. W. Symposium on Materials Science of Cement and Concrete, High Tatra, Slovakia, June 1993.

Taylor, H. F. W., Famy, C., and Scrivener, K. L. (2001). Delayed ettringite formation. Cement and Concrete Research, 31, 683-693.

Thaulow, N., Lee, R. J., Wagner, K., and Sahu, S. (2001). Effect of calcium hydroxide on the form, extent, and significance of carbonation. In J. Skalny, J. Gebauer, and I. Odler (Eds.), Calcium Hydroxide in Concrete. The American Ceramic Society. (pp. 191-201). Westerville, Ohio.

U.S. Energy Information Administration. (April 2011). Annual energy review.

Verba, C A., O'Connor, W. K., Rush, G. E. (2012). Class H Portland cement paste with CO_2 injection and the influence of brine. In submission.

Verba, C. A., O’Connor, W. K., and Rush, G. E. (2010). CO_2 alteration rates for class H Portland cement. Presented at 9th Annual Conference on Carbon Capture and Sequestration, May 10-13, at Pittsburgh, PA.

Verba, C. A., O'Connor, W. K., and Rush, G. E. (2011). Implications of geologic CO_2 sequestration for basaltic and siliceous host rocks and class H cement. Presented at 10th Annual Carbon Sequestration Conference, May 2-5, at Pittsburgh, PA.

Vlachou, P., and Piau, J. (1999). Physicochemical study of the hydration process of an oil well cement slurry before setting. Cement and Concrete Research, 29, 27-36.

White, C. M., Strazisar, B. R., Granite, E. J., Hoffman, J. S., and Pennline, H. W. (2003). Seperation and capture of CO2 from large stationary sources and sequestration in geological formations – Coalbeds and deep saline aquifers. J. Air & Waste Manage. Assoc., 53, 645-715.

Wilson, E. J., Johnson, T. L., and Keith, D. W. (2003). Regulating the ultimate sink: Managing the risks of geologic CO_2 storage. Environ. Sci. Technol., 37, 3476-3483.

Working Group III of the Intergovernmental Panel on Climate Change, IPCC Special Report on Carbon Dioxide Capture and Storage. (2005). Eds. Metz, B., Davidson, O., de Conink, H.C., and Meyer, L.A. New York: Cambridge University Press.

Xu, T, Apps, J. A., and Pruess, K. (2005). Mineral sequestration of carbon dioxide in a sandstone-shale system, Chemical Geology, 217(3-4), 295-318. DOI information: 10.1016/j.chemgeo.2004.12.015, 2005.

Yang, R., Lawrence, C. D., Lynsdale, C. I., and Sharp, I. H. (1999). Delayed ettringite formation in heat-cured Portland cement mortars. Cem. Concr. Res., 29(1), 17-25.

Zhang, *M*., and Bachu, S. (2011). Review of integrity of existing wells in relation to CO_2 geological storage: What do we know? International Journal of Greenhouse Gas Control, 5(4), 829-840.

Zhang, T., Cheeseman, C. R., and Vandeperre, L. J. (2011). Development of low pH cement systems forming magnesium silicate hydrate (*M*-S-H). Cement and Concrete Research, 41(4), 439-442. ISSN 0008-8846, 10.1016/j.cemconres.2011.01.016.

Zhang, J., Weissinger, E. A., S. Peethamparan, and G. W. Scherer. "Early hydration and setting of oil well cements", Cement and Concrete Research, 40 (2010) 1023-1033

Ziomek-Moroz, *M*., O’Connor, W., and Bullard, S. (2012). Investigations of Localized Corrosion of Stainless Steel after Exposure to Supercritical CO_2. National Association of Corrosion Engineers (NACE) Corrosion 2012 Conference in March.

Zivica, V., and Bajza, A. (2002). Acidic attack of cement-based materials – A review Part 2. Factors of rate of acidic attack and protective measures. Construction and Building Materials, 16, 215-222.